Thermoelastic properties of salt hydrates and implications for geological structures.

A thesis submitted to University College London

for the degree of Doctor of Philosophy

by

Helen Brand

Department of Earth Sciences,
University College London,
Gower Street, London WC1E 6BT, United Kingdom

May 2009

Abstract

This thesis reports the results of neutron diffraction studies and first principles *ab initio* simulations of two salt hydrates in the Na_2SO_4 – H_2O and $MgSO_4$ – H_2O systems, namely mirabilite ($Na_2SO_4 \cdot 10H_2O$) and meridianiite ($MgSO_4 \cdot 11H_2O$). Neutron diffraction experiments of deuterated mirabilite were carried on the High Resolution Powder Diffractometer (HPRD) at the ISIS spallation neutron source to measure its thermal expansion from 4.2 - 300 K and its incompressibility from 0 – 0.55 GPa. A detailed analysis of both the thermal expansion and incompressibility data is presented including determination of the thermal expansion tensor and elastic strain tensor. First principles *ab initio* calculations were also carried out on both materials to complement the experimental studies and to extend the study to higher pressures outside the experimental range. Mirabilite was simulated from 0 – 61 GPa; at least two new phases were detected resulting from first-order phase transformations. Meridianiite was simulated from 0 – 11GPa; this material shows one transition to a higher pressure phase (probably second-order).Finally, a simple model has been developed, incorporating the density of mirabilite determined in the experiments, to study the size and ascent speed of diapiric salt hydrate structures as they interact with, and travel through, a more viscous overburden layer within the upper crust of Earth, Mars and Ganymede, a large icy satellite of Jupiter.

"There is a theory which states that if ever anybody discovers exactly what the universe is for and why it is here, it will instantly disappear and be replaced by something even more bizarre and inexplicable.

There is another theory which states that this has already happened."

Douglas Adams, The Restaurant at the end of the Universe.

Acknowledgements

Firstly, this thesis could not have been produced without a Blue Skies PhD studentship funding from NERC (Grant no. NER/S/A/2005/13554), beamtime at ISIS provided by STFC (beamtime applications: RB610128 (HRPD), RB810197 (HRPD) and RB910178 (SXD)) with support from local contacts Kevin Knight and Matthias Gutmann, as well as members of the sample environment group. The calculations in this work were carried out using HPCx, the UK's national high-performance computing service, which is provided by EPCC at the University of Edinburgh and by STFC Daresbury Laboratory, and funded by the Department for Innovation, Universities and Skills through EPSRC's High End Computing Programme.

I am indebted to my supervisors, Drs. Lidunka Vočadlo, Ian Wood and Dominic Fortes for their unending red pens, for knowing everything there is to know about everything, turning it into an excel macro, and explaining it in words of one syllable (or less) and to David Dobson for being the silent supervisor; available as required.

To my beloved flatmates, Amy, Zoe and Simon, to the occupants of the planetary centre; Pete, Katie, Su, (M)Emily, Ceri, Claire, Oli, Shosh, Josh, Lottie, to other general miscreants of department, Mike, Dan and Heather; thanks for the coffee, the beer, the road trips, the champagne cocktails, the dancing, the singing and mostly the sarcasm!

It is *for* my parents, who made it all possible, and continued to humour my obsession with planets and support me even without a sniff of a “real job” and be patient when I went totally mental at the end, sorry about that…

Contents

Abstract 2
Acknowledgements 4
Contents 5
List of Figures 7
List of tables 9

Chapter 1 Introduction 11
1.1 Introduction to evaporites: terrestrial and planetary settings and perspectives. 12
1.1.1 Terrestrial evaporites. 12
1.1.2 Martian evaporitic settings. 16
1.1.3 Application of evaporitic studies to the icy satellites of Jupiter. 19
1.1.3.1 Present composition of Europa 20
1.1.3.2 Present composition of Ganymede. 21
1.1.3.3 Present composition of Callisto. 21
1.2 Mineralogy of evaporitic sulfate hydrates. 22
1.2.1 $Na_2SO_4 – H_2O$ system 22
1.2.1.1 Anhydrous Na_2SO_4 22
1.2.1.2 Sodium sulfate heptahydrate and octahydrate. 24
1.2.1.3 Mirabilite 25
1.2.2 $MgSO_4 – H_2O$ system 32
1.2.2.2 Hydrated phases of MgSO4. 33
1.2.2.3 $MgSO_4.11H_2O$ – Meridianiite. 34
1.3 Previous studies of evaporitic salt hydrates. 37
1.3.1 Previous studies of mirabilite. 37
1.3.2 Previous studies of meridianiite. 38
1.4 Aims and methodologies of this thesis. 39
1.4.1 Computer simulation techniques 39
1.4.2 Neutron diffraction techniques. 41
1.5.Thesis Outline 42

Chapter 2 Neutron diffraction studies I: Methodology 43
2.1 General introduction to diffraction. 44
2.2 Neutron diffraction 46
2.2.1 Neutron diffraction and hydrated materials. 47
2.3 Generation of neutrons. 48
2.4 HRPD – The high resolution powder diffractometer. 50
2.5 Time-of-flight neutron diffraction. 51
2.6 Data refinement 52
Summary 57

Chapter 3 Neutron diffraction studies II:Thermal expansion of mirabilite from 4.2 – 300 K 58
3.1 Sample preparation and data acquisition 59
3.1.1 Sample preparation 59
3.1.2 Thermal expansion data acquisition. 61
3.1.3 Thermal expansion data refinement - GSAS and least-squares fitting. 61
3.2. Thermal expansion results 67
3.2.1 Structure and disorder of mirabilite. 67
3.2.1.1 Hydrogen bond lengths in the long-count datasets. 69

3.2.1.2 Disorder within the mirabilite structure..... 70
3.2.2 Thermal expansion of the mirabilite structure. 74
3.2.2.1 Axial thermal expansions of mirabilite. 76
3.2.2.2 Unit cell volume thermal expansion of mirabilite. 77
3.2.2.3 Fitting of the cell parameters of mirabilite using the Grüneisen approximation. 78
3.2.2.4 The thermal expansion tensor of mirabilite. 81
***Summary** 89*

***Chapter 4 Neutron diffraction studies III: Mirabilite under pressure** 90*
4.1 Method: measuring the compressibility of mirabilite. 91
4.1.1 Sample preparation and loading. 91
4.1.2 Data acquisition. 93
4.2 Results 98
4.2.1 The incompressibility of mirabilite. 98
4.2.2 Bulk and axial incompressibility of mirabilite at 260 K and 80 K. 99
4.2.3 Derivation of the elastic strain tensor of mirabilite. 101
4.3 The thermal expansion of mirabilite at 0.55 GPa. 103
Summary 106

***Chapter 5 Ab initio studies I: Methodology** 107*
5.1 Theoretical background to ab initio calculations 109
*5.1.1 Born-Oppenheimer Approximation**.** 110*
5.1.2 Exchange and correlation 111
5.1.3 Plane waves, Pseudopotentials and the PAW method 112
5.2 Vienna Ab initio Simulation Package (VASP) setup. 115
5.2.1 Inputs and outputs. 115
5.2.2 Sampling of k - points. 116
5.2.3 Ionic relaxation within VASP. 116
5.2.4 Tests on Ice VIII. 117
5.3 VASP Setup for this study. 120
5.3.1 Simulations of mirabilite. 120
5.3.1.1 POSCAR setup 121
5.3.1.2 INCAR setup. 123
5.3.1.3 ENAUG and ENMAX tests 125
5.3.1.4 Testing of k-points 127
5.3.2 Simulations of Meridianiite, MS11. 127
5.3.2.1 INCAR setup. 128
5.3.2.2 Testing of k-points 128
5.4 Obtaining an equation of state from the total energy of a system. 129
***Summary** 131*

***Chapter 6 Ab initio studies II: Pressure-induced structural changes in mirabilite** 132*
6.1 Simulations of the structure of mirabilite 133
6.2 The zero-pressure, zero-temperature structure of mirabilite. 133
6.3 Possible phase transformations in mirabilite at high pressure 137
6.4 The equation of state of the low-pressure phase of mirabilite 142
6.5 The equations of state of the high-pressure phases of mirabilite. 144
6.6. Derivation of the elastic strain tensor of mirabilite. 145
6.7. The Pressure dependence of the structural parameters 148
6.7.1. The SO_4 and Na Coordination Polyhedra 149
6.7.2 The behaviour of bonds involving H atoms in the low-pressure phase. 152

6.7.3 The high-pressure phases of mirabilite. *152*
6.8. Discussion *162*
Summary *163*

Chapter 7 Ab initio studies III: The compressibility of meridianiite *164*
7.1 Simulation of the structure of meridianiite. *165*
7.2 The equation of state of meridianiite. *168*
7.3 The axial compressibilities of meridianiite *169*
7.4 The zero-pressure structure of MS11 ..... *171*
7.5 The Pressure dependence of the SO_4 and $Mg(H_2O)_6$ Coordination Polyhedra. *175*
7.6 The Pressure dependence of the bifurcated hydrogen bond *177*
7.7 The high-pressure phase of meridianiite. *177*
Summary *179*

Chapter 8 Summary, Application of results and future work *180*
8.1 Summary of results *181*
8.1.1 Neutron diffraction experiments to determine the thermal expansion of mirabilite. *181*
8.1.2. Neutron diffraction experiments to determine the compressibility of mirabilite. *182*
8.1.3. Ab initio simulations to determine the equation of state of mirabilite from *182*
8.1.4 Ab initio simulations to determine the equation of state of MS11. ..... *184*
8.2 Future work *186*
8.3 Application of thermoelastic properties of salt hydrates to geological structures *189*
8.3.1 Diapiric model methodology *189*
8.3.2 Diapirs on Earth *193*
8.3.3 Diapirs on Mars. *195*
8.3.4 Diapirs on the icy satellites *196*
8.3.5 Discussion *197*

References *198*

Appendices
Appendix 1 Na_2SO_4 Interatomic potential paper ..... *I*
Appendix 2 Unit-cell parameters for mirabilite from thermal expansion experiment ..... *XIV*
Appendix 3. H-bond lengths from each of the long soaks in Chapter 3 ..... *XVII*
Appendix 4. Unit-cell parameters for mirabilite from the high pressure experiment ..... *XXII*
Appendix 5. Beamtime application to study protonated and deuterated mirabilite ..... *XXIV*

List of Figures

Chapter 1
Figure 1.1: Schematic shapes of salt structures. *14*
Figure 1.2: Landsat image of salt diapirs in the Zagros mountains of central Iran.. ..... *15*
Figure 1.3 . MOC image of the northern polar cap of Mars. *17*
Figure 1.4 HiRISE image of Western Candor Chasma, Mars. *18*
Figure 1.5 the Galilean satellites of Jupiter. *19*
Figure 1.6 Pressure –Temperature phase diagram of anhydrous Na_2SO_4 . ..... *23*
Figure 1.7 T-X phase diagram of the binary sodium sulfate – water system. *24*
Figure 1.8 Polyhedral representation of the low temperature, mirabilite structure. *26*
Figure 1.9 Connectivity map illustrating the structural elements in mirabilite.. ..... *27*

Figure 1.10 One of the square rings of water molecules in mirabilite involving disordered hydrogen bonds.. 29
Figure 1.11 The two orientations of the sulfate tetrahedron described by Levy and Lisensky…. …….31
Figure 1.12 T-X phase diagram of the binary system magnesium sulfate – water. 33
Figure 1.13 Connectivity map for MS11 at zero pressure 35
Figure 1.14 Polyhedral representation of the ambient pressure, low temperature, meridianiite structure..... 36

Chapter 2
Figure 2.1: Schematic illustrating the geometry of Bragg's law. 45
Figure 2.2 A comparison of the diffraction patterns of a) Antarctic H_2O ice and b) D_2O..... 48
Figure 2.3 The layout of the experimental hall at the ISIS neutron spallation source. 50
Figure 2.4 Reitveld refinement of mirabilite using GSAS 53

Chapter 3
Figure 3.1 The aluminium-framed, vanadium-window slab 60
Figure 3.2 One of the square rings of water molecules involving disordered hydrogen bonds. 63
Figure 3.3 Neutron powder diffraction patterns of mirabilite at 4.2K, 150K & 300K 65
Figure 3.4 The two orientations of the sulfate tetrahedron described by Levy and Lisensky 72
Figure 3.5 Fourier (F_{obs}) map produced from the long-count data at 300 K 73
Figure 3.6 The temperature dependent variation of the unit cell parameters.. 75
Figure 3.7 Comparison of the volume thermal expansion coefficient for deuterated mirabilite..... 77
Figure 3.8 Fit of experimental heat capacity data 80
Figure 3.9 Diagram illustrating the relationship between the unit-cell axes the orthonormal thermal expansion tensor. 82
Figure 3.10 Temperature dependence of the thermal expansion tensor coefficients and principal axes of the thermal expansion tensor 85
Figure 3.11 Projections of the thermal expansion coefficient representation surface 86
Figure 3.12 Orientations of the O10 and O11 hydrogen bonds with respect to the direction e_1 88

Chapter 4
Figure 4.1 The pressure cell used to measure the compressibility of mirabilite. 92
Figure 4.2 The melting curve of helium at high pressure..... 93
Figure 4.3 Neutron powder diffraction patterns of mirabilite at 480 bar, 260 K..... 96
Figure 4.4 Neutron powder diffraction patterns of mirabilite at 5338 bar, 240 K..... 97
Figure 4.5 Unit-cell parameters of mirabilite as a function of pressure at 260 and 80 K. 100
Figure 4.6 Magnitudes of the principal axes of the strain tensor as a function of pressure..... 102
Figure 4.7 Thermal expansion of mirabilite at 0 and 0.55 GPa. 103
Figure 4.8 Variation of the bulk modulus $K_{0,}$ with temperature between 260 and 80 K..... 104
Figure 4.9 The Anderson- Grüneisen parameter for mirabilite compared to epsomite..... 105

Chapter 5
Figure 5.1 Schematic illustration of the generated pseudopotential wavefunction..... 114
Figure 5.2 Phase diagram of Ice..... 118
Figure 5.3 The structure of Ice VIII viewed along the b-axis. 118
Figure 5.4 E-V curve of Ice VIII..... 119
Figure 5.5 One of the square rings of water molecules involving disordered hydrogen bonds. 122
Figure 5.6The two orientations of the sulfate tetrahedron described by Levy and Lisensky..... 123
Figure 5.7 Variation in (a) Energy and (b) pressure with the value of ENMAX..... 126

Chapter 6
Figure 6.1 Total energy curves as a function of volume from ab initio calculations..... 138
Figure 6.2 V(P) curves for mirabilite..... 139
Figure 6.3 Calculated unit-cell axes of mirabilite as a function of pressure. 141
Figure 6.4 Magnitudes of the principal axes of the strain tensor as a function of pressure..... 147
Figure 6.5(a) Sulphate tetrahedron volumes with increasing pressure for epsomite..... 150
Figure 6.6 Connectivity map illustrating the relationship between structural elements in mirabilite at zero pressure 153
Figure 6.7 Connectivity map illustrating the relationship between structural elements in mirabilite at a pressure of 13.4 GPa. 154
Figure 6.8 Connectivity map illustrating the relationship between structural elements in mirabilite in the second intermediate phase at a pressure of 10.8 GPa..... 155
Figure 6.9 Connectivity map illustrating the relationship between structural elements in mirabilite at a pressure of 32.9 GPa. 157
Figure 6.10 Connectivity map illustrating the relationship between structural elements in mirabilite at a pressure of 61 GPa.. 158
Figure 6.11 Illustration of the connectivity in the high-pressure hydrogen-bond network. 160

Chapter 7
Figure 7.1 Energy - Volume and Pressure - Volume curves for calculations of meridianiite..... 167
Figure 7.2 Simulated lattice parameters with pressure for meridianiite.. 170
Figure 7.3 Connectivity map for MS11 at zero pressure. 174
Figure 7.4 Calculated polyhedral volumes for MS11. 176
Figure 7.5 Length of the bifurcated H – Bond in MS11 with pressure. 177
Figure 7.6 Connectivity map for MS11 at 8.0 GPa.. 178

Chapter 8
Figure 8.1 a) Connectivity map illustrating the relationship between structural elements in mirabilite at zero pressure and 61 GPa..... 183
Figure 8.2 Connectivity map for MS11 at 8.0 GPa.. 185
Figure 8.3 Sulfate tetrahedral volumes with increasing pressure for epsomite, MS11 and for mirabilite.. 188
Figure 8.4 Initial layer model. 190
Figure 8.5 Schematic illustration of the model diapir. 190
Figure 8.6 Log plot of diapir size against buoyant layer thickness 192
Figure 8.7 Landsat image of salt diapirs in Iran. 194

List of tables

Chapter 3
Table 3.1 Refinement statistics of the four long long count datasets. 66
Table 3.2 Comparison of the unit cell dimensions of mirabilite with the published values..... 67
Table 3.3 Sulfate bond angles and lengths in the mirabilite structure at 4.2 K, slow cooled and quenched, 150 K and 300 K. 68
Table 3.4 The refined fractional occupancies of protons in the square rings 70
Table 3.5 Changes in the size and shape of the $Na(H_2O)_6$ octahedra in mirabilite and NaO_6 octahedra in thenardite with temperature. 74
Table 3.6 Coefficients of the polynomial fits to the heat capacity data.. 79
Table 3.7 Parameters obtained by fitting equations 3.9 and 3.10 to the unit-cell volume and cell edges of mirabilite.. 83

Chapter 4
Table 4.1 Refinement statistics at 478 bar, 260 K. 95
Table 4.2 The axial compressibility of mirabilite at 260 and 80 K. 101

Chapter 5
Table 5.13BMEOS fit parameters for Ice VII 120
Table 5.2 Variation of energy and pressure with ENMAX at two volumes. 126
Table 5.3 Variation of energy and pressure with ENAUG at two volumes. 126
Table 5.4 k-point testing results for mirabilite. 127
Table 5.5 k-point testing results for MS11. 129

Chapter 6
Table 6.1 Comparison of the S-O and Na-O bond lengths (in Å) of the ambient-pressure phase of mirabilite obtained computationally with the experimental values 134
Table 6.2 Comparison of the O-H(D) and H(D)-O bond lengths of the ambient-pressure phase of mirabilite 135
Table 6.3 Parameters obtained by least-squares fitting of the 3BMEOS and 4LNEOS to the E(V) curve of the low-pressure phase of mirabilite 143
Table 6.4 Comparison of the unit-cell dimensions and axial ratios of the ambient-pressure phase of mirabilite obtained computationally with the experimental values of the deuterated isotopomer at 4.2 K. 143
Table 6.5 The axial compressibility of mirabilite from the ab initio calculations in comparison to experimental values at 80 K from Chapter 4. 145
Table 6.6 Geometry of the ionic species in the high-pressure phase of mirabilite, and their donated hydrogen bonds. 161

Chapter 7
Table 7.1 Fitted equation of state parameters for the calculations of meridianiite. 168
Table 7.2 Axial incompressibilities of the low pressure phase of meridianiite determined from 3BMEOS fits to the cube of the lattice parameters 169
Table 7.3 S - O and Mg - O distances in meridianiite at zero pressure from the simulation compared to the 4.2 K experimental values 171
Table 7.4 Hydrogen bonding in MS11 at zero pressure from this simulation. 172
Table 7.5 Experimental hydrogen bonding in MS11 at 4.2 K 173
Table 7.6 EOS fit parameters for the SO_4 tetrahedra in MS11 in comparison to mirabilite and epsomite 175

Chapter 8
Table 8.1 Density and viscosity values for the materials used in each of the planetary settings. ... 193
Table 8.2 Range of spatial scales and ascent times calculated for diapirs on Earth 194
Table 8.3 Range of spatial scales and ascent times calculated for diapirs on Mars 196
Table 8.4 Range of spatial scales and ascent times calculated for diapirs on Ganymede 196

Chapter 1

Introduction

This thesis describes an investigation into the properties of the salt hydrates, mirabilite and meridianiite; it includes determination of thermoelastic properties using a combination of both computer simulation and experimental work, and the application of these properties to modelling geological processes which may shape the surface and interiors of the Earth and other planetary bodies throughout the solar system.

This introductory chapter is laid out as follows: Section 1.1 gives a very brief introduction to evaporitic deposits (settings in which salt hydrates may be important), their formation, evolution, economic concerns and eventual removal from the geological record, both on Earth and throughout the solar system; Section 1.2 introduces the mineralogy of the main materials of study in this thesis, the salt hydrate component of the evaporite deposits and the motivation for their study in this context; Section 1.3 reviews previous studies of these salt hydrates, leading to Sections 1.4 and 1.5 where the techniques and layout of this thesis are outlined.

1.1 Introduction to evaporites: terrestrial and planetary settings and perspectives.

1.1.1 Terrestrial evaporites.

One of the most widespread types of sedimentary rocks on Earth and throughout the solar system are the evaporites. Evaporites form abundant deposits on the Earth in a wide range of geological settings both as primary evaporite deposits such as those found in hypersaline lake environments such as the salt lakes of Utah, and in geological settings such as salt domes, hydrocarbon reservoirs (Coleman *et al.*, 2002), and even as a component of cold desert salt deposits (Keys and Williams, 1981). Indeed, it is estimated that up to 30% of the continental United States may be underlain by evaporite deposits (Warren, 2006), and yet there is still a great deal about this type of rock that we do not know.

An evaporite is a deposit of soluble salts, which precipitate as a result of the removal (evaporation), of H_2O. For the purposes of this study, the term “salt” is used to indicate a rock body which is composed of halite, gypsum or other salt hydrates. Evaporites form in a variety of environmental settings and this climatic diversity is reflected and recorded in their wide range of mineralogical compositions. Evaporation is a vital part of the water cycle on Earth. It occurs naturally on the surface of Earth through the action of solar energy warming oceans and lakes. As evaporation of a body of water proceeds and the amount of water decreases, certain minerals dissolved in the water, reach the limits of their solubility. Evaporites are an

indicator of the removal of large amount of water from a specific environment in a relatively short amount of time. For example 1 litre of saline water can produce up to 35g of evaporitic NaCl salt.

Initially, to form a primary evaporite, the evaporation of sea water leads to the deposition of calcium carbonate as micritic limestone, but this is not the end of the sequence of precipitation. With a large (> 80%) decrease in the volume of water available, a selection of other precipitates will occur in accordance with the solubility of the mineral species. Salt hydrates represent the end of the sequence – either very low liquid water concentrations, or extreme supersaturation of the salt. The first salts to precipitate after the $CaCO_3$ will be gypsum ($CaSO_4.2H_2O$) and anhydrite ($CaSO_4$) when 80% of the water has evaporated. This is followed by halite (NaCl), at levels where > 90% of the water has been removed. Halite is the most common evaporitic salt on Earth due to the relative enrichment of the terrestrial crust with respect to chlorine; the Cl:S ratio in chondrites is ~0.01, making sulfur-containing compounds a much more common phenomena in other parts of the solar system. The final salts in the sequence, at extremely low water concentrations are Mg, Na and K salts such as epsomite, the so-called "bittern" salts (Warren, 2006).

Traditionally, evaporite formation is thought to result from evaporation in an aerian environment; thus, the primary zones of evaporite formation are at the margins of bodies of water, lakes, oceans, or where water exists seasonally in more arid areas. Horst and graben structures at continental spreading ridges provide an ideal locality as the flooded sections of the rift get cut off from their primary water source. However, if the evaporite deposit is not a primary deposit, all that may be required for formation might be the removal of water from the environment. Thus, it is also possible to form evaporitic salt-hydrate minerals in areas such as dehydrating sections of subducting slabs and as the alteration products of alkaline volcanic deposits. It is also common for evaporite materials such as the bittern salts to be mobilised, localised and redeposited (recrystallised) by hydrothermal activity and so another geological setting for their occurrence is in hydrothermal or volcanic areas (Hardie, 1991).

The stability fields over which different evaporitic mineralogical phases can persist can be so small that their presence can serve as a climactic indicator. However, by the same measure, this also means that just because they are a certain phase today does not mean they were originally deposited as that phase. Salt hydrate recrystallisation is common and results in many of the internal textures of evaporite deposits reminiscent of those found in intrusive igneous rocks.

Compared to most sediments, evaporitic salts have a relatively low density e.g. gypsum has a density of 2317 kg m^{-3} (Schofield *et al*., 1996), and mirabilite, a density of 1490 kg m^{-3} (this work), compared to 2800 kg m^{-3} for basalt (Beyer *et al*., 2000). As with all materials deposited on the surface, over time evaporites will be buried by younger deposits. This may lead to a density inversion when evaporites are buried beneath denser sediments. Evaporitic materials are also mechanically weak compared to other sediments and so will flow under relatively low loads (Hudec and Jackson, 2007). The combination of these two properties makes salt layers mobile with respect to the sediments around them. This can have two consequences depending on the rheology of the surrounding sediments and their ability to constrain the salt movement: firstly, in orogenic settings such as the edge of the Pyrenean fold and thrust belt in northern Spain, where the salt is constrained by the surrounding sediments, evaporitic layers can act as dislocation surface for thrust planes, promoting regional shortening (Pinto *et al.*, 2002). Secondly, if the salt layers are able to move relatively freely with respect to surrounding sediments, as is seen in another more distal part of the same sequence in Spain, the salt buoyancy can allow the salt to move and produce a variety of geological structures (see Figure 1.1) typified by salt diapirs.

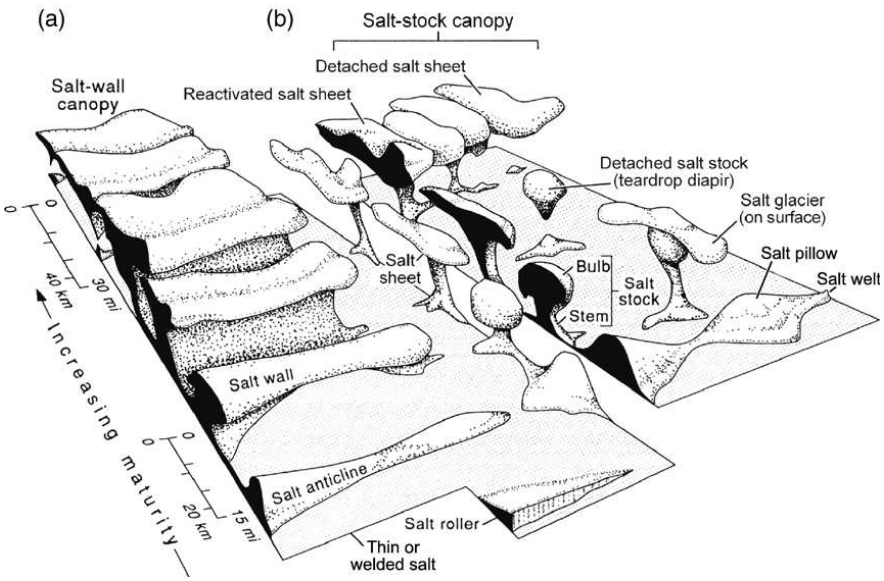

Figure 1.1: Schematic shapes of salt structures. Maturity of the structures increases away from the reader. Series a) are features arising from line sources akin to a dyke and b) are features produced by a point source. From Hudec and Jackson (2007), after Jackson and Talbot (1991).

The term "diapir" literally means upwelling. It can be equally well applied to volcanic material as it travels up through the crust or to an evaporite moving through overlying

sediments. In both cases, the underlying cause of the diapir is a density contrast between adjacent materials. Density inversions within sedimentary sequences provide an opportunity for underlying sediments to deform those above them and can have a significant effect on the evolution of geological structures within a planetary crust. Diapiric structures are also of significant interest to economic geologists as they can provide both a means of transporting hydrocarbons, often found in association with evaporite deposits, toward the surface and their movement can set up the conditions for structures which trap said hydrocarbons, as is frequently seen under the North Sea and in the gulf of Mexico (Waltham, 1996).

Initiation of a diapir occurs when Rayleigh-Taylor instabilities, small perturbations of the interface between a low-density layer and the denser rocks above lead, to an upwelling. This is typically seen in sedimentary sequences which contain evaporites, and these have been studied most extensively on the Earth, due mainly to their association with economic concerns such as oil and gas. Salt domes are the surface expression of a rising diapir of halite. Once these diapirs reach the surface, they may then extrude salt material onto the surface forming salt glaciers. Figure 8.2 shows a Landsat image of a series of outcropping salt diapirs in central Iran highlighting typical terrestrial diapir length scales of a few hundred metres to a few kilometres. Typical diapir ascent times are of the order of 10^4-10^6 years. The Zagros mountain belt in central Iran is a classic salt diapir locality, it is of alpine age and contains a wide variety of salt structures.

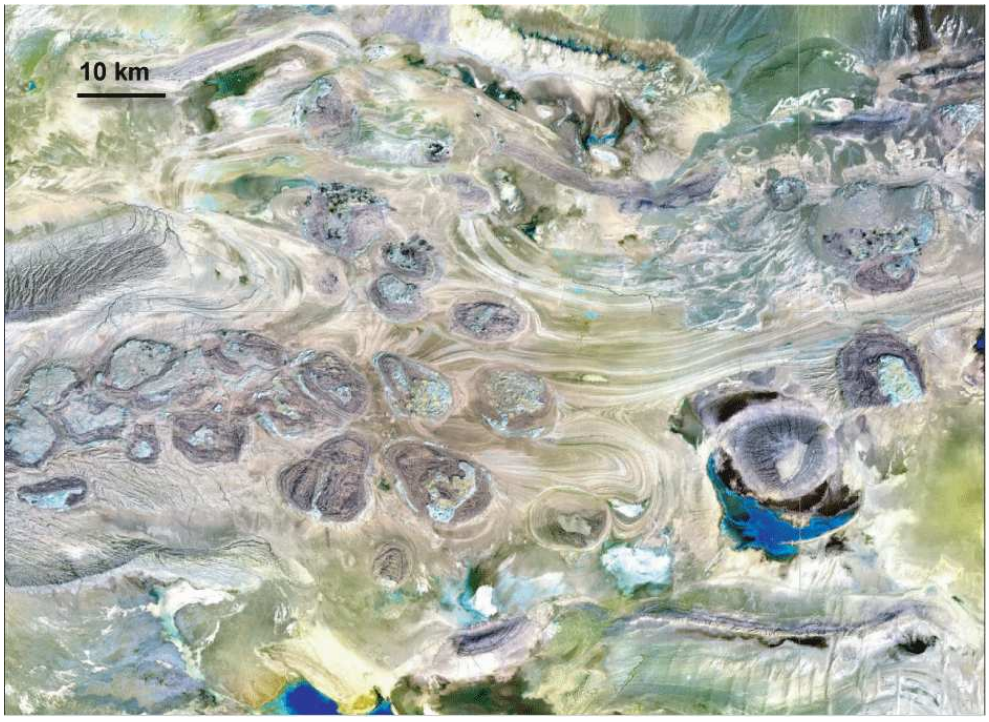

Figure 1.2: Landsat image of salt diapirs in the Zagros mountains of central Iran. Image: USGS/NASA.

1.1.2 Martian evaporitic settings.

Evaporitic deposits are likely to be a constituent of the geological record wherever water is, or has been, a major component of the environment. Whereas on Earth liquid water is active currently, the climactic conditions at the surface of Mars today are prohibitive to the long term survival of liquid water. However, there is evidence to suggest that in the past (on a geological timescale at least) Mars was a warmer and wetter place (Kargel, 2004) thus allowing water to be stable at the surface of Mars for longer periods. Moreover, there is evidence for liquid (and solid) H_2O in the near surface and subsurface of Mars today. This, together with the recent findings of the TEGA (Thermal and Evolved-Gas Analyzer) instrument on NASA's Phoenix lander, makes it likely that evaporites will be present in the sedimentary record of the Martian subsurface. Furthermore, ice is likely to be a major component of the near-surface regolith, particularly at high latitudes. Figure 1.3 shows an image of the Martian polar caps which are formed of alternating layers of dust, H_2O ice and CO_2 ice. Both ice and mineral hydrates (epsomite, $MgSO_4 \cdot 7H_2O$, meridianiite, $MgSO_4 \cdot 11H_2O$, mirabilite, $Na_2SO_4 \cdot 10H_2O$, and gypsum, $Ca_2SO_4 \cdot 2H_2O$) are believed to be present, based on *in situ* observations by landers and rovers, and from remote neutron and gamma-ray spectroscopy. Another important source of salt hydrates on Mars is likely to be from alteration of basaltic bedrock. There are extensive basalt flow fields on the surface of Mars which have been eroded and reworked by millennia of exposure to the Martian atmosphere.

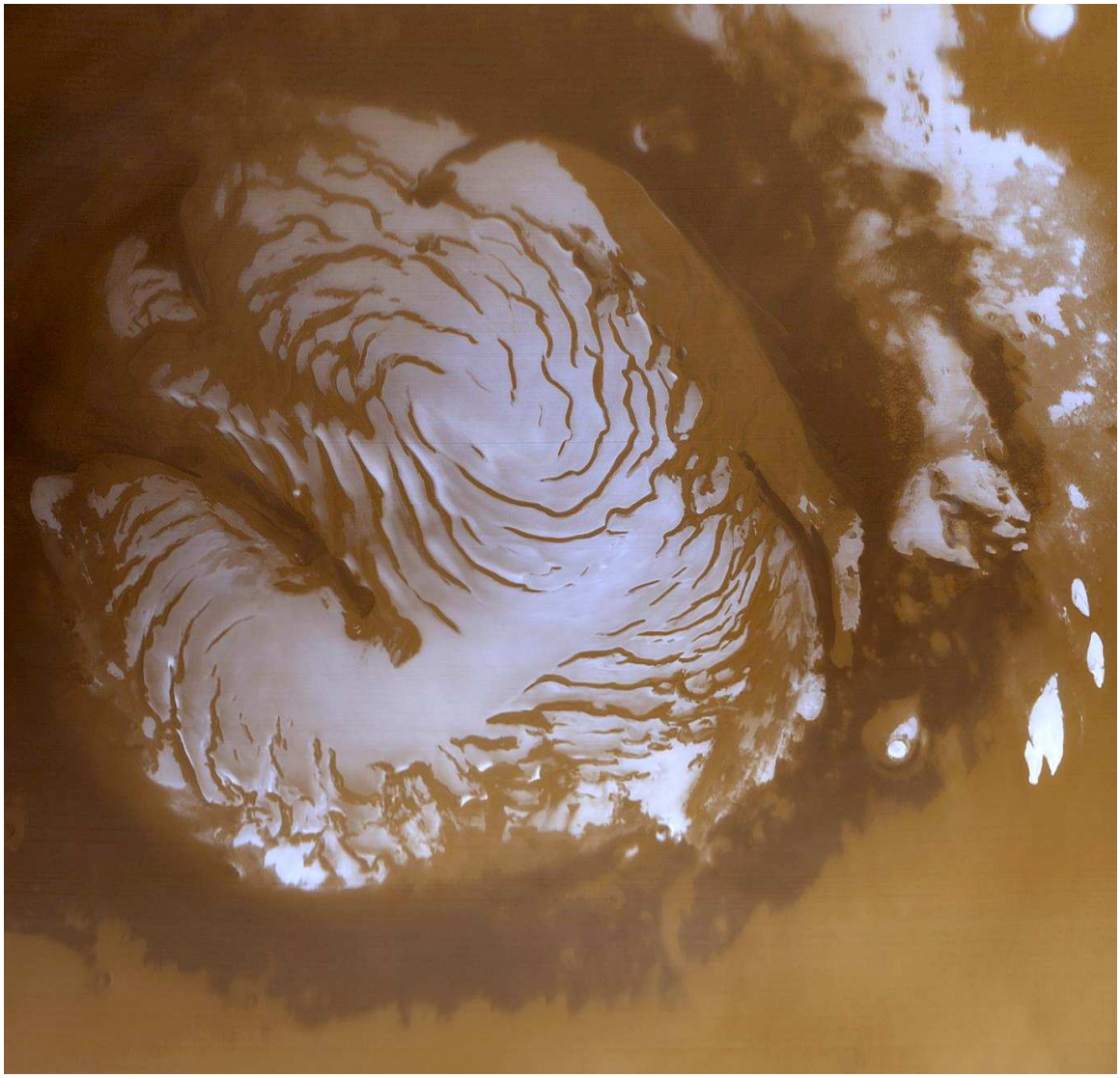

Figure 1.3 Mars Global Surveyor MOC image of the northern polar cap of Mars taken in early Martian northern hemisphere summer. The light coloured material is residual water ice that persists through the summer. The surrounding circular dark material is made up of wind-formed sand dunes. In this image the polar cap is approximately 1100 km across. Image credit: NASA/JPL/MSSS.

There have been several different studies to investigate the likely composition of a Martian evaporite deposit, including experiments on meteorites of Martian origin (Bridges and Grady, 2000) and experimental studies of Mars-analogue brines (Bullock *et al.*, 2008); these concluded that the most abundant evaporite on Mars would be gypsum, due to its relative low solubility. A similar conclusion was drawn by Kargel (1991) for the same reasons, that gypsum is likely the bedrock in the icy satellites with Mg and Na rich salts concentrating as the components of the metasomatic fluid.

With regard to diapiric structures on Mars, Beyer *et al.* (2000) have modelled a halite salt diapir under Martian conditions, as there has been some debate as to the origin of several surface features which appear reminiscent of the morphology of terrestrial diapirs e.g. the

plentiful circular features in Figure 1.4 (an updated version of an image from Beyer *et al.*, 2000).

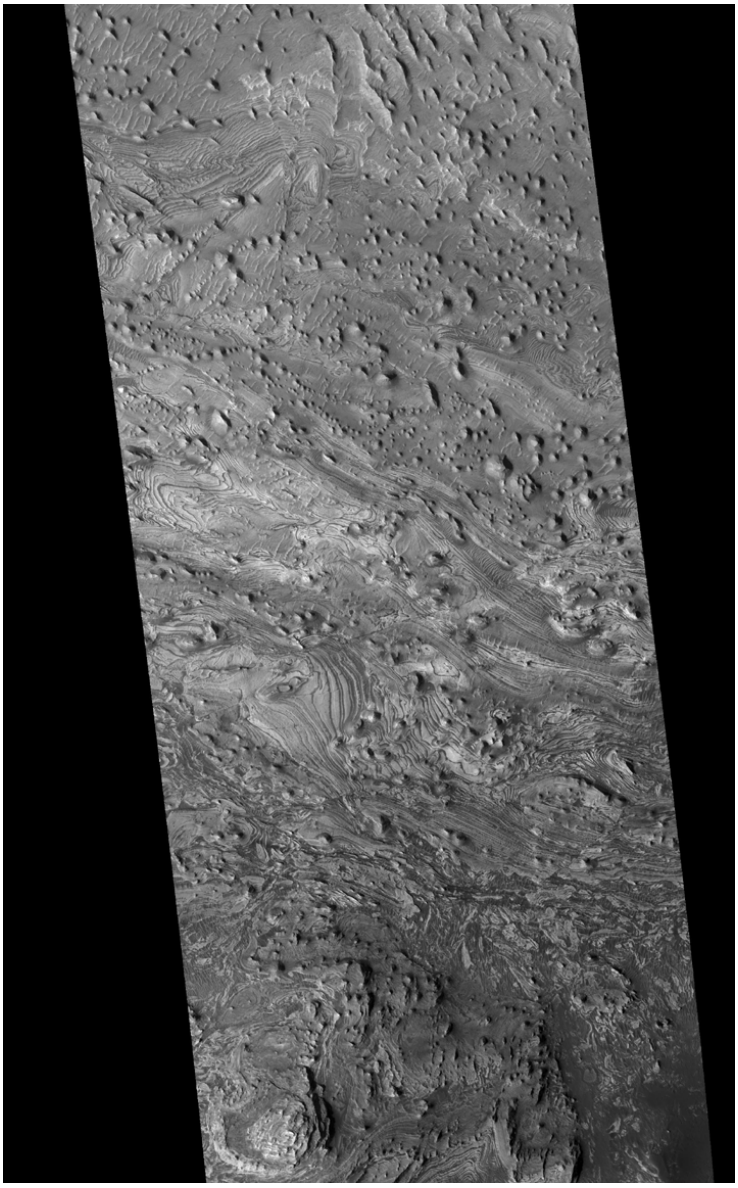

Figure 1.4 HiRISE image of Western Candor Chasma, Mars. The image is approximately 15 km across. Image credit: NASA/JPL/University of Arizona.

1.1.3 Application of evaporitic studies to the icy satellites of Jupiter.

Figure 1.65 shows the four large satellites of Jupiter (the Galilean satellites) of which three, Europa, Ganymede and Callisto, are icy. These images show the vast difference in surface appearance between the satellites. Io is characterised by volcanoes and their deposits, Europa has a bright surface criss-crossed with darker lineations, while Ganymede has a mixture of dark and light terrain and Callisto has a surface dominated by impact craters. These differences hint at differences in the processes which have shaped the interiors of these moons as a result of their positions in relation to, and tidal interactions with, Jupiter. However, even though these moons are now very different in appearance and internal structure, they are likely to have formed from material of the same composition in the same part of the proto-solar nebula.

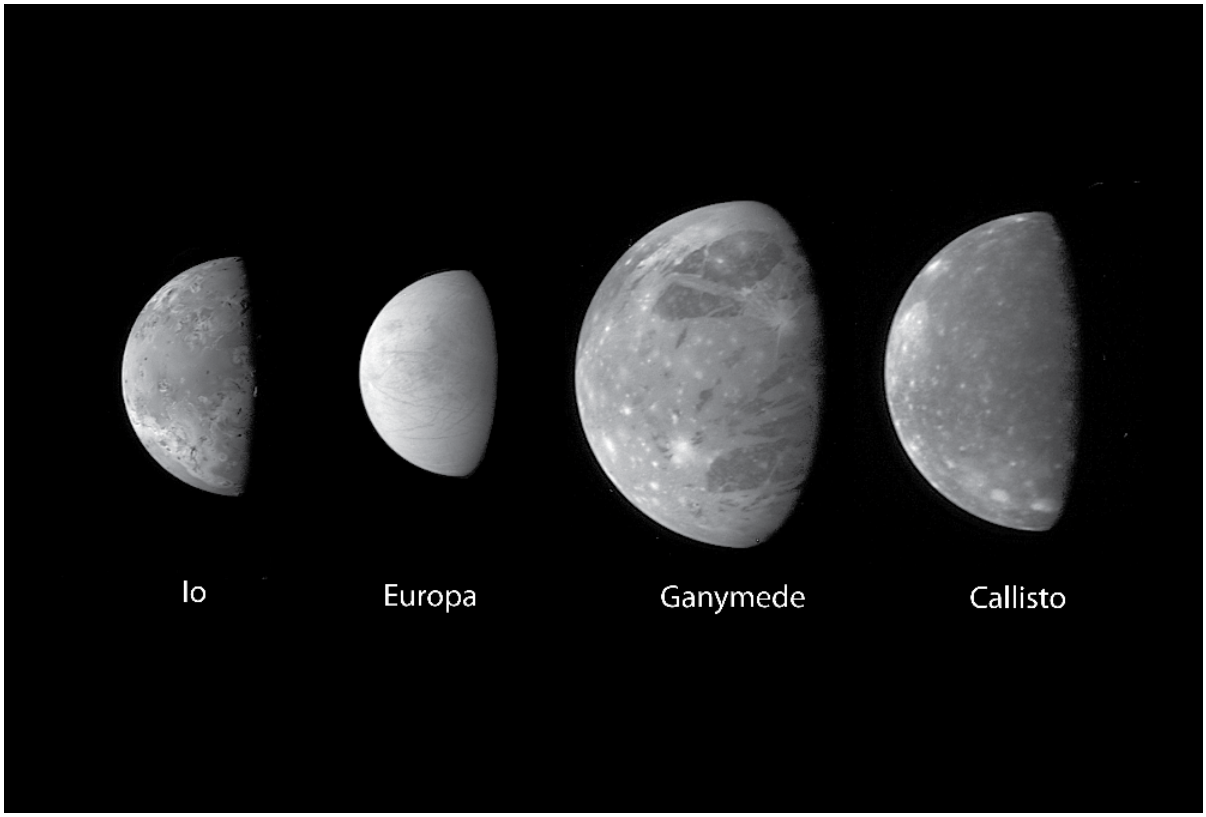

Figure 1.5 the Galilean satellites of Jupiter. Image credit NASA/JPL.

The satellites of the Jovian system are likely to have formed with an initial composition analogous to that of carbonaceous chondrite meteorites. They would have formed on the warm side of Jupiter's snow line (Kargel, 1991). The primary phases in chondritic meteorites are similar to those seen in terrestrial crustal rocks and include species such as olivine, pyroxene, feldspar and sulphides. There would have been no volatile ices within these early bodies and they would have had an initial elemental involatile content equal to the solar value, with a volatile content that was slightly raised with respect to the solar value (Kargel, 1991).

The salt fraction in materials forming the Jovian satellites is dominated by metal sulfates, particularly epsomite ($MgSO_4.7H_2O$), and other Mg bearing sulfates, closely followed by Ca and Na sulfates and then their carbonates (Kargel, 1991). Any $CaSO_4$ present is likely to have been precipitated *in situ*, probably in the form of gypsum, and remained so over time rather than being mobilised by hydrous activity in the body, due to its sparing solubility. Carbonates are likely to be less plentiful than sulfates as carbonates are less soluble than sulfates. Salt hydrates within the body may have condensed directly into the chondrite or may be the products of secondary alteration processes, such as leaching. The most important leachates from chondritic meteorites are those which fall into the $MgSO_4$-Na_2SO_4-H_2O system. As there is a negligible solid solution between $MgSO_4$ and Na_2SO_4 (the difference in valence states means the cations are not interchangeable), only combinations of $MgSO_4 – H_2O$ and $Na_2SO_4 – H_2O$ need be considered, rather like K and Ca in feldspars.

Unlike the satellites of Saturn, it is thought that Jupiter's satellites would have formed in a largely ammonia free region of the solar system as the temperature in this part of the proto-solar nebula is likely to have been high enough to prohibit the condensation of ammonia hydrates (Kargel, 1991). This means that the majority of the nitrogen in this region would be in the form of molecular N_2 rather than NH_3 and so ammonium sulfates are probably rarer in this region of the solar system than further out from the sun.

More detailed descriptions of the compositions of the three icy Jovian satellites at the present time are given below.

1.1.3.1 Present composition of Europa

Measurements of the moment of inertia of Europa, together with density and gravity field measurements suggest a differentiated four layer body (Anderson *et al*., 1997). The internal structure of Europa is suggested to be a silicate core with a salt-hydrate mantle below an ocean and icy crust (Kargel, 1991). There is a great deal of debate as to the thickness of this icy crust (Bray, 2008). It is though that the near surface composition of Europa is likely to be either a frozen/partially molten eutectic mixture of ice and hydrated Mg-Na salts or hydrated H_2SO_4 and that there may be solid anhydrous Mg–Na sulfates near the base of the crust (Kargel, 1991). The Near Infrared Mapping spectrometer (NIMS) spectrum at Europa is a good fit for a mixture of salts which appear concentrated in the lineaments and chaotic terrain. (McCord *et al*., 1998).

1.1.3.2 Present composition of Ganymede.

Ganymede is the largest satellite in the solar system. It is thought to have a 300 km thick crust composed of a 10:1 mixture of ice : $Na_2SO_4.10H_2O$; this crust overlies a 500 km thick mantle, which could be 1:1 ice : hydrated Mg-Na sulfates (Kargel, 1991). From NIMS data it appears that the salt hydrates at the surface are clustered in dark and chaotic terrain with both amorphous and crystalline ice concentrated at the poles. NIMS data also suggests that the Ganymede surface material is either less hydrated than that at Europa, or of a smaller grain size (McCord *et al*., 1998).

1.1.3.3 Present composition of Callisto.

Callisto is the furthest of the Galilean satellites outward from Jupiter. Unlike the other Galilean satellites, the surface of Callisto is heavily cratered and shows little evidence of recent resurfacing. This is unexpected as it is comparable in size to Ganymede and so would be expected to be active. There is much speculation as to the state of differentiation of the interior of Callisto The moment of inertia measurement can be interpreted by assuming that the interior can be represented by anything between a completely differentiated three-layer model to an undifferentiated body with random mass anomalies. However the flattening of impact craters suggests that the upper 10 km at least are “mechanically dominated” by ice so this region at least must be partially differentiated. IR measurements suggest there is water and other non-ice material at the surface but that overall Callisto is 50/50 rock: ice. There is likely to be 10 – 50% free ice at the surface (Kargel *et al.*, 1991).

1.2 Mineralogy of evaporitic sulfate hydrates.

1.2.1 $Na_2SO_4 – H_2O$ system

The majority of this thesis is concerned with the determination of the thermoelastic properties of mirabilite, the decahydrate of the Na_2SO_4–H_2O system. As we have seen in the preceding sections of this chapter, the Na_2SO_4–H_2O system is of great importance to the study of terrestrial and Martian evaporites and the interiors of the icy satellites of Jupiter. To this end, this section describes the mineralogy and crystallography of these materials in detail.

1.2.1.1 Anhydrous Na_2SO_4

The Na_2SO_4 - H_2O system has a seeming dearth of hydrates, compared to other candidate salt-hydrate systems such as the $MgSO_4$ - H_2O system (three phases versus eight). This, combined with the comparative ease of growing single crystals, and the low decomposition temperature of mirabilite (32.4°C), has meant that anhydrous sodium sulfate has received more attention than anhydrous magnesium sulfate in the literature. Nonetheless, the structures and phase transitions of anhydrous sodium sulfate have not been studied fully, mainly due to the complexity and metastability of the phase relations. The physical properties of this substance have also been neglected. Several studies have concentrated on the ionic conduction and electrical properties of sodium sulfate (Ahmad, 2006), but ignored the thermo-elastic properties. The only investigations of the phase diagram of sodium sulfate (Pistorius, 1965) were to 45 kbar using a piston-cylinder cell and an investigation of the elastic properties of thenardite using interferometry (Von Bayh, 1966).

Anhydrous sodium sulfate is thought to have as many as eight polymorphs up to 4.5 kbar (Pistorius, 1965) (Figure 1.6), but to date only four of these have been structurally characterised: I, II, III and V (Rasmussen *et al*., 1996), (the latter being the naturally occurring phase called thenardite). Phase I, which occurs above 510 K, is hexagonal, space group $P6_3/mmc$ and is characterized by complete orientational disorder of the SO_4 tetrahedra (Eysel *et al*., 1985). Phase II is orthorhombic, space group *Pbnm* but is only stable over a very small temperature range (503 – 510K) and has been considered by some to be metastable (Wang *et al*., 1999) Phase III (orthorhombic, space group *Cmcm*) is stable between 473 and 503 K at atmospheric pressure, whilst the room P,T form of Na_2SO_4, thenardite, is phase V (orthorhombic, space group *Fddd* (Hawthorne and Furguson, 1975; Nord, 1973)). There is still some debate in the literature as to the existence of a phase IV as there have not been any

studies which report this phase. The higher pressure polymorphs, VI, VII, and VIII, have yet to be investigated.

The structure of the ambient phase of Na_2SO_4, thenardite, consists of sheets of octahedra which are connected by direct coordination of the sodium atoms by the sulfate oxygens. This is also true of the other anhydrous phases of Na_2SO_4.

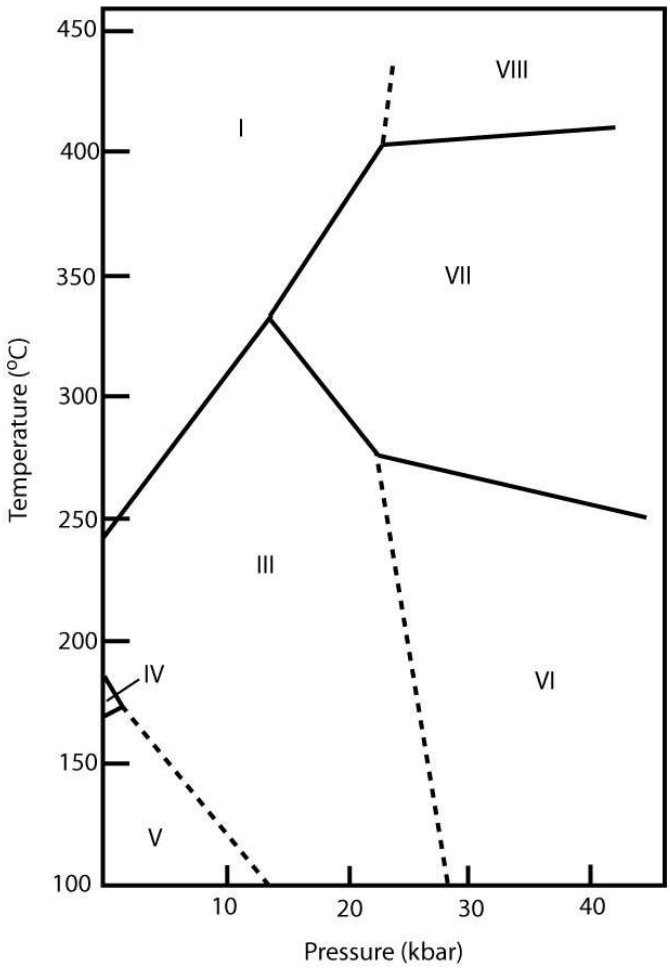

Figure 1.6 Pressure –Temperature phase diagram of anhydrous Na_2SO_4 from 0 – 4.5 kbar and 100 – 450 ^{o}C. Redrawn from Pistorius (1965).

1.2.1.2 Sodium sulfate heptahydrate and octahydrate.

Figure 1.7 shows the phase diagram for the Na_2SO_4 – H_2O system. A metastable phase, $Na_2SO_4 \cdot 7H_2O$, is known at room pressure and temperature (Löwel, 1851, 1853, 1857; Viollette, 1866; Tomlinson, 1868, 1871; de Coppet, 1907; Hartley *et al*., 1908; Wuite, 1914; Hills & Wills, 1938; Washburn & Clem, 1938; Braitsch, 1971; Gans, 1978; Balarew, 2002; Rijniers *et al*., 2005; Genkinger & Putnis, 2007), although Löwel (1850) described an octahydrate, detailing the growth of large and beautiful prismatic crystals, and Genkinger & Putnis (2007) report a phase which does not match the X-ray diffraction patterns of either the decahydrate or heptahydrate; these lesser hydrates, or indeed other hydration states may become stable at higher pressures (e.g. Hogenboom *et al*., 1999). The metastable heptahydrate - ice Ih eutectic is at 269.60 K, 12.8 wt. % Na_2SO_4, and the incongruent melting point of this phase is at 296.615K (Washburn & Clem, 1938). Most recently, sodium sulfate heptahydrate was fully characterised for the first time (Hamilton & Hall, 2008; Hall & Hamilton, 2008), and sodium sulfate octahydrate was identified as an exclusively high-pressure phase (Oswald *et al*., 2008).

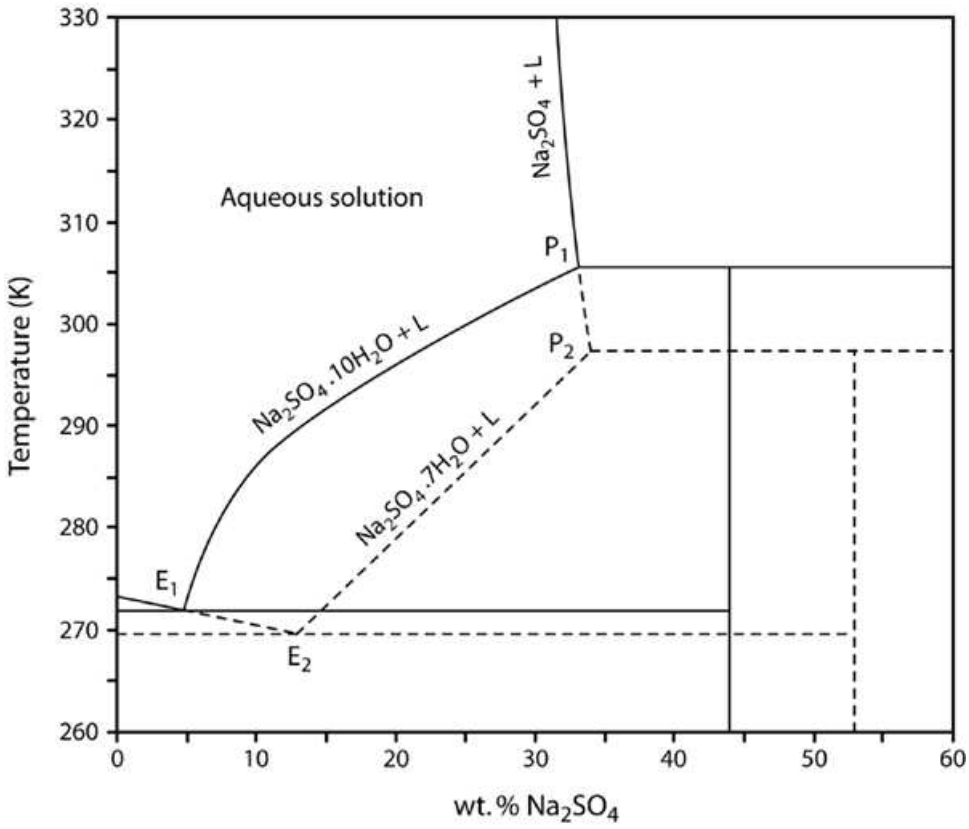

Figure 1.7 T-X phase diagram of the binary system sodium sulfate – water at room pressure showing stable phase boundaries (solid lines) and metastable phase boundaries (dashed lines). E_1 and E_2 are the mirabilite - ice and the $Na_2SO_4 \cdot 7H_2O$ - ice eutectics, respectively. P_1 and P_2 are the peritectics $Na_2SO_4 \cdot 10H_2O(s) \leftrightarrow Na_2SO_4(s)$ + liquid (L) and $Na_2SO_4 \cdot 7H_2O(s) \leftrightarrow Na_2SO_4(s)$ + L respectively. The solid vertical line at 44.09 wt. % Na_2SO_4 corresponds to the composition of mirabilite, and the dashed vertical line at 52.97 wt. % corresponds to the heptahydrate. Redrawn after Negi and Anand (1985) with solubility data tabulated in Garrett (2001).

1.2.1.3 Mirabilite

Sodium sulfate decahydrate — $Na_2SO_4 \cdot 10H_2O$ — mirabilite — is the stable phase in contact with an equilibrium mixture of Na_2SO_4 and H_2O at room temperature and pressure (Figure 1.7); the synthetic form of the substance is referred to as Glauber's salt, after its first manufacturer (Glauber, 1658); and the naturally occurring form is the mineral mirabilite (e.g. Palache *et al.*, 1951). The eutectic between mirabilite and ice Ih is at 271.85 K, 4.15 wt. % Na_2SO_4, and the solubility increases rapidly with temperature up to the peritectic at 305.534 K, 33.2 wt. % Na_2SO_4 where mirabilite undergoes incongruent melting to anhydrous sodium sulfate (orthorhombic phase V, *Fddd*, thenardite). This is the highest dissociation temperature amongst the isostructural decahydrates of Na_2SO_4, Na_2SeO_4, Na_2WO_4, Na_2VO_4, or Na_2MoO_4. Above this point, the solubility is retrograde, reaching a minimum near 400 K.

Mirabilite easily forms as large (cm sized) prismatic crystals from a saturated solution of Na_2SO_4 in water. Typical daily temperature variations in most climates are enough to promote the growth of such large crystals over relatively short timescales (days to weeks). Mirabilite crystals are monoclinic, space-group $P\ 2_1/c$ (Z = 4), with unit-cell dimensions a = 11.512(3) Å, b = 10.370(3) Å, c = 12.847(2) Å and β = 107.789(10)° at 4.2 K (Levy and Lisensky, 1978). Throughout this work the atom labelling scheme of Levy and Lisensky (1978) has been used. In this scheme, the sulfur atom is labelled S1, the sodium atoms are Na2 and Na3, the oxygens number from O4 to O17 and finally the hydrogens are labelled with respect to the oxygen with which they form a water molecule, for example the O8 water molecule will include O8, H8a and H8b (see Fig. 1.8d).

The structure of mirabilite is illustrated in Figure 1.8, which shows views along each of the crystallographic axes and Figure 1.9 which shows a connectivity map for mirabilite. As shown in Figure 1.8a, the structure of mirabilite consists of edge sharing $Na(H_2O)_6$ octahedra arranged in sinuous ribbons extending along the *c*-axis, with a net stoichiometry of $Na_2(H_2O)_8$. The octahedra comprise H_2O molecules, labelled as O8, O9, and O12-O17, with O12-O15 forming the shared edges. These ribbons of octahedra alternate with chains of sulfate tetrahedra (oxygens O4-O7) and the two are linked together by the remaining water molecules (labelled O10 and O11), that are not coordinated to Na. The alternating ribbons of $Na_2(H_2O)_8$ and SO_4 tetrahedra + H_2O thus form a flat sheet extending in the *b* - *c* plane (Figures 1.8b, 1.8c). The sheets are stacked A—B—A—B along the *a*-axis, being connected by a combination of orientationally ordered and disordered hydrogen bonds. This layering accounts for the perfect cleavage on {100} (Palache *et al.*, 1951, pp 439-442). Figure 1.9 is a connectivity map revealing the patterns of bonding between the various structural elements.

There is extensive hydrogen bonding within the structure as might be expected with such a highly hydrated salt (Ruben *et al.*, 1961).

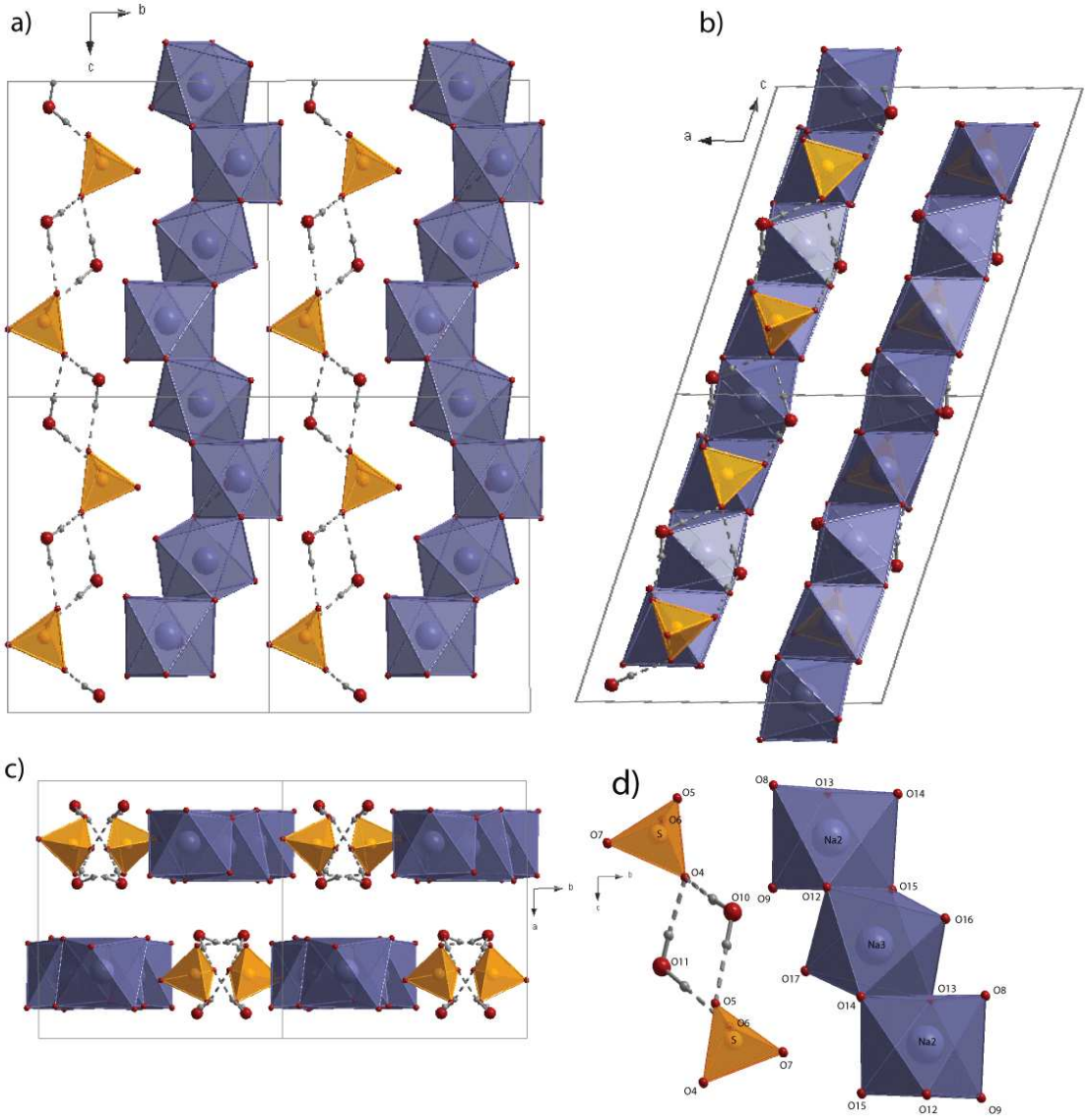

Figure 1.8 Polyhedral representation of the ambient pressure, low temperature, mirabilite structure, with the unit cell outlined in black: a) view along the *a*-axis, b) along the *b*-axis, and c) along the *c*-axis; the labelling of the atoms is shown in d) in an enlarged section of the structure as in a). The $Na(H_2O)_6$ octahedra are shown in dark blue and the SO_4 tetrahedra in orange. The interstitial H_2O molecules are shown, but the H-atoms bonded to the $Na(H_2O)_6$ octahedra have been omitted for clarity.

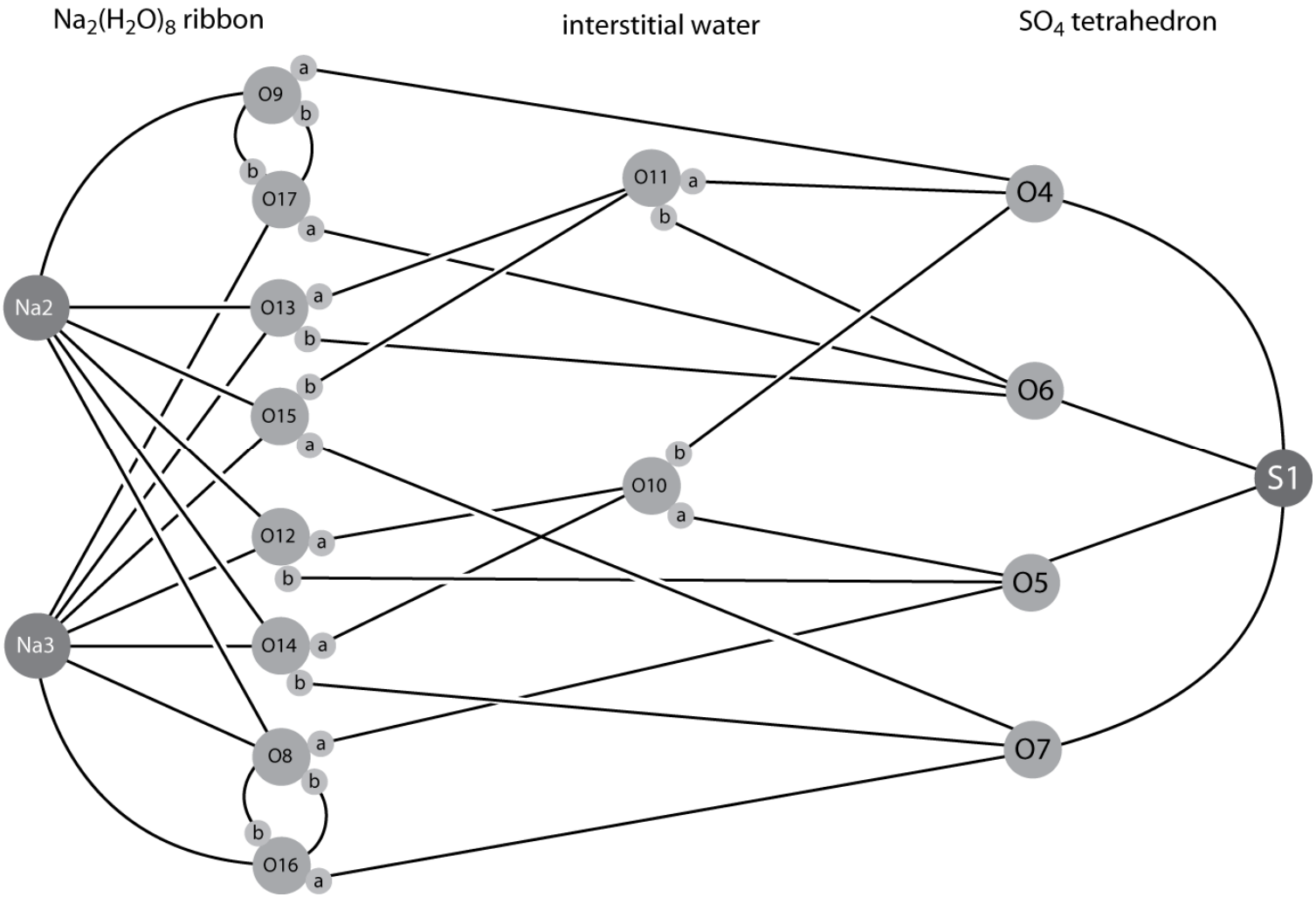

Figure 1.9 Connectivity map illustrating the relationship between structural elements in mirabilite. Note that the disorder involving the sulfate tetrahedron (and associated hydrogen bonds) as described by Levy and Lisensky (1978) has been left out; the hydrogen bond structure depicted corresponds to the fully ordered sulfate orientations obtained in this work.

The heat capacity data for mirabilite (Pitzer & Coulter, 1938; Brodale & Giauque, 1972) were used by Ruben *et al.,* (1961) to infer that hydrogen bonds in the mirabilite structure were disordered, and that this disorder became frozen-in at limiting low temperatures. In their single-crystal study, Levy and Lisensky (1978) identified two areas of orientational disorder, the first associated with a pair of square rings between adjacent octahedral apices, and the second associated with the sulfate tetrahedra. The square rings involve the molecule pairs O8/O16 (ring 1, shown in Figure. 1.10) and O9/O17 (ring 2) which form the apices of Na octahedra and donate hydrogen bonds to sulfate oxygens O5 and O7 (ring 1) and O4 and O6 (ring 2).

Each corner of the ring donates and receives one hydrogen bond from a neighbouring corner, with two possible orientations denoted 'b' and 'c' (the 'a' hydrogen are donating bonds to the sulfate oxygens). In any one ring, all hydrogens must all be on either the 'b' sites or all on the 'c' sites, although a small fraction of rings will contain a mixture of 'b' and 'c' orientations. Thermally activated hopping between sites means that the time- and space-averaged structure sensed by diffraction experiments will observe two partially occupied sites (both 'b' and 'c') along each O···O vector ofthe ring. Complete orientational disorder corresponds to 50:50 occupancy of the 'b' and 'c' sites, whereas complete orientational order corresponds to either 100:0 or 0:100 occupancy of these sites. Levy and Lisensky (1978) refined this ratio to be equal to 50:50 at room temperature.

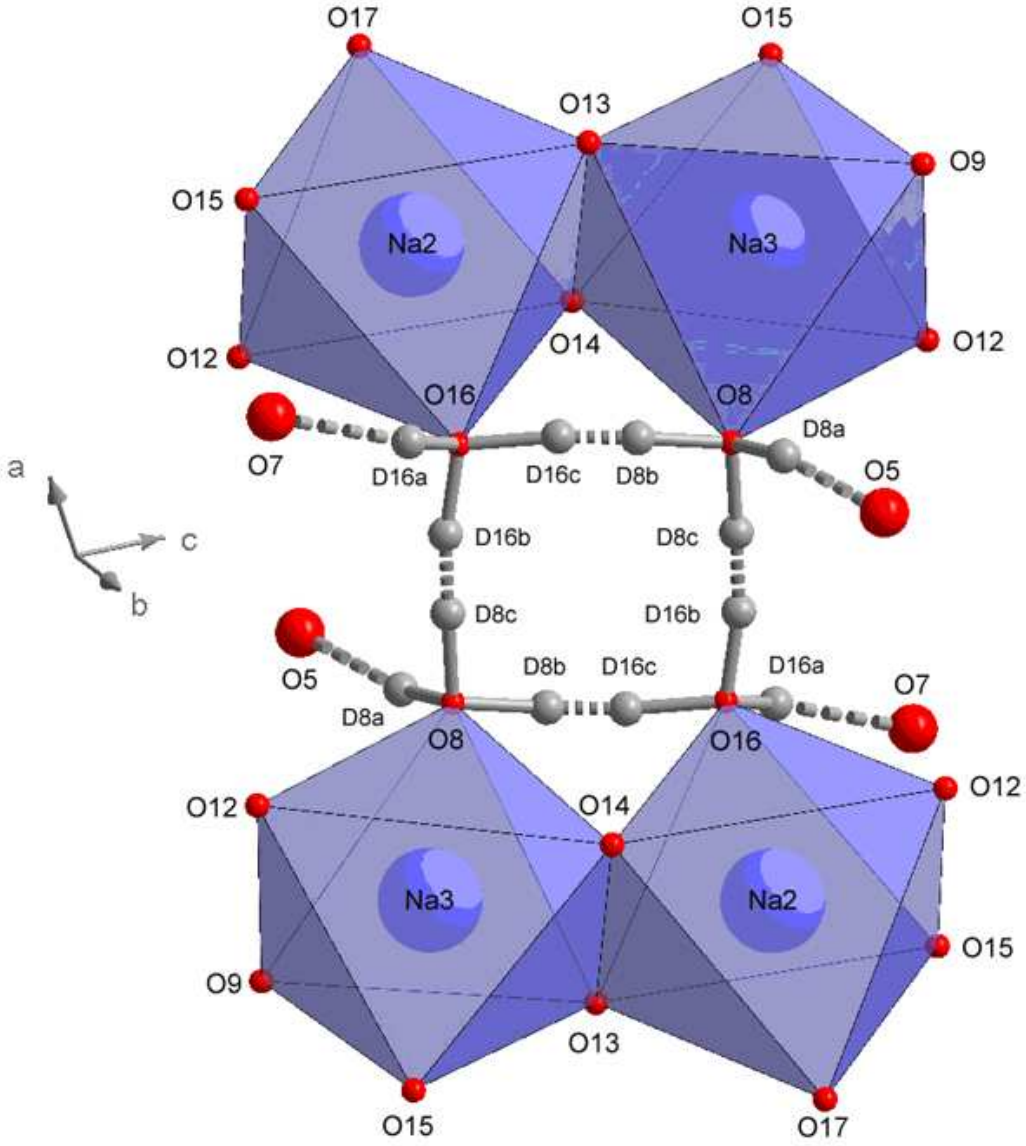

Figure 1.10 One of the square rings of water molecules in mirabilite involving disordered hydrogen bonds. The two-fold axis of rotational symmetry passes through the middle of the ring.

Levy and Lisensky also identified disorder over two orientations of the sulfate tetrahedra, which they denoted with 'prime' and 'double-prime' superscripts. The two orientations, related by a rotation of about 30° about the S···O5 vector (Figure 1.11), generate pairs of partially occupied sulfate oxygen sites (O4'/O4", O6'/O6", and O7'/O7" in their notation), which Levy and Lisensky (1978) found to be occupied in the ratio ≈ 25:75 (Figure 1.11b). The sulfate apices accept hydrogen bonds from neighbouring water molecules. The bonds donated to the O5 apex (from H8a, H10a, and H12b) are fully ordered. The bonds to the partially occupied apical sites are a mixture of ordered hydrogen bonds (donated by H10b, H11b, and H14b) and disordered hydrogen bonds (donated by H9a'/H9a", H16a'/H16a", and H17a'/H17a"). In Levy and Lisensky's refinement of the structure the occupancies of these hydrogen sites share the same occupancy as the apical oxygen sites; i.e., the 'primed' sites are ~ 25 % occupied, and the 'double-primed' sites are ~ 75 % occupied. Notice that the proposed switch in orientation from 'prime' to 'double-prime' involves breaking of the hydrogen bonds donated by H9a', H16a', and H17a' (the thicker, long-dashed bonds in Figure 1.11a), and the formation of new hydrogen bonds from H9a", H16a", and H17a" (the thin, short-dashed bonds in Figure 1.11a). Levy and Lisensky (1978) used the room temperature occupancies to determine the energy difference between the two orientations as 2713 ± 197 J mol^{-1}, which is approximately 10 % of the energy contained in a single hydrogen bond.

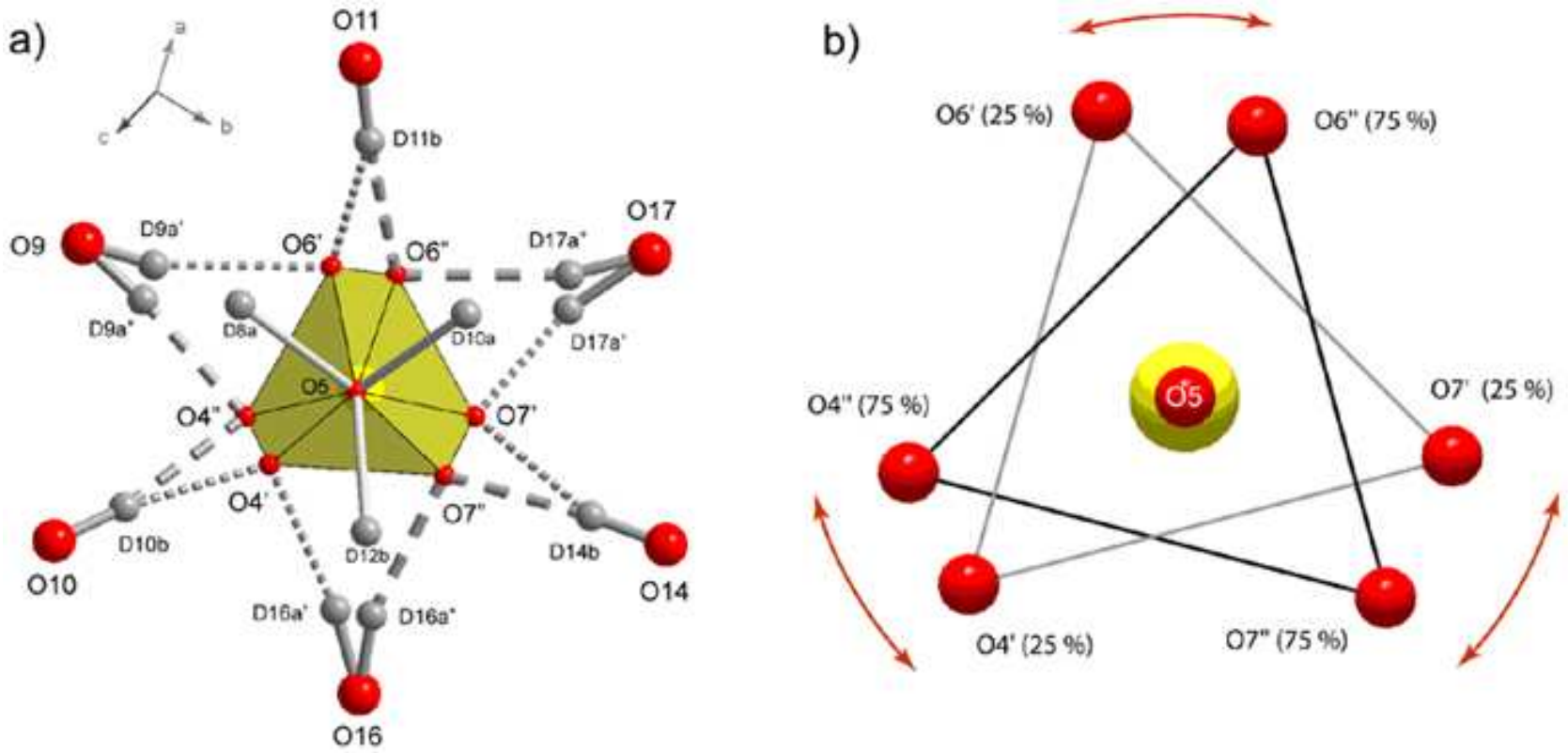

Figure 1.11 The two orientations of the sulfate tetrahedron described by Levy and Lisensky (1978) as viewed down the rotation axis (the S···O5 vector) - orientation relative to the crystallographic axes is shown by the legend in 1.8(a). The hydrogen bonds donated to the ordered apex (O5) are shown with solid grey rods; those donated to the lesser occupied apices (O4', O6', and O7') are depicted as thinner, short-dashed rods; those donated to the more fully occupied apices (O4", O6", and O7") are depicted as thicker, long-dashed rods.

1.2.2 $MgSO_4 – H_2O$ system

1.2.2.1 Anhydrous MgSO4

There are three known polymorphs of anhydrous $MgSO_4$, two that are stable at relatively low temperatures (but formed by different methods), and one that is stable at high temperatures. The phase which is grown from a solution of MgO in H_2SO_4 at ambient conditions is α-$MgSO_4$. It has the $CrVO_4$-type structure and it is orthorhombic, space-group *Cmcm*, *a* = 5.17471(3) Å, *b* = 7.87563(5) Å, *c* = 6.49517(5) Å, V = 264.705(2) $Å^3$ [ρ_{calc} = 3020.29(2) kg m^{-3}] at 300 K (Fortes *et al*., 2007). Another phase may be formed, either by dehydration of $MgSO_4$-hydrates or by heating α-$MgSO_4$ to 595°C (Yamaguchi and Kato, 1972); this is β-$MgSO_4$ which has the $ZnSO_4$-type structure; it is orthorhombic, space-group *Pbnm*, *a* = 4.74608(7) Å, *b* = 8.58317(10) Å, *c* = 6.70931(10) Å, V = 273.313(4) $Å^3$ [ρ_{calc} = 2925.17(4) kg m^{-3}] at 300 K (Eysel *et al*., 1985). β-$MgSO_4$ can be quenched easily to room temperature, and commercially available $MgSO_4$ is the β-phase. A third phase, γ-$MgSO_4$, has been discovered at temperatures above ~1000°C (Daimon and Kato, 1984; Rowe, 1967) but its structure remains unknown.

Very little work exists on the bulk properties of $MgSO_4$ and its phase transition behaviour. The structures and thermal expansivities of the α- and β-phases were measured by powder neutron diffraction methods from 4.2 – 300 K (Eysel *et al*., 1985) but work on the high temperature phase transitions and determination of the γ-$MgSO_4$ structure is outstanding. Livshits *et al.* (1963) compressed $MgSO_4$ to ~3 GPa, although it is possible that the material they report to be anhydrous was in fact the monohydrate (kieserite). Wang *et al*. (1999) compressed β-$MgSO_4$ to 7.7 GPa at 1800°C ($MgSO_4$ melts at ~1950°C at 7.7 GPa); upon quenching, they observed an X-ray diffraction pattern from α–$MgSO_4$.

1.2.2.2 Hydrated phases of MgSO4.

The $MgSO_4$ – H_2O system is far more extensive than the Na_2SO_4 - H_2O system. There are 8 phases: anhydrous $MgSO_4$, the monohydrate - kieserite, the dihydrate - sanderite, $MgSO_4 \cdot 4H_2O$ - starkyite, $MgSO_4 \cdot 5H_2O$ - pentahydrite, $MgSO_4 \cdot 6H_2O$ - hexahydrite, $MgSO_4 \cdot 7H_2O$ - epsomite, and finally $MgSO_4 \cdot 11H_2O$ - the undecahydrate meridianiite (MS11). The ambient pressure phase diagram of $MgSO_4$ - H_2O between 260 and 350 K with variation in $MgSO_4$ concentration is shown in Figure 1.12. Of the hydrated phases, only MS11 is discussed in detail here as it is the only $MgSO_4$ phase to be studied in this thesis.

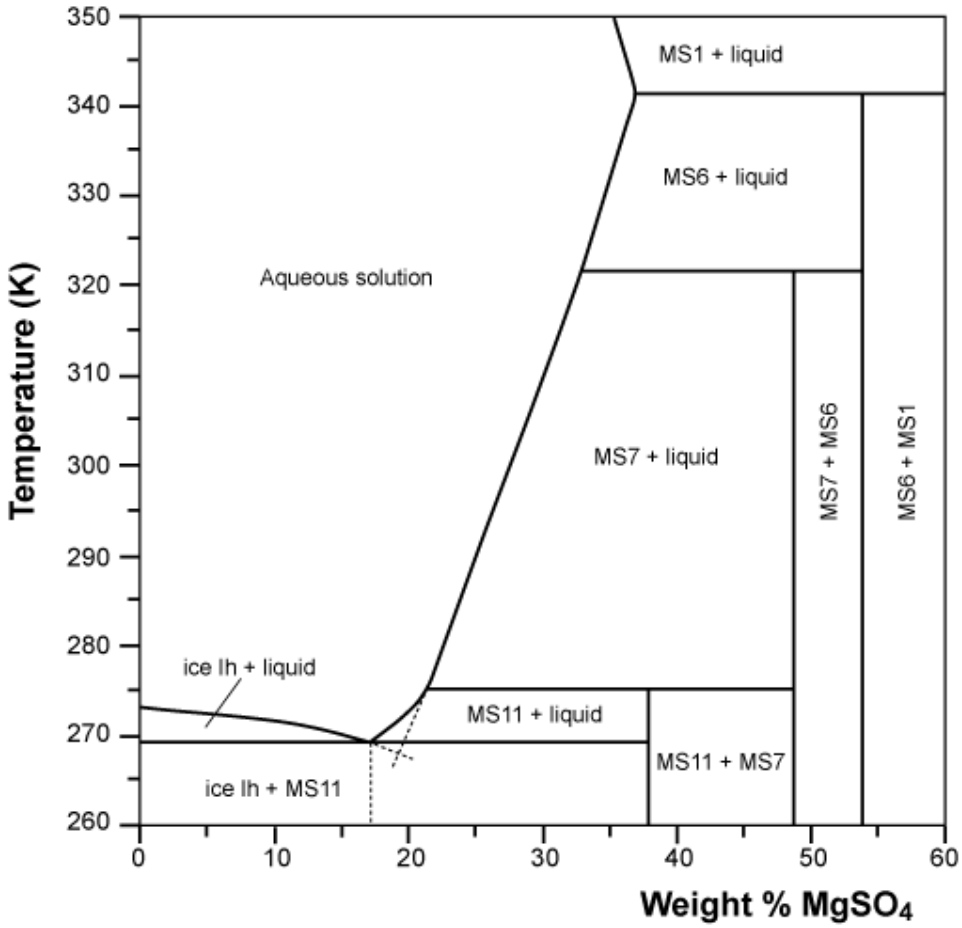

Figure 1.12 T-X phase diagram of the binary system magnesium sulfate – water at room pressure showing stable phase boundaries. From Grindrod *et al.* (2008), after Hogenboom *et al.* (1995) and Petersen and Wang (2006).

1.2.2.3 $MgSO_4.11H_2O$ – Meridianiite.

$MgSO_4 \cdot 11H_2O$ (MS11) is the most water-rich of the $MgSO_4$ hydrates; it was made in synthetic form by Fritzsche in 1837 and subsequently named after its discoverer (Fritzsche's salt). It was recently found as a naturally occurring deposit at a frozen brine pond in Canada (Peterson *et al.*, 2007), and the natural mineral was called meridianiite after a possible locality on Mars.

MS11 crystals are triclinic, space group P $\bar{1}$, (Z = 2) with a = 6.72746 (6) Å, b = 6.78141 (6) Å, c = 17.31803 (13) Å, α = 88.2062 (6) °, β = 89.4473 (8) °, γ = 62.6075 (5) ° and V = 701.140(6) $Å^3$ at 4.2 K (Fortes *et al.*, 2008). The atom naming scheme used throughout this work is a variation of the scheme used in Fortes *et al*. (2008) modified to make it similar to the naming scheme used for mirabilite. Figure 1.13 is a connectivity map showing the bonding scheme in MS11 and Figure 1.14 is a polyhedral representation of the MS11 structure. Oxygen atoms *O1 – O4* are the sulfate oxygens, *O5 – O10* are Mg-coordinated oxygens and the remaining 5 oxygens, *O11 – O15* are the free water molecules. The hydrogen atoms are named for their associated oxygen atoms, for example the water molecule containing *O11* will then also contain *H11a* and *H11b*. In this scheme, the water molecule with the bifurcated H – bond (see Fortes *et al.*, 2008) is denoted *O14*. The Mg-octahedra and sulfate tetrahedra are connected through the five free water molecules. Figure 1.13 shows that the two Mg- octahedra are symmetry independent and have differing bonding schemes. The water molecules coordinating Mg1 are H-bonded to both the free water and the sulfate tetrahedra, while those forming the octahedron around Mg2 are only hydrogen bonded to the interstitial water molecules (Fortes *et al*., 2008). The sulfate tetrahedra in MS11 accept fewer (10 vs. 12) hydrogen bonds than the tetrahedra in mirabilite, presumably as a result of the difference in electron density between the Mg and Na cations.

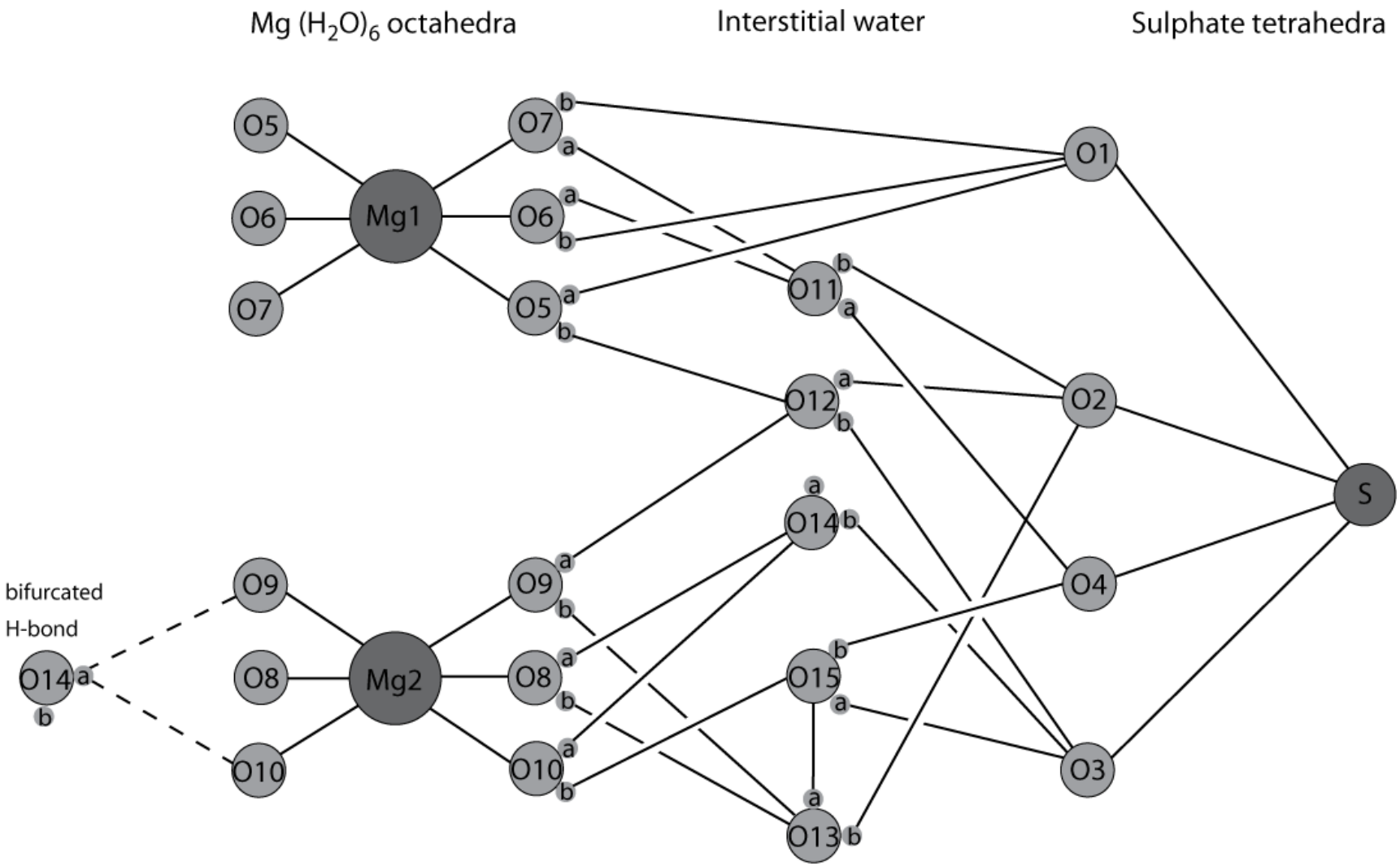

Figure 1.13 Connectivity map for MS11 at zero pressure, after Fortes *et al*. (2008)

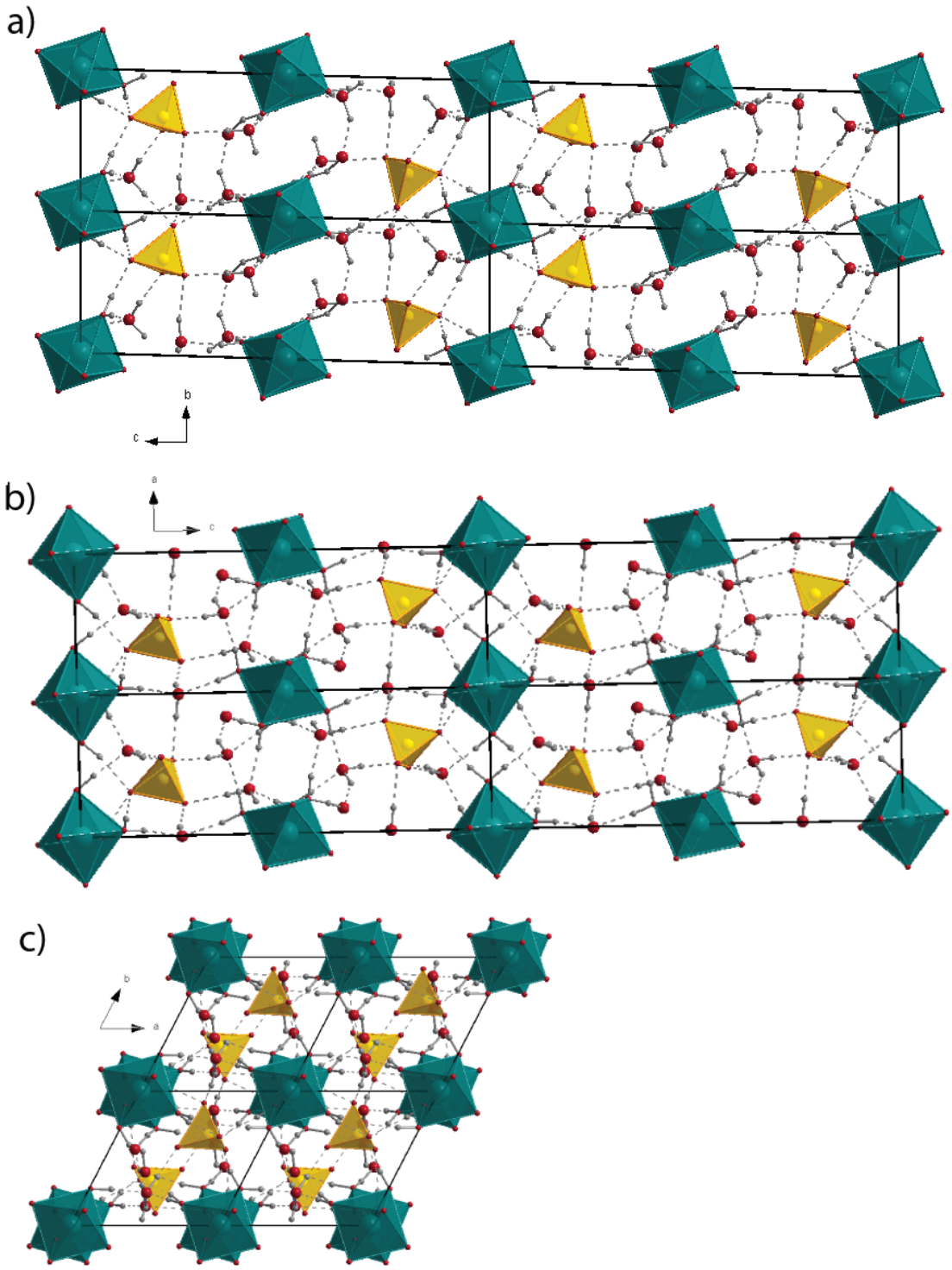

Figure 1.14 Polyhedral representation of the ambient pressure, low temperature, meridianiite structure, with the unit cell outlined in black: a) view along the *a*-axis, b) along the *b*-axis, and c) along the *c*-axis. The $Mg(H_2O)_8$ octahedra are shown in dark green and the SO_4 tetrahedra in orange.

1.3 Previous studies of evaporitic salt hydrates.

1.3.1 Previous studies of mirabilite.

To date there have been few structural studies of mirabilite. The crystal system and unit cell shape were known from early goniometric analysis (e.g., Brooke, 1824: see Groth, 1908, pp371-372). The earliest X-ray data are presented by Hanawalt *et al*. (1938), in the form of relatively inexact d-spacings vs. intensity. The unit-cell dimensions and space-group were determined using single-crystal X-ray methods by Alietti (1959) and Cocco & Rossetti (1959), and the heavy atom structure was later solved, apparently independently, by Ruben *et al*. (1961) and by Cocco (1962). Both studies obtained the same structure, although the latter displaces the unit-cell origin by 0, 0, ½. Levy & Lisensky (1978) carried out a single-crystal neutron diffraction study, publishing accurate hydrogen atom positions and describing orientational disorder within the structure.

No values of the incompressibility or thermal expansion as a function of temperature had been published before this study began. In light of the association of hydrated salts with extraterrestrial applications, there has been an interest within the planetary science community in measuring the solubility and density of mirabilite at non-ambient conditions (e.g., Hogenboom *et al.*, 1999; Dougherty *et al.*, 2006) to extend earlier high-pressure investigations of the pressure dependence of the ice-mirabilite eutectic in the range from $0 < P < 0.8$ GPa and $263 < T < 343$ K (Block, 1913; Geller, 1924; Tammann, 1929; Tanaka *et al*., 1992; Kryukov & Manikin, 1960).

1.3.2 Previous studies of meridianiite.

As with mirabilite, there have been relatively few structural studies of meridianiite; indeed, until 2006 it was thought that this compound was not the undecahydrate but the dodecahydrate of magnesium sulfate. The phase relations of MS11 were first investigated around the turn of the 20th century by Cottrell and reported in Van't Hoff (1901). The crystal structure of meridianiite was determined by Petersen and Wang (2006) who also recorded the first discovery of naturally occurring MS11 in Canada (Petersen *et al*.,2007). There have, as yet, been no studies of the compressibility of MS11 although the thermal expansion was recently measured using neutron diffraction techniques (Fortes *et al.,* 2008).

Recently, there has been a renewed interest in MS11 in light of the discovery of multiply hydrated Mg-sulfates at the surface of Mars. The densities and solubilities at planetary conditions have been of particular interest (Hogenboom *et al*., 1995); Grasset *et al*., 2001; Fortes *et al*., 2006; Dougherty *et al*., 2007) and it was suggested that the volume change by dehydration of MS11 could be responsible for rifting on Ganymede (Day *et al*., 2002; Hogenboom *et al.,* 2002). High pressure studies of meridianiite have focused on the rheology of eutectic MS11- H_2O mixtures (McCarthy *et al*., 2007).

1.4 Aims and methodologies of this thesis.

It is clear that there is a great deal still unknown about mirabilite and meridianiite even though these materials and their properties are important in a wide range of geological situations and processes. The objectives of this work were to obtain the thermoelastic properties over a range of temperatures and pressures which are relevant to both industrial and planetary processes and then to apply these properties to appropriate simulations of those processes. More specifically, the work aimed to quantify the thermal expansion and compressibility of mirabilite from 0 – 5.5 kbar and 4.2 – 300 K and the compressibility of meridianiite from 0 – 5.5 kbar.

The techniques used in this work involve both computational and experimental methods as a means of investigating the pressure-temperature-volume space. These techniques are explained in detail in Chapter 2: *Neutron diffraction studies I,* and Chapter 4: *Ab intio simulations I,* but there follows here a brief overview and explanation of the reasoning behind the selection of the particular methodology.

1.4.1 Computer simulation techniques

Computer simulations are an exceedingly valuable tool in the investigation of planetary materials. Three major advantages of using simulations are:

1. There are no constraints on the pressures and temperatures that can be simulated.

2. The primary output from a simulation is usually the relationship between the energy and the volume (an E-V curve), for the material under simulation and most physical properties which are relevant to Earth and planetary scientists can be derived from this, thereby reducing the experimental need for an array of different set ups to measure each class of physical property.

3. Errors encountered in theoretical simulations (e.g., statistical errors in molecular dynamics methods, system size and k-point sampling convergence in *ab initio* calculations) although present, are quantifiable.

There have traditionally been two computational approaches employed in the simulation of materials. The first of these uses classical relations to represent the interactions between constituent atoms as a potential function; the second, which is becoming increasingly

popular as the available computational power increases, is to use quantum mechanical first principles relations to describe the interactions between atoms.

Relatively complex systems such as salt hydrates present a challenge to potential calculations as both bonded and non-bonded interactions must be accounted for by any potential model. The potential models that have been developed are adapted versions of models applied to ionic materials. Hydrated sulfates have yet to be represented in interatomic potential calculations due to the added complexity brought by the water molecule to the interatomic interactions.

The earliest investigation of anhydrous sulfates (Meenan, 1992) developed potentials for potassium sulfate, which were then transferred to sodium sulfate. However, these potentials did not discriminate between the bonded and non-bonded interactions present in the structures. A subsequent study by Allan *et al*. (1993) did distinguish between these interactions through the inclusion of a Morse potential and was successful in simulating a range of anhydrous sulfates, including $MgSO_4$ and Na_2SO_4. Most recently, Jackson (2001) modified the results of Allan *et al*. (1993) by including a harmonic potential (in place of the Morse potential) to represent the S-O interaction. However, neither Allan *et al*. (1993) nor Jackson (2001) refitted the sulfate potentials to reflect a change in cation; only the cation – oxygen interaction has been modified with each new sulfate system modelled.

Potential calculations, although generally adequate for simulating the bulk lattice parameters of the sulfates as a group, are not sufficiently robust to represent accurately the complexity of the multiple phases for each different cation sulfate system. Appendix 1 details an attempt to use interatomic potential calculations to simulate Na_2SO_4 (there is a companion study for $MgSO_4$ but this has not been included). This work has not been presented in the main part of the thesis as the results are not considered sufficiently reliable.

Quantum mechanical *ab initio* calculations have long been employed to simulate materials of geological interest. They have been used successfully to simulate a wide range of materials such as iron in the Earth's core (e.g. Alfè *et al.*, 2004; Belonoshko *et al.*, 2000; Laio *et al.*, 2000), copper (Moriaty *et al.*, 1986; Belonoshko *et al*., 2000; Vočadlo *et al*,. 2004) polymorphs of H_2O (Fortes, 2004) and multiple hydrates such as epsomite ($MgSO_4.7H_2O$) (Fortes, 2006a) and ammonia hydrates (Fortes, 2004). Within the umbrella of "*ab intio* calculations" there are a large variety of flavours of calculation depending on the assumptions which go into the energy minimisation and determination.

Ab initio methods have been used to simulate both mirabilite and meridianiite, as, although they are somewhat more computationally expensive than classical methods, they have proved superior in the simulation of multiply hydrated compounds such as these (Fortes *et al.*, 2006b).

1.4.2 Neutron diffraction techniques.

Diffraction is an extremely powerful diagnostic tool in the study of materials. Thanks to the properties of quantum mechanics, in particular to wave-particle duality, particles such as neutrons and electrons can produce diffraction effects. Neutrons are particularly useful for the study of crystalline solids for several reasons. Firstly, as with X-rays, neutrons can be produced with a wavelength of approximately 1Å; this is comparable to the interatomic distances within the materials of interest. Secondly, neutrons are scattered by the nucleus, rather than by electrons, so the scattering cross-section is relatively small which allows the neutrons to penetrate the whole sample rather than just the surface layer as in X-ray diffraction. Thirdly, the neutron scattering factor of an atom is not related proportionally to atomic number and, therefore, neutron diffraction can "see" lighter elements such as hydrogen much better than X-ray diffraction where the scattering factor is linked in this way.

1.5.Thesis Outline

This thesis is divided into two main sections: Chapters 2, 3 and 4 are experimental and Chapters 5, 6 and 7 describe *ab initio* calculations. In particular, Chapter 2 describes the background and experimental methodology employed in the neutron diffraction experiments carried out here. Chapter 3 reports the results of the first of these neutron diffraction experiments, an experiment to determine the thermal expansion of mirabilite, one of the candidate salt hydrates, over a temperature range of 4.2 – 300 K at ambient pressure. Chapter 4 describes a neutron diffraction experiment to measure the compressibility of mirabilite from 0 – 0.55 GPa at 260 K and 80 K. Chapter 5 describes the *ab initio* methodology using the Vienna *Ab initio* Simulation Package (VASP) to simulate the structures and in compressibilities. The results of these simulations for mirabilite (0 – 60 GPa) and MS11 (0 – 11 GPa) are given in Chapter 6 and Chapter 7 respectively. The final chapter then summarises the results obtained from the experiments and simulations, and also describes details of a preliminary investigation in which the thermoelastic properties of some of the salt hydrates have been used to model diapiric structures on Earth, Mars and the icy satellites.

Chapter 2

Neutron diffraction studies I: Methodology

2.1 General introduction to diffraction.

Diffraction arises from the interaction of waves with periodically repeating objects; it provides an extremely powerful diagnostic tool for the study of the structure and properties of materials. The basic principle of diffraction can be most easily visualised by considering a "diffraction grating", essentially a regularly spaced set of holes. When a wave approaches such a barrier containing regularly spaced gaps similar in separation to the wavelength of the incoming wave, each gap will act as a new wave source, producing a secondary wave. As the secondary waves radiate away from the regularly spaced gaps and interact with each other there will be some directions where waves constructively interfere and some where they destructively interfere. This effect is observed for any type of wave, or group of waves, provided the wavelength of the incoming wave is smaller than that of the periodic spacing in the obstructing object.

Crystalline solids can act as 3-dimensional diffraction gratings as they are built up of a regular repeating set of base blocks - their unit-cells; now, the secondary waves are produced by scattering of the radiation by the atoms within the crystal. Incorporating three dimensions of diffraction complicates the resulting pattern significantly but we can simplify the problem using Bragg's law. In this approach, the incoming waves are, in effect, reflected from planes of atoms within the crystal (see Figure 2.1) and constructive interference (i.e., a diffraction maximum) will occur when each successive scattered wave is exactly one wavelength out of phase with the preceding one. For this to be true, Equation 2.1 must be satisfied:

$$2d\sin(\theta) = \lambda \qquad \textbf{Equation 2.1}$$

where λ is the wavelength of the incoming radiation, θ is the angle of incidence (which is equal to the angle of reflection), and 'd' is the spacing between the planes of atoms in the crystal structure.

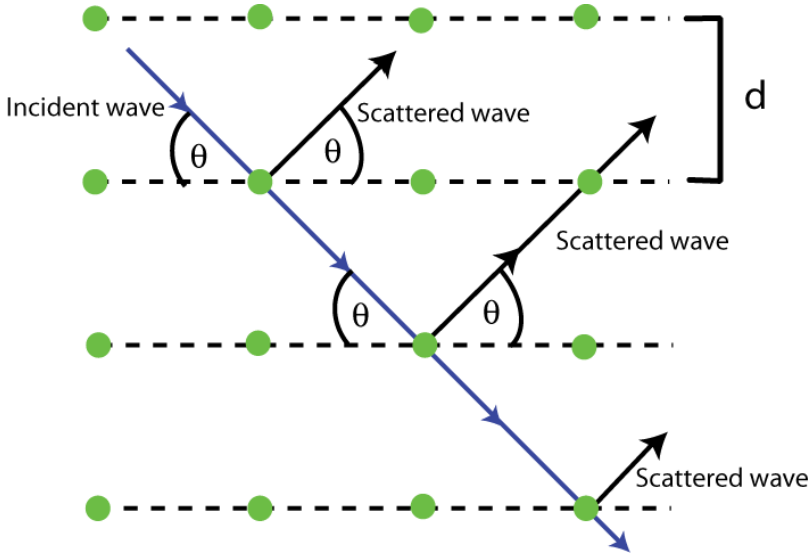

Figure 2.1: Schematic illustrating the geometry of Bragg's law. The green circles represent atoms in a crystal. The blue arrow is an incident wave and the black arrows are scattered waves. The dashed lines are planes within the lattice and "d" is the perpendicular distance between the planes.

Practically, in a diffraction experiment, it is the intensity of the diffracted waves with varying d-spacing and/or 2θ which is recorded by detectors around the sample. The crystalline samples used in diffraction experiments can be either powders or single crystals. Powders have the advantage over single crystals that the experiments are simpler to perform, particularly in controlled sample environments, although interpretation of the data may be more difficult. Statistically, in a well-randomised powder, every possible crystallographic orientation is represented; however, preferred orientation effects, which can alter the observed intensities, cannot always be avoided.

If diffraction is to be used to analyse the structure of crystalline materials, the incoming wave must have a wavelength less than twice the distance between the planes within the crystal; this length-scale is of the order of 1 Å. In the electromagnetic spectrum, this wavelength is within the X-ray region and X-rays are widely used in diffraction applications. However, thanks to the properties of quantum mechanics, in particular wave-particle duality, particles such as neutrons can also be used to form diffraction patterns from crystalline materials.

2.2 Neutron diffraction

Neutrons can be produced artificially with wavelengths of the same order as the interatomic distances within the lattices of typical crystalline solids and so these are ideal particles to use in the study of these materials. There are significant differences between the interactions and behaviour of X-ray radiation and neutrons that make each suited to different applications. Neutron diffraction is more suitable for investigating the large-unit-cell salt hydrate compounds of interest to this study for several reasons:

Neutrons are scattered by the nucleus, rather than by the electron cloud, so the neutron scattering cross-section is relatively small. This allows the neutrons to penetrate further into the sample rather than just the surface layer, as is the case in X-ray diffraction. Neutrons are also more readily able to penetrate sample containers and other components used to generate the sample environment.

The neutron scattering factor of an atom is not related proportionally to atomic number; therefore neutron diffraction allows us to "see" lighter elements better than X-ray diffraction where the scattering factor is linked to the number of electrons in the atom. Hydrated compounds, and others with large amounts of hydrogen in their structures, therefore benefit greatly from a neutron approach. Similarly, whereas the X-ray scattering factor can be very similar for neighbouring atoms and is identical for isotopes of the same element, for neutrons it can be very different, so it is easy to distinguish between neighbouring atoms in the periodic table using neutrons. An example of this is the disparity between the coherent scattering lengths of hydrogen and deuterium (- 0.374 x 10^{-12} cm and + 0.667 x 10^{-12} cm respectively (Neutron News, Vol. 3, No. 3, 1992, pp. 29-37). Variations in neutron scattering factor also means that combinations of particular isotopes and elements can be used to produce null scattering materials such as alloys of Ti and Zr where the negative and positive (respectively) coherent scattering amplitudes cancel each other out and the resulting alloy is effectively invisible to neutrons. Such materials are excellent for fabricating sample environment equipment as they will not interfere with the passage of the neutrons.

2.2.1 Neutron diffraction and hydrated materials.

As well as a difference between the coherent scattering lengths for isotopes of hydrogen, there is also a large difference between their incoherent scattering cross sections. The hydrogen atom has a large incoherent neutron scattering cross section, 79.9 $x10^{-24}$ cm^2, while deuterium has a much smaller one, 2.0 $x10^{-24}$ cm^2 (Neutron News, Vol. 3, No. 3, 1992, pp. 29-37). This is exemplified in Figure 2.2, which shows a neutron powder diffraction pattern for a) a protonated Antarctic ice sample and b) a deuterated ice sample. It is clear that protonation has a significant effect on the amount of background recorded. To avoid this effect, deuterated samples are commonly used in neutron powder diffraction experiments and, therefore, for the experiments reported in this thesis a perdeuterated mirabilite analogue has been used in order to achieve good signal to noise in the measured diffraction data (e.g., Finney, 1995). Deuteration is likely to have a minimal impact on the properties under investigation here; by comparison with water ice, we would expect the unit cell of the deuterated isotopomer to be slightly larger (order 0.1 %), and the bulk modulus to be slightly smaller (order 1 %) than for the hydrogen-bearing analogue. The work of Röttger *et al.* (1994) does not show a significant difference in volume thermal expansion between D_2O and H_2O.

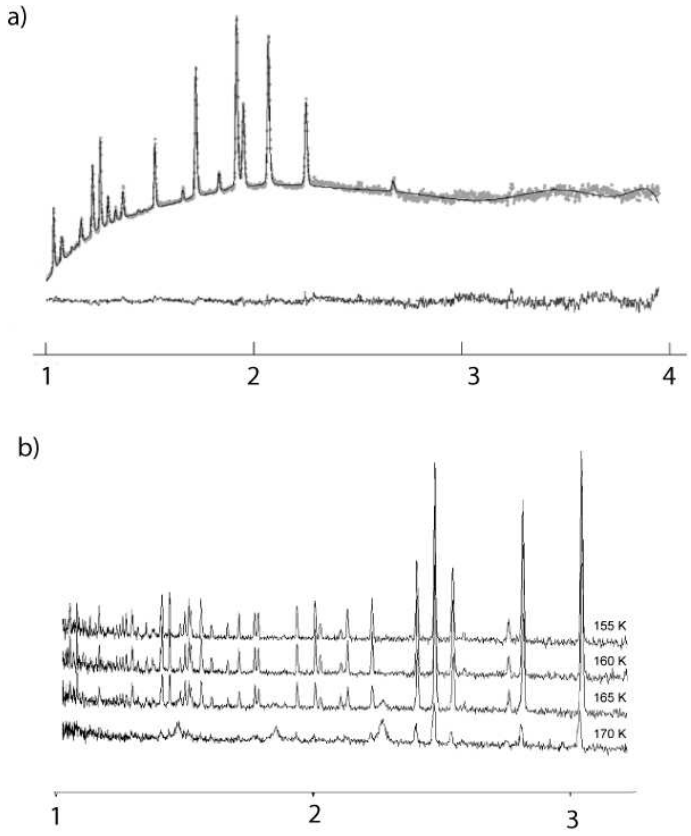

Figure 2.2 A comparison of the diffraction patterns of a) Antarctic H_2O ice (Fortes *et al. (*2004)), and b) a pattern for D_2O collected upon warming ice II through the transition to Ice Ic (at 160 K) on HRPD .

2.3 Generation of neutrons.

There are two ways of producing neutrons that are regularly used at research facilities engaged in crystallographic studies. The first is to use a nuclear reactor, as at the Institute Laue-Langevin (ILL) in Grenoble, or the OPAL reactor in Sydney, where fission generated neutrons are moderated to suitable wavelengths and then directed to the various instruments.

The second method of neutron production is spallation, which is the method employed by the ISIS facility at the Rutherford Appleton Laboratories in Chilton, Oxfordshire, where the diffraction experiments presented here were carried out. Spallation production of neutrons uses an accelerator to generate neutrons as the product of the collision of an accelerated particle beam with a heavy metal target; the neutrons are then moderated en route to the individual instruments. Reactor neutron sources are generally more powerful than spallation sources but the pulsed nature of a spallation source allows for a similar data collection rate via application of the time-of-flight method (See Section 2.6).

Figure 2.3 shows the layout of the experimental hall at the ISIS facility. At ISIS, to generate neutrons, first a beam of H^- ions is accelerated to high speeds with resulting energies of ~70 MeV, in a linear accelerator. This beam is then injected at a frequency of 50 Hz into a synchrotron. On entry, both electrons are removed from the H^- beam, converting it to a proton beam, which is then accelerated further to increase the energy of the particles to around 800 MeV over the course of approximately 10,000 revolutions in the accelerator. The beam is then fed from the synchrotron to the experimental hall where it collides with the tantalum-clad tungsten target at the centre of the hall. This collision excites the nuclei of the target causing them to release neutrons as a means of losing energy.

Neutrons produced at spallation sources in this way will have a range of very high velocities and energies. Thus, the neutrons must be moderated to a suitable energy range before being used by the instruments. The moderated neutron beam may require further conditioning. This is performed, as necessary, at instrument level, by devices termed "choppers". At spallation sources, chopper blades, made of neutron-absorbing material not only block high energy neutrons and gamma radiation, another product of the fission process which would cause severe background and damage the sample, but also curtail slow neutrons from the previous pulse.

At ISIS, there are 31 instruments arranged at different distances and orientations from the target around the ISIS experiment hall. Each instrument has unique capabilities and so each is used for a distinctive set of research activities and was specifically designed for that purpose. Once the neutrons arrive at the instrument and interact with the sample, detectors arranged at instrument-specific values of 2θ relative to the incoming beam, record the diffracted neutrons. The majority of the instruments at ISIS use the neutrons, but five are dedicated to the study of muons, which are produced by interaction of the proton beam with a graphite intermediate target. There are six instruments whose primary activities are crystallographic, and of these HRPD – the High Resolution Powder Diffractometer - is the most powerful in applications to structural studies of the type described here.

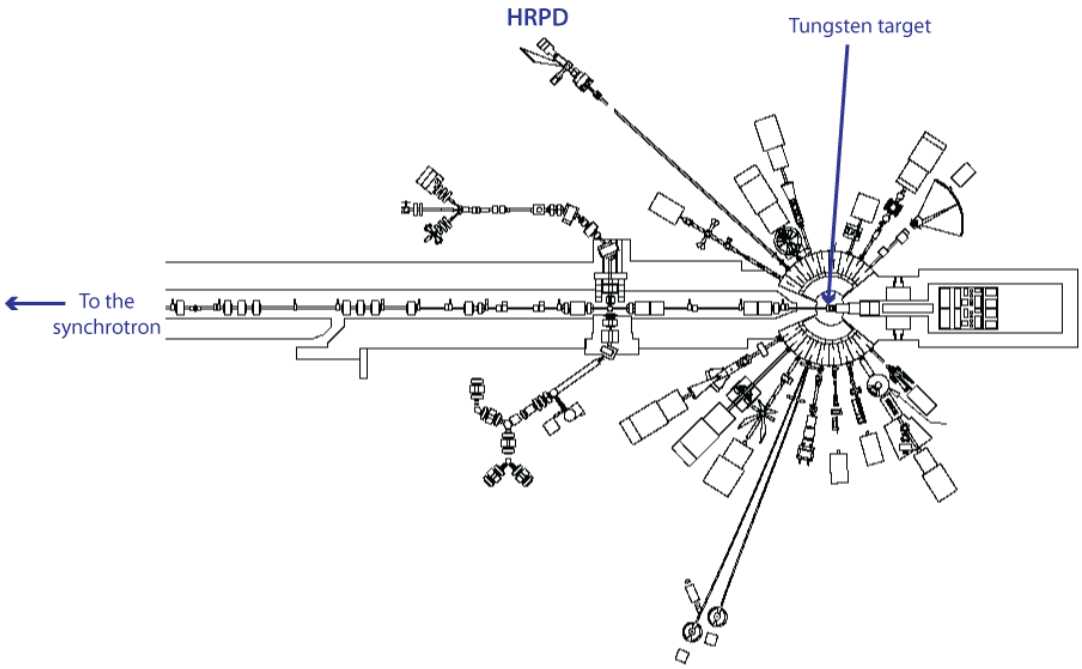

Figure 2.3 The layout of the experimental hall at the ISIS neutron spallation source at the Rutherford Appleton Laboratory showing the location of the heavy metal target and the HRPD instrument.

2.4 HRPD – The high resolution powder diffractometer.

The High Resolution Powder Diffractometer (HRPD) is set outside the main experimental hall at ISIS. This affords HRPD an unusually long neutron flight path (95m). This, combined with almost constant resolution ($\Delta d/d = 4 \times 10^{-4}$ in the backscattering detectors, $2\theta = 168.33°$) across all d-spacings, makes HRPD ideally suited to the rapid and accurate determination of cell parameters. Moreover, the instrument is sensitive to shifts in peak positions roughly two orders of magnitude smaller than the nominally stated resolution.

2.5 Time-of-flight neutron diffraction.

The most common diffraction method employed at pulsed neutron sources is that of time-of-flight (t-o-f), neutron diffraction. By equating quantum mechanical momentum with classical momentum and incorporating Bragg's law, it is possible to derive an expression in which the d-spacing within a crystal is proportional to the t-o-f of the diffracting particle. Thus:

The quantum mechanical momentum of a particle is defined by:

$$\hbar k = mv \qquad \textbf{Equation 2.2}$$

where $\hbar = h/2\pi$ (h is Planck's constant), k is the angular wavenumber, $k = 2\pi/\lambda$ (λ being the wavelength); the velocity of the particle, v, is simply L, the distance travelled, divided by t, the time of flight (v = L/t).

Equation. 2.2 becomes:

$$h\,k / 2\pi = m\mathrm{L} / \mathrm{t} \qquad \textbf{Equation 2.3}$$

and,

$$h / \lambda = m\mathrm{L} / \mathrm{t} \qquad \textbf{Equation 2.4}$$

which becomes,

$$\lambda = \frac{ht}{mL} \qquad \textbf{Equation 2.5}$$

Therefore, if we combine this with Bragg's law, Equation 2.1 becomes:

$$2d \sin\theta = \frac{ht}{mL} \qquad \textbf{Equation 2.6}$$

and finally $$d = \frac{h}{2mL\sin\theta} \cdot t \qquad \textbf{Equation 2.7}$$

Therefore the d-spacing of the diffraction peak is proportional to the t-o-f, t, which can be determined to extremely high accuracy. T-o-f experiments are carried out at constant 2θ. On HRPD, data can be collected in the backscatter (2θ = 168.4 °), 90 degree and low angle (2θ = 30°) banks. To obtain results with low d-spacing, the higher the value of 2θ, the better. Correspondingly, the low angle banks provide data at longer d-spacings. As well as the d-spacing range, the other primary characteristic of each detector bank is the resolution it provides in the diffraction pattern. Clearly, since *dd/dt* is proportional to 1/sinθ, the highest resolution will be obtained in backscattering geometry.

2.6 Data refinement.

The data analysis was carried out using the Rietveld method implemented in the *General Structure Analysis System* (GSAS) package (Larsen and Von Dreele 2000) with the EXPGUI user interface (Toby, 2001). The intensities of the peaks of a diffraction pattern are related to the atomic arrangement and unit-cell parameters by a Fourier transform. Rietveld refinement is a specific application of a least-squares approach for crystalline materials which refines a theoretical diffraction profile until it matches the measured profile (within a certain tolerance). This is illustrated below in Figure 2.4 which is an example of the graphical output from GSAS, showing a portion of a typical diffraction pattern. The red dots are the observations, the green line the calculated profile, the red and black tick marks below the pattern show the position of the peaks expected from the 2 phases present, and the purple trace at the bottom of the figure is the difference between the calculated and observed profiles.

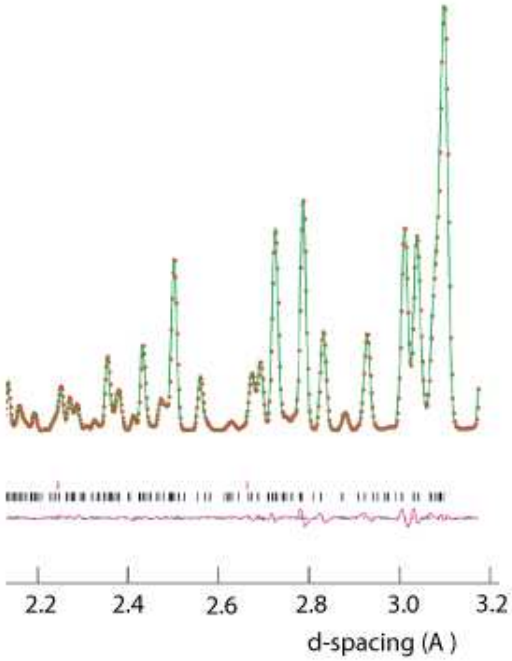

Figure 2.4 Reitveld refinement of mirabilite using GSAS. For clarity, only a limited d-spacing range is shown.The red dots are the observations, the green line the calculated profile, the red and black tick marks below the pattern are expected peaks for the 2 phases present and the purple trace at the bottom of the figure is the difference between the calculated and observed profiles.

The intensity of a diffraction pattern received at the detectors of a diffractometer at any point is a combination of the background scattering and contributions from nearby reflections so both must be accounted for in any calculated pattern and subsequent refinement. In GSAS a generalised least squares refinement is used whereby a fit is obtained by minimisation of the sum of the squares of the differences between observed and calculated values at each point recorded in the diffraction pattern. In the case of a set of crystallographic observations, the equations governing the diffraction intensities are transcendental, the minimisation function non-linear and so any refinement requires an initial estimate for all variables.

Often, in the first instance it is advantageous to use what is termed a Le Bail fit to the diffraction data. A Le Bail fit is a modification of the Rietveld method, which uses the diffraction intensities to fit the pattern to the unit cell parameters, without taking into account the contribution from the atoms within the unit cell. This allows fitting of the "whole" pattern and background, which can then be fixed in subsequent refinements involving other elements of the structure. In theory, a Le Bail fit is the best possible fit to a particular spacegroup, however, it has been shown that it is inaccurate in dealing with the detail of large-volume, low-symmetry structures such as the salt hydrates of interest here

(Petersen, 2005). This is because the powder diffraction patterns from these materials contain a very high density of peaks which Le Bail refinements struggle to fit.

A key advantage of Rietveld refinement over structural refinement methods which preceded it was the ability of this method to account for overlapping reflections in a powder diffraction pattern. The quantity minimised in Rietveld refinement is:

$$M = \sum_i W_i \left\{ y_i^{obs} - \frac{1}{c} y_i^{calc} \right\} \qquad \textbf{Equation 2.8}$$

where W_i is statistical weighting of the i^{th} observation y_i^{obs}; y_i^{calc} is the calculated intensity at the position of observation, i, and c is the scale factor relating the observed and calculated intensities. Since crystallographic refinements are not linear, several cycles of refinement are needed to achieve convergence.

A measure of how the refinement is progressing can be gleaned through the "goodness of fit" χ^2 . χ^2 is defined as:

$$\chi^2 = M / (N_{obs} - N_{var}) \qquad \textbf{Equation 2.9}$$

where N_{obs} is the total number of observations and N_{var} the number of variables in the least squares refinement. Other useful indicators of the goodness-of-fit can be obtained from the "R-factors" which are defined as follows:

$$R_P = \sum \left| I_0 - I_c \right| \Big/ \sum I_0 \qquad \textbf{Equation 2.10}$$

$$R_{wp} = \sqrt{M_P \Big/ \sum w I_c^2} \qquad \textbf{Equation 2.11}$$

$$R_{pb} = \sum \frac{\left| I_0 - I_c \right| \cdot \left| I_0 - I_b \right|}{I_0} \Big/ \sum \left| I_0 - I_b \right| \qquad \textbf{Equation 2.12}$$

$$R_{wpb} = \sqrt{\sum w\left(\frac{(I_0 - I_c)(I_0 - I_b)}{I_0}\right)^2 \Big/ \sum w(I_0 - I_b)^2} \qquad \textbf{Equation 2.13}$$

In these equations, M_p is the contribution to the minimisation function for powder data, w is the weighting, I is the intensity of the contribution with the subscripts "o" denoting observation, "c", the calculated intensity and "b" describes the background contribution.

As stated previously, the intensity of the peaks in a diffraction pattern received at the detectors of a diffractometer at any point is a combination of the background scattering and contributions from nearby reflections. Background intensity is accounted for in GSAS using a combination of an instrument parameter file and a generated profile. This component of the instrument parameter file is essentially a diffraction pattern for that particular instrument and beam current conditions obtained by running an empty sample can. The instrument parameter file also includes values for parameters such as the primary and secondary flight paths of the diffractometer which have been determined by running a standard sample (typically Si powder); such parameters can be varied during a refinement but there is rarely a need to do so. In GSAS, the background profile can be fitted using a variety of functions depending on the pattern. These functions include: power series, logarithmic interpolation or shifted Chebysechev polynomials; if all else fails, the background profile can be fitted graphically by the user.

The intensity that an individual Bragg peak will contribute to the intensity of a pattern, Y_h, depends largely on its structure factor, multiplicity and the amount of a particular phase. In addition, the intensity of a peak can also be affected by the shape and width of the peak relative to its position as well as other important factors such as absorption, extinction and preferred orientation. Thus (Von Dreele and Larsen, 2004),

$$Y_h = S\, F^2_h\, (T\text{-}T_h)\, K_h \qquad \textbf{Equation 2.14}$$

Where S is the scale factor for the phase, F_h is the structure factor for the reflection, $H(T\text{-}T_h)$ is a peak shape function for the reflection at the position T, when the peak centre is located at T_h. The term K_h is the product of the other intensity correction factors mention above, which depend on the geometry of the sample and environment and the type of radiation used, and is given by:

$$K_h = (E_h A_h O_h m_h L)/ V \qquad \textbf{Equation 2.15}$$

E_h is an extinction correction, A_h is an absorption correction, O_h is the preferred orientation correction, m_h is the reflection multiplicity, L is the angle-dependent Lorentz factor and V is the unit-cell volume for the phase (Von Dreele and Larsen, 2004).

Extinction, E_h, may be observed in strong Bragg reflections; effectively the strength of the reflection attenuates the incident beam as it passes further into the powder sample, and so the observed reflection appears weaker than might otherwise be expected. Extinction is strongly dependent on wavelength. If it is not properly accounted for, extinction in powders can lead to the erroneous values for atomic temperature factors and may also produce small shifts in atomic coordinates The correction to account for extinction used in GSAS was developed by Sabine (1985) and Sabine *et al.* (1988). The absorption factor, A_h, determines the absorption by the sample and again is wavelength dependent. L, the Lorentz factor is an additional factor to account for the variation of intensity with wavelength.

Preferred orientation, O_h, refers to a preferential alignment of crystals within a sample. In the case of a well-randomised powder, there should be little or no preferred orientation. However, if there is any recrystallisation during the course of an experiment then it is likely that there may well be preferred orientation produced within the sample. There are two types of preferred orientation correction in GSAS and in these experiments a spherical harmonic function, which takes into account the symmetry of the sample environment and the crystal, is used.

The shape of the peaks in a diffraction pattern is refined in GSAS using a set of profile coefficients. Typically the peak shape can be adequately represented by only refining a limited number of key coefficients, usually only those denoted σ_1 and γ_1. σ_1 and γ_1 adjust the shape of the peaks (Von Dreele and Larsen, 2004). There are further coefficients which can be used for more complex cases.

GSAS also allows users to apply constraints and restraints to the model of the structure that is being fitted. Though these parameters sound similar, they are not. Soft-bond restraints are used to limit the distances between bonded pairs of atoms to a certain length, within a tolerance specified by the user. Soft-bond restraints are weighted to reflect the effect of the

restraint component on the minimisation function and are usually balanced against each other and the diffraction pattern to ensure that the restraints do not overwhelm the other contributions to the minimisation function. Constraints can be used to confine a variety of properties of an atom, or group of atoms, to a particular value or relative value. They are imposed on parameters which would normally be unrelated, but for some presumed relation within the structure. Constraints which can be included are applied to the values of fractional occupancies, isotropic displacement parameters (temperature factors) and atomic positions. The exact detail of the restraints and constraints used in each experiment are explained at the start of the relevant chapter.

Summary

This chapter summarises the key aspects of diffraction experiments and their application to the study of hydrated materials. I have described the production of neutrons at spallation sources such as ISIS and the time-of-flight methodology which is typically used at such facilities. The results of the following chapters (3 and 4), will be analysed using a Rietveld refinement package called GSAS which employs a least-squares fitting approach to the refinement of a diffraction pattern. Chapters 3 and 4 detail the results of two experiments carried out to determine the thermal expansion and compressibility of mirabilite at temperatures and pressures relevant to planetary applications (0 – 0.55 GPa and 4.2 – 300 K).

Chapter 3

Neutron diffraction studies II:

The thermal expansion of mirabilite from 4.2 – 300 K

For this thesis two powder neutron diffraction experiments were carried out on HRPD at ISIS. The first, in July 2006, was a three day experiment to measure the thermal expansion of the salt-hydrate, mirabilite ($Na_2SO_4.10H_2O$), over a temperature range of 4 – 300 K at ambient pressure.

To measure the thermal expansion of a material we may simply monitor its unit-cell volume over a range of temperatures. To date, there have been no measurements of the thermal expansion of mirabilite (see Chapter 1, Section 1.4 for a description of the previous work on this material).

The work from this chapter has formed the basis of a paper, published in Physics and Chemistry of Minerals (Brand et al., 2009).

3.1 Sample preparation and data acquisition

3.1.1 Sample preparation

To make the sample, crystals of perdeuterated mirabilite were grown from a supersaturated solution of Na_2SO_4 (Sigma Ultra) in D_2O (Aldrich, 99 wt. % D) in a sealed flask. Large (~1 cm^3) crystalline lumps of mirabilite were extracted from the mother liquor and characterised by powder X-ray diffraction at University College London prior to the ISIS experiments to confirm their phase identity.

At ISIS, solid lumps of mirabilite were extracted from the liquor, dried on filter paper, and then quickly powdered in the ISIS cold room (to prevent dehydration which occurs at 305 K), using an agate pestle and mortar; the resulting coarse powder was loaded into an aluminium-framed slab can (sample size 25x18x10 mm) with vanadium windows (see Figure 3.1). During the data analysis (see section 3.1.3. below) it was discovered that a small amount (order 1 wt. %) of D_2O ice Ih was present in the sample, which probably originated from aqueous solution adhering to the polycrystalline chunks after extraction from the mother liquor. Any ice formed from atmospheric water vapour would contain a large amount of ^1H, resulting in an incoherent contribution to the background that is not apparent.

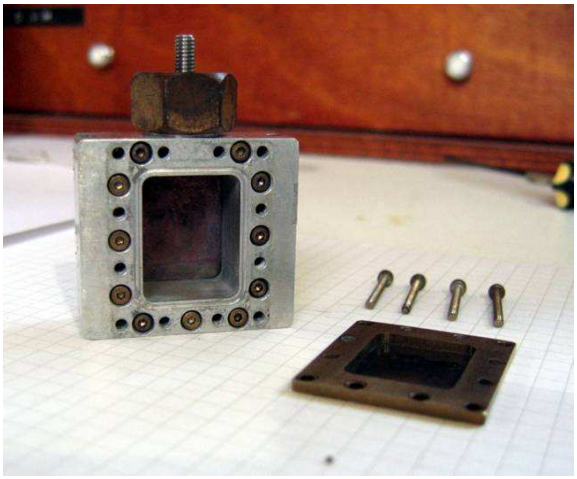

Figure 3.1 The aluminium-framed, vanadium-window slab can used in this experiment.

Gadolinium foil shielding was screwed over the front face of the can whilst a small electric heater and a RhFe temperature sensor were inserted into holes drilled in the aluminium frame to enable accurate measurement and control of the sample temperature. The sample can was screwed onto a cryostat centre stick and quenched to liquid nitrogen temperatures before being placed in a pre-cooled OC50 'Orange' cryostat (AS Scientific, Abingdon, U.K.) mounted on the HRPD beamline.

3.1.2 Thermal expansion data acquisition.

The sample temperature was reduced to 4.2 K and data were collected in the backscattering detector banks (2θ = 168°), the 90° banks, and the low angle banks (2θ = 30°), over the time-of-flight range 30 – 130 ms for 100 μAhr.

Data were then collected upon warming of the sample from 10 K to 300 K in 10 K increments, counting for approximately 20 minutes (7 μAhr), at each datum, and allowing 10 minutes equilibration time. At 300 K, another long count (100 μAhr) was undertaken to obtain another structural data set. Preliminary LeBail profile refinement of the warming data showed an abrupt change in the behaviour of the unit cell parameter β near 150 K (see Figure 3.6); it was therefore decided to collect further data whilst the sample was slowly cooled to 4.2 K (in 10 K steps interleaved between the warming points), again counting for 20 minutes (7 μAhr), with 10 minutes of equilibration at each point. Further structural datasets (100 μAhr) were collected at 4.2 K after the slow cooling, and at 150 K during a subsequent (second) slow warming run.

Data were normalised to the incident monitor spectrum and corrected for detector efficiency using a vanadium standard. After normalisation, the data were truncated to yield diffraction patterns over the d-spacing ranges 0.726 – 2.480 Å (backscattering), 1.017 – 3.180 Å (90° banks), and 2.724 – 9.300 Å (low-angle banks), although additional 'clipping' at the shortest and longest flight time edges of the t-o-f windows was done during refinement to eliminate some residual normalisation errors.

3.1.3 Thermal expansion data refinement - GSAS and least-squares fitting.

The data analysis was carried out using the Rietveld method implemented in the *General Structure Analysis System* (GSAS) package (Larsen & von Dreele, 2000) with the EXPGUI user interface (Toby, 2001). Starting with the 4.2 K quenched dataset, the unit cell (*a*,*b*,*c*,β) and structural parameters (*x*,*y*,*z*,U_{iso}) of mirabilite, the unit cell of ice Ih (*a*,*c*), scale factors and phase fractions, background coefficients (12 term shifted Chebyschev polynomial), and profile coefficients (σ_1 and σ_2, γ_1, L_{11}, L_{22}, L_{33} and γ_{1ec}) were refined; the initial atomic coordinates were taken from Levy and Lisensky (1978) for mirabilite and from Fortes *et al.* (2004) for ice Ih.

Soft bond length restraints were imposed upon the sulfate tetrahedra and the water molecules, fixing S – O = 1.47 (2) Å and O – O = 2.39 (2) Å (the latter forcing ∠O–S–O = 109 ±4°), O – H = 0.99 (2) Å and H – H = 1.56 (2) Å (forcing ∠H–O–H = 105 ±6°), with a χ^2 weighting FACTR = 200. Isotropic temperature factors (U_{iso}) for "like atoms" were constrained to be identical, these being grouped as: 1; Na atoms (Na2 and Na3), 2; S atoms, 3; sulfate oxygen atoms (O4 - O7), 4; water oxygen atoms coordinated to Na (O8, O9, O12 - O17), 5; other water oxygen atoms (O10 and O11), 6; deuterons H-bonded to sulfate oxygens (H8A, H9A, H10A, H10B, H11A, H11B, H12B, H13B, H14B, H15B, H16A and H17A), 7; deuterons H - bonded to free water molecules (H12A, H13A, H14A, H15A) and 8; protons in the disordered ring (H8B, H8C, H9B, H9C, H16B, H16C, H17B and H17C).

Sample texture was refined using the spherical harmonic model implemented in GSAS (10 terms for mirabilite only). Although the sample was not strongly textured, this term was found to have a significant effect on the refined values of the structural parameters, and gave improved agreement factors. Finally, it was found that it was necessary to include an extinction correction to avoid negative temperature factors; this is likely due to the coarse nature of the powder produced in an effort to avoid dehydrating the sample by excessive grinding.

It was found that the use of a single set of texture parameters for all three detector banks introduced bias into the refinements since the 90° and low-angle detectors, unlike the backscattering detectors, do not sense the whole Debye-Scherrer powder ring; for any structural model, the agreement of fit for each bank could be improved if the texture index for that bank was allowed to refine.

It was decided, therefore, that the backscattering data alone should be used for refinement of the structural model since the vast majority of the Bragg reflections (3911) were observed in the highest resolution backscattering data, whereas the 90° data contained only an additional 37 reflections (1291 reflections in total in the 90^o banks from mirabilite) and the low angle bank an additional 50 mirabilite reflections (only 96 reflections in total in this bank). However, as a final check of the validity of this procedure, the structural model obtained by fitting to the backscattering data was then fixed and used to fit the 90° and low-angle data varying only the background and peak profile coefficients, scale factors, the diffractometer constants DIFA and DIFC, and spherical harmonic texture coefficients.

In the later stages of the refinement, the fractional occupancies of the disordered atoms described by Levy and Lisensky (1978) – see Chapter 1, Section 1.3.1.3 for a full description of the structure of mirabilite and Figure 3.2 below as an aide memoir - were allowed to vary. As with the similar ring of water molecules seen in the ice Ih structure, the square ring of Na-coordinated water molecules within the mirabilite structure is formed of disordered hydrogen bonds, each O···O vector having two half-occupied hydrogen sites at high temperatures. The occupancies of these sites (constrained to sum to 1) were refined to obtain consistent and physically meaningful results (see Chapter 1, Section 1.3.1.3).

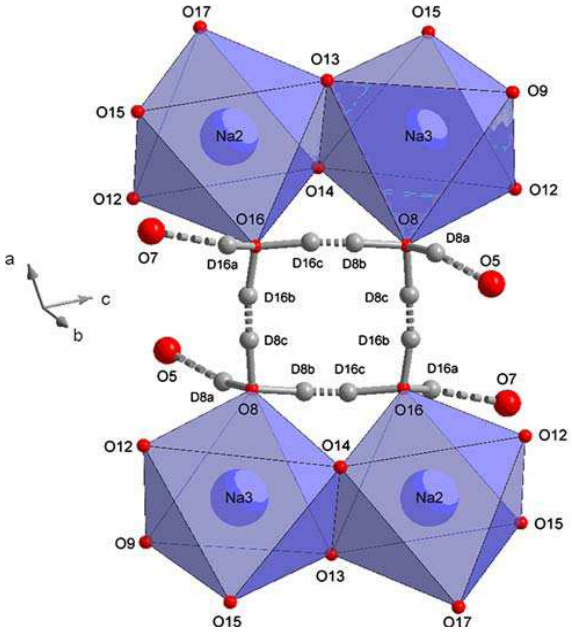

Figure 3.2 One of the square rings of water molecules involving disordered hydrogen bonds. The twofold axis of rotational symmetry passes through the middle of the ring, although not quite perpendicular to the plane of the page, as shown by the unit-cell axes.

Levy and Lisensky (1978) also identified two orientations for the sulfate tetrahedra in the structure (See Figure 3.4 in the results section of this Chapter) with occupancies of ~ 75:25 at room temperature, with correspondingly occupied sites for the hydrogen atoms bonded to the sulfate oxygens. However, refinement of the sulfate site occupancies in the present study resulted in a shift from 75:25 to 100:0. This occurred in all four structural datasets. Great care was taken to test the effect on χ^2 of fixing partial occupancies on these sites; the data are only consistent with ordered sulfate tetrahedra and ordered hydrogen bonds donated to the tetrahedra's apices (Section 3.2.1).

The quality of all the fits to the long count data, as exemplified by the 4.2 K slow cooled fit in Figure 3.3 and reported as Rietveld powder statistics in Table 3.1, is very good, even in the 90° and low-angle banks where the structural model was fixed; R_p values are all below 3

% for the 4.2K slow cooled data. The texture index of mirabilite is ≈ 1.01, indicative of a well randomised powder, and the refined phase fraction of mirabilite is 0.986(3). Note that the extinction coefficient is much higher at 300 K than it is at lower temperatures; this is probably due to grain growth since the specimen was above its binary eutectic temperature and a small amount of partial melting must have occurred; this is also reflected in an increase and change in form of the background in the diffraction pattern at 300 K.

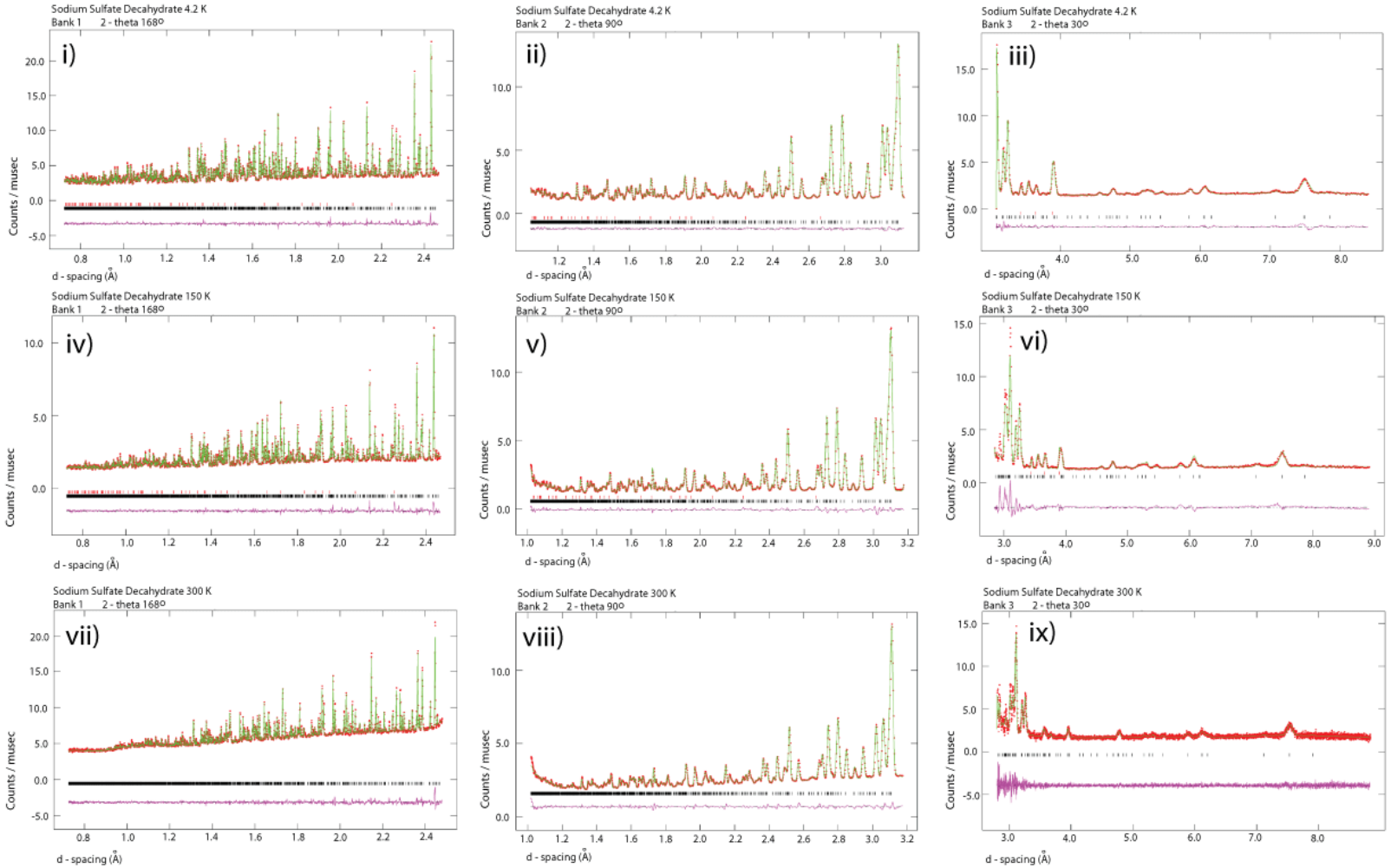

Figure 3.3 Neutron powder diffraction patterns of slowly cooled mirabilite at 4.2 K (i, ii and iii), 150 K (iv, v and vi) and 300 K (vii, viii and ix) obtained on HRPD; i, iv and vii are from the backscattering banks, ii, v and viii are from the 90° banks and iii, vi and ix are from the 30° banks. In each case the red circles are the observations, the green line the fit to the observations and the pink line below is the difference between the fit and the observations. The lower set of black tick marks denote the positions of the mirabilite peaks and the upper set of red tick marks are the positions of D_2O ice Ih peaks

Table 3.1 Refinement statistics of the four long long count datasets.

4.2 K slow cooled						
	No. of		Fitted		Minus Background	
Histogram	reflections	χ^2	*w*Rp	Rp	*w*Rp	Rp
Backscattering banks	3911	2.569	2.6%	2.2%	2.9%	2.4%
90 degree banks	1291	18.110	2.9%	2.2%	2.8%	1.5%
Low angle banks	51	4.015	3.4%	2.9%	3.5%	2.3%
Total	5253					
150 K						
Backscattering banks	4108	1.942	2.4%	2.1%	2.9%	5.2%
90 degree banks	1278	15.570	2.9%	2.2%	2.9%	1.7%
Low angle banks	58	8.564	6.9%	5.6%	10.8%	8.9%
Total	5444					
300 K						
Backscattering banks	4144	1.182	1.9%	1.7%	2.4%	2.2%
90 degree banks	1676	12.360	2.6%	2.3 %	2.3%	2.3%
Low angle banks	96	1.419	8.0%	7.0%	9.8%	8.7%
Total	5916					
4.2 K quenched						
Backscattering banks	4108	2.676	2.7%	2.3%	3.0%	2.6%
90 degree banks	1630	16.90	2.9%	2.2%	2.7%	1.7%
Low angle banks	63	4.044	3.9%	3.2%	4.2%	6.5%
Total	5801					

	4.2 K slow cooled	150 K	300 K	4.2 K quenched
Extinction (µm²)	245.24	295.00	926.77	265.33
Texture indices	1.0087	1.0115	1.0924	1.0094

3.2. Thermal expansion results

During the course of this experiment, while most of the data were collected in short, 7 μAhr per temperature sections, there were 3 temperatures in addition to the initial 4.2 K dataset at counts of the order of 100 μAhr which produced high resolution structural data sets: a second 4.2 K data set (after slow cooling), a 150 K data set and a 300 K dataset. It is these long-count datasets and their findings that are reported and analysed firstly in section 3.2.1, before section 3.2.2 discusses the thermal expansion behaviour of the mirabilite structure.

3.2.1 Structure and disorder of mirabilite.

The unit cell dimensions obtained from the four structural refinements at 4.2 (slow and rapidly cooled), 150 and 300 K are shown in Table 3.2; atomic coordinates, and selected interatomic bond distances and angles at each temperature are given in Table 3.3 below. Whilst these results do not offer a significant improvement in uncertainty on the atomic coordinates over Levy and Lisenky's (1978) single-crystal study, they do allow the determination of the temperature dependence of key structural parameters which may be related to the anisotropy of the thermal expansion, as described in the subsequent section. The agreement between the 300 K deuterated unit cell measured here and the 298 K hydrogenous unit cell (Levy & Lisensky, 1978) is excellent; only β differs by more than 2σ.

Table 3.2 Comparison of the unit cell dimensions of mirabilite at 4.2 K (slow cooled and quenched), 150 K and 300 K with the published values of Levy and Lisensky (1978).

	4.2 K Quenched	4.2 K slow cooled	150 K	300 K	298 K L & L (1978)
a (Å)	11.44190(6)	11.44214(4)	11.46417(5)	11.51473(7)	11.512(3)
b (Å)	10.34307(5)	10.34276(4)	10.34689(5)	10.36496(6)	10.370(3)
c (Å)	12.75316(6)	12.75468(6)	12.77201(6)	12.84653(7)	12.847(2)
β (°)	107.838(1)	107.847(1)	107.826(1)	107.7545(1)	107.789(10)
Volume ($Å^3$)	1436.714(8)	1436.794(8)	1442.266(8)	1460.20(1)	1460.3(5)

Table 3.3 Sulfate bond angles and lengths in the mirabilite structure at 4.2 K, slow cooled and quenched, 150 K and 300 K.

	4.2 K quenched	4.2 K slow cooled	150 K	300 K	Levy and Lisensky (1978)
Length (Å)					
S-O4	1.467(2)	1.466(2)	1.467(2)	1.467(1)	1.487(6)
S-O5	1.466(2)	1.467(2)	1.466(2)	1.467(1)	1.481(7)
S-O6	1.468(2)	1.469(2)	1.468(2)	1.467(1)	1.467(7)
S-O7	1.467(2)	1.468(2)	1.466(2)	1.467(1)	1.486(7)
Angle (°)					
O4-S-O5	109.3(2)	109.5(2)	109.4(2)	109.5(2)	109.7 (4)
O4-S-O6	109.6(2)	109.6(2)	109.5(2)	109.5(1)	110.0 (5)
O4-S-O7	109.5(2)	109.6(2)	109.5(2)	109.5(1)	109.4 (5)
O5-S-O6	109.3(2)	109.4(2)	109.4(2)	109.4(1)	109.0 (4)
O5-S-O7	109.9(2)	109.8(2)	109.8(2)	109.5(1)	108.7 (5)
O6-S-O7	109.2(2)	109.0(2)	109.3(2)	109.5(1)	110.0 (5)
Length (Å)					
Na2-O12	2.432(9)	2.433(9)	2.418(10)	2.416(16)	2.450 (7)
Na2-O13	2.413(9)	2.409(9)	2.414(10)	2.451(16)	2.440 (7)
Na2-O14	2.413(10)	2.403(9)	2.392(11)	2.409(16)	2.390 (6)
Na2-O15	2.374(10)	2.378(9)	2.410(11)	2.391(16)	2.402 (6)
Na2-O16	2.444(9)	2.429(9)	2.438(10)	2.460(17)	2.454 (8)
Na2-O17	2.383(9)	2.390(9)	2.397(10)	2.467(17)	2.425 (8)
Na3-O8	2.381(9)	2.386(8)	2.417(10)	2.433(14)	2.385 (7)
Na3-O9	2.357(8)	2.369(8)	2.345(9)	2.321(14)	2.389 (7)
Na3-O12	2.439(9)	2.459(8)	2.457(9)	2.534(15)	2.450 (6)
Na3-O13	2.424(9)	2.409(8)	2.430(9)	2.363(16)	2.474 (6)
Na3-O14	2.371(9)	2.354(8)	2.360(9)	2.425(14)	2.420 (6)
Na3-O15	2.424(9)	2.418(8)	2.406(10)	2.407(15)	2.432 (7)
Angle (^{o})					
O12-Na2-O14	91.9(3)	91.9(3)	92.6(4)	92.4(6)	91.8 (2)
O12-Na2-O15	86.3(3)	86.2(3)	86.1(3)	87.2(5)	86.3 (2)
O12-Na2-O16	88.6(3)	88.7(3)	88.2(3)	91.1(5)	91.0 (3)
O12-Na2-O17	89.0(3)	88.4(3)	88.2(4)	88.7(6)	88.7 (3)
O13-Na2-O14	85.9(3)	86.1(3)	86.1(3)	85.4(5)	87.1 (2)
O13-Na2-O15	95.6(3)	95.6(3)	94.9(4)	95.0(6)	94.7 (2)
O13-Na2-O16	86.6(3)	86.9(3)	87.9(4)	87.5(6)	86.6 (3)
O13-Na2-O17	95.9(3)	96.1(3)	95.7(4)	92.7(5)	93.7 (3)
O14-Na2-O16	88.8(3)	89.0(3)	89.7(3)	90.1(5)	91.3 (3)
O14-Na2-O17	92.4(3)	92.9(3)	92.9(4)	91.1(6)	90.5 (3)
O15-Na2-O16	87.5(3)	87.6(3)	87.2(3)	88.3(5)	86.7 (2)
O15-Na2-O17	91.3(3)	90.5(3)	90.2(3)	90.5(6)	91.6 (3)
O8-Na3-O9	93.5(3)	93.4(3)	93.7(3)	93.1(4)	92.9 (3)

O8-Na3-O12	92.9(3)	92.4(3)	92.7(3)	88.9(5)	92.1 (3)
O8-Na3-O13	88.3(3)	88.5(3)	88.0(3)	90.2(5)	89.0 (2)
O8-Na3-O14	92.1(3)	92.0(3)	91.6(4)	90.1(5)	92.3 (2)
O9-Na3-O12	87.4(3)	86.7(3)	87.0(3)	87.0(5)	87.5 (2)
O9-Na3-O13	89.6(3)	89.6(3)	89.9(3)	91.8(5)	89.6 (2)
O9-Na3-O15	90.4(3)	90.1(3)	90.8(4)	93.5(6)	91.6 (3)
O12-Na3-O14	96.3(3)	96.4(3)	96.7(3)	94.2(5)	97.1 (2)
O12-Na3-O15	85.0(3)	84.7(3)	85.4(3)	84.2(5)	85.7 (2)
O13-Na3-O14	86.6(3)	87.2(3)	86.5(3)	87.0(5)	85.8 (2)
O13-Na3-O15	94.0(3)	94.6(3)	94.2(3)	96.8(6)	93.5 (2)
O14-Na3-O15	84.2(3)	84.7(3)	84.1(3)	83.4(4)	83.4 (2)

3.2.1.1 Hydrogen bond lengths in the long-count datasets.

There are four types of hydrogen bond in the mirabilite structure, which may or may not behave differently with temperature; these are 1) those donated by Na-coordinated waters to other Na-coordinated waters (i.e., those involved in the square rings), 2) those donated by Na-coordinated waters to interstitial waters, 3) those donated by Na-coordinated waters to sulfate oxygens and finally 4) those donated by interstitial waters to sulfate oxygens. It is interesting to note that the deuteron disorder is confined to the type 1 bond.

At 4.2 K H-bond types 1 - 4 have mean lengths of 1.797(2) Å, 1.840(3) Å, 1.859(3) Å, and 1.848(2) Å, respectively. At 300 K, the mean lengths of these bonds are, respectively, 1.7995(4) Å, 1.8508(5) Å, 1.8500(4) Å, and 1.910(3) Å, The difference in the mean length of hydrogen bond type 1 is not significantly different from zero (0.003 ± 0.002 Å), and in the type 2 and 3 bonds it is very small (0.010 ± 0.004 Å). However, the type 4 H-bonds, those donated by interstitial waters to sulfate oxygens, exhibit a significant increase in their mean length on warming from 4.2 - 300 K (0.062 ± 0.005 Å). This behaviour is similar to that observed in $MgSO_4 \cdot 11D_2O$ where the water - water H-bonds do not change in length, but the water - sulfate H - bonds weaken significantly upon warming (Fortes *et al*., 2008b).

The type 1 hydrogen bonds which form the disordered ring structure exhibit insignificant differences in length between quenched and slow cooled specimens. The average quenched and slow cooled values of bond lengths are 1.802(3) Å and 1.797(2) Å, respectively.

Considering the hydrogen bond angles (∠ O-D···O), type 2 are the most linear (172 ± 0.2°) and type 1 are the least linear (164 ± 0.2°) at 4.2 K. This bond angle does not change significantly with temperature across types 1—3 (< 1%). However, the average value for type 4 H-bonds changes by 6(1)° (4%) revealing that much of the strain in the structure is accommodated by bending of bonds donated by interstitial water molecules.

3.2.1.2 Disorder within the mirabilite structure.

The existing mirabilite heat capacity data (Pitzer & Coulter, 1938; Brodale & Giauque, 1972; Ruben *et al.*, 1961) have been used to infer that hydrogen bonds in the mirabilite structure were disordered, and that this disorder became frozen-in at limiting low temperatures. In their single-crystal study, Levy and Lisensky (1978) identified two areas of orientational disorder, the first associated with a pair of square rings of water molecules between adjacent octahedral apices, and the second associated with the sulfate tetrahedra.

The results at 300 K show complete orientational disorder of the water molecules in the square rings; the occupancy ratios of the deuterons in the 'b' and 'c' sites in both rings are 49.5(8):50.5(8). As the temperature is reduced slowly, the trend is towards greater orientational order, the 'b' site having the larger occupancy. On the timescale of these experiments, full orientational order was not achieved at liquid helium temperatures, the 'b':'c' occupancy ratio being ~ 70:30 (see Table 3.4), although it is possible that sufficiently long timescales at low temperatures (e.g., on the surfaces of icy moons in the outer solar system) will permit full ordering of these sites to be attained. This is in agreement with measurements of the heat capacity as a function of temperature (Pitzer & Coulter, 1938; Brodale & Giauque, 1972; Ruben *et al.*, 1961). More rapid cooling (in this instance, quenching in liquid nitrogen) results in a non-equilibrium value for the occupancies becoming frozen-in. The refined occupancies from the quenched sample measured at 4.2 K are the same as those observed in the slow-cooled sample measured at 150 K (see Table 3.4). As discussed in section 3.2.2.1 below, the variation of the unit-cell parameter β appears to support the hypothesis that this orientational disorder becomes frozen in near 150 K when mirabilite is quenched rapidly.

Table 3.4 The refined fractional occupancies (constrained to sum to unity) of deuterons in the square rings defined by oxygen atoms O8/O16 (ring 1) and O9/O17 (ring 2) as a function of temperature which were constrained to be the same in both rings.

Species	300 K	150 K	Slow cooled at 4.2 K	Quenched 4.2 K
'b'	0.494(6)	0.652(5)	0.693(4)	0.654(5)
'c'	0.506(6)	0.348(5)	0.307(4)	0.346(5)

Levy and Lisensky also identified disorder over two orientations of the sulfate tetrahedra, which they denoted with 'prime' and 'double-prime' superscripts. The two orientations, related by a rotation of about 30° about the S···O5 vector (Figure 3.4), generate pairs of

partially occupied sulfate oxygen sites (O4'/O4", O6'/O6", and O7'/O7" in their notation), which Levy and Lisensky (1978) found to be occupied in the ratio ≈ 25:75 (Figure 3.4b). The sulfate apices accept hydrogen bonds from neighbouring water molecules. The bonds donated to the O5 apex (from D8a, D10a, and D12b) are fully ordered. The bonds to the partially occupied apical sites are a mixture of ordered hydrogen bonds (donated by D10b, D11b, and D14b) and disordered hydrogen bonds (donated by D9a'/D9a", D16a'/D16a", and D17a'/D17a"). In Levy and Lisensky's refinement of the structure the occupancies of these hydrogen sites share the same occupancy as the apical oxygen sites; i.e., the 'primed' sites are ~ 25 % occupied, and the 'double-primed' sites are ~ 75 % occupied. Notice that the proposed switch in orientation from 'prime' to 'double-prime' involves breaking of the hydrogen bonds donated by D9a', D16a', and D17a' (the thicker, long-dashed bonds in Figure 3.4a), and the formation of new hydrogen bonds from D9a", D16a", and D17a" (the thin, short-dashed bonds in Figure 3.4a). Levy and Lisensky (1978) used the room temperature occupancies to determine the energy difference between the two orientations as 2713 ± 197 J mol^{-1}, which is approximately 10 % of the energy contained in a single hydrogen bond.

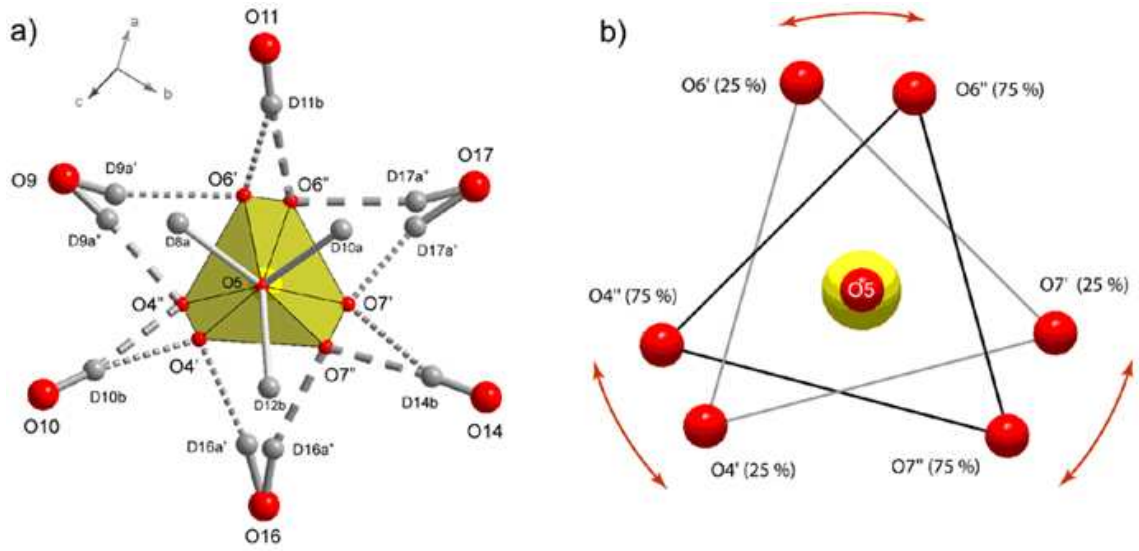

Figure 3.4 The two orientations of the sulfate tetrahedron described by Levy and Lisensky (1978) as viewed down the rotation axis (the S···O5 vector) -orientation relative to the crystallographic axes is shown in (a). The hydrogen bonds donated to the ordered apex (O5) are shown with solid grey rods; those donated to the lesser occupied apices (O4', O6', and O7') are depicted as thinner, short-dashed rods; those donated to the more fully occupied apices (O4", O6", and O7") are depicted as thicker, long-dashed rods.

In the present study, refinement of these site occupancies yielded ratios of 'prime':'double-prime' = 0:100 at all temperatures and this was confirmed by production of a Fourier map of the neutron scattering density in GSAS. This map can be seen in Figure 3.5; the plane of the map is defined by the three oxygen atoms O4, O6 and O7, and the centre of the map is defined by the position of the sulfur atom, with the viewing direction normal to the plane which contains the O4, O6 and O7 atoms. This corresponds to looking directly down from the O5 vertex of the sulfate tetahedron. The map shows no “extra” observable peaks which could be coincident with the alternative ‘double primed’ oxygen sites. This is the sole point of significant disagreement between the present work and that of Levy and Lisensky; it is plausible that the difference is the result of deuteration, or that it is due to the thermal history of the sample during the diffraction data collection, or some other aspect of the crystal growth or sample preparation prior to the start of the experiment.

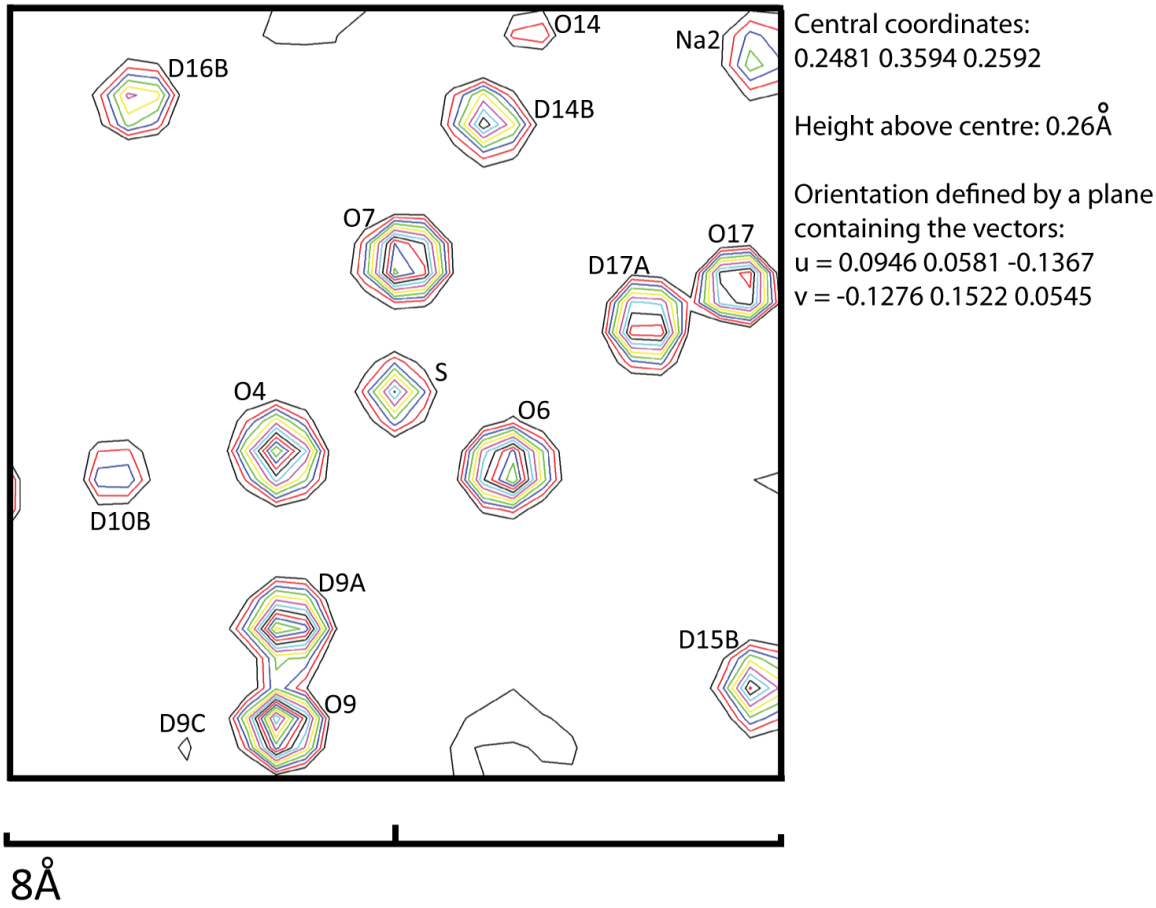

Figure 3.5 Fourier (F_{obs}) map produced from the long-count data at 300 K showing the observed scattering density as a function of position within part of the mirabilite unit-cell.

The volume and distortion parameters of the two symmetry-independent $Na(H_2O)_6$ octahedra as a function of temperature are given in Table 3.5. These octahedra have a volume ~ 65 % greater than in Mg-sulfate hydrates, but exhibit the same trend towards smaller volume and less distortion with increasing hydration number; room temperature data for thenardite are compared in Table 3.5. Upon cooling to 4.2 K, the Na2 octahedron increases in volume by 0.7 % whereas the Na3 octahedron shrinks by 2%, the former being similar to the increase in volume (1-2 %) in the MgO_6 octahedra observed in epsomite and meridianiite (Fortes *et al*., 2006b, 2008b). The Na-O distances between apical oxygens, and shared-edge oxygens follow the same trend, the former shrinking from a mean of 2.420(8) Å at 300 K to a mean of 2.394(4) Å at 4.2 K ($\Delta L/L$ = -1.1 ± 0.1 %); the latter shrink from a mean of 2.425(5) Å at 300 K to a mean of 2.408(3) Å at 4.2 K ($\Delta L/L$ = -0.7 ±0. 2 %).

Since the S-O bond lengths and angles in the sulfate tetrahedron were restrained, it is not possible to draw any conclusions as to the temperature dependent behaviour of this unit; however, Fortes *et al.* (2008b) note the trend of negligible change in volume with temperature in a range of anhydrous and hydrated Mg-sulfate crystals.

Table 3.5 Changes in the size and shape of the octahedra in mirabilite and NaO_6 octahedra in thenardite with temperature. Volumes and distortion parameters (as defined by Robinson *et al*., 1971) were calculated using the program DRAWxtl (Finger *et al*., 2007).

	300 K	150 K	Slow cooled 4.2 K	Quenched 4.2 K
Na2 octahedron				
Volume ($Å^3$)	19.719	19.854	19.813	19.854
Na3 octahedron				
Volume ($Å^3$)	20.317	19.977	19.913	19.918
Thenardite[(a)]				
Volume ($Å^3$)	25.500	-	-	-

(a) Rasmussen *et al.*, (1996).

3.2.2 Thermal expansion of the mirabilite structure.

Lattice parameters (*a, b, c,* β) for mirabilite were obtained at 31 temperatures from 4.2 K to 300 K (in 10 K increments) during slow warming of the initially quenched sample, and at 30 temperatures from 300 K to 4.2 K (also in 10 K increments) during slow cooling; these data are shown in Figure 3.6 and shown in a table in Appendix 2. Rietveld refinement of these 7 μA hr datasets yielded unit-cell parameters with a precision of ~ 3 parts in 100,000, which is comparable to the precision achieved in earlier studies of $MgSO_4 \cdot 7D_2O$ (Fortes *et al.*, 2006b) and $MgSO_4 \cdot 11D_2O$ (Fortes *et al.*, 2008b).

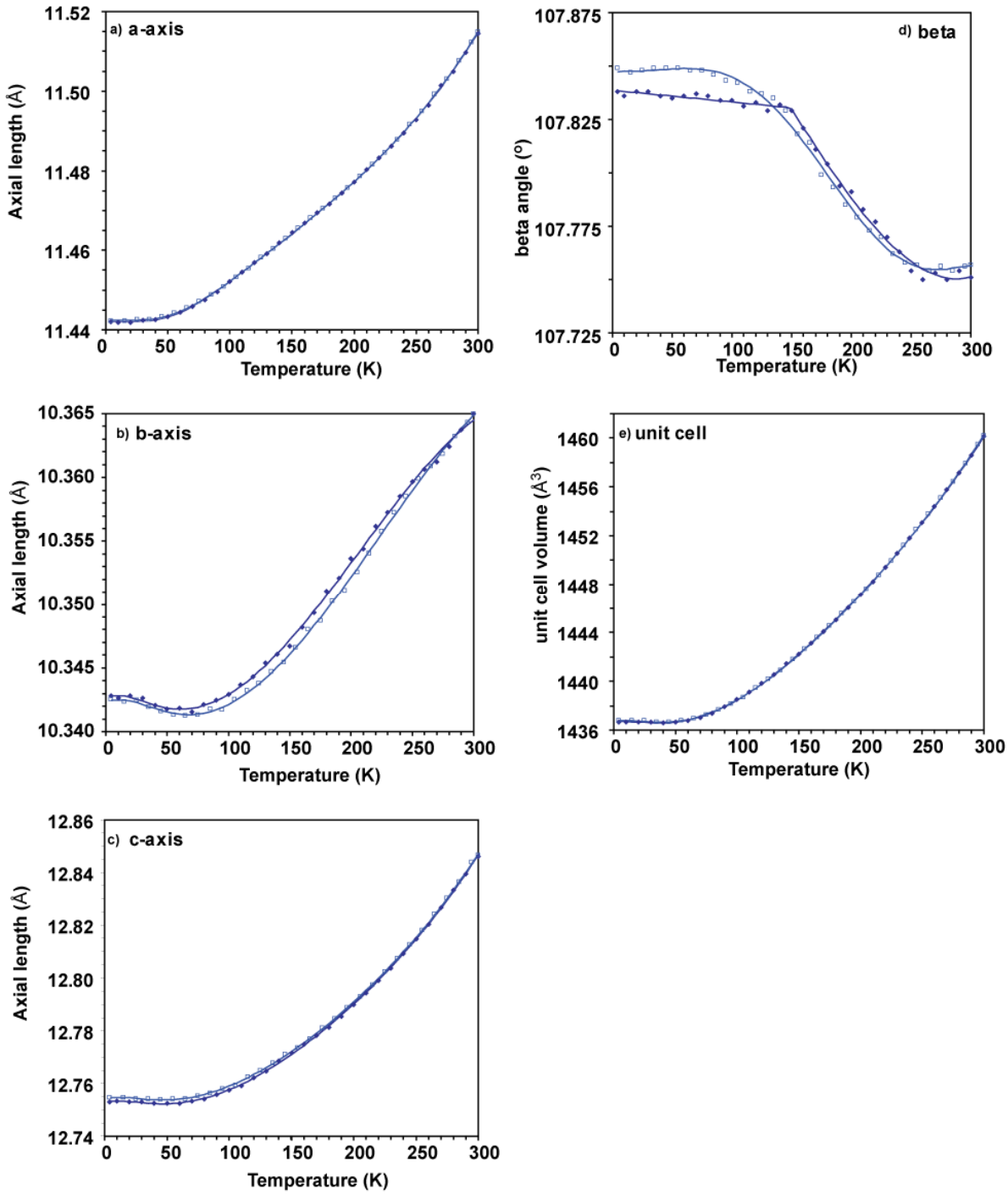

Figure 3.6 The temperature dependent variation of the unit cell parameters; a) *a*-axis; b) *b*-axis; c) *c*-axis; d) monoclinic angle β; e) unit cell volume, over the temperature range 4.2 - 300 K. Values obtained upon warming of the quenched specimen are shown as filled diamonds, and those obtained during subsequent slow cooling of the specimen equilibrated at 300 K are shown as open squares. Standard errors are comparable in size to the symbols used. The solid lines shown in a) – c) and e) are Einstein model fits to both data sets (Eqs. 3.9 and 3.10) and the lines shown in d) are polynomial fits. See Section 3.2.2.4.

3.2.2.1 Axial thermal expansions of mirabilite.

During the first warming run, the unit-cell parameter β (see Figure 3.6) was observed to show relatively little variation with temperature up to 150 K ($-5 \pm 1 \times 10^{-5}$ deg. K^{-1}), whereafter the angle began to decrease at a much larger rate ($-7.2 \pm 0.2 \times 10^{-4}$ deg. K^{-1}). The decrease ceases at ~ 250 K whereupon the angle reaches a limiting value of ~107.75°. The behaviour at 150 K suggests that the initial quenching of the specimen to 80 K had locked-in the dynamic disorder (either of the deuterons or the sulfate tetrahedra) described by Levy and Lisensky (1978). As a result, a second series of data were collected upon slow cooling. Above 150 K, the behaviour of β during slow cooling is very similar to that on warming. However below 150 K, β continues to increase, in what is considered a 'normal' fashion, and reaching a value at 4.2 K that is ~ 0.01° larger than the quenched value. This small difference (~10 % of the total variation over the range 4.2—300 K) is nonetheless clearly resolvable.

Given that no evidence for disorder of the sulfate tetrahedron and its related hydrogen bonds, has been observed, it can be concluded that the behaviour of β at 150 K during warming is due to 'unlocking' of deuteron disorder in the square rings. The change in β during continued warming can be inferred to be a proxy for the change in occupancy, the observed saturation of β above 250 K being due to complete disorder (50:50 occupancy of the 'b' and 'c' sites) being achieved. Since the two-fold axis of rotational symmetry passes through the centre of these rings, it is logical that changes in the shape of the rings (mediated by changes in site occupancies) should influence the monoclinic angle.

The axial expansivities are largely positive over the temperature range investigated, although the *b*- and *c*-axes display a small amount of negative thermal expansion at low temperatures (below ~50 K). This behaviour is common to a number of sulfates, including $CuSO_4 \cdot 5D_2O$, (Schofield and Knight, 2000), $MgSO_4 \cdot 7D_2O$, (Fortes *et al.*, 2006b) and $MgSO_4 \cdot 11D_2O$, (Fortes *et al.*, 2008b) each of which has one axis which displays negative thermal expansion. There is little discernible hysteresis between the warming and cooling data for the *a*- and *c*-axes. The small amount of hysteresis in the length of the *b*-axis may be related to the variations in β noted earlier. Overall, the expansivities of the *a*- and *c*-axes are of similar magnitude, whilst the *b*-axis shows a much smaller thermal expansion. In order to arrive at a better understanding of how the thermal expansion is related to structural elements in the crystal and the bonding between them, the next step is to derive the coefficients of the thermal expansion tensor, as discussed in Section 3.2.2.4.

3.2.2.2 Unit cell volume thermal expansion of mirabilite.

Using the results obtained from the refinements of the powder diffraction data the volume and axial thermal expansivities of mirabilite were calculated over the temperature range 4.2 – 300 K. The volume thermal expansion is positive and behaves normally above 40 K, below which it is slightly negative, as can be seen in Figure 3.7 where the volume thermal expansion coefficient α_V, for deuterated mirabilite from Debye (solid line) and Einstein (dotted line) models are shown, together with the experimental values. The dashed line shows the volume thermal expansion of meridianiite (Fortes *et al.,* 2008b) for comparison.

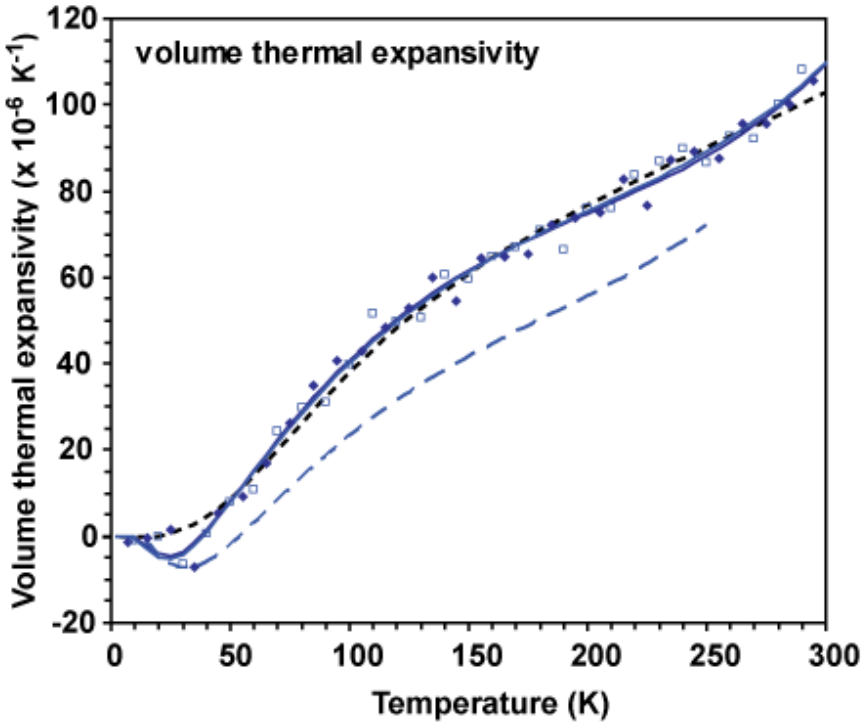

Figure 3.7 Comparison of the volume thermal expansion coefficient α_V, for deuterated mirabilite: a) as calculated via equation 3.2 and the heat capacity data (dotted line) b) via the Einstein model (solid lines; Eq. 3.9 and 3.10), fitted to both data sets. The points shown were obtained from simple point by point numerical differentiation of the refined unit-cell volumes; values upon warming of the quenched specimen are shown as filled diamonds and those obtained on subsequent slow cooling as open squares. Note the misfit below 40 K. The dashed line shows the volume thermal expansion of meridianiite (Fortes *et al.,* 2008b) for comparison.

For the purpose of making a simple density calculation (e.g., for planetary interior modelling), a 3rd order polynomial was fitted to the density of mirabilite calculated from the unit-cell volume between 50—300 K of the form $\rho/\rho_0 = AT^3 + BT^2 + CT + 1$. The coefficients obtained are: A = 2.9(1) x 10^{-11} K^{-3}, B = -3.19(5) K^{-2}, C = 1.61(5) K^{-1} with ρ_0 = 1527.85 kg m^{-3} for deuterated mirabilite (R^2 = 99.986 %) and the maximum density difference between the observed data and those from the polynomial fit is 0.012 %).

Assuming that the unit cell volume of *hydrogenous* mirabilite shows the same temperature dependence as the deuterated isotopomer, then for $Na_2SO_4 \cdot 10H_2O$ ρ_0 = 1489.63 kg m^{-3}.

The unit-cell volume thermal expansion is negative below 40 K and reaches a maximum value of $\alpha_V \approx 110 \times 10^{-6}$ K at 300 K. Although the volume thermal expansion near 300 K gives no indication of impending dehydration, there are subtleties in the thermal expansion tensor (as described in Section 3.2.2.4); in particular, α_2 exhibits a very large rate of increase approaching 300 K.

3.2.2.3 Fitting of the cell parameters of mirabilite using the Grüneisen approximation.

The temperature dependence of the unit-cell volume from 4.2 - 300 K is well represented by a simple polynomial of the form V ($Å^3$) = -4.143(1) $x10^{-7}$ T^3 + 0.00047(2) T^2 - 0.027(2) T + 1437.0(1) $Å^3$ (R^2 = 99.98%). However, a more physically meaningful interpretation of the thermal expansion curve can be obtained by using Grüneisen approximations for the zero-pressure equation of state (see Wallace, 1998), in which the effects of thermal expansion are considered to be equivalent to elastic strain induced by the thermal pressure. These take the form, to first order,

$$V(T) = V_0 + \frac{\gamma U}{K_0} \qquad \textbf{Equation. 3.1}$$

and to second order,

$$V(T) = V_0\left[1 + \frac{U}{Q - bU}\right] \qquad \textbf{Equation. 3.2}$$

where Q = ($V_0 K_0 / \gamma$) and b = ½ (K_0' -1); V_0 is the unit-cell volume at zero pressure and temperature, K_0 is the zero pressure and temperature bulk modulus, K_0' is its first derivative with respect to pressure (also evaluated at P = 0 and T = 0), and γ is a Grüneisen parameter (assumed constant).

The internal energy of the crystal, U(T), may be calculated via the Debye approximation (Cochran, 1973),

$$U(T) = 9Nk_B T\left(\frac{T}{\theta_D}\right)^3 \int_0^{\theta_D/T} \frac{x^3}{e^x - 1} dx \qquad \textbf{Equation. 3.3}$$

where θ_D is the Debye temperature, N is the number of atoms per unit cell, k_B is the Boltzmann constant, and $x = \hbar\omega/k_BT$. Note that the vibrational zero-point energy of $9Nk_B\theta_D/8$ is included in equation 3.2 via the term V_0. The integral in Equation. 3.3 may be evaluated numerically.

Least-squares fitting of the first-order approximation (Equation. 3.1) to the V(T) data yielded the parameters θ_D = 529(8) K, V_0 = 1436.72(4) Å^3, Q = 5.56(7) x 10^{-17} J. This value of Q gives a value of K_0 / γ = 39(1) GPa.

When the second-order approximation was fitted, the values of the variable parameters were found to be θ_D = 441(3) K, V_0 = 1436.66(3) Å^3, Q = 7.3(3) x 10^{-17} J and b = 11(2); these imply K_0 / γ = 51 (2) GPa and K_0' = 23(4). In both of these approximations the values of K_0 (and also of K'_0 in the second case) are much higher than might reasonably be expected and so, in order to try to obtain more realistic elastic parameters, Equation 3.2 was employed but with the internal energy term calculated via the measured heat capacity data (Brodale & Giauque, 1957; note, however, that these values are for hydrogenous, rather than deuterated mirabilite). In order to do this it is necessary to have an integratable expression for C_v(T). A fit of the heat capacity data to a single Debye model proved poor so a three-region empirical polynomial approach was employed, the coefficients of which are reported in Table 3.6; U(T) was then determined by integration of these polynomials. Before fitting, the published C_p values were converted to C_v values using the expression $C_p = C_v(1+ \alpha_v \gamma T)$; the values of α_v(T) were taken from the present work and γ was assumed to be 1.3. Figure 3.8 shows the fit of these polynomials to the modified heat capacity data.

Table 3.6 Coefficients of the polynomial fits to the heat capacity data (see Figure 3.8). Data were converted to units of Joules per unit-cell per Kelvin in preparation for use in Equation 3.2.

Temperature range	A (K)	B (K^{-1})	C (K^{-2})	D (K^{-3})	E (K^{-4})
0 - 25.5 K	0	0	-1.38753×10^{-26}	2.27323×10^{-26}	-3.78677×10^{-28}
25.5 - 120.5 K	-1.30744×10^{-22}	5.97279×10^{-24}	3.79132×10^{-25}	-4.02835×10^{-27}	1.31661×10^{-29}
120.5 - 300 K	-3.88657×10^{-22}	2.57786×10^{-23}	-8.0734×10^{-26}	1.72849×10^{-28}	-1.29846×10^{-31}

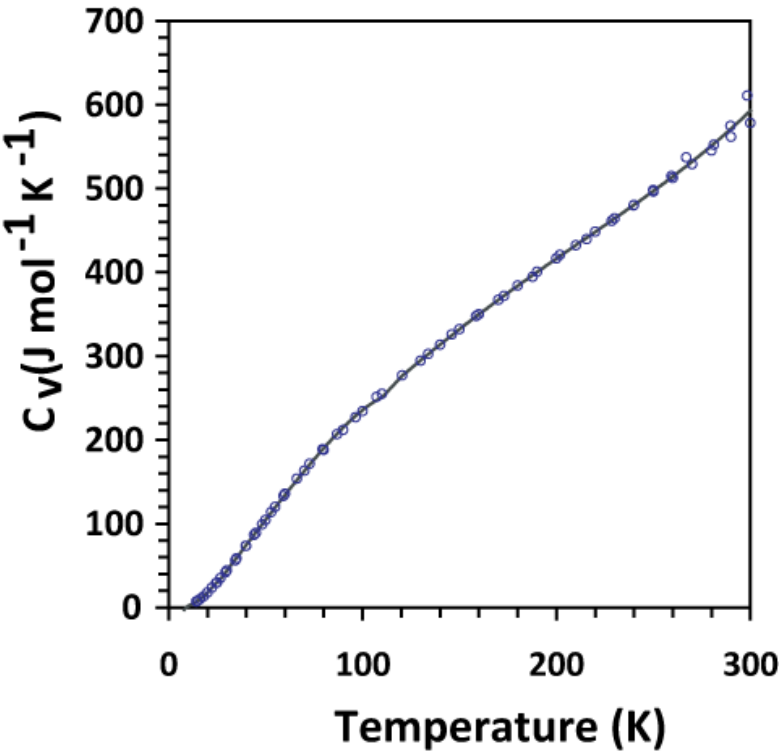

Figure 3.8 Fit of experimental heat capacity data (converted to C_v values), taken from Brodale & Giauque (1957) using a multiple fits of third-order polynomials for different temperature ranges. Coefficients of the fits are given in 3.7.

With U(T) calculated from the specific heat data, the second-order approximation gave good agreement with the data above 40 K; below this temperature it is unable to accommodate the negative thermal expansion of the crystal (see Figure. 3.7). The values of the fitted parameters were: V_0 = 1436.41(7) Å^3, Q = 4.2 (1) x 10^{-17} J and *b* = 9(2), leading to values for K_0 / γ = 29(1) GPa, and K_0' = 19(4). Once again, the values of K_0 / γ and K_0' are much higher than might be expected but are comparable to those previously obtained by Fortes *et al.* (2006b) using a similar procedure for epsomite where it was found that K_0 / γ = 31.9(3) GPa and K_0' = 26(1). The failure of this approximation to produce realistic values of K_0 and K_0' is interesting as for non-molecular solids such as FeSi, (Vočadlo *et al.* 2002) and $KMgF_3$ (Wood *et al.* 2002), this technique has been used successfully, producing physically reasonable elastic parameters. It is possible that epsomite and mirabilite show a greater temperature dependence of γ and K_0, which are both assumed to be constant in this approximation. Further high-pressure measurements upon mirabilite, specifically of the bulk modulus and its pressure and temperature derivatives are presented in Chapter 4.

3.2.2.4 The thermal expansion tensor of mirabilite.

The thermal expansion of a monoclinic crystal is described by a symmetrical second rank tensor of the form:

$$\begin{bmatrix} \alpha_{11} & 0 & \alpha_{13} \\ 0 & \alpha_{22} & 0 \\ \alpha_{31} & 0 & \alpha_{33} \end{bmatrix} \qquad \textbf{Equation 3.4}$$

where $\alpha_{13} = \alpha_{31}$. Using the Institute of Radio Engineers' convention for the orthonormal tensor basis, where $\mathbf{e_3} \parallel \mathbf{c}$, $\mathbf{e_2} \parallel \mathbf{b^*}$, and $\mathbf{e_1} \parallel \mathbf{e_2} \times \mathbf{e_3}$, (see Figure 3.9), then the Lagrangian thermal expansion tensor coefficients for a monoclinic crystal with *b* as the unique axis may be written in terms of the unit-cell parameters as shown below (Schlenker *et al.*, 1975):

$$\alpha_{11}(T) = \frac{1}{a_0 \sin\beta_0}\left[\sin\beta\frac{da}{dT} + a\cos\beta\frac{d\beta}{dT}\right] \qquad \textbf{Equation. 3.5}$$

$$\alpha_{22}(T) = \frac{1}{b_0}\frac{db}{dT} \qquad \textbf{Equation. 3.6}$$

$$\alpha_{33}(T) = \frac{1}{c_0}\frac{dc}{dT} \qquad \textbf{Equation. 3.7}$$

$$\alpha_{13}(T) = \frac{1}{a_0}\frac{da}{dT}\left[\frac{1}{\sin 2\beta_0} - \frac{\sin\beta}{2\cos\beta_0}\right] - \frac{a\cos\beta}{2a_0\cos\beta_0}\frac{d\beta}{dT} - \frac{\cot\beta_0}{2c_0}\frac{dc}{dT}$$

Equation. 3.8

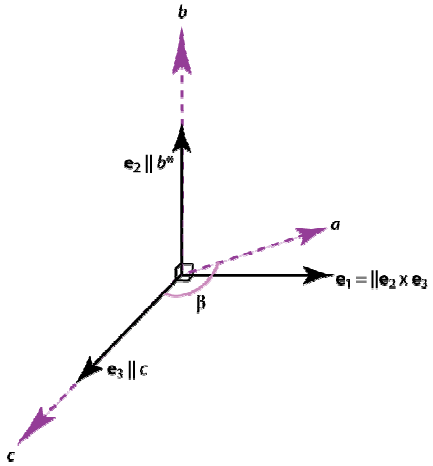

Figure 3.9 Diagram illustrating the relationship between the unit-cell axes (purple dashed lines), and the directions of the principal axes of the orthonormal thermal expansion tensor (black full lines). Note: e_1 is in the *a*-*c* plane.

In order to derive the components of the thermal expansion tensor via equations (3.5) – (3.8) it is necessary to obtain suitable differentiable representations of the cell parameters as a function of temperature. This has been done by using a modified Einstein oscillator model to fit the unit-cell data as a function of temperature rather than by using the Debye approximation described previously. Although the latter provides a more physically correct model of the behaviour of the solid than the mathematically simpler Einstein model, the functional form of the Einstein model is such that a better fit to the experimental data was obtained (particularly in the regions of negative axial expansion), as required for proper determination of the coefficients of the thermal expansion tensor. The derivation of the modified Einstein model is discussed elsewhere (see Fortes *et al.*, 2008b); using this approach the temperature dependencies of the unit cell parameters *a*, *b*, and *c*, are described by an expression of the form,

$$X(T) = X_0 + \frac{E}{\left(\exp\left(\theta_E/T\right)-1\right)} \qquad \textbf{Equation. 3.9}$$

where X_0 is the value of the fitted parameter at 0 Kelvin, θ_E is a characteristic Einstein temperature = $\hbar\omega_E/k_B$, and E is the internal energy of the crystal multiplied by K_T/γ (where K_T is either a volumetric or axial incompressibility and γ is a Grüneisen parameter). For mirabilite, a sufficiently good fit (with the correct asymptotic behaviour as $T > 0$) can only be obtained when the parameter E is allowed to vary as a function of temperature:

$$E = e_0 + e_1 T + e_2 T^2 + e_3 T^3 \qquad \textbf{Equation. 3.10}$$

and the thermal expansion coefficient $\alpha = X^{-1}(\partial X/\partial T)$ is then:

$$\alpha = \frac{(\exp(\theta_E/T)-1)(3e_3T^2 + 2e_2T + e_1) + ((\theta_E/T^2)(\exp(\theta_E/T))(e_3T^3 + e_2T^2 + e_1T + e_0))}{X(\exp(\theta_E/T)-1)^2} \qquad \textbf{Equation. 3.11}$$

It has been observed previously (Fortes *et al*., 2008b) that the temperature dependence of E may be understood in terms of the Grüneisen ratio being negative at low temperatures and positive at higher temperatures, giving a reasonable match to $\gamma(T)$ in ice Ih despite the *ad hoc* nature of the parameterisation.

Table 3.7 Parameters obtained by fitting equations 3.9 and 3.10 to the unit-cell volume and cell edges of mirabilite. Note that the unit of X_0 are $Å^3$ for the volume, and Å for the parameters *a*, *b*, and *c*: the units of e_0, e_1, e_2, and e_3 are $Å^3$, $Å^3\ K^{-1}$, $Å^3\ K^{-2}$, and $Å^3\ K^{-3}$, respectively, for the unit cell volume, and follow the same system in Å for the axes.

	Volume (warming)	Volume (cooling)	*a*-axis (warming)	*a*-axis (cooling)	*b*-axis (warming)	*b*-axis (cooling)	*c*-axis (warming)	*c*-axis (cooling)
X_0	1436.70(2)	1436.77(3)	11.4421(1)	11.4425(1)	10.3428(2)	10.3429(1)	12.7533(2)	12.7548(2)
θ_E (K)	85(11)	78(11)	234(7)	233(6)	76(16)	92(14)	87(22)	80(17)
e_0	-3.8(6)	-3.4(6)	$1.3(1)\times10^{-1}$	$1.26(9)\times10^{-1}$	$-8(2)\times10^{-3}$	$-1.1(2)\times10^{-2}$	$-1.9(7)\times10^{-2}$	$-1.6(5)\times10^{-2}$
e_1	$8(1)\times10^{-2}$	$7(1)\times10^{-2}$	$-5.1(6)\times10^{-4}$	$-4.6(5)\times10^{-4}$	$1.0(3)\times10^{-4}$	$1.2(2)\times10^{-4}$	$3.3(1)\times10^{-4}$	$2.8(9)\times10^{-4}$
e_2	$-2.5(5)\times10^{-4}$	$-2.0(5)\times10^{-4}$	$1.2(1)\times10^{-6}$	$1.1(1)\times10^{-6}$	$-1.7(5)\times10^{-7}$	$-1.9(4)\times10^{-7}$	$-1.0(4)\times10^{-6}$	$-8(3)\times10^{-7}$
e_3	$3.3(7)\times10^{-7}$	$2.7(7)\times10^{-7}$	-	-	-	-	$1.4(7)\times10^{-9}$	$1.1(4)\times10^{-9}$

The parameters obtained from fitting equation 3.9 (and 3.10) to the unit-cell volume and axial lengths are listed in Table 3.7. The resulting curves are shown in Figures 3.6 (axial lengths) and 3.7 (unit-cell volume). For the cell parameter β, polynomial functions were used. The values of β on warming were fitted with a linear expression from 4 - 140 K, $\beta(T) = a_0T + \beta_0$, with $a_0 = -5(1) \times 10^{-5}$ deg. K^{-1} and $\beta_0 = 107.8387(8)°$. Above 140 K, a polynomial of the form $\beta(T) = a_0T^3 + a_1T^2 + \beta_0$, with $a_0 = -6.1(4) \times 10^{-6}$ deg. K^{-3}, $a_1 = 1.4(1) \times 10^{-8}$ deg. K^{-2}, and $\beta_0 = 107.920(6)°$ was used. The data collected on cooling were fitted from 4 - 300 K with a function of the form $\beta(T) = a_0T^6 + a_1T^5 + a_2T^4 + a_3T^3 + \beta_0$, with $a_0 = -3.1(4) \times 10^{-15}$ deg. K^{-6}, $a_1 = 2.3(3) \times 10^{-12}$ deg. K^{-5}, $a_2 = -5.4(7) \times 10^{-10}$ deg. K^{-4}, $a_3 = 3.1(6) \times 10^{-8}$ deg. K^{-3}, and $\beta_0 = 107.8474\ (9)°$.

Fitting the data across the full temperature range produces very large uncertainties in some of the fitted parameters, resulting in the propagation of large errors onto the thermal expansion coefficients. Better estimates of the uncertainty on these coefficients were found by linear fits to short segments of the cell parameter data; estimated 3σ values in the thermal expansion coefficient are $\pm$ 1.65 x 10^{-6} K^{-1}. The Einstein temperatures obtained here are very similar to those found by fitting the same expressions to the unit cell of $MgSO_4 \cdot 11D_2O$ (Fortes *et al.*, 2008b), θ_E from the volume data being ~ 90 K for both. This temperature corresponds to very low-frequency vibrational modes, (wavenumbers of ~ 60 cm^{-1}), which dominate the low-temperature thermal expansivity; they have not been observed directly, but may be detectable in the phonon dispersion spectrum.

The modified Einstein fits to the *a*-, *b*-, and *c*-axes, and the polynomial fits to the angle β, were then used to calculate the magnitudes of the thermal expansion tensor coefficients (from Equations 3.5-8) as a function of temperature. Decomposition of the tensor matrix (Equation 3.4) yields the magnitude (eigenvalues) and orientation (eigenvectors) of the thermal expansion along the principal axes, α_1, α_2, and α_3. The temperature dependence of coefficients α_{11}, α_{22}, α_{33}, α_{13}, and the principal axes α_1, α_2, and α_3 is shown in Figure 3.10; θ is the angle between α_1 and $\mathbf{e_1}$.

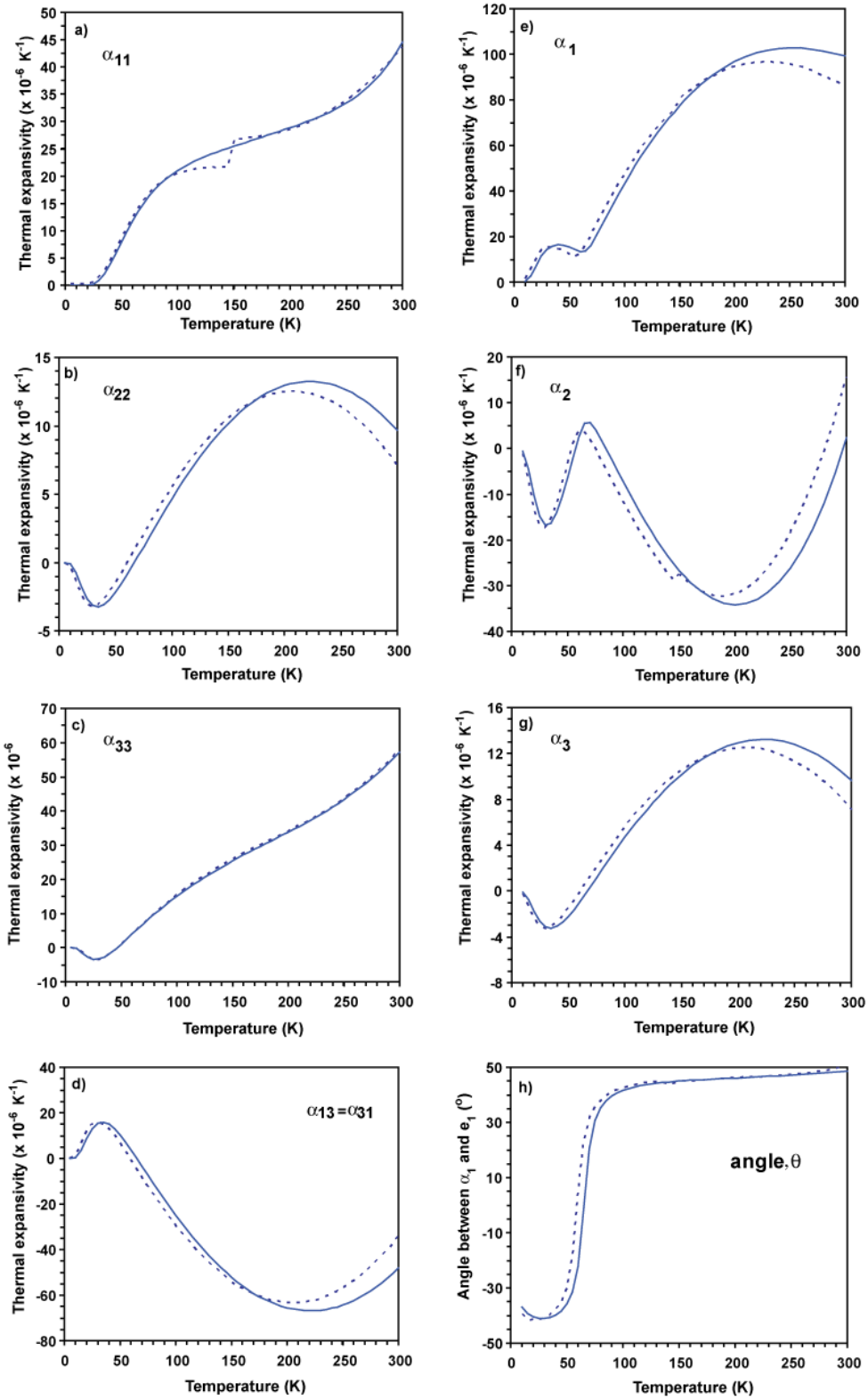

Figure 3.10 Panels a - d (left): temperature dependence of the thermal expansion tensor coefficients, α_{11}, α_{22}, α_{33} and α_{13}. Panels e-g (right): temperature dependence of the principal axes of the thermal expansion tensor, α_1, α_2, and α_3, and (panel h, right) the angle between α_1 and $\mathbf{e_1}$. The dotted lines are the warming, the bold lines the slow cooling data.

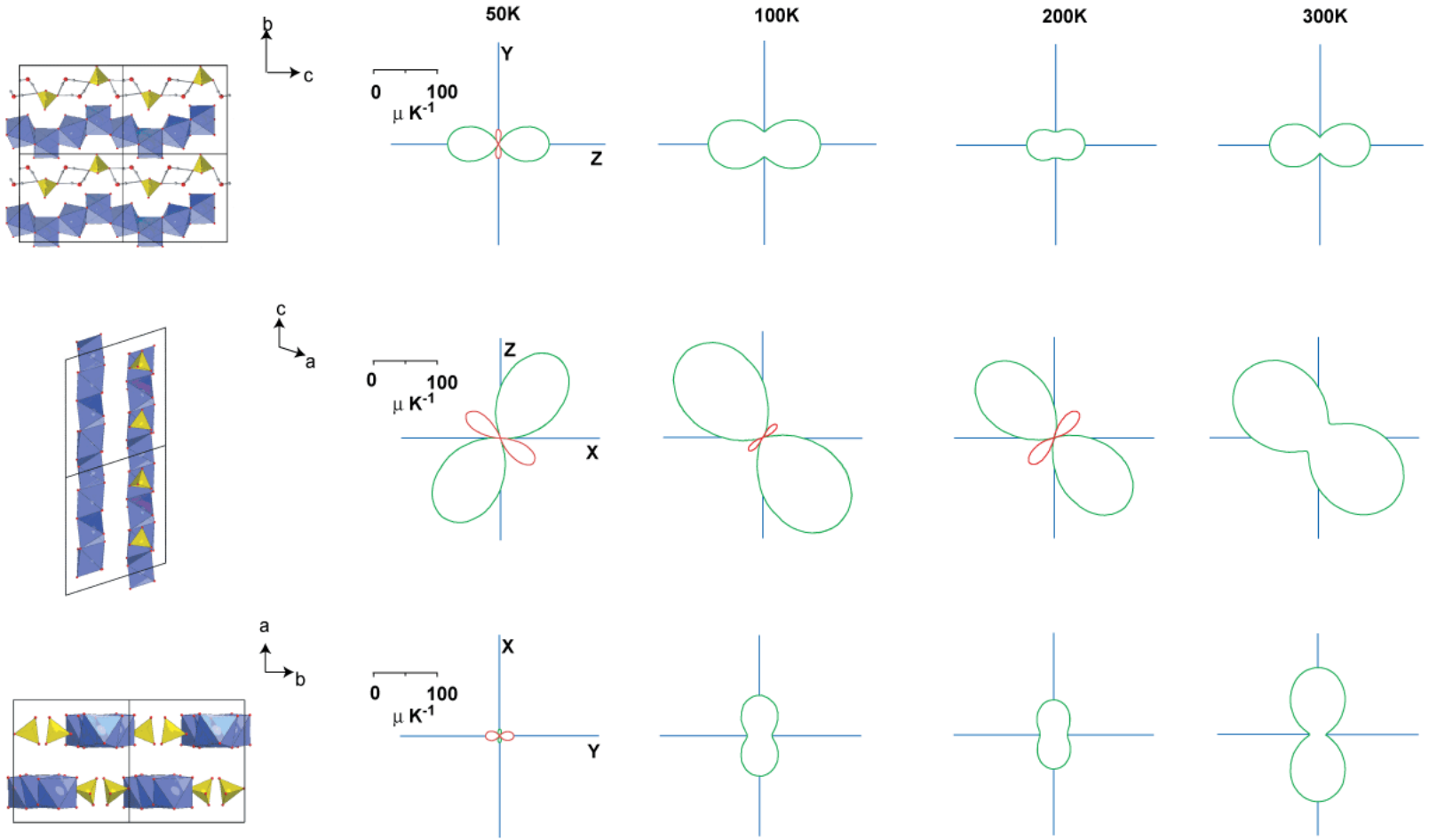

Figure 3.11 Projections of the thermal expansion coefficient representation surface on the y-z (b-c) planes (top), x-z ($\mathbf{e_1}$-c) plane (middle), and the x-y ($\mathbf{e_1}$-b) plane (bottom) at 50 K, 100 K, 200 K, and 300 K. Solid green lines indicate positive values, and dotted red lines indicate negative values. The corresponding projections of the mirabilite structure are shown on the left.

Projections of the representation surface of the expansion coefficients onto the three orthogonal planes, y-z ($\mathbf{e_2}$-$\mathbf{e_3}$), x-y ($\mathbf{e_1}$-$\mathbf{e_2}$), and x-z ($\mathbf{e_1}$-$\mathbf{e_3}$), at a range of temperatures from the slow cooled data are shown in Figure 3.11.

Principal axes α_1 and α_3 exhibit mostly positive thermal expansion at all temperatures greater than ~50 K, although the values of α_1 are roughly an order of magnitude greater than α_3. However, α_2 is mostly negative, and its temperature dependence is a mirror image of α_1. The main difference between the warming and cooling data is a temperature offset between the two which becomes significant above 150 K; in the quenched sample, α_1 and α_3 have smaller values than the slow-cooled sample at a given temperature (above 150 K), whereas α_2 has a more positive value. The orientation of the expansion tensor does not differ between the two data sets; α_1 appears to be saturating at high temperature but the large changes in α_2 (increase) and α_3 (decrease) may be signalling the impending dehydration at 305 K.

The orientation of the thermal expansion tensor undergoes a major shift (as manifested by the angle θ between $\mathbf{e_1}$ and α_1), swinging through ~80° near 50 K. After this reorientation the value of θ increases very slowly from +40° to +50° over the temperature range 100 K—300 K.

It is clear that the volumes of the various polyhedra within the mirabilite structure do not contribute greatly to the thermal expansion; as in other salt hydrates that have been recently studied, the subtleties of the thermal expansion are controlled by the hydrogen-bond network. In gypsum, for example, the orientation of the water molecules determines the direction of maximum thermal expansion (Schofield *et al*., 2004), and in meridianiite it is a weak bifurcated hydrogen bond which dominates the orientation of the expansion tensor (Fortes *et al*., 2008b). In mirabilite, much of the interlayer hydrogen bonding is aligned with the *a*-axis; it is therefore slightly surprising to find that the direction of maximum thermal expansion is inclined by more than 30° to this direction. It is possibly of relevance that the hydrogen bonds donated by the two interstitial water molecules O10 and O11 are more closely aligned with α_1 and α_2, as shown in Figure 3.12.

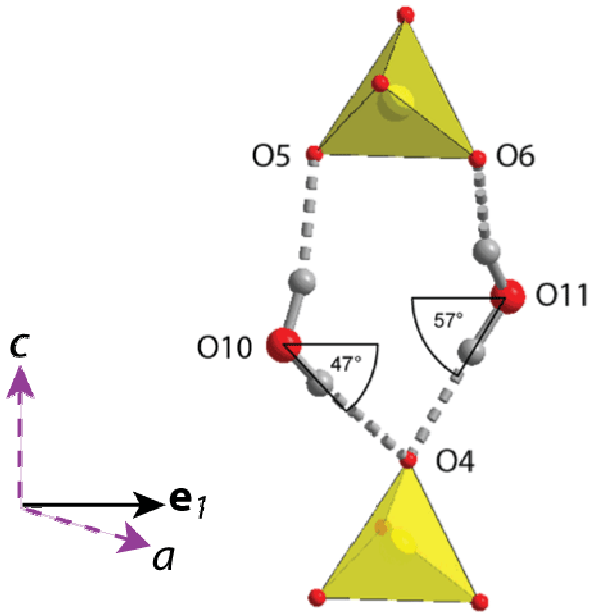

Figure 3.12 Orientations of the O10 and O11 hydrogen bonds with respect to the direction e_1, illustrating the similarity between the orientation of these bonds and the orientation of the thermal expansion tensor.

It is possible that the reorientation of the expansion tensor is the result of shifts in the relative strength of hydrogen bonds donated by these two molecules to neighbouring sulfate tetrahedra. Further detailed study of the anisotropic vibrational behaviour of the deuterons, using single-crystal neutron diffraction techniques, may yield insights into the factors controlling the orientation of the thermal expansion tensor.

Summary

Time-of-flight powder neutron diffraction has been used to measure the crystal structure and thermal expansion of $Na_2SO_4.10D_2O$ from 4.2—300 K under ambient pressure conditions. No evidence was observed of the sulfate disorder reported previously by Levy and Lisensky (1978). The volume thermal expansion is positive above 40 K, and similar in magnitude to that of other multiply-hydrated salts such as epsomite and meridianiite. A second-order Grüneisen model fitted to the data gives estimates of the elastic properties; however, as has also been found for epsomite, the values of K and K_0' obtained are too high. Further neutron powder diffraction measurements, combined with *ab initio* calculations, were, therefore, necessary to obtain details of the elastic strain tensor at high pressure, and to determine $\gamma(T)$ and the Anderson-Grüneisen parameter, δ_T; details of such experiments and simulations can be found in following Chapters of this work.

Chapter 4

Neutron diffraction studies III:

Mirabilite under Pressure

This chapter describes a high pressure neutron diffraction experiment, carried out on HRPD at ISIS in March 2008, designed to measure the compressibility of mirabilite from 0 – 5.5 kbar at temperatures from 80 – 260 K.

4.1 Method: measuring the compressibility of mirabilite.

Measuring the compressibility of a material is a similar process to that of measuring the thermal expansion. It is achieved through observation of the variation of unit-cell parameters over a range of pressures. However, the experimental requirements for generating and maintaining high pressures are somewhat more involved than for low temperature experiments.

4.1.1 Sample preparation and loading.

The sample used for high pressure experiments came from the same supersaturated solution of Na_2SO_4 in D_2O as was used for the thermal expansion experiment. To prepare the sample, solid lumps of mirabilite were again extracted from the liquor, dried on filter paper, and then quickly powdered in an agate pestle and mortar, which had been cooled in solid carbon dioxide (since no cold room facilities were able at ISIS at the time of the experiment). Roughly 1 cm^3 of the resulting coarse powder was loaded into a TiZr gas-pressure cell, which had also been cooled in solid CO_2. This pressure cell allows for continuous hydrostatic loading of the sample up to ~ 5.5 kbar.

These experiments were carried out after HRPD had undergone a major upgrade in 2007 with the installation of a new high-reflectivity supermirror guide in the primary flightpath. This produced substantial gains in flux compared with the old guide (between a factor of 10 to 40 times greater across the incident wavelength range). Despite this, however, the observed diffraction patterns (see Sections 4.1.2 and 4.1.3) were much weaker than were expected on the basis of previous high-pressure studies of $MgSO_4.7D_2O$, epsomite, (Fortes *et al*. 2006a) carried out with a TiZr pressure cell on HRPD before the upgrade. The reasons for this are still not clear; experiments on $MgSO_4.11D_2O$, meridianiite, subsequent to this study of mirabilite have also been similarly affected.

Figure 4.1 shows the high-pressure gas cell used to contain the sample: a) shows an internal cross section of the pressure cell; b) is a photograph of the pressure cell taken during the loading of an experiment on HRPD, showing the position of the copper rings and

temperature sensors. The copper rings, clamped to the top and bottom of the pressure cell, carry small electric heaters and RhFe temperature sensors inserted into holes drilled in the copper to enable accurate measurement and control of the sample temperature.

The sample volume in this pressure cell is of the order of 1 cm^3, five times less than in the vanadium sample can used for the thermal expansion measurements. Once the sample was loaded, the cell was then screwed onto a cryostat centre stick, sealed under a nominal pressure of 478 bar of He gas, and placed in a closed cycle refrigerator (CCR), with a 100 ml tail, which was masked with gadolinium foil, and mounted on the HRPD beamline. Throughout the experiment, the pressure of helium gas on the sample was maintained using an intensifier.

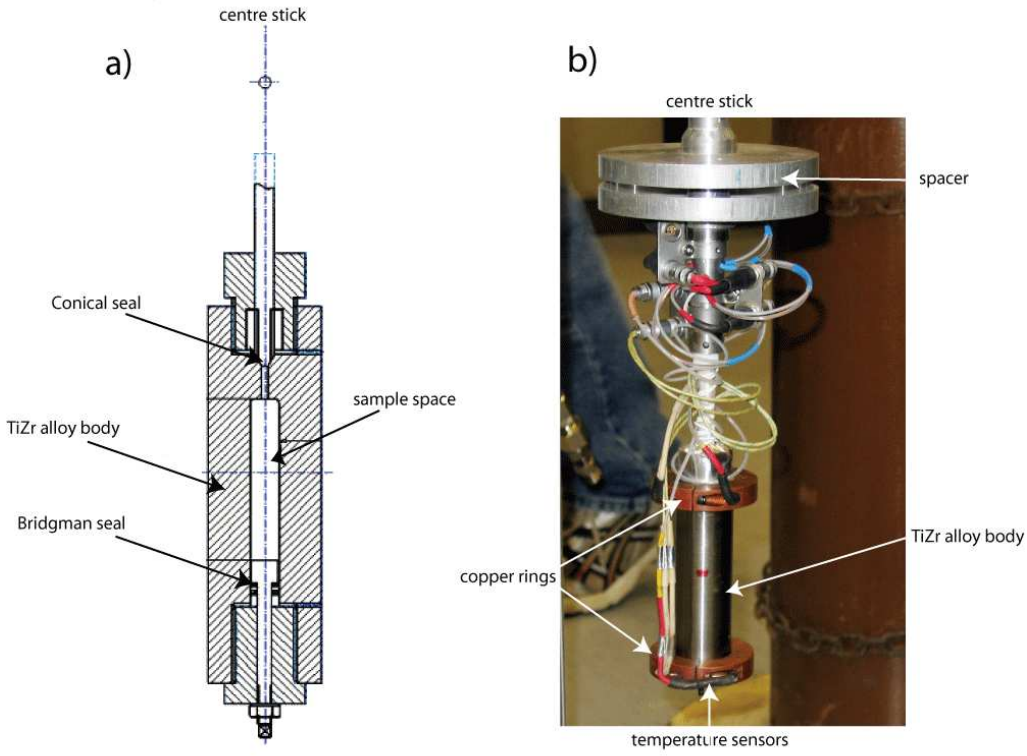

Figure 4.1 The pressure cell used to measure the compressibility of mirabilite on the HRPD beamline. Insert a) shows an internal plan view and is redrawn after Kuhs *et al*. (2005), b) is a photograph of the pressure cell taken during loading of another experiment on HRPD.

4.1.2 Data acquisition.

In devising the pressure-temperature pathways which were followed in this experiment, care was taken to ensure that the temperature remained well below the dehydration limit of mirabilite (305 K at atmospheric pressure). Another important consideration when working with this experimental setup is the pressure melting curve of helium. Fluid helium is used as the pressure medium in these experiments and it would not be advantageous to solidify the helium in the pressure system. Figure 4.2 shows the helium melting curve from 0 – 10 kbar as determined by Spain and Segall (1971), with annotation to show the temperature at which the helium would freeze under the highest pressures attained in these experiments.

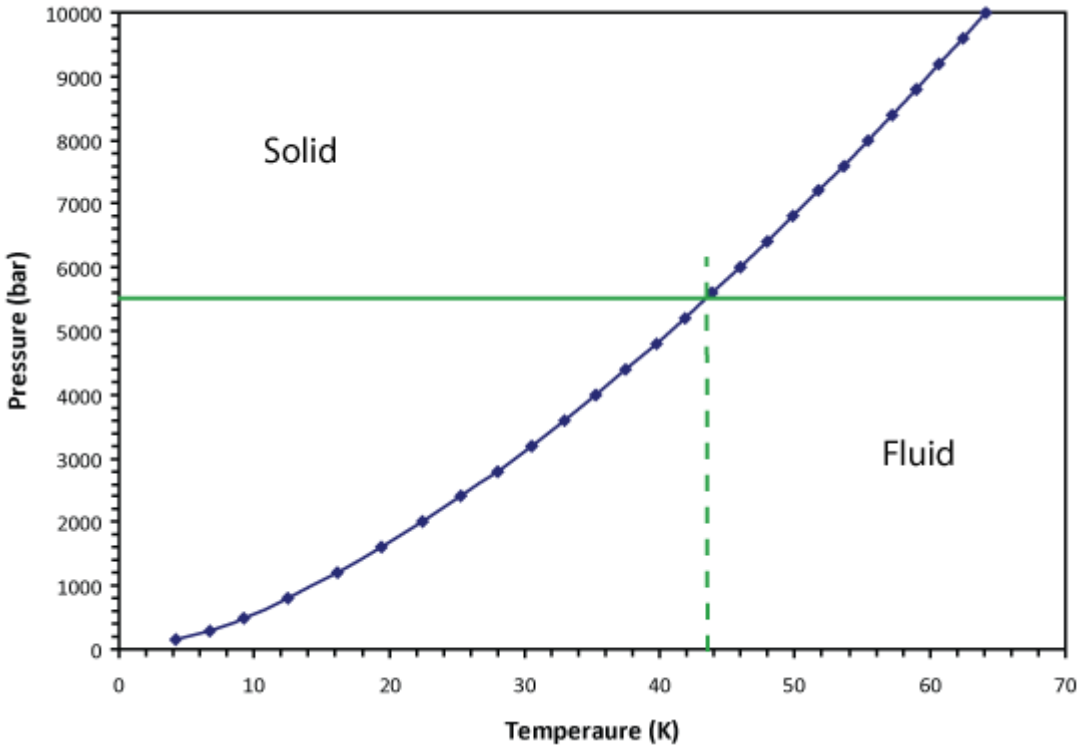

Figure 4.2 The melting curve of helium at high pressure. The blue line and points are the data from Spain and Segall (1971), the solid green line is the maximum pressure attained during these high pressure experiments and the dashed line shows the corresponding melting (freezing) temperature of helium at this pressure.

The signal received at the HRPD detectors from a sample in a TiZr gas cell is much smaller than that received from a thin-walled vanadium slab can. In these experiments the signal from the backscattering and low-angle banks of HRPD were too weak to be useful and so only the data collected in the 90 degree detector banks were analysed.

With the sample initially at 260 K and 478 bar, data were collected in the 90° banks in the time of flight window of 60 – 160 msec for approximately 2 hours (70 μAhr). The sample was then compressed from 478 bar to 5415 bar in ~500 bar increments, counting for approximately 2 hours (70 μAhr), at each datum. After counting for 70 μAhr at 5415 bar, the sample was cooled to 80 K in 20 K steps, counting for 60 μAhr at each step, with 10 minutes equilibration time at each temperature set-point. Over the course of this cooling, the pressure on the sample decreased marginally to 5338 bar. The sample was then depressurised from 5338 bar to 20 bar at 80 K in steps of approximately 600 bar, again counting for 60 μAhr at each pressure.

4.1.3 Compression data refinement - GSAS and least-squares fitting.

The data analysis was carried out using GSAS. Because of the very poor quality of the data (see Figure 4.3), with weak peaks on a high background, it was decided that it would be futile to attempt to refine the atomic coordinates and temperature factors; the following procedure was, therefore, adopted. Starting with the 478 bar, 260 K dataset, the unit cell (*a*,*b*,*c*,β), scale factors, background coefficients (13 term shifted Chebyschev polynomial), and profile coefficients (σ_1 and γ_1), of mirabilite were refined; the atomic coordinates were taken from the 300 K long-count data obtained in the earlier thermal expansion experiment; as before, the sulfate disorder described by Levy and Lisensky (1978), was not included following the results obtained in the thermal expansion experiments (see Chapter 3). The fractional occupancies of the disordered hydrogen atoms were constrained to their 300 K values (b = 0.494 and c = 0.506) and were not refined. Isotropic temperature factors (U_{iso}) were constrained to be 0.025 $Å^2$ (the GSAS default value), and not refined. Sample texture was modelled using the spherical harmonic model implemented in GSAS (4^{th} order - 8 terms). The sample was found to be slightly more textured than in the thermal expansion experiment (texture index of 1.89 at 478 bar, 260 K), most likely as a result of the time constraints placed on the sample preparation by the need to keep the sample cool without access to a suitably temperature controlled sample preparation laboratory.

Table 4.1 shows the Rietveld powder statistics and Figure 4.3 shows the fit to the data at 478 bar and 260 K which is typical of the set as a whole. In the powder statistics, if only the value of χ^2 is considered, the quality of the fits would seem not as good as for the thermal expansion experiments; however, the values of the residuals are still all below 8 %, indicating that in the case of this experiment, χ^2 is not necessarily the sole quantity which should be used in the determination of the agreement of the fit.

Table 4.1 Refinement statistics at 478 bar, 260 K.

478 bar, 260 K						
	No. of		Fitted		Minus Background	
Histogram	reflections	χ^2	*w*Rp	Rp	*w*Rp	Rp
90 degree banks	1146	62.74	3.2 %	1.7 %	7.0 %	2.8 %

As seen in Figure 4.3, there were a small number of additional peaks evident in the diffraction pattern, the majority of which were successfully modelled as ice Ih at a concentration of approximately 6%. These peaks disappear between 1500 and 2000 bar, corresponding to an intersection with the solidus of D_2O (Bridgman, 1935). It was expected that these peaks would reappear either as Ice V at higher pressures (~4 kbar), as Ice II on cooling, or as Ice Ih again on decompression, however, there was no evidence of this in later refinements. The 3 remaining unfitted peaks at d = 2.1 Å, d = 2.355 Å and d = 2.55 Å, marked with arrows in Figure 4.4, are likely the result of materials comprising the sample environment; the d = 2.1 Å peak is, probably, due to the presence of vanadium but is resistant to being fitted as such in GSAS. These regions were excluded in subsequent refinements.

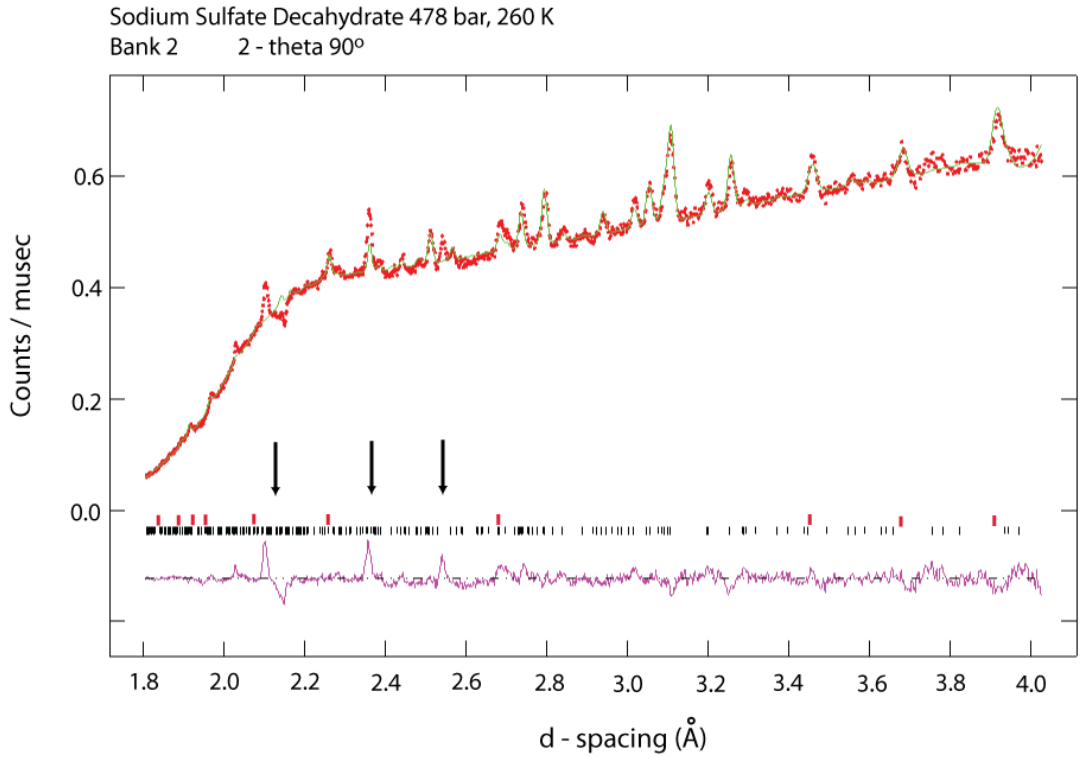

Figure 4.3 Neutron powder diffraction patterns of mirabilite at 480 bar, 260 K obtained on HRPD from the 90° banks. The red circles are the observations, the green line the fit to the observations and the pink line below is the difference between the fit and the observations. The lower set of black tick marks denote the positions of the mirabilite peaks and the upper set of red tick marks are the positions of D_2O ice Ih peaks. The black arrows denote peaks unaccounted for by either ice or mirabilite.

With the decrease in temperature at maximum pressure, a few new peaks appear in the diffraction pattern at 240 K which have proved difficult to identify (see Figure 4.4). These peaks are much less evident in subsequent refinements at decreased temperatures and pressures. They cannot be accounted for simply by using a single phase of: (i) any of the known materials from the sample environment equipment (e.g. vanadium, gadolinium or aluminium), (ii) any of the phases of ice for which structural information is available or (iii) the anhydrous (thenardite), or lesser hydrated (the hepta- or octa-hydrate) phases of Na_2SO_4. From this point, (5338 kbar and 240 K), these regions were excluded. The data were then refitted including additional profile coefficients in the refinement, namely, $\gamma 1$, $\sigma 2$, g1ec and rsca. Attention was paid to the phase diagram of ice (see Chapter 1) throughout the refinement process and at appropriate pressure-temperatures where phase boundaries within the structure might be expected to be encountered, the appropriate phases were reintroduced to the GSAS file. However, none of these fits were successful.

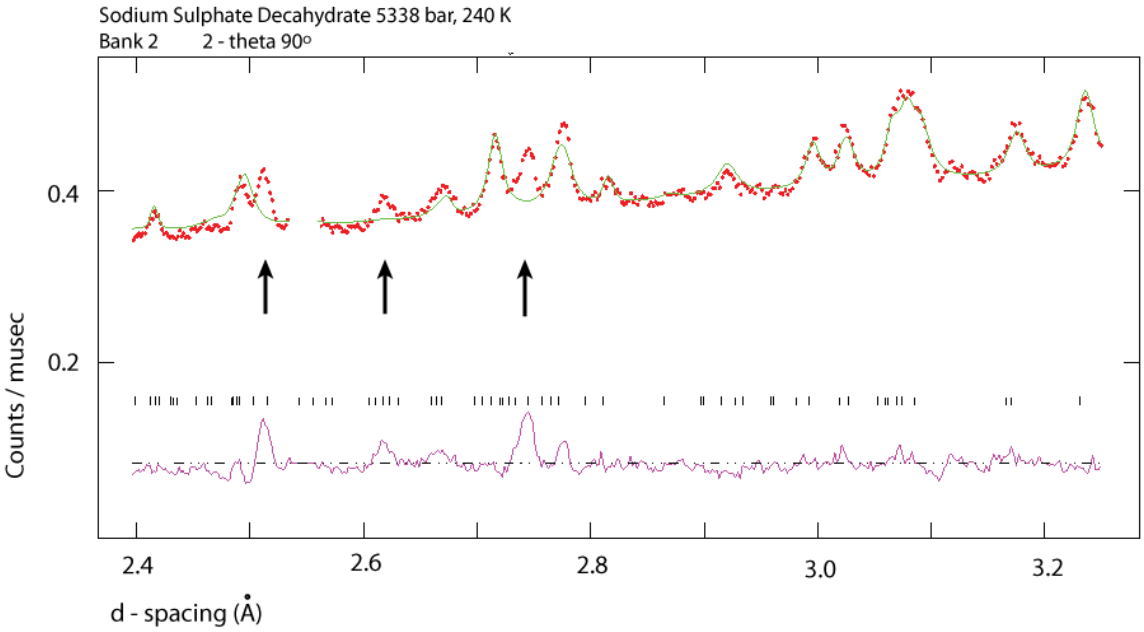

Figure 4.4 Neutron powder diffraction patterns of mirabilite at 5338 bar, 240 K obtained on HRPD from the 90° banks. The red circles are the observations, the green line the fit to the observations and the pink line below is the difference between the fit and the observations. The lower set of black tick marks denote the positions of the mirabilite peaks. The black arrows denote peaks unaccounted for by using a single phase of: (i) any of the known materials from the sample environment equipment (e.g. vanadium, gadolinium or aluminium), (ii) any of the phases of ice for which structural information is available or (iii) the anhydrous (thenardite), or lesser hydrated (the hepta- or octa-hydrate) phases of Na_2SO_4. the gap in the data is the previously excluded region at 2.55 Å (see text).

4.2 Results

4.2.1 The incompressibility of mirabilite.

The equation of state of a material is a relation that describes how that material behaves under a set of variable conditions. Traditionally, thermodynamic equations of state describe the changes in the volume (or density) of a material with variations in pressure and/or temperature. The pressure volume relationship, the incompressibility of the material, can be expressed using an isothermal equation of state. Here a 3rd-order Birch-Murnaghan equation of state (3BMEOS), (Birch, 1952), has been used to fit to the data. This equation of state is of the form:

$$P(V) = \frac{3K_0}{2}\left[\left(\frac{V_0}{V}\right)^{\frac{7}{3}} - \left(\frac{V_0}{V}\right)^{\frac{5}{3}}\right]\left\{1 + \frac{3}{4}\left(K'_0 - 4\right)\left[\left(\frac{V_0}{V}\right)^{\frac{2}{3}} - 1\right]\right\}$$

Equation 4.1

Where P is the pressure, V is the unit-cell volume and V_0 the unit-cell volume at zero pressure. The quantity "K_0" is the incompressibility at zero pressure, with " K_0' " its first derivative with respect to pressure (also evaluated at zero pressure). The incompressibility (also known as the bulk modulus), is defined as:

$$K = -V\left(\frac{dP}{dV}\right) \qquad \textbf{Equation 4.2}$$

Expressions similar to Equation 4.1 were also used to fit the unit-cell axes as a function of pressure; the axes, as opposed to their cubes, were fitted and thus the axial incompressibilities quoted are of the form

$$K_b = -b\left(\frac{dP}{db}\right) \qquad \textbf{Equation 4.3}$$

It was found that the variation of the monoclinic angle with pressure could be adequately represented by a straight line.

4.2.2 Bulk and axial incompressibility of mirabilite at 260 K and 80 K.

The refined values of the cell parameters and cell volumes obtained in this high-pressure study are shown in the table in Appendix 4. Figure 4.5 shows the volume and axial equation of state fits along the 260 K and 80 K isotherms. It was necessary to constrain the value of K_0' to ensure it remained positive. It was therefore fixed at the value obtained in the *ab initio* calculations performed as part of this thesis (Chapters 5-7, $K_0' = 5.6$) for both isotherms. This fit yields values at 260 K of $V_0 = 1456.7(6)$ Å^3 and $K_0 = 18.0(5)$ GPa; at 80 K the corresponding values are$V_0 = 1440.2(4)$ Å^3 and $K_0 = 22.7(6)$ GPa. These values are similar to the experimental incompressibilities obtained for epsomite (Fortes *et al*. 2006a) for which $K_0 = 21.5(4)$ GPa at 290 K and $K_0 = 24.9(8)$ GPa at 50 K. The V_0 values at both temperatures are within 0.2% of the zero pressure values obtained during the thermal expansion experiment described in Chapter 3 (0.155% at 260 K and 0.189% at 80 K). Although these differences are small, there is clearly a systematic error between the slab can used in the thermal expansion experiments and the TiZr pressure cell used in the high pressure experiments. This is probably due to a difference in the position of the sample within the diffractometer, although it may possibly have arisen from the recent recalibration of HRPD following the installation of the new beamguide. This offset is taken into account in later sections as appropriate.

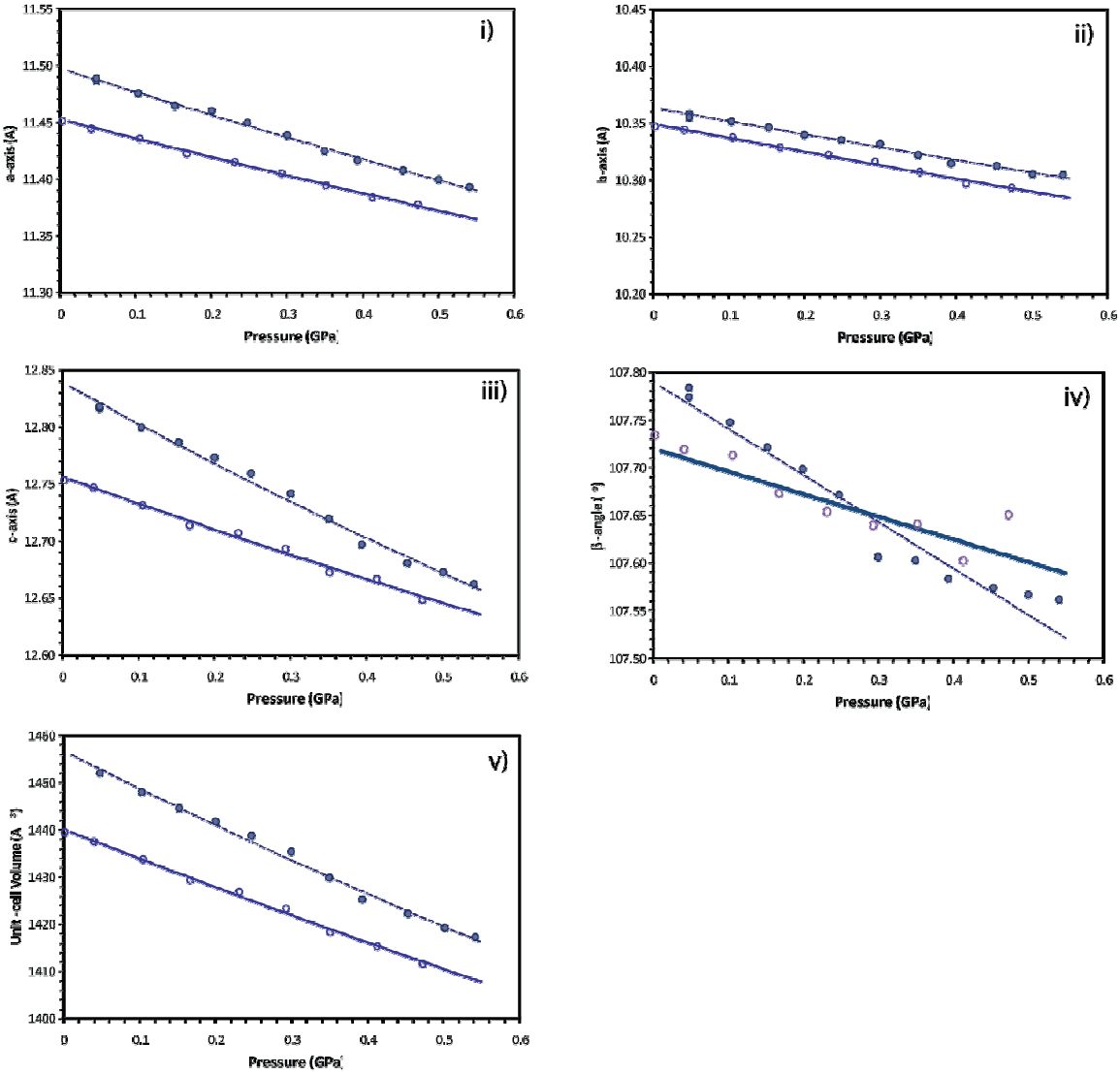

Figure 4.5 Unit-cell parameters of mirabilite as a function of pressure at 260 and 80 K. i) to iii) are the unit-cell axes, iv) is the beta-angle and v) is the unit-cell volume. In each case, the full lines and open circles are the 260 K data and the dashed lines and filled circles, the 80 K data. Note that panels i) to iii) have been plotted on the same vertical scale to facilitate comparison of the relative incompressibility of each axis. The lines are 3rd-order Birch-Murnaghan EoS fits to the unit-cell axes with linear fits to the beta-angle.

The unit-cell parameters of mirabilite, referred to orthogonal axes, (Figure 4.5, Table 4.2), were also fitted with 3rd-order Birch-Murnaghan expressions to obtain the axial incompressibilities. The K_0' values were again fixed (at 16.8 – three times the bulk value of K_0'), to ensure that they remained positive. As a check, the zero-pressure bulk modulus was calculated, yielding: $K = [(K_{a\sin\beta})^{-1} + (K_b)^{-1} + (K_c)^{-1}]^{-1}$ = 18(1) GPa at 260 K and 23(1) GPa at 80 K, which is in excellent agreement with the values obtained from the bulk 3BMEOS fits.

The relative axial behaviour of mirabilite on compression is similar to the relative axial thermal expansion behaviour; for both isotherms the *c*-axis is the most compressible, with the a_{sinb} direction intermediate and the *b*-axis stiffest of the three axes along both isotherms and showing the least variation between the two temperatures. It is surprising to find that the most compressible direction is along the *c*-axis; is this due to the co-location of the $Na(H_2O)_6$ octahedra along this axis and are they able to accommodate compression by folding at the shared hinges? As these experiments give us no detail about changes in the positions of the atoms within the mirabilite structure, no structural mechanisms to explain this axial heterogeneity can be determined from these experiments. However, the *ab initio* calculations described in later chapters do yield such information and so further discussion of this can be found in Chapter 6.

Table 4.2 The axial compressibility of mirabilite at 260 and 80 K.

	260 K			80 K		
	a_{sinb}	b	c	a_{sinb}	b	c
a_0 (Å³)	10.948(1)	10.364(1)	12.839(3)	10.9090(1)	10.349(1)	12.756(3)
K_0 (GPa)	64 (2)	87 (3)	34 (1)	75 (2)	83 (3)	54 (2)
K_0'	16.8	16.8	16.8	15.9	15.9	15.9

4.2.3 Derivation of the elastic strain tensor of mirabilite.

The unit-cell dimensions as a function of pressure have also been used to determine the coefficients of the elastic strain tensor using the method described by Hazen *et al.* (2000) implemented in a custom spreadsheet; a similar procedure was used in the analysis of the *ab initio* computer simulations of mirabilite at high pressure (see Section 6.5 in Chapter 6). The eigenvalues and eigenvectors of the strain tensor are obtained by matrix decomposition, yielding the magnitudes and orientations of the principal axes of the strain ellipsoid. The magnitudes of the principal axes are strains per unit stress, and are effectively the axial compressibilities, and their sum is the bulk compressibility. The ellipsoid is constrained by the symmetry of the crystal. In this monoclinic case, the ellipsoid is constrained to rotate only about the two-fold axis and the convention that the principal strain axis $\mathbf{e_2}$ is parallel to the *b*-axis of the crystal has been adopted.

Strains were calculated using the raw unit-cell dimensions directly output from the structural refinements in GSAS, and also using equations of state fitted to the same output. The solid lines in Figure 4.6 are the strains obtained from the various EoS fits; only for the volumes are the raw strains shown since the strains computed from the 'raw' unit-cell dimensions are very noisy. As in Figure 4.5, the full lines show the 80 K results and the dashed lines the

260 K results. Also shown in Figure 4.5 is the angle between $\mathbf{e_3}$ and the crystallographic *c*-axis. The strain ellipsoid is very sensitive to the uncertainties in the EoS fitting, particularly to the order of the fit to the beta-angle.

The most obvious feature of note in the strain plots is that the $\mathbf{e}_2$ strain magnitude behaves in a manner contrary to $\mathbf{e}_1$ and $\mathbf{e}_3$; upon cooling $\mathbf{e}_2$ softens rather than stiffening as is usual. The overall volume compression stiffens on cooling and so the $\mathbf{e}_2$ softening must be compensated by the other principal axes. In this case the softening is more than compensated for by $\mathbf{e}_3$ which shows the largest change, by an order of magnitude, between 260 and 80 K.

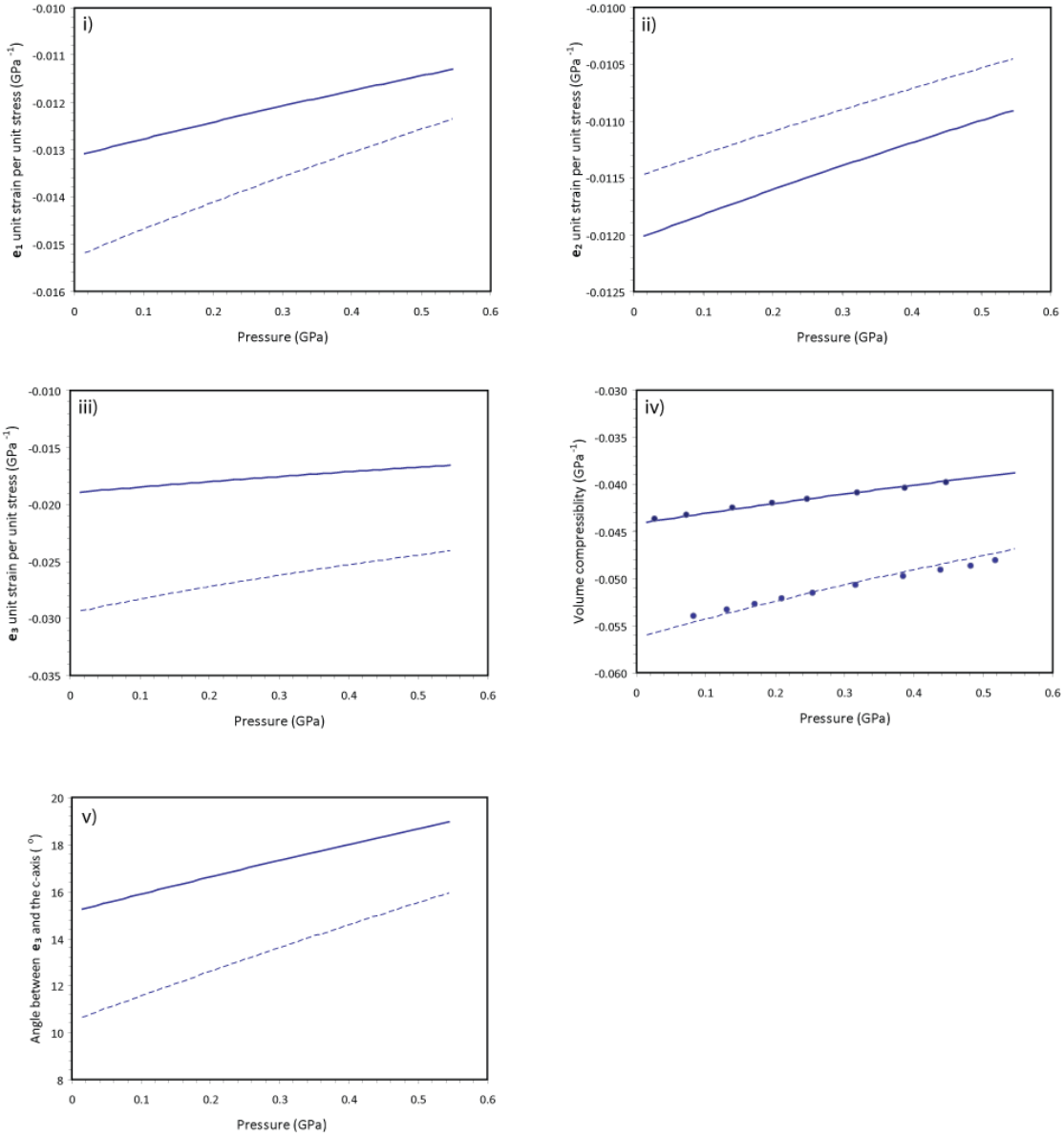

Figure 4.6 Panels (i) to (iii) show the magnitudes of the principal axes of the strain tensor, e_1, e_2 and e_3 as a function of pressure. Their sum, the volume compressibility, is shown in (iv), and the angle between e_3 and the crystallographic *c*-axis is shown in (v). In each case, the full line represents the 80 K results and the dashed line the 260 K results.

4.3 The thermal expansion of mirabilite at 0.55 GPa.

During the high-pressure HRPD investigation of mirabilite, data were collected at 20 K intervals as the sample was cooled from 260 K to 80 K under a load of 0.55 GPa. Although there are only 10 points in this data set and the high pressure sample environment prohibits collection of data detailed enough to extract atomic positions, these data can still be used to extract bulk properties. However, these fits should not be extrapolated above 260 K or below 80 K and are not quite truly isobaric as the pressure varies by 77 bar over the temperature range.

Figure 4.7 shows the variation of the unit-cell volume with temperature at 0.55 GPa, compared to a section of the thermal expansion data from the previous chapter measured at zero pressure. The high-pressure results lie on a shallower and more linear curve than the zero pressure data, as might be expected. The lack of data and lower accuracy of the high pressure experiment makes it impractical to fit the complex relations which were applied to the thermal expansion data so a 2nd order polynomial has been fitted to the 0.55 GPa data, giving the relation: $V = -2.107 \times 10^{-5} T^2 + 4.858 \times 10^{-4} T + 1406.01$ ($R^2 = 99.84\%$).

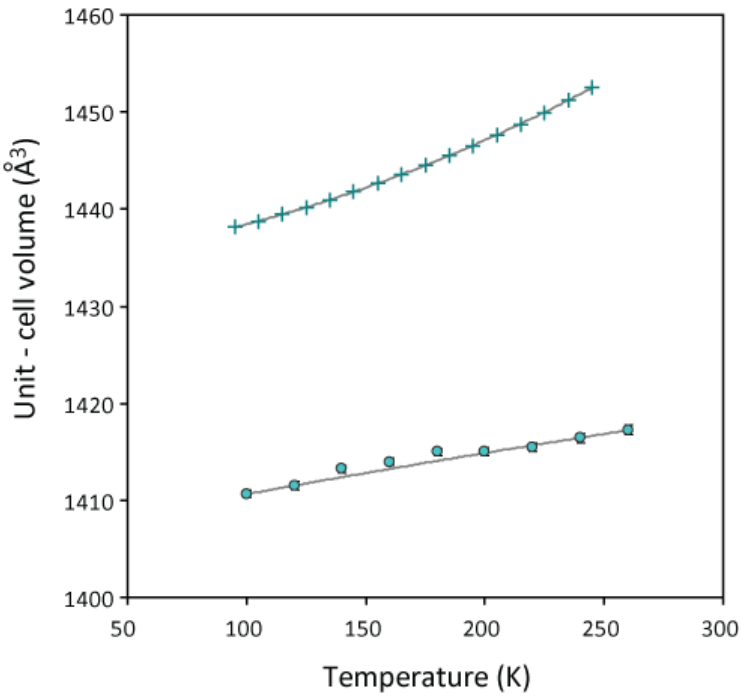

Figure 4.7 Thermal expansion of mirabilite at 0 and 0.55 GPa. The crosses are the zero pressure data and the blue filled circles the 0.55 GPa data. In both cases the line through the data points is a 2nd order polynomial fit to the data. The errors in the measurements are of the same order as the size of the symbols.

The data at high pressure have been used in combination with the thermal expansion data from Chapter 3 to determine a series of bulk moduli at temperatures from 260 – 100 K. For each temperature, a 3BMEOS was fitted to the data at 0 and 0.55 GPa (with K_0' fixed at 5.6, see above). Since each fit is only to two points the resulting isothermal moduli are extremely imprecise. To improve the accuracy as much as possible, $V_{P,T}$ has also been calculated using the smoothing polynomials reported above. The results can be seen in Figure 4.8 which shows the variation in K_0 with temperature in comparison to the same property determined in this way for epsomite (Fortes *et al*. 2006a). The results for mirabilite are very similar in magnitude to those for epsomite. The mirabilite results are less linear than for epsomite, although this may be an artefact of the fitting to such sparse data.

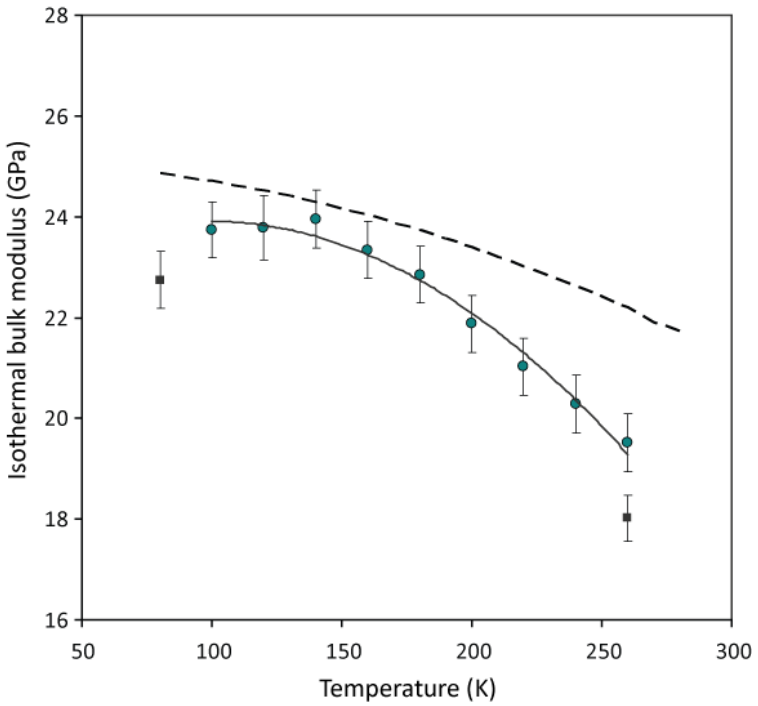

Figure 4.8 Variation of the bulk modulus K_0, with temperature between 260 and 80 K. The data points and full line are the mirabilite data from this study. The two data-points marked by square markers are the well constrained values of K_0 from the two main compression experiments; the circles indicate the more unconstrained points determined upon cooling of the sample. The dashed line is the same property for epsomite.

The final information which has been extracted from this compression and cooling data is the relation between the isothermal bulk modulus and thermal expansivity through the Anderson–Grüneisen parameter, δ_T, defined by:

$$\delta_T = \left(\frac{\partial K_T}{\partial T}\right) \cdot \left(\frac{1}{\alpha_V K_T}\right) \qquad \textbf{Equation 4.4}$$

where α_V is the thermal expansivity (Anderson and Issak, 1993). As for the variation of K_T with temperature, δ_T was calculated by instantaneous differentiation of the K_T points calculated in Figure 4.8, as well as using the smoothed expression for K_T. The values of α_V were taken from the thermal expansion experiments of chapter 3. Figure 4.9 gives a comparison of the mirabilite values of δ_T with the epsomite value over a similar temperature range. It is interesting that the values of δ_T for mirabilite and epsomite start at very similar magnitudes at ~ 100 K but mirabilite soon overtakes epsomite and at 260 K is more than six times the epsomite value reflecting the greater temperature dependence of K_T.

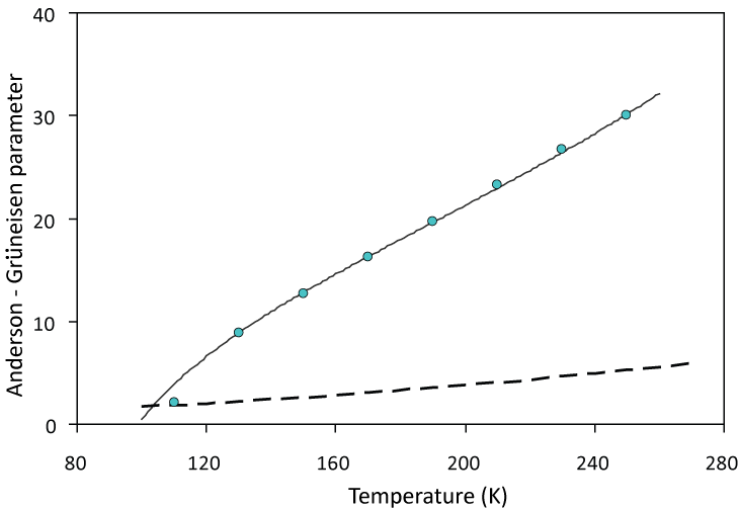

Figure 4.9 The Anderson- Grüneisen parameter for mirabilite (circles and full line) compared to epsomite (dashed line).

Summary

This chapter reports the results of neutron diffraction experiments to determine the compressibility of mirabilite from 0 – 5.5 kbar at 80 and 260 K. The bulk moduli at 80 K and 260 K are found to be 22.7 (6) GPa and 18.0 (5) GPa respectively when K_0' is constrained to the *ab initio* value of 5.6 obtained in Chapter 6. Further comparison between these data and the *ab initio* simulations of mirabilite will be drawn in the relevant section of Chapter 6. The variation in the bulk modulus with temperature has also been studied, with a view to investigating the pressure-volume-temperature parameter space of mirabilite. The variation in K_0 with temperature is similar to that of epsomite over the same temperature range but mirabilite shows a less linear relation; the incompressibility of mirabilite is more temperature sensitive than that of epsomite. However, the number of data-points is very limited and further measurements at intermediate temperatures and pressure are required before these data can be properly put into context.

Chapter 5

Ab intio simulations I:

Methodology.

In the experimental studies described in the previous three chapters we have seen how challenging it can be to attain and maintain the conditions of pressure and temperature relevant to investigation of the material properties of salt hydrates in planetary settings. Calculations offer a solution whereby difficult environmental conditions can be investigated with relative ease. In these simulations, we aim to determine physical properties, such as the equation of state and elastic properties of the material, from the total energy of the system as a function of volume. There are two computational approaches used to find total energy that have been considered in the present work. The first uses interatomic potentials and classical equations of motion to represent the interactions between atoms; this approach was used initially, but was found to be inadequate, mainly due to the difficulty of constructing suitable interatomic potentials (see Appendix 1). The second approach, described below, uses quantum mechanics (*ab initio* simulations) to describe interactions between electrons and ions within a system.

Sulfate hydrate structures are a very challenging proposition for calculations. They typically consist of large, low symmetry, unit cells with many hydrogen atoms and associated hydrogen bonds. These hydrogen bonds mean that the binding energy of the crystal will be low. This tends to make the total energy, as a function of the system variables, a very flat hypersurface containing many weak minima. When simulating such a system, care must be taken to ensure a true minimum in the energy surface has been found.

The first calculations carried out as part of this project were classical simulations of anhydrous sulfates, with a view to adapting and transferring the potentials to hydrated sulfates. Descriptions of these interatomic potential calculations of anhydrous $NaSO_4$ can be found in Appendix 1. Despite considerable effort, it was not possible, using this approach, to calculate sufficiently accurate elastic constants, and so it seemed unlikely that empirical potentials capable of being transferred to the mirabilite structure would be obtained in this way. Subsequently, therefore, quantum mechanical methods were used; although they are more computationally expensive than classical methods, they are more reliable since they do not depend on the transfer of fitted parameters from one material to another.

This chapter explains some of the theory behind the *ab initio* methodology and its application to planetary ices, before describing the specific set up of the calculations for 1) mirabilite and 2) MS11.

5.1 Theoretical background to ab initio calculations.

This section serves as a brief overview of the main concepts of *ab initio* calculations. It is by no means exhaustive and for more in-depth reviews please refer to Payne *et al*. (1992) and Gillan (1997).

In quantum mechanics, the energy of a non-relativistic system is determined through the approximate solution of the time-independent Schrödinger equation.

$$\hat{H}\psi_i = E_i\psi_i \qquad \textbf{Equation 5.1}$$

where E_i is the energy of the i_{th} state, ψ_i is the wavefunction of that i_{th} state and $\hat{H}$ is the Hamilton operator. The Hamiltonian is a differential operator, a rule book which describes how particles interact with each other. The wavefunction describes the particular configuration of the system under investigation and cannot be directly observed. The wavefunction depends on the coordinates and spin state (in the case of the electrons) of all the particles in the system. The square of the wavefunction determines the probability of finding an electron with a specific wavefunction within a given volume, $d\vec{r}$, (Equation 5.2).

$$\int \left|\psi(\vec{r})\right|^2 d\vec{r} \qquad \textbf{Equation 5.2}$$

The Hamiltonian can be written as (Fortes (2004)):

$$\hat{H} = -\frac{1}{2}\sum_{i=1}^{N}\nabla_i^2 \; -\frac{1}{2}\sum_{A=1}^{M}\frac{\nabla_A^2}{M_A} - \sum_{i=1}^{N}\sum_{A=1}^{M}\frac{Z_A}{r_{iA}} + \sum_{i=1}^{N}\sum_{i\neq j}^{N}\frac{1}{r_{ij}} + \sum_{A=1}^{M}\sum_{A\neq B}^{M} Z_A\frac{Z_B}{R_{AB}}$$

Equation 5.3

where there are N electrons in the system and M nuclei. The electrons are denoted with subscripts *i* and *j* and the nuclei with subscripts A and B. M_A is the mass of nucleus A and Z_A its charge. R_A and r_i denote the spatial coordinates of the relevant species. The first two components of Equation 5.3 are the kinetic energies of the electrons and the nuclei, the third

is the electrostatic attraction between electrons and nuclei and the final two components are repulsive potentials between like species of electrons and nuclei (Fortes, 2004a).

The Hamiltonian and the wavefunction are not tractable for systems with more than one electron so approximations are employed in quantum mechanical simulations to overcome this difficulty (see below).

5.1.1 Born-Oppenheimer Approximation.

The first approximation is the Born-Oppenheimer approximation. This states that as there is such a large difference in mass between nuclei and the electrons, the electrons will react much more quickly than the nuclei, almost instantaneously by comparison. This allows the nuclei and the electrons of a system to be considered separately in the calculation of the Hamiltonian (and the wavefunction). The nuclei are treated as "static" and so their kinetic energy component is no longer necessary in the Hamiltonian and only the dynamics of the electrons need be considered. This then reduces the Schrödinger equation to:

$$\hat{H}_{elec}\psi_{elec} = E_{elec}\psi_{elec} \qquad \textbf{Equation 5.4}$$

Note: Subscript *elec* refers to the electronic contribution.

And the total energy of the system, E_{tot}, becomes:

$$E_{tot} = E_{elec} + E_{nuc} \qquad \textbf{Equation 5.5}$$

With E_{nuc} , the energy of the nucleus, being simplified to just the electrostatic repulsion between the nuclei as described in Equation 5.3 and equal to:

$$E_{nuc} = \sum_{A=1}^{M}\sum_{A\neq B}^{M} Z_A \frac{Z_B}{R_{AB}} \qquad \textbf{Equation 5.6}$$

This then reduces the Hamiltonian to the electronic Hamiltonian, $\hat{H}_{elec}$:

$$\hat{H}_{elec} = -\frac{1}{2}\sum_{i=1}^{N}\nabla_i^2 - \sum_{i=1}^{N}\sum_{A=1}^{M}\frac{Z_A}{r_{iA}} + \sum_{i=1}^{N}\sum_{i\neq j}^{M}\frac{i}{r_{ij}} \qquad \textbf{Equation 5.7}$$

However, it is still the case that this Hamiltonian can be calculated exactly and the Schrödinger equation solved only if there is just one electron in the system. If, as is usually the case, there is more than one electron in the system, another important part of the Hamiltonian which must be addressed is the electron-electron interaction, i.e. the third component of the Hamiltonian in Equation 5.7, the Coulomb interaction between the electronic charges:

5.1.2 Exchange and correlation

To take into account the Coulombic interaction we must consider the wavefunction of the electrons, Ψ_e, which depends on not only the position, *r*, of the electron, but also on the spin state of that electron. The component of the angular spin of an electron along a given direction can only have values of $\pm \frac{1}{2} \hbar^2$ (Gillan, 1997), represented as up, ↑, and down, ↓, so the probability of finding an electron at point *r* with its spin pointing up is:

$$\left|\uparrow(r)\right|^2 \qquad \textbf{Equation 5.8}$$

The Pauli Exclusion Principle states that no two identical fermions can occupy the same quantum state simultaneously; two electrons cannot have the same spin and occupy the same space. If two electron positions are interchanged, their wavefunctions must change sign. This is known as exchange symmetry. Exchange symmetry results in a lowering of the energy of a system as it keeps the electrons apart. The effect of exchange symmetry can be demonstrated if we consider two electrons which both have their spins up. The combined wavefunction of these two electrons is the product of their individual wavefunctions:

$$\psi_a \uparrow(r_1)\psi_b \uparrow(r_2) - \psi_a \uparrow(r_2)\psi_b \uparrow(r_1) \qquad \textbf{Equation 5.9}$$

If we place the electrons in the same place, i.e. if $r_1 = r_2$, then the wavefunction vanishes and there is zero probability that the electrons exist at the same position. Equation 5.9 is termed an "antisymmetrized" product of the wavefunction and its inclusion allows the exchange symmetry behaviour of the electron to be addressed. This is Hartree-Fock theory.

Another consequence of the Pauli Exclusion principle is that the movement of an electron within a system is related – correlated – to the movements of the other electrons in that

system in an effort to prevent two electrons occupying the same space and spin state. Both exchange and correlation work to lower the energy of the system as they both result in the electrons avoiding each other. This reduction in energy is denoted E_{xc}, the exchange-correlation energy.

Hartree-Fock theory does not address the *correlation* portion of the *exchange-correlation* problem, so additional measures are needed to do this. It is possible to represent the movement of the electrons through a static potential and correlation can be included as a modification to this potential. This is the main premise of Density Functional theory (DFT).

Density functional theory (DFT) assumes that the electron density, $n(\mathbf{r})$, can be used as a proxy for the positions of the electrons. This leads to the expression:

$$E_{xc} = \int n(r) \cdot \varepsilon_{xc}(n(r))dr \qquad \textbf{Equation 5.10}$$

where the amount of *exchange-correlation energy*, E_{xc} in a unit volume is $n(\mathrm{r})\varepsilon_{xc}(n(\mathrm{r}))$. This expression is termed the *local density approximation*; it has more recently been extended to include gradients of $n(\mathrm{r})$, giving rise to the *generalised gradient approximation* (GGA) (Perdew 1986).

The key statement of DFT (Hohenberg and Kohn 1964, Kohn and Sham 1965) is that E_{xc} can be expressed as a function of the electron density. Hohenberg-Kohn (1964) (H-K theory) and later developments such as those by Kohn and Sham (1965), allow the construction of a rigorous many-body theory using the electron density as the fundamental quantity.

5.1.3 Plane waves, Pseudopotentials and the PAW method.

The next step in solving Schrödinger's equation is to represent the wavefunction of the system. One way in which this may be done is by means of *plane-waves*. This methodology says that electrons within condensed matter can be treated as though they were free particles and so can be represented as such. The wavefunction of a free electron is $\exp\left(i\mathbf{k}\cdot\mathbf{r}\right)$, where $\mathbf{k}$ is the wavevector of the de Broglie wave. The total wavefunction is then:

$$\psi_i(r) = \sum_{\mathbf{k}} c_{i\mathbf{K}} \exp(i\mathbf{k}\cdot\mathbf{r}) \qquad \textbf{Equation 5.11}$$

Where c_{ik} are coefficients to be varied until the energy of the system is minimized and therefore the electrons are in their ground state. The set of functions which represent $\phi_a(\vec{r})$, the atomic wavefunction, are known as "basis-sets" and form the repeating basis of the wavefunction.

In reality, this representation of atoms and electrons in matter is not necessarily a realistic one. Probabilistically, not all electrons are "free" to move throughout a structure. The inner electrons of the atoms, closest to the nucleus, have high energies and are tightly bound, not generally taking part in bonding. The physical properties of solids rely on the interactions and bonding of the outer valence electrons. This suggests, therefore, that it would be simpler to represent the core electrons as a bound unit and then consider the valence electrons as a separate entity. This representation can be achieved through replacement of the core electrons and the strong nuclear potential by a weaker pseudopotential which acts on a set of pseudo wavefunctions rather than the true valence wave function (Payne *et al*., 1992).

Figure 5.1 shows a schematic of this, where Ψ_{Pseudo} is a pseudowavefunction which substitutes for the true wavefunction of the valence electrons (Ψ_V), in the core region ($r < r_c$). In the core, Ψ_V oscillates rapidly so Ψ_{Pseudo} substitutes a smoother wavefunction. Beyond r_c, the two potentials are identical.

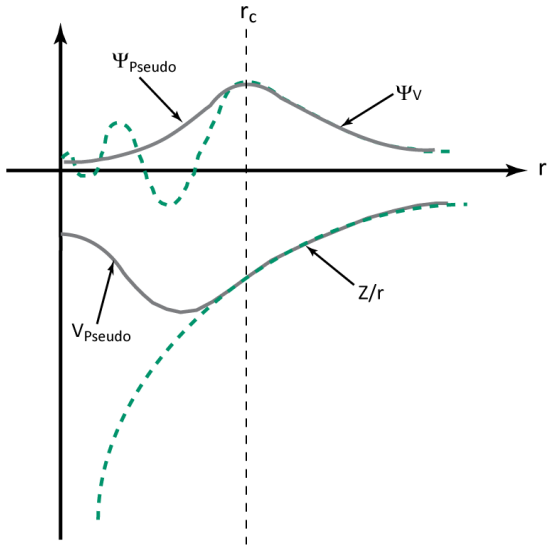

Figure 5.1 Schematic illustration of the generated pseudopotential wavefunction, Ψ_{Pseudo}, in relation to that of the valence electrons, Ψ_V, and the corresponding potentials V_{pseudo} and Z/r. r_c represents the point at which Ψ_V and Ψ_{pseudo} are identical.

However, this representation is not without complications. Elements in the first row of the periodic table have limited numbers of core electrons (in the case of hydrogen – none); in such cases Ψ_V tends to be large and so there must be a large cutoff in the plane wave basis set to compensate, i.e., a large number of plane waves are required. However, *non-norm conserving ultrasoft pseudopotentials* have been developed which are able to adequately represent systems containing atoms of low atomic numbers using a lower cutoff (e.g. Vanderbilt, 1990).

In the calculations reported here, an alternative, more recently developed approach, the *Projector Augmented-Wave* (PAW) method (Blöchl, 1994) has been used. PAW is a combination of density functional theory techniques, combining the true all-electron wavefunction (i.e., treating the core region with planewaves) with pseudopotentials so as to better represent the core region and obtain smoother pseudowavefunctions. This combination is achieved by relaxation of the norm-conservation of the wavefunctions. This creates a deficit between the all-electron and pseudopotential wavefunctions which is compensated for by the introduction of augmentation charges.

5.2 Vienna Ab initio Simulation Package (VASP) setup.

The calculations carried out here used VASP – the Vienna *Ab initio* Simulation Package (Kresse and Furthmüller, 1996). VASP calculations are based on DFT (Hohenberg and Kohn, 1964) within the GGA (Wang and Perdew, 1991) using the PAW method (Blöchl, 1994) to calculate the total energy of each system. The details of the computational setup are detailed in the sections below and the results reported in Chapters 6 and 7 for mirabilite and MS11 respectively.

5.2.1 Inputs and outputs.

VASP requires four files to form an input. The first of these is the POSCAR file. This file gives the position and number of atoms within the structure to be studied as well as the unit-cell dimensions and angles. As the name suggests, the KPOINTS file gives the configuration of the electronic *k*-points to be sampled by this calculation. The INCAR file consists of a list of switches which tell VASP the limits and specifications of the calculations. The detailed options which were employed during the calculations reported in this thesis will be discussed below in section 5.3.1.2 for mirabilite and 5.3.2.1 for MS11. The final input file required by VASP is the POTCAR file. This file contains all the PAW information for the atoms within the structure to be studied and so, for mirabilite, it is a concatenated file containing such information for sodium, sulfur, hydrogen and oxygen.

Depending on the calculation, VASP produces a large swathe of output files. The most important of these for the work presented here are the OUTCAR and CONTCAR files. The OUTCAR file contains a large amount of information including the final positions of the atoms, the forces on each of them, the eigenvalues and energies of the system and technical details of the computer run-time required to carry out the calculation. The CONTCAR file contains a record of the atomic positions obtained in the final minimisation step carried out by VASP. Another useful output from VASP is the OSZICAR file which contains a summary of the minimisation cycles.

5.2.2 Sampling of k - points.

The KPOINTS file specifies how many *k*-points will be used in a calculation and in what arrangement. The *k*-points are the points in reciprocal space over which the energy of the structure will be calculated. The chosen positions and number are heavily dependent on the shape and size of the unit-cell and thus on the symmetry of the crystal. VASP can be set up to either generate a grid of *k*–points in reciprocal space, or the user can specify particular points for sampling. Ideally, to get the best results, there would be an infinite number of these *k*-points. However, the computational cost of such a simulation would be astronomical as the calculation must be performed over each of these *k*-points. Therefore, there is a trade-off between having enough *k*-points to have a sufficient degree of accuracy while not having a very computationally expensive calculation. To achieve this, the number of *k*-points is selected after a series of tests with varying numbers and configurations of *k*-points to ensure convergence. For these calculations, VASP was set to automatically generate the *k*-point grid, sampling the Brillouin zone using the Monkhorst-Pack scheme, (Monkhorst and Pack (1976)).

5.2.3 Ionic relaxation within VASP.

To ensure that the structure being simulated is fully minimised, it must undergo ionic relaxation as well as electronic minimisation. This means that the atoms are allowed to move until they are in their lowest-energy state. The movement of the atoms is described by Newton's equations of motion such that the atomic positions, $\boldsymbol{R}_i$, obey:

$$\frac{d^2 R_i}{dt^2} = \frac{F_i}{M_i} \qquad \textbf{Equation 5.12}$$

Where $\mathbf{M_i}$ is the mass of atom $\boldsymbol{i}$, and $\boldsymbol{F}_\mathbf{i}$ is the force on the atom. As the atoms move, the electrons respond and move in turn. At each timestep, the ground state and the forces on the atoms are recalculated until an energy minimum within a chosen tolerance is achieved. The shape and size of the unit cell are also parameters which can be optimised and so the same process can be applied to these.

5.2.4 Hydrogen bonding in DFT

The bonding schemes of mirabilite and meridianiite described in chapter 1 are dominated by hydrogen bond interactions and so a suitable description of such interactions is important for any simulation of these materials. Simulating hydrogen bonds is not a straightforward prospect with both experiments and calculations finding it difficult to determine the strength and geometry of hydrogen bonds (Ireta *et al.* 2004, Perrin and Nielson 1997, Muller-Dethlefs and Hobza 2000).

There have been several studies on the accuracy of a variety of DFT techniques to represent hydrogen bonding within a range of different materials (e.g. Ireta et al. 2004, Laasonen et al. 1992, Tuma et al. 1999, Hamann 1997 and Tsuuki and Luthi 2001). These have shown that the ability of a particular functional to describe hydrogen bonding can vary greatly for different systems. In general hydrogen bond interactions are not formally accounted for in current DFT functionals. However, GGAs have been shown to offer a good compromise between computational efficiency and accuracy (Silvestrelli 2009), in the simulation of hydrogen bond interactions over a range of materials (Tsuki and Luthi, 2001), more accurately describing the interaction than LDAs. Such functionals have also been successfully employed to represent other hydrogen bonded salt hydrates such as epsomite (Fortes *et al.* 2006).

5.2.5 Tests on Ice VIII.

In order to gain familiarity with the process of using both VASP and the super-computer interfaces necessary for carrying out *ab initio* calculations, simulations were first performed on a substance with a "simpler" hydrogen bonded structure, one of the polymorphs of ice, ice VIII. Ice VIII has previously been simulated through *ab initio* calculations using VASP (Fortes, 2004a) and so it is a good material for an initial venture into *ab initio* simulation techniques.

Ice VIII is stable above ~2 GPa and below about 270 K, as can be seen in the ice phase diagram (Figure 5.2). Ice VIII (Figure 5.3) is tetragonal (space group $I4_1/amd$), with 24 atoms in the unit-cell (8 water molecules). However, unlike the structurally-similar polymorph Ice VII, Ice VIII is fully ordered and can also be represented by two interpenetrating cubic ice structures.

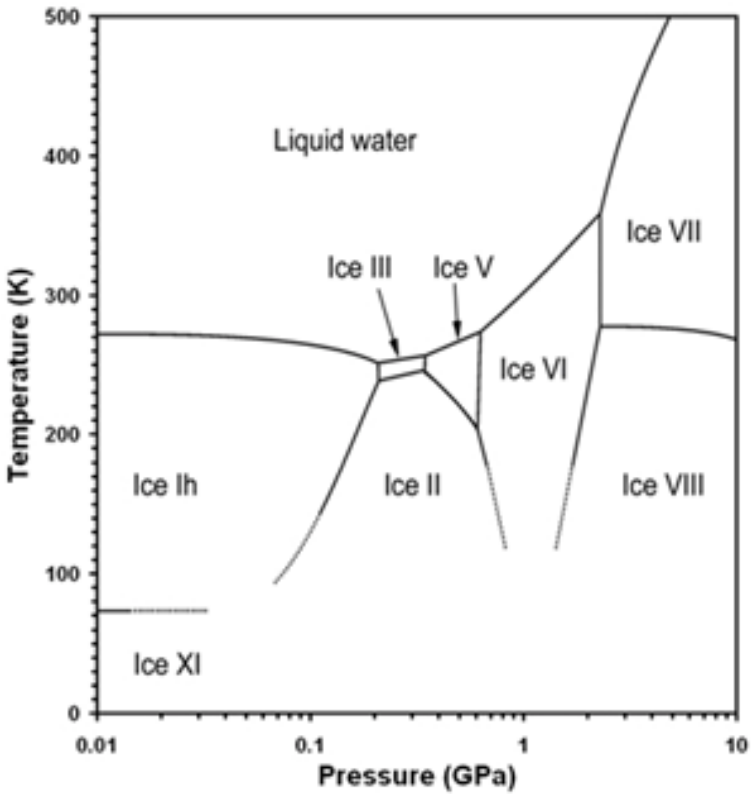

Figure 5.2 Phase diagram of Ice, after Fortes (2004a).

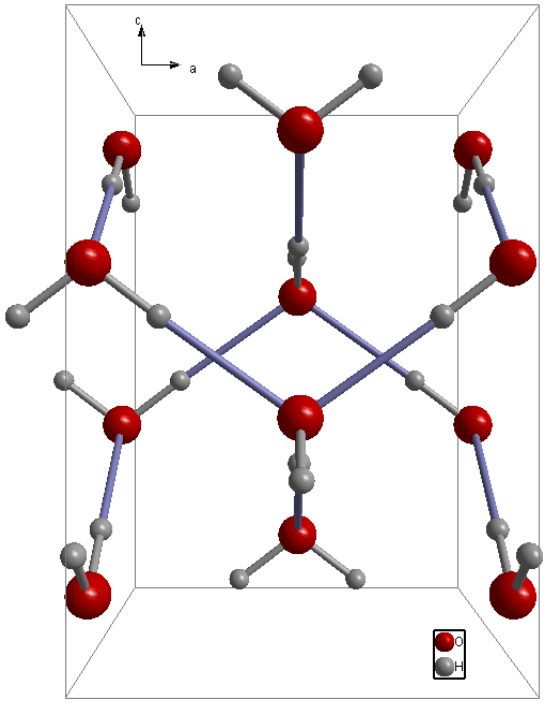

Figure 5.3 The structure of Ice VIII viewed along the b-axis. The grey bonds are the molecular hydrogen bonds and the blue bonds the intermolecular H-bonds.

A series of fixed volume calculations were performed over a range of volumes from 67 $Å^3$ to 118 $Å^3$. The atomic positions were kept constant, the objective being to successfully set up and run a series of calculations to produce an E-V curve rather than to fully relax the structure. The calculations were carried out using the same conditions as Fortes (2004a). These included 45 irreducible *k*-points on a *6x6x5* grid, energy cutoffs of 800 eV in both the plane waves and augmentation charge and convergence in the total energy to within 1 x 10^{-6} eV. Figure 5.4 shows the E-V curve obtained in these calculations compared to that of Fortes (2004a); clearly the results have been successfully reproduced.

As a further check of consistency with previous work, the energy–volume points from these simulations were also fitted with a third order Birch-Murnaghan equation of state (see section 5.4). Table 5.1 shows a comparison of the equation-of-state parameters with those of Fortes (2004a). Within error, the results obtained here are identical, as indeed they should be.

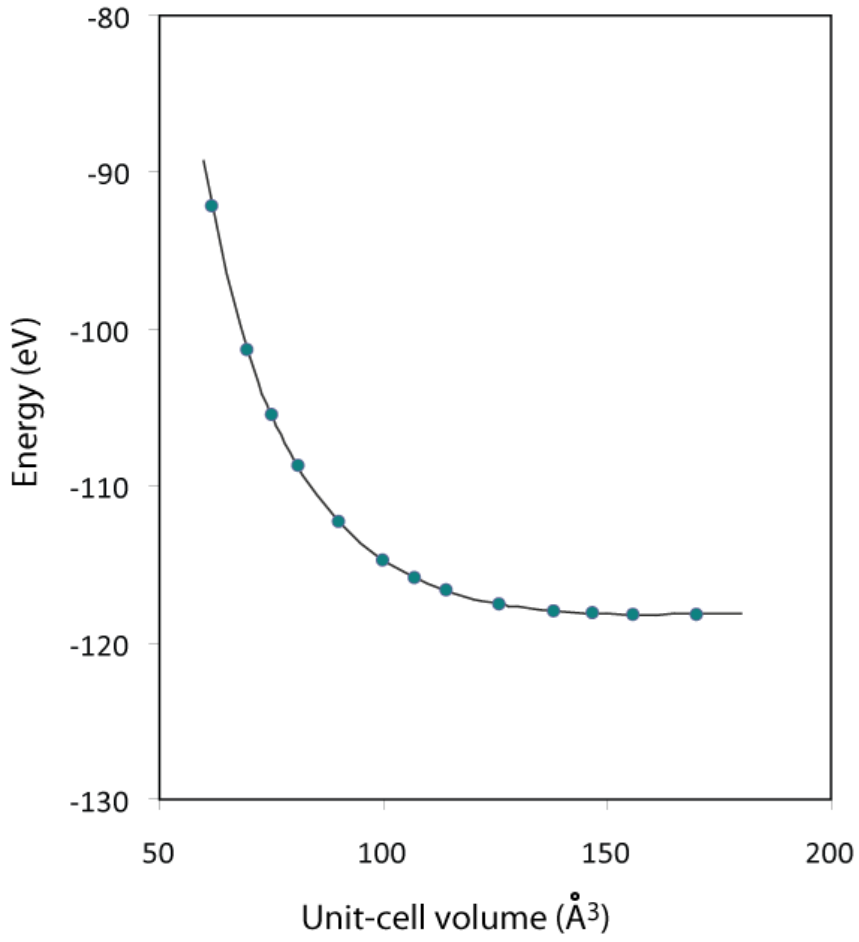

Figure 5.4 E-V curve of Ice VIII. The circular points are the test calculations carried out here. The full line is the calculations of Fortes (2004a).

Table 5.13BMEOS fit parameters for Ice VII obtained in this study and Fortes (2004a).

	This study	Fortes (2004)
V_0 (Å³)	166 (4)	163 (2)
K_0 (GPa)	13 (3)	14 (1)
K’	6.0(4)	6.0 (1)
E_0 (eV)	-118.29(5)	-118.22(2)

5.3 VASP Setup for this study.

The calculations in this work were carried out using HPCx, the UK's national high-performance computing service, which is based at the STFC’s Daresbury Laboratory. HPCx is a cluster of 2608 CPUs. Each calculation submitted in this project was carried out over 16 processors (the minimum number), and was initially given 8 hours to run. This represents a significant amount of CPU time which was the limiting factor on how many volumes were simulated.

In general, because of the step-wise running of the simulations, where the structure from the previous volume was used as the starting point for the next, the calculations converged well within this 8 hour window. In fact, in the case of the fine scale volumes between V/V_0 0.991 – 1.009, the calculations all converged within an hour.

For the smallest volumes, where $V/V_0 < 0.88$, it was necessary to restart the calculations to allow a second session of 8 hours for convergence due to the large difference in volume between the initial structural input and the volume to be simulated, but after this time they had all converged successfully.

5.3.1 Simulations of mirabilite.

Mirabilite forms a low symmetry crystal structure with a large primitive unit-cell. The unit-cell volume is over 1400 Å³ and the cell contains 148 atoms (Z = 4), all of which are in general positions. Thus, care was taken to thoroughly test the mirabilite structure to ensure that full convergence was achieved during the minimisation. The following sections describe the simulation setup for mirabilite and the testing undertaken.

5.3.1.1 POSCAR setup.

The POSCAR file determines the structure of the system and atomic positions. The first line of the POSCAR file is a comment line, allowing the user to add a memorable description for this particular calculation. The next line specifies the unit cell volume; this may be done in one of two ways: the value entered is either a chosen multiplier for the cell parameters or, if preceded by an en-dash, the total volume of the cell. In the mirabilite calculations, the initial volume was set at that determined from the present neutron diffraction experiments at 4.2 K. The next section of the POSCAR file is the unit-cell parameters expressed as a three lattice vectors, followed by the number of each atomic species within the unit-cell. These must be in the same order as the concatenated POTCAR file. The next instruction, "direct" or "Cartesian", tells VASP whether the atoms are specified in terms of fractional coordinates or physical values in Angstroms on orthogonal axes. The final section of the POSCAR file is a list of the atomic coordinates for each species; again, these must be in the same order as listed in the POTCAR file.

The fractional atomic coordinates used to start the calculations were taken from Levy and Lisensky (1978). However, since VASP is unable to incorporate disorder into calculations of the energy of a crystal it was necessary to "select" an ordered state for the structure. The disorder within the mirabilite structure, and the investigation of it, is described fully in Chapters 1 and 3. In the case of the ring disorder involving the O8/O16 (ring 1, shown in Chapter 1 and here again for reference as Figure 5.5), and similarly for O9/O17 (ring 2) we have "selected" the more occupied hydrogen atom site as determined from the experiments described previously; this is the "b" orientation as given by Levy and Lisensky (1978). Both orientations were initially simulated but there was no significant energy difference between them.

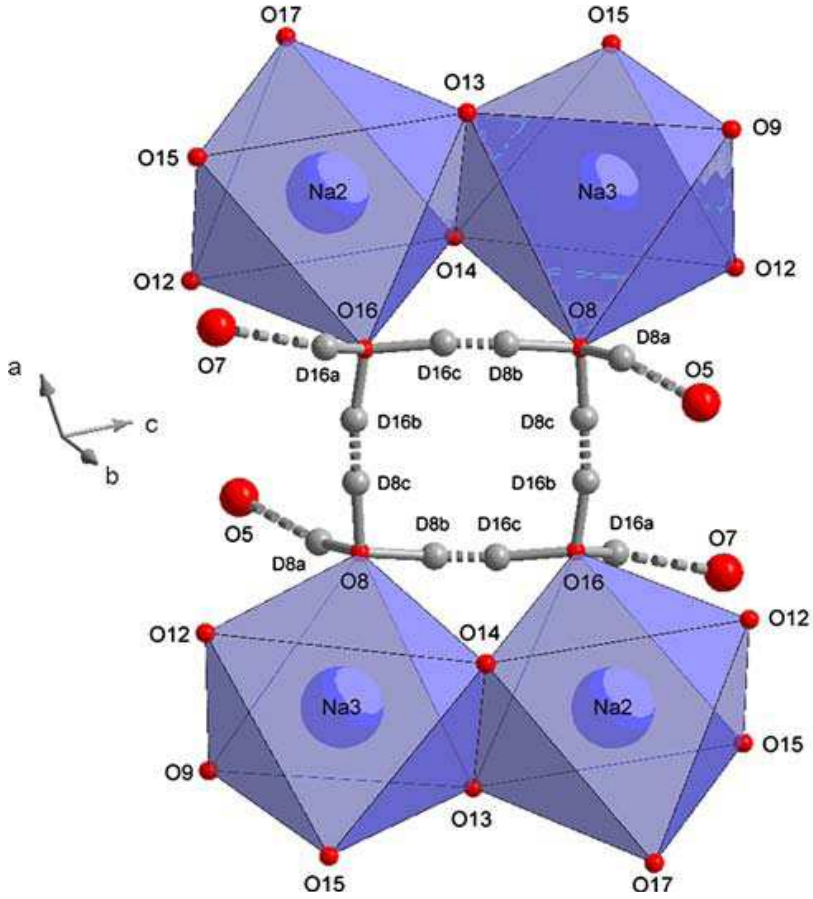

Figure 5.5 One of the square rings of water molecules involving disordered hydrogen bonds. The twofold axis of rotational symmetry passes through the middle of the ring, although not quite perpendicular to the plane of the page, as shown by the unit-cell axes.

The second type of disorder described by Levy and Lisensky (1978) involves the sulfate tetrahedra (see Figure 5.6). The neutron diffraction experiments show no evidence of partial occupancies of the sulfate tetrahedral sites over the temperature range observed and so in these calculations was assumed that the oxygens in the sulfate tetrahedra are fully ordered in the “double-primed” sites.

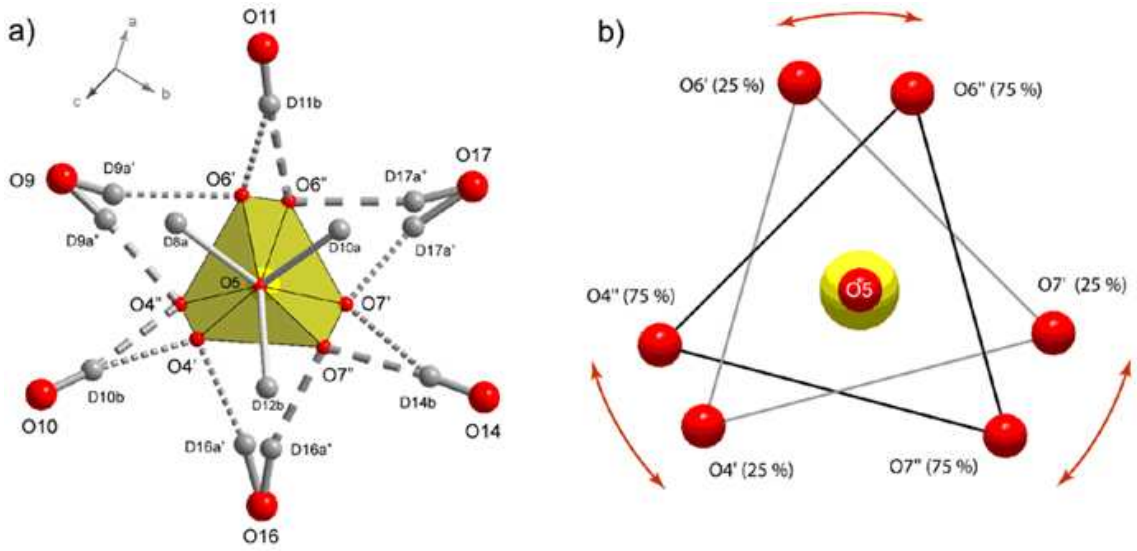

Figure 5.6The two orientations of the sulfate tetrahedron described by Levy and Lisensky (1978) as viewed down the rotation axis (the S···O5 vector) -orientation relative to the crystallographic axes is shown by the legend in (a). The hydrogen bonds donated to the ordered apex (O5) are shown with solid grey rods; those donated to the lesser occupied apices (O4', O6', and O7') are depicted as thinner, short-dashed rods; those donated to the more fully occupied apices (O4", O6", and O7") are depicted as thicker, long-dashed rods

5.3.1.2 INCAR setup.

The INCAR file contains instructions that VASP needs to run the calculations. There are many switches and options which can be set in VASP through the INCAR file; however, the optimum values of many of these are set as defaults within VSAP.

The mirabilite INCAR file is listed here and followed by a brief explanation of each entry:

NPAR = 8
NBANDS = 280
ENMAX = 800
ENAUG = 800
ISIF = 4
IBRION = 2
LWAVE=.FALSE.
LCHARG=.FALSE.
ALGO=Fast
NSW = 150

NPAR

The calculations were run on HPCX and HECToR, both parallel architecture computers; NPAR defines the number of nodes over which the calculation is run, in this case 8.

NBANDS

The number following the tag of NBANDS denotes the number of bands over which the calculation is to be split. VASP needs there to be at least one empty band. Therefore, the number of bands > the number of ions in the unit cell.

ENMAX

ENMAX is the kinetic energy cutoff for the planewave basis set (in eV); for the way in which this value was tested and set, see sections 5.3.1.3 for mirabilite and 5.3.2.1for MS11.

ENAUG

ENAUG is the kinetic energy cut off for augmentation charges. See section 5.3.1.3 below for further explanation of ENAUG testing for mirabilite (and section 5.3.2.1 for MS11).

ISIF

The ISIF tag determines whether the stress-tensor is calculated; it also determines which parameters (ionic positions, cell volume, cell shape etc.) are relaxed. Here ISIF = 4 is used which means that VASP will calculate the forces and the stress tensor and allow relaxation of the ionic positions, cell shape and cell volume.

IBRION

This tag tells VASP how to move and update the ionic coordinates. IBRION = 2 selects a conjugate gradient algorithm to ensure convergence of a system which may prove challenging.

LWAVE and LCHARGE

These two tags (respectively) tell VASP, whether to write the WAVECAR and CHGCAR output files. The entry “TRUE” instructs VASP to write these files.

ALGO

The ALGO switch tells VASP which algorithm to use for the energy minimisation. The FAST setting uses two different algorithms, allowing a mixture of the two to mix the advantages of each algorithm throughout the calculation.

NSW

NSW tells VASP how many ionic steps to run (unless convergence is achieved), in effect how many times to carry out the calculation. In the case of mirabilite, NSW is set to 150 steps. NSW should be set to more steps than it is expected that the structure will take to converge.

5.3.1.3 ENAUG and ENMAX tests.

ENMAX and ENAUG are the kinetic energy cut-offs of the plane-wave basis set and augmentation charges respectively. As we shall see, their value can have a significant effect on the outcome of a set of simulations, so it is imperative that their value is optimised. This optimisation is achieved by the observation of the systematic variation of the minimised energy as each quantity is changed. Here, the values of ENMAX and ENAUG have been varied from 200 eV to 1200 eV in 200 eV steps, repeated at two volumes. It is important to consider the convergence in pressure as well as in energy.

Firstly, the effect of changes in ENMAX, the kinetic energy cutoff of the plane-wave basis set is considered. Figure 5.7 shows the variation in (a) energy and (b) pressure with the value of ENMAX at $V=V_0$.

In these calculations, the important quantity to converge is the *difference* in energy between two volumes (per atom), V_1 and V_2, in the unit cell. This difference will be denoted ΔE ($\Delta E = E_2-E_1$), from here onwards. Table 5.2 shows E_1, P_1, E_2, P_2, ΔE and ΔP ($\Delta P = P_2-P_1$) as a function of ENMAX, for the volumes, $V_1 = V_0$ and $V_2 = 0.99^3V_0$. ΔE is very small at all but the first value of ENMAX, typically 1-2 meV. Table 5.1 therefore suggests that values of ENMAX > 600 eV will give sufficient convergence in energy. ΔP shows that, although the absolute pressures vary slightly, the pressure difference between the two sets of simulations converges for ENMAX < 800 eV; it was therefore decided to use a value of ENMAX = 800 eV in the production runs.

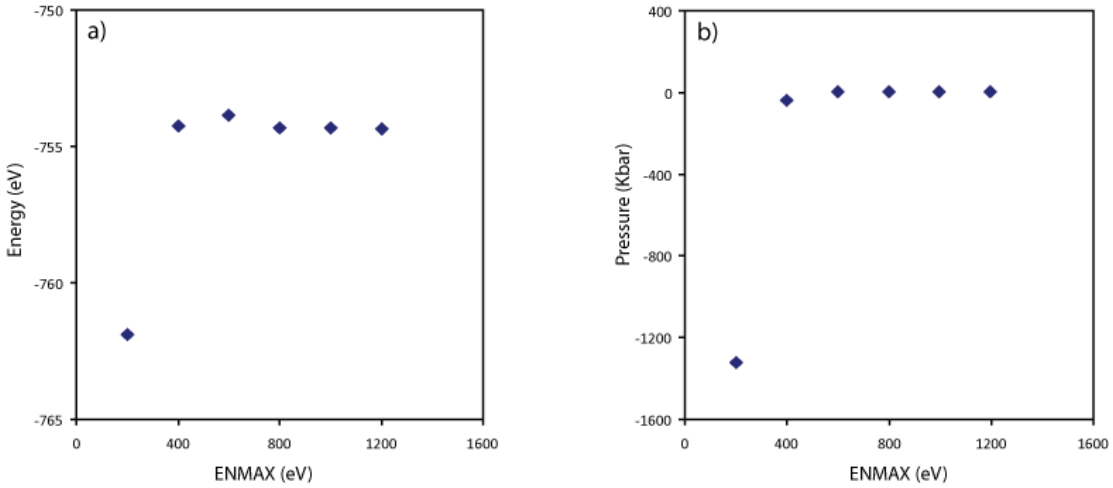

Figure 5.7 Variation in (a) Energy and (b) pressure with the value of ENMAX, the kinetic energy cutoff of the plane-wave basis set.

Table 5.2 Variation of energy and pressure with ENMAX at two volumes, together with ΔE and ΔP.

ENMAX (eV)	$V = V_0$		$V = 0.99^3 V_0$		ΔE per atom (eV)	ΔP (kBar)
	Energy (eV)	Pressure (kbar)	Energy (eV)	Pressure (kbar)		
200	-761.879762	-1323.68	-760.625665	-1263.99	0.008474	59.69
400	-754.238526	-38.66	-753.982214	-32.97	0.001732	5.69
600	-753.867652	1.86	-753.638057	8.74	0.001551	6.88
800	-754.312145	4.21	-754.083309	11.35	0.001546	7.14
1000	-754.336281	5.15	-754.106765	12.33	0.001551	7.18
1200	-754.363502	5.06	-754.133863	12.24	0.001552	7.18

The same procedure was carried out with ENAUG, the augmentation charge cutoff, and Table 5.3 shows the results. The augmentation charge cutoff value has a similar effect on the energy and pressure outputs from the calculations as the ENMAX cutoff. ENAUG was fixed at 800 eV for the calculations of mirabilite.

Table 5.3 Variation of energy and pressure with ENAUG at two volumes, together with ΔE and ΔP.

ENAUG (eV)	$V = V_0$		$V = 0.99^3 V_0$		ΔE per atom (eV)	ΔP (kBar)
	Energy (eV)	Pressure (kbar)	Energy (eV)	Pressure (kbar)		
200	-754.327812	4.06	-754.116737	10.91	0.001426	6.85
400	-754.347711	4.24	-754.120228	11.35	0.001537	7.11
600	-754.319882	4.22	-753.638057	8.74	0.004607	4.52
800	-754.312145	4.21	-754.083309	11.35	0.001546	7.14
1000	-754.307056	4.18	-754.079148	11.32	0.001540	7.14
1200	-754.306516	4.19	-754.078834	11.33	0.001538	7.14

5.3.1.4 Testing of k-points.

Tests were carried out with varying numbers and configurations of *k*-points from 1-16 in the symmetry irreducible wedge in reciprocal space; the results are shown in Table 5.4. The difference in energy obtained using 1 kpt and 16 kpts is so small (~0.2 meV/atom) as to be negligible, and therefore single gamma point calculations were performed. The results from these calculations on mirabilite can be found in Chapter 6.

Table 5.4 *k*-point testing results for mirabilite. Note that these simulations were carried out before any of the other tests had been performed and so the energies reported here are significantly different from the final energy values given in the next chapter.

Grid Geometry	Number of *k*-points	Energy (eV)	Energy per atom (eV per atom)
111	1	-751.361764	-5.0767687
222	2	-751.396900	-5.0770061
323	5	-751.3968909	-5.0770060
324	6	-751.3966915	-5.0770047
333	10	-751.396975	-5.0770066
434	16	-751.396948	-5.0770064
444	16	-751.397015	-5.0770069

5.3.2 Simulations of Meridianiite, MS11.

Much of the technical detail of the simulation methods used for MS11 has already been described in depth for the simulations of mirabilite. The following sections describe where the MS11 calculations differ from the mirabilite calculations.

Structurally, MS11 is simpler than mirabilite in that it has fewer (78) atoms in the unit-cell and does not have any of the fractional occupancy or disorder of mirabilite. However, it is triclinic, a lower symmetry than mirabilite, which potentially makes it computationally more expensive as a larger *k*-point grid may be required to adequately represent it.

5.3.2.1 INCAR setup.

The INCAR file for MS11 (shown below) is broadly the same as for mirabilite; however, there are a couple of important changes. Firstly, NBANDS is reduced to 150; this is possible because there are fewer atoms in the unit-cell. The other changes are in the value of ENAUG, which is discussed below, and the inclusion of the EDIFF tag. EDIFF gives the order of magnitude of the error allowed in the total energy, i.e. it defines the convergence criteria of the simulation. In this case, the value of EDIFF has been decreased by an order of magnitude (which increases the accuracy by an order of magnitude), from the VASP default value to ensure sufficient accuracy in convergence.

NBANDS = 150
ENMAX = 800
ENAUG = 1200
ISIF = 4
IBRION = 2
NSW = 150
EDIFF=1E-5
LWAVE=.FALSE.
ALGO=FAST
LCHARGE=.FALSE.

ENMAX and ENAUG testing was carried out in the same manner as for mirabilite and again an ENMAX value of 800 eV was used. ENAUG for MS11 required a higher value, 1200 eV.

5.3.2.2 Testing of *k*-points.

k-point testing for MS11 again produced results showing only a very small difference for calculations using a different number of *k*-points. Table 5.5 shows the results of the *k*-point testing for MS11. In this case, there was a relatively large difference between the use of 1 kpt and 4 kpts; the latter was adopted in subsequent calculations. The results from the simulations of MS11 can be found in Chapter 7.

Table 5.5 *k*-point testing results for MS11.

Grid Geometry	Number of *k*-points	Energy (eV)	Energy per atom (eV per atom)
111	1	-403.069035	-5.167552
222	4	-403.606556	-5.174443
323	9	-403.607436	-5.174454
332	9	-403.607297	-5.174453
324	12	-403.608597	-5.174469
333	14	-403.603516	-5.174404
444	32	-403.601231	-5.174375

5.4 Obtaining an equation of state from the total energy of a system.

In Chapter 4 of this thesis, an isothermal equation of state, the 3rd order Birch-Murnaghan equation (3BMEOS; Birch, 1952) was applied to the pressure-volume data from the t-o-f neutron diffraction experiments described there. The 3BMEOS (equation 5.14), can also be fitted to the results of the *ab initio* simulations, by integrating it so as to obtain an energy-volume relation rather than a pressure-volume relation.

$$P_{V,T} = \frac{3}{2}K_{0,T}\left[\left(\frac{V_0}{V}\right)^{\frac{7}{3}} - \left(\frac{V_0}{V}\right)^{\frac{5}{3}}\right]\left\{1+\frac{3}{4}\left(K_0' - 4\right)\left[\left(\frac{V_0}{V}\right)^{\frac{2}{3}} - 1\right]\right\} \quad \textbf{Equation 5.14}$$

The First and Second laws of Thermodynamics tell us that:

$$P = -\left(\frac{\partial E}{\partial V}\right)_T \quad \textbf{Equation 5.15}$$

and so,

$$E = -\int P\partial V \quad \textbf{Equation 5.16}$$

The 3BMEOS can thus be integrated to give:

$$E = E_0 + \left(\frac{9}{4}\right)K_0V_0\left(\frac{V_0}{V}\right)\left[\frac{1}{2}\left(\frac{V_0}{V}\right)^{\frac{1}{3}} - \left(\frac{V}{V_0}\right)^{\frac{1}{3}}\right] \qquad \textbf{Equation 5.17}$$

$$+\left\{\left(\frac{9}{16}\right)K_0\left(K_0' - 4\right)V_0\left(\frac{V_0}{V}\right)\left[\left(\frac{V_0}{V}\right) - 3\left(\frac{V_0}{V}\right)^{\frac{1}{3}} + 3\left(\frac{V_0}{V}\right)^{\frac{1}{3}}\right]\right\}$$

$$-\left(\frac{9}{16}\right)K_0\left(K_0' - 6\right)V_0$$

Another EOS, the 4th order logarithmic equation of state (4LNEOS) (Poirier and Tarantola, 1998), has also been used, which was originally published in its integrated form:

$$E = E_0 + V_0\left[\frac{a\ln^2\left(\frac{V_0}{V}\right)}{2} + \frac{b\ln^3\left(\frac{V_0}{V}\right)}{3} + \frac{c\ln^4\left(\frac{V_0}{V}\right)}{4}\right] \qquad \textbf{Equation 5.18}$$

where:

$$a = K_{0,T} \qquad \textbf{Equation 5.19}$$

$$b = \frac{K_{0,T}\left(K_{0,T}' - 2\right)}{2} \qquad \textbf{Equation 5.20}$$

$$c = \frac{K_{0,T}^2K_{0,T}'' + \left(K_{0,T}' - 2\right)K_{0,T}\left(K_{0,T}' - 2\right)^2}{6} \qquad \textbf{Equation 5.21}$$

Summary

This chapter describes one of the ways in which quantum mechanics may be used to determine material properties. It summarises the application of density functional theory, implemented in the VASP program using the generalised gradient approximation and the projector augmented wave method. The particular setup and specifications of the two material simulations reported in Chapters 6 and 7 are set out and explained, as well as the post-processing of these simulations to produce equations of state.

Chapter 6

Ab initio calculations II:

Elastic properties and pressure-induced structural changes in mirabilite.

This chapter describes computer simulations of the behaviour of mirabilite as a function of pressure. The total energy of the mirabilite was calculated (athermally) using density functional theory methods (Hohenberg & Kohn, 1964; Kohn & Sham, 1965) implemented in the Vienna *Ab initio* Simulation Package, VASP (Kresse & Furthmüller, 1996) as described in Chapter 5. The chapter is arranged as follows: Section 2 describes the computational method, paying particular attention to how the disorder in the mirabilite crystal structure was handled within these static calculations; Section 3 reports the results and analysis of the calculations, Section 4 discusses the results and, finally, Section 5 summarises this study.

6.1 Simulations of the structure of mirabilite

The structural relaxations were begun using the atomic coordinates determined from neutron single-crystal diffraction analysis by Levy and Lisensky (1978), which were the most precise available at the time when the calculations were made. These calculations were carried out before the thermal expansion experiments of Chapter 3. Using these coordinates and cell parameters, the athermal simulations were begun by relaxing the crystal structure and cell parameters until a minimum energy was found with zero pressure on the unit cell; this point corresponded to a unit-cell volume of ~1470 $Å^3$. Starting from this structure, a series of relaxations were then performed with the unit-cell volumes fixed both at successively smaller and successively larger volumes; in each case the unit cell (subject to the constraint of fixed volume) and atomic coordinates were relaxed. With one exception (see Section 6.3), the simulations were performed stepwise, with the structure from the previous simulation used as the starting structure for the next.

6.2 The zero-pressure, zero-temperature structure of mirabilite.

Tables 6.1 and 6.2 report comparisons of the calculated bond lengths at zero-pressure in the athermal limit with the experimentally observed bond lengths in mirabilite at atmospheric pressure and 4.2 K (From Chapter 3). It should be noted, however, that the difficulty of the neutron powder refinement (with respect to the large number of refined variables) required heavy bond-length restraints on S-O and O-D bond lengths and angles (see Chapter 3 for a full discussion of the refinement process) which will bias the experimental values. Table 6.1 shows that both the calculated S-O bond lengths, and the Na-O bond lengths (with two exceptions), are systematically 2-3 % longer than is observed experimentally. This means that the zero-pressure volume of the SO_4 tetrahedron, 1.7358(5) $Å^3$, is 7.0 % greater than the

experimental value. Similarly, the volumes of the Na2 and Na3 octahedra, 21.17(7) $Å^3$ and 22.0(2) $Å^3$ respectively, are 6.9 % and 10.5 % greater than the equivalent experimental volumes. Indeed, of the 31.8 $Å^3$ difference between the experimental and DFT unit-cell volume, fully 43 % is due to over-inflation of the NaO_6 octahedra, and just 1.4 % is due to over-inflation of the SO_4 tetrahedra.

Table 6.1 Comparison of the S-O and Na-O bond lengths (in Å) of the ambient-pressure phase of mirabilite obtained computationally with the experimental values from the deuterated isotopomer at 4.2 K (Chapter 3).

	Experimental at 4.2 K	DFT calculations at 0k, 0 GPa.	Difference (%)
S-O4	1.466(2)	1.5060(2)	2.7(1)
S-O5	1.467(2)	1.5015(2)	2.4(1)
S-O6	1.469(2)	1.5017(2)	2.2(1)
S-O7	1.468(2)	1.4952(3)	1.9(1)
Na2-O12	2.433(9)	2.479(3)	1.9(4)
Na2-O13	2.409(9)	2.470(2)	2.5(4)
Na2-O14	2.403(9)	2.393(2)	-0.4(4)
Na2-O15	2.378(9)	2.414(3)	1.5(4)
Na2-O16	2.429(9)	2.513(2)	3.5(4)
Na2-O17	2.390(9)	2.461(2)	3.0(4)
Na3-O8	2.386(8)	2.437(1)	2.1(3)
Na3-O9	2.369(8)	2.422(1)	2.2(3)
Na3-O12	2.459(8)	2.466(1)	0.3(3)
Na3-O13	2.409(8)	2.485(2)	3.2(3)
Na3-O14	2.354(8)	2.420(2)	2.8(4)
Na3-O15	2.418(8)	2.481(2)	2.6(3)

	Covalent bond lengths, O-H(D)			**Hydrogen bond lengths, H(D)···O**			**Hydrogen bond angles ∠ O-H(D)···O**		
	Experiment	Calculation	Difference (%)	Experiment	Calculation	Difference (%)	Experiment	Calculation	Difference (%)
	O-D	O-H		D···O	H···O		∠ O-D···O	∠ O-H···O	
O8-H8b···O16	0.9897(21)	1.0048(1) (+)	1.5(2)	1.842(6)	1.705(1)	-7.4(3)	157.7(5)	171.0(2)	8.4(3)
O9-H9b···O17	0.9899(21)	1.0034(2) (+)	1.4(2)	1.786(6)	1.711(3)	-4.2(4)	168.8(6)	170.6(3)	1.1(4)
O16-H16b···O8	0.9886(21)	1.0005(2) (+)	0.6(2)	1.766(6)	1.726(3)	-2.3(4)	171.6(5)	160.8(2)	-6.3(3)
O17-H17b···O9	0.9924(21)	1.0072(1) (+)	0.2(2)	1.753(6)	1.678(1)	-4.3(3)	167.5(5)	169.9(2)	1.4(3)
O12-H12a···O10	0.9845(21)	0.9913(2)	0.7(2)	1.863(6)	1.835(2)	-1.5(3)	177.7(5)	178.9(2)	0.7(3)
O13-H13a···O11	0.9842(21)	0.9892(2)	0.5(2)	1.866(6)	1.880(3)	0.8(4)	177.0(5)	178.3(2)	0.7(3)
O14-H14a···O10	0.9876(21)	0.9937(2)	0.6(2)	1.802(6)	1.782(4)	-1.1(4)	168.1(4)	171.7(2)	2.1(3)
O15-H15b···O11	0.9865(21)	0.9939(2)	0.8(2)	1.829(6)	1.788(5)	-2.2(4)	166.5(4)	172.5(3)	3.6(3)
O10-H10a···O5	0.9864(21)	0.9903(2)	0.4(2)	1.839(5)	1.857(8)	-1.0(5)	170.4(4)	170.9(2)	0.3(3)
O10-H10b···O4	0.9836(21)	0.9885(2)	0.5(2)	1.849(5)	1.837(2)	-0.6(3)	170.2(4)	170.3(2)	0.1(3)
O11-H11a···O4	0.9856(21)	0.9887(2)	0.3(2)	1.848(5)	1.859(5)	0.6(4)	174.8(5)	176.8(2)	1.1(3)
O11-H11b···O6	0.9860(21)	0.9901(2)	0.4(2)	1.855(5)	1.862(6)	0.4(4)	165.9(4)	169.5(3)	2.2(3)
O9-H9a···O4	0.9851(21)	0.9893(2) (-)	0.4(2)	1.764(6)	1.753(5) *	-0.6(4)	174.8(4)	175.2(3)	0.2(3)
O8-H8a···O5	0.9845(21)	0.9876(2) (-)	0.3(2)	1.811(6)	1.804(6)	-0.4(5)	165.7(4)	166.7(1)	0.6(2)
O12-H12b···O5	0.9813(20)	0.9824(2) (-)	0.1(2)	1.946(5)	1.977(3)	1.6(3)	170.7(5)	170.7(3)	0.0(3)
O13-H13b···O6	0.9869(20)	0.9832(2) (-)	-0.4(2)	1.938(5)	1.937(5)	-0.1(4)	171.6(4)	172.9(1)	0.8(2)
O17-H17a···O6	0.9847(21)	0.9863(2) (-)	0.2(2)	1.941(6)	1.898(2)	-2.2(3)	170.5(5)	171.7(3)	0.7(3)
O14-H14b···O7	0.9901(21)	0.9862(2) (-)	-0.4(2)	1.828(5)	1.816(1)	-0.7(3)	168.3(5)	171.49(4)	1.9(3)
O15-H15a···O7	0.9892(21)	0.9849(2) (-)	-0.4(2)	1.825(5)	1.808(3) *	-1.0(3)	167.4(4)	167.2(1)	-0.1(2)
O16-H16a···O7	0.9850(21)	0.9855(2) (-)	0.0(2)	1.821(5)	1.828(7)	0.4(5)	165.4(5)	161.3(4)	-2.5(4)

Table 6.2 Comparison of the O-H(D) and H(D)-O bond lengths (in Å) of the ambient-pressure phase of mirabilite obtained computationally with the experimental values of the deuterated isotopomer at 4.2 K (Chapter 3). Note that these have been grouped as follows; hydrogen bonds involved in forming the square rings in the low-P phase (first four rows); hydrogen bonds donated to interstitial waters (rows 5 - 8); hydrogen bonds donated by interstitial waters (rows 9 - 12); all other hydrogen bonds, Na-coordinated waters donating to sulphate oxygens. In column 3, the symbol (+) indicates that the bond increases in length as a function of pressure, (-) denotes a decrease in length with pressure, and the absence of a symbol indicates a negligible change in length with pressure (see text for further discussion). In column 6, asterisks mark the two hydrogen bonds which are exceptionally stiff in comparison to all the others (see text).

In Table 6.2 the experimental and computational bond distances involving the hydrogen atoms are compared; it can be seen that, with the marked exception of the hydrogen bonds in the square rings (i.e. those involving H8b, H9b, H16b and H17b), the agreement between calculation and experiment is excellent. Covalent O-H bonds are generally longer by approximately 0.5 %; given the restraints employed in the neutron powder refinement, this difference is not considered to be significant. The calculated hydrogen bonds (H···O) are slightly stronger, resulting in bond lengths which, for the most part, are shorter by 0.5 to 2% than is observed experimentally. Nonetheless, the correlation between the calculated and experimental H···O bond lengths is high (excluding the square ring H···O bonds, the correlation coefficient = 0.935), showing that the pattern of hydrogen-bonding has been faithfully reproduced in spite of the lack of van der Waals contributions in the DFT approximation. This is supported by an examination of the hydrogen-bond angles (∠ O-H···O), reported in Table 6.5; with the exception of two outliers, both of which are involved in the square rings, and which differ by > 5 %, the correlation coefficient between the calculated and observed bond angles is 0.869. All but three of the H-bonds in the DFT structure are straighter than in the observed structure at 4.2 K (i.e., bond angles closer to 180°), with the differences in angle in the range 0 - 3.3 %. However, this difference in the bending of the H-bonds is not responsible for the remaining 55 % of the volume difference not already accommodated by over-inflated SO_4 and NaO_6 polyhedra. In fact, the straightening of the bonds is offset by the shortening of the H···O contact, resulting in calculated O—O distances which differ by barely 0.5 % from experiment.

The major difference between experiment and DFT calculation is found in the O-H and H···O bonds involved in the square rings. These O-H bonds are roughly 1.5 % longer than any of the other O-H bonds in the DFT structure, and the H···O bonds are significantly shorter. The difference in H···O bond length between experiment and calculation is also large (average 4.5 %). These differences are most likely due to the elimination of the partially ordered 'c' hydrogen sites in the structure; the orientational disorder of the O8/16 and O9/17 water molecules certainly contributes additional volume in the form of Bjerrum defects, and these are wholly lacking in the simulated structure. This difference between the observed and simulated structure also affects the behaviour under pressure, as described in the following section.

6.3 Possible phase transformations in mirabilite at high pressure

The total energy per unit-cell was calculated as described above at a series of fixed unit-cell volumes in the range $682 < V < 1810$ Å^3 ($0.78 < (V/V_0)^{1/3} < 1.08$); the corresponding pressure range is $61.0 > P > -2.7$ GPa. The volume dependence of the total energy, E(V), is shown in Figure 6.1. Clearly, there is a break in slope at $V \approx 1200$ Å^3 which is indicative of a phase transition. Closer inspection of this figure also reveals that for ~1080 Å^3 < V < ~1200 Å^3 the relationship between energy and volume is linear; since $P = -(\partial E/\partial V)_T$, this region is, therefore, isobaric, indicating that the phase transition must be first-order in nature, i.e. V(P) is discontinuous.

This first phase transition is more clearly seen in Figure 6.2, which shows the behaviour of the unit-cell volume as a function of pressure (the pressure values used were taken from the VASP output). The discontinuous nature of the phase transition means that the material would not exist in nature in the volume range from ~1080 Å^3 < V < ~1200 Å^3; the four simulations performed in this region thus correspond to transition states between low- and high-pressure phases. The transition pressure determined from the slope of the isobar on the E(V) curve is 5.7 ± 0.2 GPa, in fair agreement with the mean pressure from the four VASP outputs (7.7 ± 1 GPa).

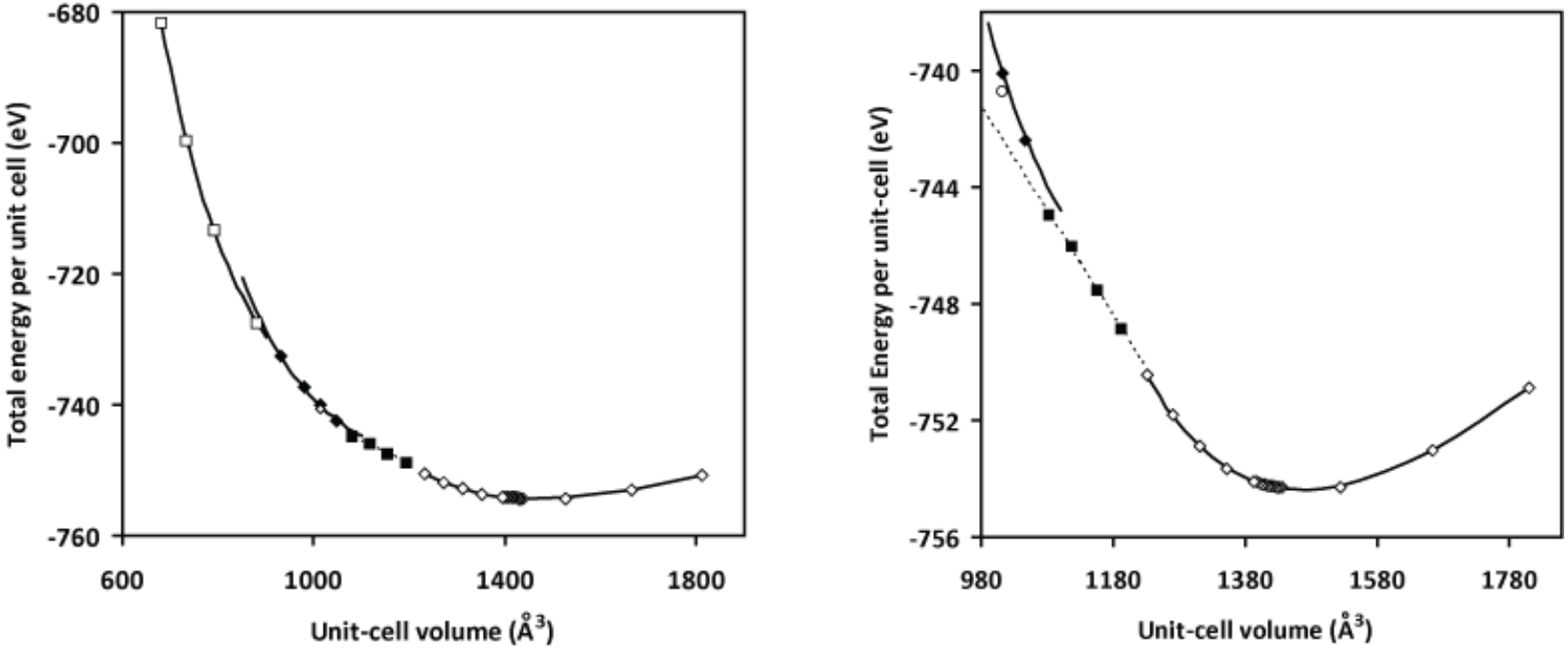

Figure 6.1 Total energy curves as a function of volume from *ab initio* calculations; panel (a) shows the entire range of volumes investigated, and panel (b) shows an expanded view of the low-pressure region. The ambient-pressure phase is represented by open diamonds and the highest-pressure phase by open squares; the intermediate-pressure phases are indicated by filled diamonds and open circles; the "transition region" is indicated by filled squares (see text). The solid lines shown are 3rd-order Birch Murnaghan EoS (see text). A 4th-order logarithmic EoS was also fitted to the low-pressure results but the two lines are indistinguishable in these figures. For ~1080 < V < ~1200 Å^3 the points lie on a straight line (shown as a dashed line in the figures) and are therefore isobaric (see text).

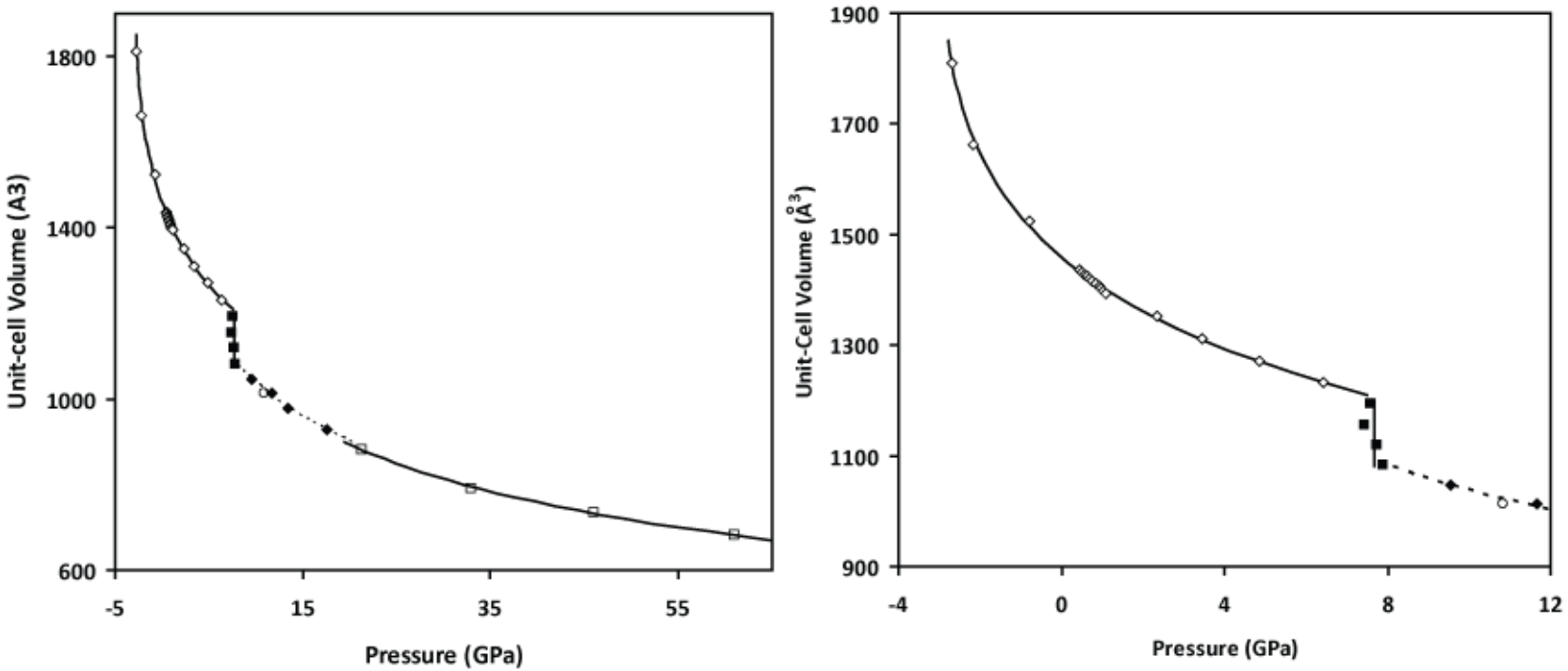

Figure 6.2 V(P) curves for mirabilite showing the full range of the calculations in (a) and an expanded view of the low-pressure region in (b). The ambient-pressure phase is represented by open diamonds and the highest-pressure phase by open squares; the intermediate-pressure phases are indicated by filled diamonds and open circles; the "transition region" is indicated by filled squares (see text). The pressure values shown are the VASP output pressures. The strongly discontinuous transition at ~7.7 GPa is indicated by a vertical line. The solid line shown for the low-pressure phase is a 3BMEOS fitted to P(V), i.e. to the VASP output pressures (V_0 = 1459.2(1) Å^3, K_0 = 23.4(3) GPa, K'_0 = 5.8(1)). For the high-pressure phases, 3BMEOS were fitted to the data (with K'_0 fixed at 5.8, the value for the low-pressure phase) to act as guides for the eye.

Examination of the pressure dependence of the individual unit-cell parameters, shown in Figure 6.3, however, strongly suggests that a further first-order phase transition occurs at a pressure between 15 and 20 GPa. This transition is most clearly seen in the behaviour of the monoclinic angle, β (Figure 6.3d), which takes a value of ~108° in the ambient pressure phase; at the first phase transition (P ~7.7 GPa on Figure 6.3d) β falls discontinuously to ~99° and at the second transition, which occurs between 18 GPa and 21 GPa, there is a further drop to ~92°. A similar large discontinuous reduction (of ~0.6 Å) is observed in the *a*-axis between 18 and 21 GPa, following a drop of ~0.75 Å at the first phase transition. The *b*-axis shows a discontinuous increase of about 0.05 Å at the lower-pressure transition and 0.15 Å at the higher one, whereas the *c*-axis shrinks by ~1.3 Å at the first transition but shows little, if any, discontinuity at the second. The combined effect of these changes in the cell parameters is such that no obvious discontinuity in the unit-cell volume is apparent.

Analysis of the relaxed atomic coordinates using the computer program "Endeavour" (Putz *et al.*, 1999) indicated that the structures at ~13.4 GPa (intermediate phase) and 61 GPa (high-pressure phase) both retain the $P2_1/c$ symmetry of the ambient-pressure phase of mirabilite. This is unexpected as there is no requirement for the VASP simulations to adopt any particular space-group. This is discussed further in Section 6.7.3, below, which describes the details of the major structural re-organisations that occur at high pressure.

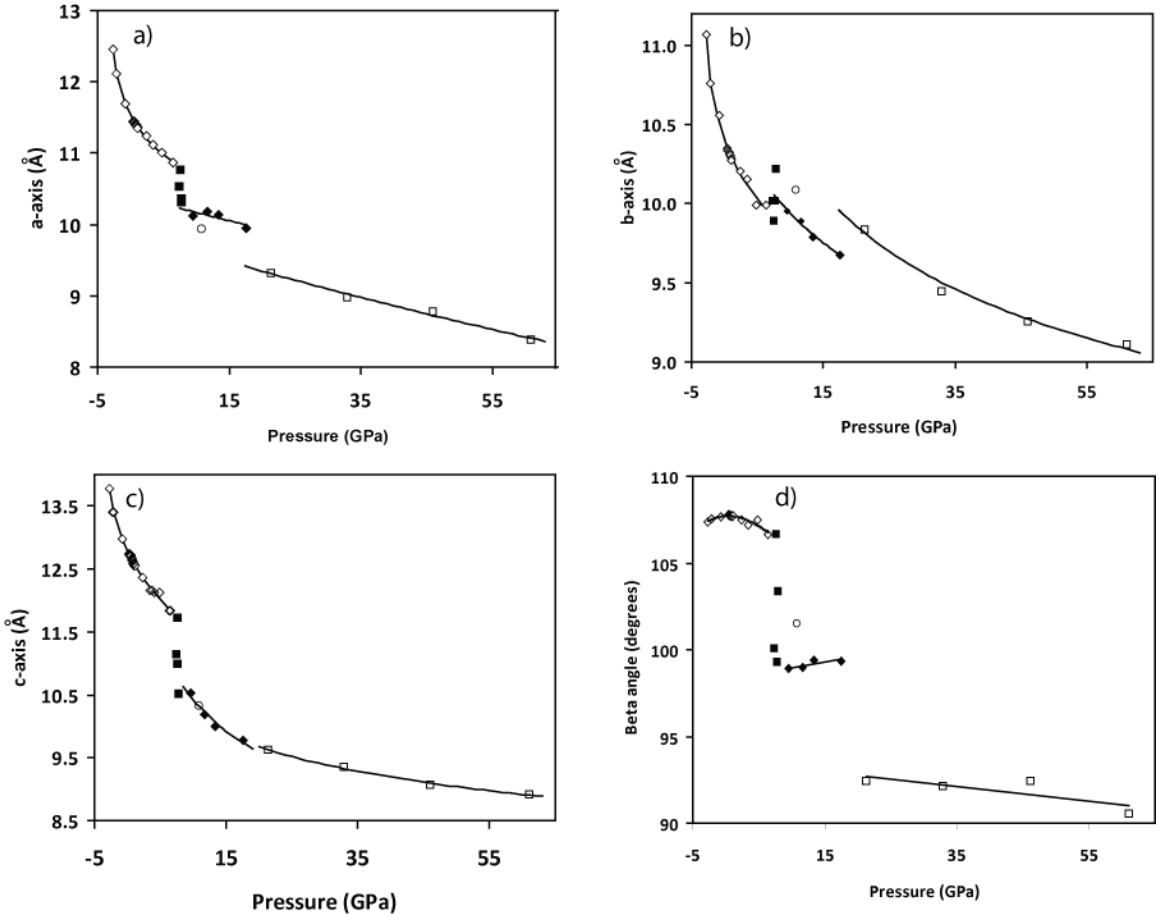

Figure 6.3 Calculated unit-cell axes of mirabilite as a function of pressure. The ambient-pressure phase is represented by open diamonds and the highest-pressure phase by open squares; the intermediate-pressure phases are indicated by filled diamonds and open circles; the "transition region" is indicated by filled squares (see text). For the low-pressure phase, the solid lines shown are 3rd-order Birch-Murnaghan EoS fits to the cubes of the unit-cell axes (with a 3rd-order polynomial fit for β). For the high-pressure phases the lines shown correspond to Murnaghan integrated linear equations of state (with a linear expression for β); in the intermediate-pressure phase the value of K'_0 for the a-axis was arbitrarily fixed at that found for the c-axis to prevent the fit converging to physically meaningless values.

These calculations also suggest that there may be a second stable, or metastable, phase of mirabilite in the pressure range from 8 GPa to 21 GPa. In Figure 6.1, it can be seen that two data points, having different energies, are shown for a unit-cell volume of 1012.8 $Å^3$. The point indicated by a "filled diamond" was obtained by relaxing the structure starting from the point at higher volume immediately preceding it; the point indicated by the "open circle" was obtained by relaxing the structure with next-lower volume (the three other points plotted in this region were all obtained by relaxing the structure from a higher volume). Examination of the SO_4 polyhedral volume of these two relaxed structures clearly shows that they have different hydrogen bond schemes (see Section 6.7.1 below). However, the difference in internal energy between them is very small, ~ 4 meV $atom^{-1}$ (the enthalpy difference is ~39 meV $atom^{-1}$) and, although the data point marked by a "open circle" is of

marginally lower internal energy and enthalpy, all of the other VASP simulations in this volume range converged to the structure marked by the "filled diamonds". The values of the unit-cell volume and cell parameters for this second intermediate-pressure phase have been included in Figures 6.2 and 6.3 (marked by an "open circle") and its crystal structure is discussed in Section 6.7.3; however, no attempt has been made to further investigate its stability field; the reasons for this are discussed in Section 6.8.

6.4 The equation of state of the low-pressure phase of mirabilite.

The E(V) values shown in Figure 6.1 for the low-pressure phase were fitted with an integrated form of the third-order Birch-Murnaghan equation of state (Birch, 1952; referred to as 3BMEOS; see Chapter 5 for details) and an integrated form of the 4th-order logarithmic equation of state (Poirier & Tarantola, 1998; referred to as 4LNEOS). Both equations were fitted to E(V) values in the range $1231.78 < V < 1810.61$ Å^3, $(0.95 < (V/V_0)^{1/3} < 1.08)$. As expected, the E(V) curves are very flat, so the parameters obtained from these fits exhibit greater uncertainties than those obtained in earlier work on smaller systems with higher symmetry. The fitted parameters are given in Table 6.1; note the agreement in all of the parameters for the low-pressure phase between 3BMEOS3 and 4LNEOS4. The value for the second pressure derivative of the incompressibility, $(\partial^2 K/\partial P^2)_0$ or K_0'', for the 3BMEOS given in Table 6.3 was calculated from:

$$K_0'' = \frac{K_0' / K_0}{(7 - K_0')} - \frac{(143/24)}{(8/3K_0)} \qquad \textbf{Equation 6.1}$$

The E(V) curve shown in Figure 6.1 is that for the 3BMEOS; the two equations of state are indistinguishable to the eye in this Figure.

	Low pressure phase 3BMEOS	Low pressure phase 4LNEOS
V_0 (Å^3)	1468.6(9)	1468.4(8)
E_0 (eV per unit cell)	-754.374(5)	-754.370(5)
K_0 (GPa)	22.21(9)	21.7(3)
K'	5.6(1)	5.9(2)
K" (GPa^{-1})	*-0.37(2)**	0.0(2)

Table 6.3 Parameters obtained by least-squares fitting of the 3rd-order Birch-Murnaghan equation of state (3BMEOS), and the 4th-order logarithmic equation of state (4LNEOS), to the E(V) curve of the low-pressure phase of mirabilite (unit-cell volume range: 1231.78 < V < 1810.61 Å^3).
*Derived from K_0 and K' - see text.

The method described above will give the most reliable equation of state parameters and the hence best estimate of V(P) for the low-pressure phase of mirabilite. The pressure-volume curves shown in Figure 6.2, however, were plotted using the VASP output pressures, so as to keep a common pressure scale for the full range of the simulations; the line for the 3BMEOS given in Figure 6.2 was, therefore, obtained by fitting the P(V) values shown in the Figure directly (the fitted parameters, which differ slightly from those shown in Table 6.1 are listed in the Figure caption).

The unit-cell volume and the cell parameters corresponding to the calculated V_0 are compared with the experimental values measured at 4.2 K using neutron powder diffraction (from Chapter 3) in Table 6.4. The agreement between the DFT values and the experimental values is very good, and comparable with much of the earlier work on hydrogen-bonded solids (see Chapter 1). The difference in volume ($\Delta V/V \approx 2.2$ %) corresponds to a difference in pressure of only 0.51(1) GPa, which is small, both in absolute terms and relative to the incompressibility of the material.

	Experimental at 4.2 K		DFT calculations at 0 K	Difference (%)
V (Å^3)	1436.794(8)	V_0 (Å^3)	1468.6(9)	2.21(6)
a (Å)	11.44214(4)	a_O (Å)	11.539(2)	0.85(3)
b (Å)	10.34276(4)	b_O (Å)	10.415(8)	0.70(8)
c (Å)	12.75468(6)	c_O (Å)	12.828(11)	0.57(8)
β(°)	107.847(1)	β_O(°)	107.74(3)	-0.10(3)
b/a	0.903918(5)	b_O/a_O	0.9026(7)	-0.14(8)
c/a	1.114711(7)	c_O/a_O	1.1120(10)	-0.27(9)
b/c	0.810899(5)	b_O/c_O	0.8119(9)	0.13(11)

Table 6.4 Comparison of the unit-cell dimensions and axial ratios of the ambient-pressure phase of mirabilite obtained computationally with the experimental values of the deuterated isotopomer at 4.2 K (from Chapter 3). The computational V_0 is from the 3BMEOS fit to the E(V) curve (see Table 6.1), and the cell parameters are from independent 3BMEOS fits to the relaxed unit-cell dimensions as a function of the EoS-derived pressure scale (axial K and K' from these fits are cited in the text), with β taken from a 3rd-order polynomial fit; note that the computational unit-cell dimensions give V_0 = 1468(2) Å^3.

There are, as yet, no published experimental measurements of the incompressibility of mirabilite and so the only values with which these calculations can be compared are those presented in Chapter 4 of this thesis. The value of K_0 obtained from the VASP simulations, 22.21(9), is in very good agreement with the experimental value from the HRPD data at 80 K, 22.7(6), but the poor quality of the experimental data has prevented any comparison of the values of K_0'. It is interesting to note that the elastic moduli of mirabilite are remarkably similar to those found in recent experimental and *ab initio* studies of epsomite (for $MgSO_4 \cdot 7D_2O$ and $MgSO_4 \cdot 7H_2O$, respectively) by Fortes *et al.* (2006b). For epsomite, DFT calculations in the range $-2 < P < +6$ GPa give an incompressibility of $K_0 = 23.2(2)$ GPa, with $K'_0 = 5.3(2)$, in the athermal limit, whereas fits to neutron powder diffraction data in the range $0.01 < P < 0.55$ GPa at 50 K gave $K_0 = 24.9(8)$ GPa, with $K'_0 = 6(3)$, and at 290 K gave $K_0 = 21.5(4)$ GPa, with $K_0' = 6(1)$. Despite major differences in the structures of epsomite and mirabilite, they clearly have similar bulk elastic properties, both as a function of pressure and of temperature (see Chapter 3).

6.5 The equations of state of the high-pressure phases of mirabilite.

The instability at low pressures of the two proposed high-pressure phases of mirabilite prevents the calculation of the total energy of either of these phases in the region of their value of V_0. It has not, therefore, been possible reliably to fit their equations of state. For example, if the E(V) results for the highest-pressure phase (i.e. the four points for which $V <$ ~882 Å^3, $(V/V_0)^{1/3} < 0.85$) are fitted to an unconstrained 3BMEOS, the values $V_0 = 1460$ Å^3, $K_0 = 7.6$ GPa, $K_0' = 6.8$ and $E_0 = -746.9$ eV are obtained (no errors are given as the number of data points is equal to the number of fitted parameters); however, if K'_0 is fixed at the value obtained from the low-pressure phase ($K'_0 = 5.6$), very different values of V_0 =1333 (27) Å^3, $K_0 = 14.625(8)$ GPa, and $E_0 = -744.9(9)$ eV result. For the intermediate-pressure phase, the corresponding sets of values are $V_0 = 1461$ Å^3, $K_0 = 14.7$ GPa, $K'_0 = 4.2$ and $E_0 =$ -752 eV (free refinement), and $V_0 = 1334$ Å^3, $K_0 = 19$ GPa and $E_0 = -748.5$ eV (with $K'_0 =$ 5.6). Thus, no firm conclusions can be drawn as to the values of the 3BMEOS parameters. It is interesting to note, however, that for all of the fits described above, the values of V_0 obtained were less than the value of V_0 for the low-pressure phase, as one would expect of a more densely packed structure; also, the value for V_0 that is found with K_0' fixed at 5.6 is identical to that which is obtained by applying the relative volume change at the ~7.7 GPa phase transition to the value of V_0 for the low-P phase.

Since reliable equation of state parameters cannot be obtained for the high-pressure phases, the lines shown in Figure 6.2, which are fits to the 3BMEOS with K'_0 fixed at the value for the low-pressure phase (see Figure caption), should be considered as merely providing a method of smoothing the data for use in later analysis (see Section 6.6).

6.6. Derivation of the elastic strain tensor of mirabilite.

In the first instance, the unit-cell parameters of the low-pressure phase of mirabilite (Figure 6.3) were also fitted with 3rd-order Birch-Murnaghan expressions in order to obtain information about the axial incompressibilities. Referred to orthogonal axes, the zero-pressure axial incompressibilities and their first pressure derivatives were found to be, $K_{0a\sin\square}$ = 76(1) GPa, $K_0'_{a\sin\beta}$ = 17.9(5), K_{0b} = 92(4) GPa, $K_0'_b$ = 21(2), and K_{0c} = 55(2) GPa, $K_0'_c$ = 10.4(9), these incompressibility values being in good agreement with those found experimentally at 80 K (see Table 6.5).

	ab initio calculations			80 K experimental data from Chapter 4		
	a_{sinb}	b	c	a_{sinb}	b	c
a_0 (Å³)	10.99(1)	10.14(1)	12.83(2)	10.9090(1)	10.349(1)	12.756(3)
K_0 (GPa)	76(1)	92(4)	55(2)	75 (2)	83 (3)	54 (2)
K_0'	17.9(5)	21(2)	10.4(9)	15.9	15.9	15.9

Table 6.5 The axial compressibility of mirabilite from the *ab initio* calculations in comparison to experimental values at 80 K from Chapter 4.

As a further check, the zero-pressure bulk modulus was computed from the expression $K_0 = [(K_{0a\sin\beta})^{-1} + (K_{0b})^{-1} + (K_{0c})^{-1}]^{-1}$, giving a value of K_0 = 23.0(4) GPa, which is in fair agreement with that found earlier. It is surprising to find that the most compressible direction is along the *c*-axis; this is most likely due to the softness of the NaO_6 octahedra rather than any propensity to accommodate compression by folding at the shared hinges (see section 6.7.1).

This simple analysis of the elastic anisotropy does not reveal the changes in elastic behaviour brought about by the significant structural changes as a function of pressure. The relaxed unit-cell dimensions (Figure 6.3) were therefore used to determine the coefficients of the elastic strain tensor as a function of pressure using the method described by Hazen *et al.* (2000). The eigenvalues and eigenvectors of the strain tensor were obtained by matrix decomposition, yielding the magnitudes and orientations of the principal axes of the strain ellipsoid. The magnitudes of the principal axes are strains per unit stress, and are effectively

axial compressibilities; their sum is the bulk compressibility. The ellipsoid is constrained by the symmetry of the crystal to rotate only about the two-fold axis and the convention has been adopted that the principal strain axis $\mathbf{e_2}$ is parallel to the *b*-axis of the crystal.

Strains were calculated using the relaxed unit-cell dimensions directly output by VASP, and also using equations of state fitted to the same output. For the low-pressure unit-cell, it was possible to fit BMEOS3 expressions to the *a*-, *b*-, and *c*-axes, together with a 3rd- order polynomial to represent the behaviour of the monoclinic angle, β. Due to the limited number of high-pressure points, Murnaghan integrated linear equations of state (MILEOS, Equation 6.2) were fitted to the unit-cell axes of the two high-pressure phases, and linear expressions for the β-angle (see Figure 6.3 for details).

$$X = X_0 \left(\frac{K_0}{K_0 + K_0' P} \right)^{1/K_0'} \qquad \textbf{Equation 6.2}$$

The solid lines in Figure 6.4 are the strains obtained from the various EoS fits; only for the volumes are strains computed from the 'raw' VASP output shown, since the strains computed from the 'raw' unit-cell dimensions are very noisy. Also shown in Figure 6.4 is the angle between $\mathbf{e_3}$ and the crystallographic *c*-axis.

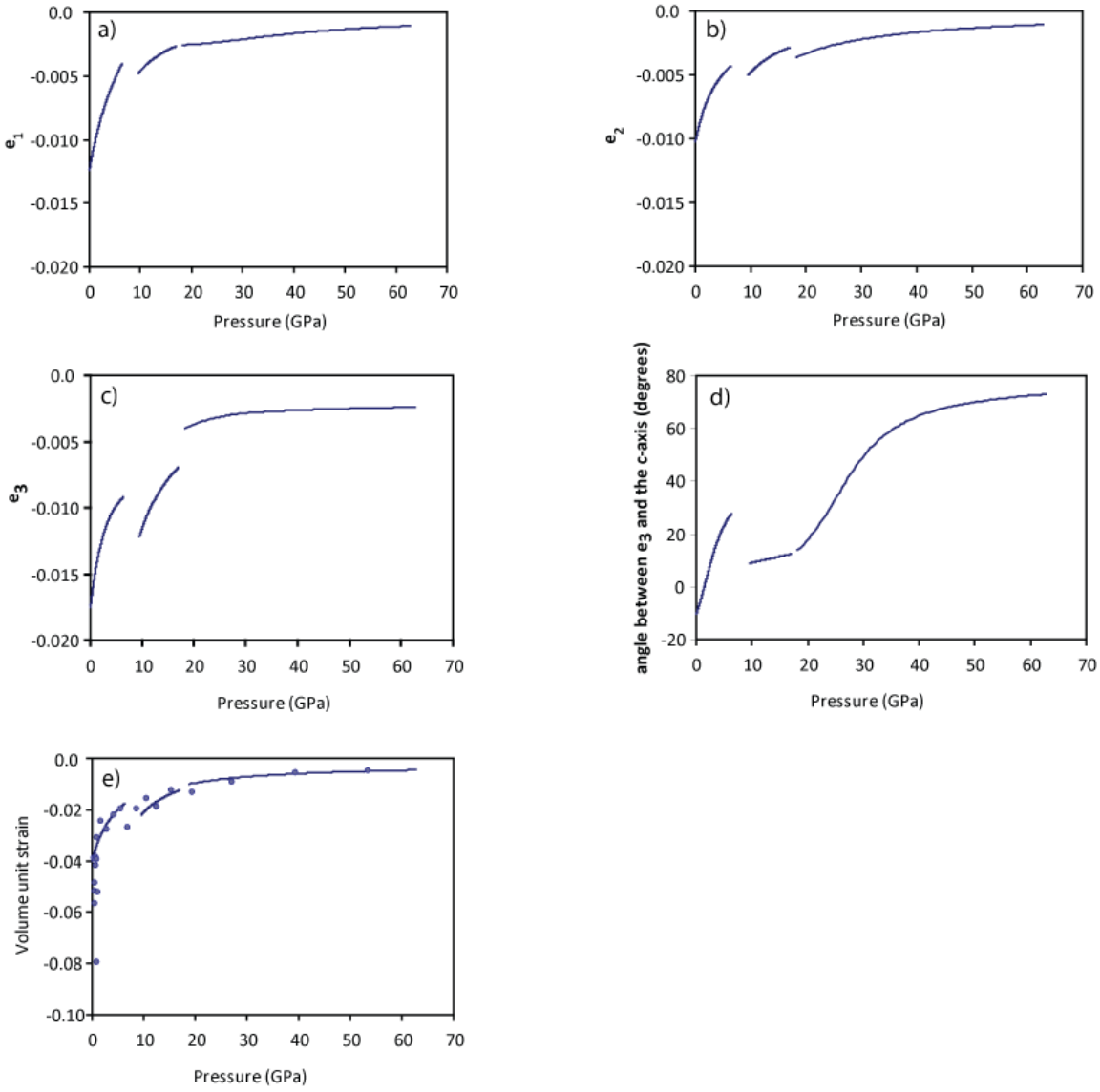

Figure 6.4 Panels (a) to (c) report the magnitudes of the principal axes of the strain tensor, e_1, e_2 and e_3 as a function of pressure (all on a common scale). The angle between e_3 and the crystallographic *c*-axis is shown in (d) and the volume compressibility is shown in (e).

Bearing in mind that the strain ellipsoid for the high-pressure phase is quite sensitive to the uncertainties in the EoS fitting, Figure 6.4 reveals significant discontinuities in all three principal axes. In each of the axes the three separate phases, low, intermediate and high pressures are clearly visible, with a smaller offset at the transition from intermediate to high pressure than from low to intermediate pressure phases.

The calculated volume strain per unit stress has been used to determine the pressure dependence of the bulk modulus for the low-pressure phase as the volume strain per unit stress is effectively $[K]^{-1}$; the values K_0 = 22.99(1) GPa, K_0' = 4.95(1), and K_0'' = -0.171(2) GPa^{-1} were obtained which agrees very well indeed with the EoS parameters reported in Table 6.1.

The orientation of the strain ellipsoid in the *a*-*c* plane changes considerably as a function of pressure (Figure 6.4e). At P = 0, $\mathbf{e_1}$ is closely aligned with the crystallographic *a*-axis, and $\mathbf{e_3}$ is consequently tilted ~10° from the *c*-axis towards the +ve *a*-axis. Under compression, the angle between $\mathbf{e_3}$ and the *c*-axis shrinks, passing through zero at ~ 1.2 GPa, and continuing to rotate through a further 23° with increasing pressure. At the transition, the ellipsoid 'slips' back, bringing $\mathbf{e_3}$ to near coincidence with the *c*-axis before rotating through ~ 10° until the transition to the high pressure structure, at which point the rate of rotation increases and the angle rapidly changes as $\mathbf{e_3}$ saturates at about 20^o from the *a*- axis.

It has not been possible to identify any single mechanism which might explain the rotation of the ellipsoid through ~35° from 0 - 7.5 GPa. There are very small rotations with respect to the crystallographic axes of various structural units (such as the SO_4 tetrahedra and the square H-bonded rings), but these amount to little more than ~3°. Furthermore, there is no evidence of rotation due to kinking of the Na-O chains along the shared hinges. The stiffening roughly along the *c*-axis is probably due to the expansion and stiffening of the Na-O polyhedra (see 6.7.1 below) whereas the softening roughly along the *a*-axis is likely due to a reduction in interlayer hydrogen bonding.

The following section reports the agreement between the simulated structure at zero-pressure and the experimentally observed structure, before going on to describe the pressure-dependent changes.

6.7. The Pressure dependence of the structural parameters

In the majority of crystal structures, the application of pressure results in shortening of interatomic and intermolecular bonds. However, in hydrogen-bonded crystals it is typical to observe lengthening of O-H bonds under pressure as the electron density in the hydrogen bond increases. In water ice this results in the hydrogen moving to a position midway between neighbouring oxygens at pressures of 60-70 GPa; this is the so-called bond-symmetric phase ice X. In many other hydrogen-bonded crystals however, proton transfer may occur, resulting in a partially or wholly ionic structure. It is therefore of interest to establish the pressure dependence of the various bond lengths in mirabilite.

6.7.1. The SO_4 and Na Coordination Polyhedra

3rd-order Birch-Murnaghan expressions have been fitted to the calculated volumes of the polyhedral units in the mirabilite structure as a function of pressure; these fits provide the zero-pressure volumes reported in Section 6.6, and the polyhedral bulk moduli. The SO_4 tetrahedron is comparatively stiff, with V_0 = 1.7358(5) Å^3, K_0 = 170(5) GPa, and K_0' = 17(3) in the low-pressure phase. When these values are compared to the DFT equation of state of the SO_4 tetrahedron in epsomite (Fortes *et al.*, 2006b), which has V_0 = 1.7374(7) Å^3, K_0 = 244(11) GPa, and K' = 25(8), it is apparent that the values of V_0 are in very close agreement; the only significant dissimilarity is in the stiffness, which is attributable to the disparity in electron density around the apical oxygens caused by the difference in the number of accepted hydrogen bonds - twelve in mirabilite and eight in epsomite. Thus, although the rate at which the SO_4 tetrahedron stiffens is structure dependent, the volume that it occupies at zero-pressure is insensitive to the crystal structure. This hypothesis is supported by the observation that when the number of hydrogen bonds donated to the SO_4 tetrahedron in mirabilite drops to nine following the first high-pressure phase transition at ~7.7 GPa, the volume of the SO_4 tetrahedron increases so that it is similar to that predicted by the equation of state of the epsomite SO_4 tetrahedron (Figure 6.5a). Moreover, at pressures above the second phase transition at ~19 GPa, when the number of H-bonds donated to the mirabilite SO_4 tetrahedron drops to seven and then to five there is a further expansion and stiffening (K_0 > 550 GPa, with V_0 fixed at 1.736 Å^3, see above), as shown in Figure 6.5b.

Figure 6.5 also reveals very clearly the difference in crystal structure between the two polymorphs found in the pressure range from ~7.7 to ~19 GPa. The majority of the data in this region correspond to structures with nine hydrogen bonds donated to the SO_4 tetrahedron, whereas the second polymorph, represented in Figures 6.1 - 6.3 by the single data point, has a structure in which ten hydrogen bonds are donated to the SO_4 tetrahedron.

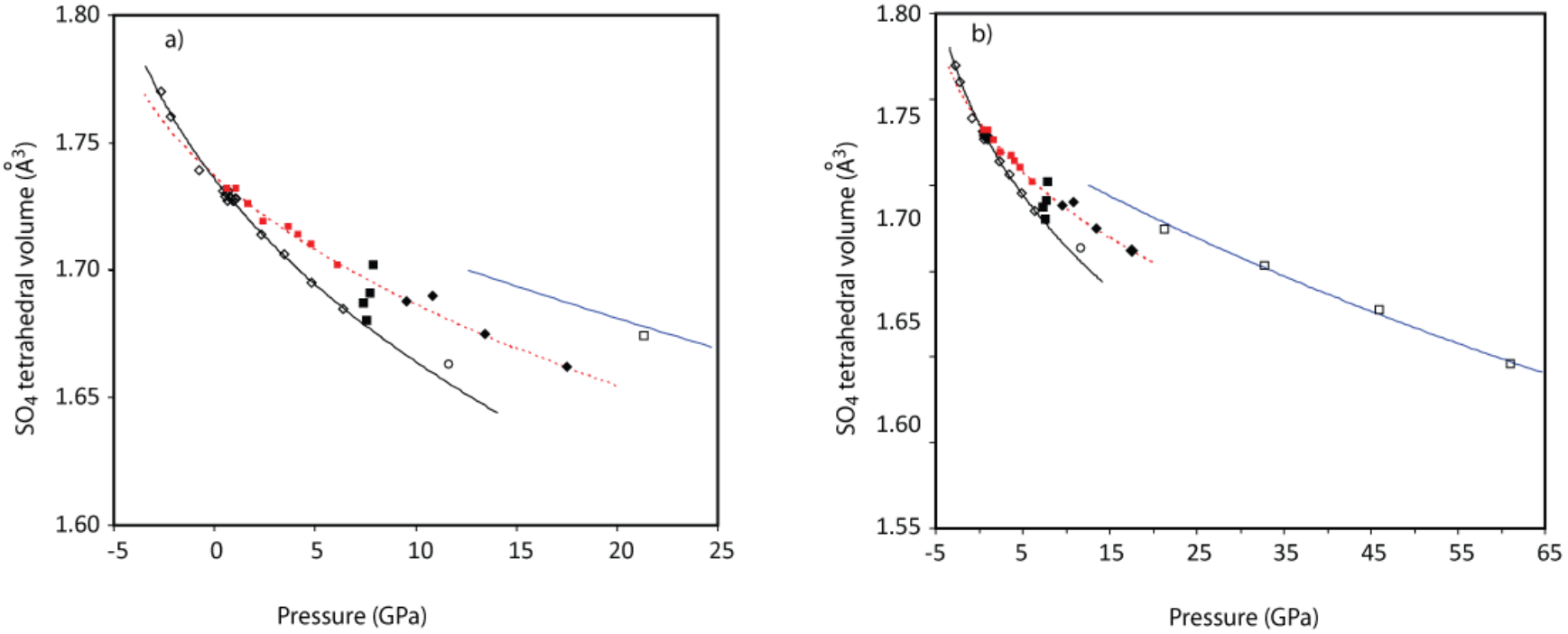

Figure 6.5(a) Sulphate tetrahedron volumes with increasing pressure for epsomite (red filled squares, Fortes *et al*., 2006b), and for mirabilite (this work); the symbols used for mirabilite are: open diamonds (low-pressure phase), filled squares (transition region), filled diamonds (intermediate-pressure phase), open circle (second intermediate-pressure phase), open squares (high-pressure phase). The lone point denoted by the open circle is the "odd" point where the calculation was not carried out step-wise (see text). The solid lines are 3BMEOS fits to the SO_4 volumes in mirabilite for the low-pressure and high-pressure phases, and the dashed line is a 3BMEOS fit to the SO_4 volumes in epsomite.
(b) Variation of the SO_4 volume in mirabilite over the entire pressure range simulated. The solid black line and the dashed line are the same as in panel (a). The solid blue line at higher pressure is a 3BMEOS fit to the four values above 20 GPa with V_0 fixed equal to 1.736 $Å^3$ (for details see text

Similar changes are observed in the NaO_6 octahedra under compression. In the low-pressure phase, the Na2 octahedron has 3BMEOS3 parameters V_0 = 21.17(7) Å^3, K_0 = 19(2) GPa and K_0' = 5.6(9), while the Na3 octahedron has 3BMEOS parameters V_0 = 22.0(2) Å^3, K_0 = 14(3) GPa and K_0' = 4.4(11). The NaO_6 octahedra are roughly an order of magnitude softer than the SO_4 tetrahedra and indeed are more compressible than the bulk crystal. The only literature reporting the polyhedral bulk modulus of NaO_6 octahedra pertains to the sodium-bearing clinopyroxenes aegirine and jadeite, where Na^+ is coordinated by O^{2-}, rather than by neutral H_2O; these have bulk moduli of ~67 GPa and ~70 GPa, respectively (McCarthy, 2007). Interestingly, in both of these minerals, the NaO_6 octahedra are also more compressible than the bulk crystal. However, by applying the theoretical relationship of Hazen & Finger (1979), it is possible to make an estimate of the expected incompressibilities of the NaO_6 octahedra in mirabilite from the incompressibility of the MgO_6 octahedron in epsomite, which has a value of 52(2) GPa (Fortes *et al.,* 2006b). The ratio of the bulk moduli is simply:

$$\frac{K_{Na-O}^{mirabilite}}{K_{Mg-O}^{epsomite}} = \frac{z_{Na}}{z_{Mg}} \cdot \frac{\langle Mg-O \rangle^3}{\langle Na-O \rangle^3} \qquad \textbf{Equation 6.3}$$

where z_{Na} and z_{Mg} are the formal charges on the ions (+1 and +2, respectively), and ⟨Mg-O⟩ and ⟨Na-O⟩ are the average cation—anion distances in the polyhedra (2.090 Å and 2.454 Å, respectively). Hazen & Finger (1979) observe that the connectivity (i.e., isolated polyhedra vs. edge-sharing or face-sharing) does not affect the validity of the relationship. Using Equation 6.3 the ratio of the bulk moduli is 0.309 and therefore the predicted incompressibility of the NaO_6 octahedra in mirabilite in the low-pressure phase is 16 GPa, in excellent agreement with the *ab initio* calculations. Analysis of the angles between opposing plane faces on the shared hinges reveals that these are extremely stiff, permitting no more than 0.3° GPa^{-1} of tilt between adjacent octahedra in the low-P phase. Hence, in this phase, it is solely the *compression* of these octahedra that is responsible for the softness of the *c*-axis rather than tilting along shared hinges.

As described below, the transitions to the high-pressure phases are characterised primarily by a change in sodium coordination, which finally changes the NaO_6 octahedra into NaO_7 decahedra, whereupon the volume of these polyhedra increases from ~17 Å^3 to ~35 Å^3, with a consequent stiffening of the polyhedral bulk modulus (see section 6.7.3).

6.7.2 The behaviour of bonds involving H atoms in the low-pressure phase.

In the low-pressure phase, the O-H bonds respond to pressure in one of three ways. One group of bonds shrinks at a rate of -1×10^{-3} Å GPa^{-1}; a second group expands at a rate of 1.5 - 2.0×10^{-3} Å GPa^{-1}; and a third group exhibits a negligible change in length (10^{-4}-10^{-5} Å GPa^{-1}). In Table 6.4, the first group are marked (-), the second are marked (+), and the third have no extra mark. It is very clear that all of the O-H bonds which increase in length occur in the square rings (O8/16 and O9/17), and all of the O-H bonds which are insensitive to pressure either donate H-bonds to interstitial waters, or form the interstitial waters (O10 and O11). The remainder of the H-bonds shrink under pressure, which is the opposite response to that observed in, for example, water ice. The O-H bonds in the square rings are notable for being longer than all of the other O-H bonds at zero-pressure and thus their donation of much shorter (and hence stronger) hydrogen bonds.

The pressure response of the hydrogen bonds themselves is quite interesting. If MILEOS expressions are fitted to the bond lengths to obtain their linear incompressibility ($K = x \cdot dP/dx$), it is found that there is no correlation between bond length and bond stiffness. Two H-bonds (marked by asterisks in Table 6.4) stand out as being exceptionally stiff (K_0 = 125-130 GPa) compared to the average ($K_0 = 35 \pm 12$ GPa excluding these two outliers), but it is not at all obvious why this should be so. The weakest H-bonds, with linear incompressibilities of 17-30 GPa, are those donated by the interstitial waters O10 and O11 to the sulphate oxygens O4, O5, and O6.

6.7.3 The high-pressure phases of mirabilite.

As described previously, the calculations reveal that mirabilite experiences two phase transformations at ~ 7.5 and ~ 20 GPa. In order to appreciate the complex structural changes which occur, structure maps illustrating the molecular connectivity are shown below for the low-pressure phase (Figure 6.6), the intermediate phase (Figure 6.7), the "odd point" described in Section 6.2 (Figure 6.8) and the high-pressure phase (Figures 6.9 and 6.10).

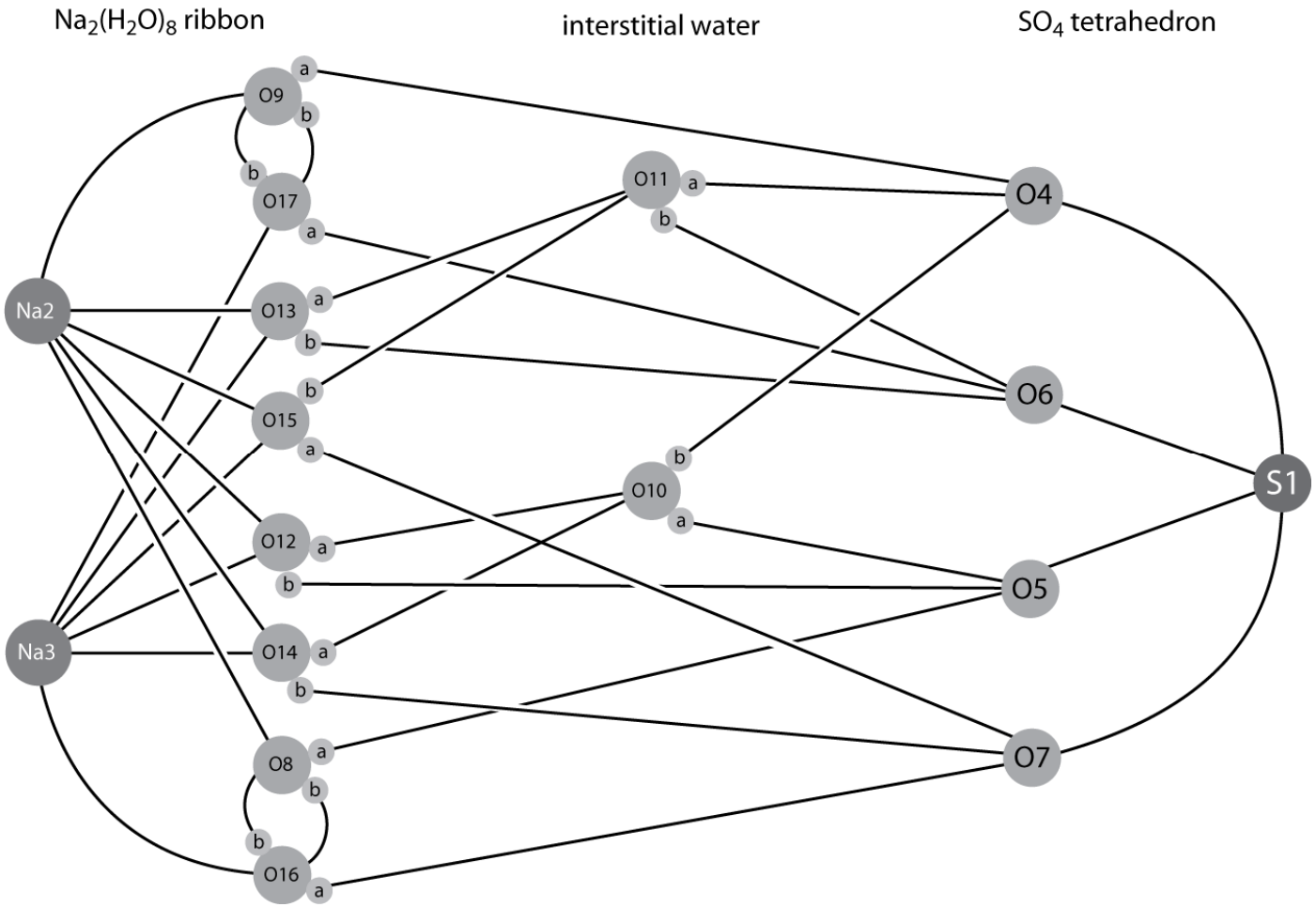

Figure 6.6 Connectivity map illustrating the relationship between structural elements in mirabilite at zero pressure; the hydrogen bond structure depicted corresponds to the full ordering of the 'b' sites attached to O9/17 and O8/16.

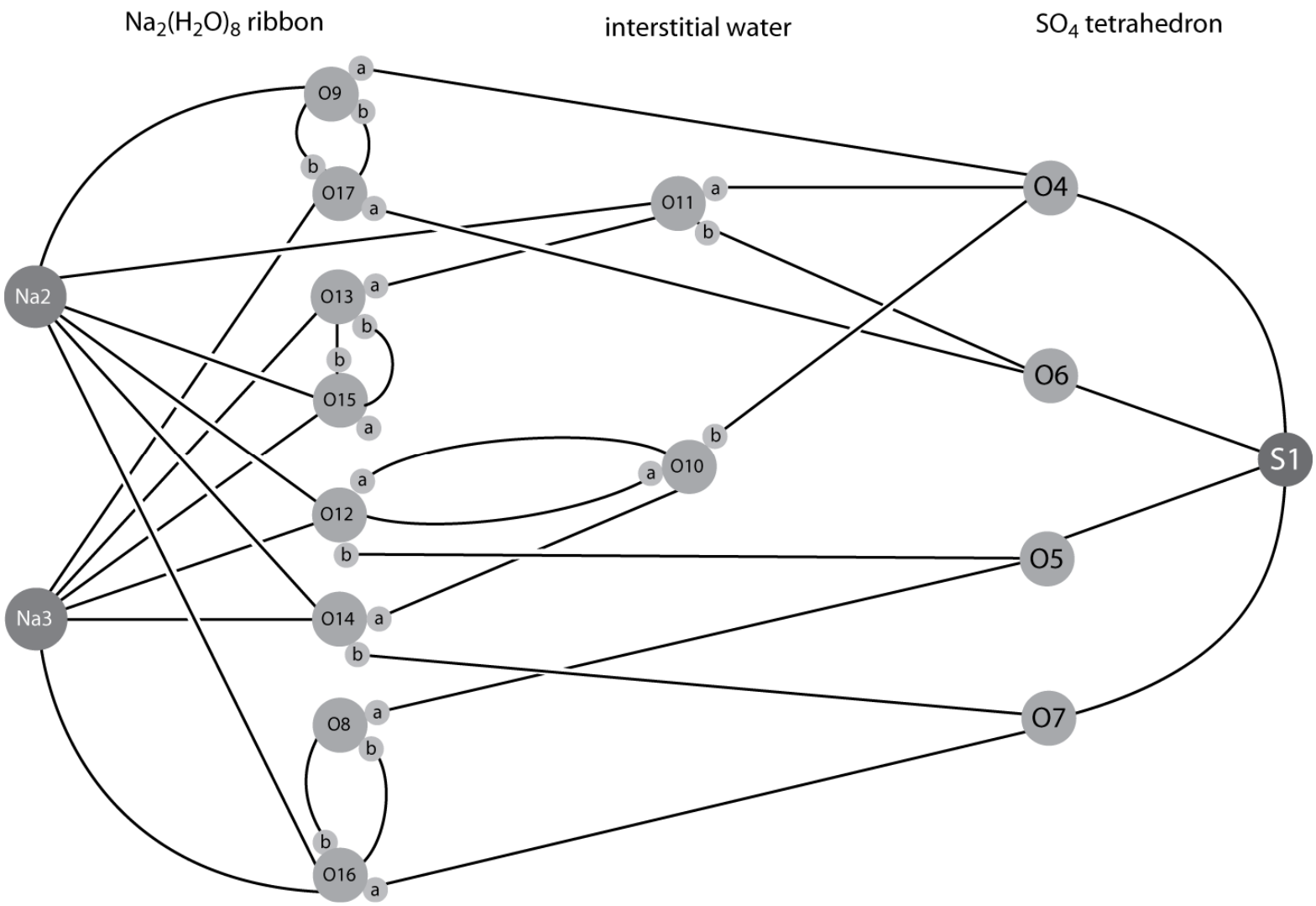

Figure 6.7 Connectivity map illustrating the relationship between structural elements in mirabilite at a pressure of 13.4 GPa.

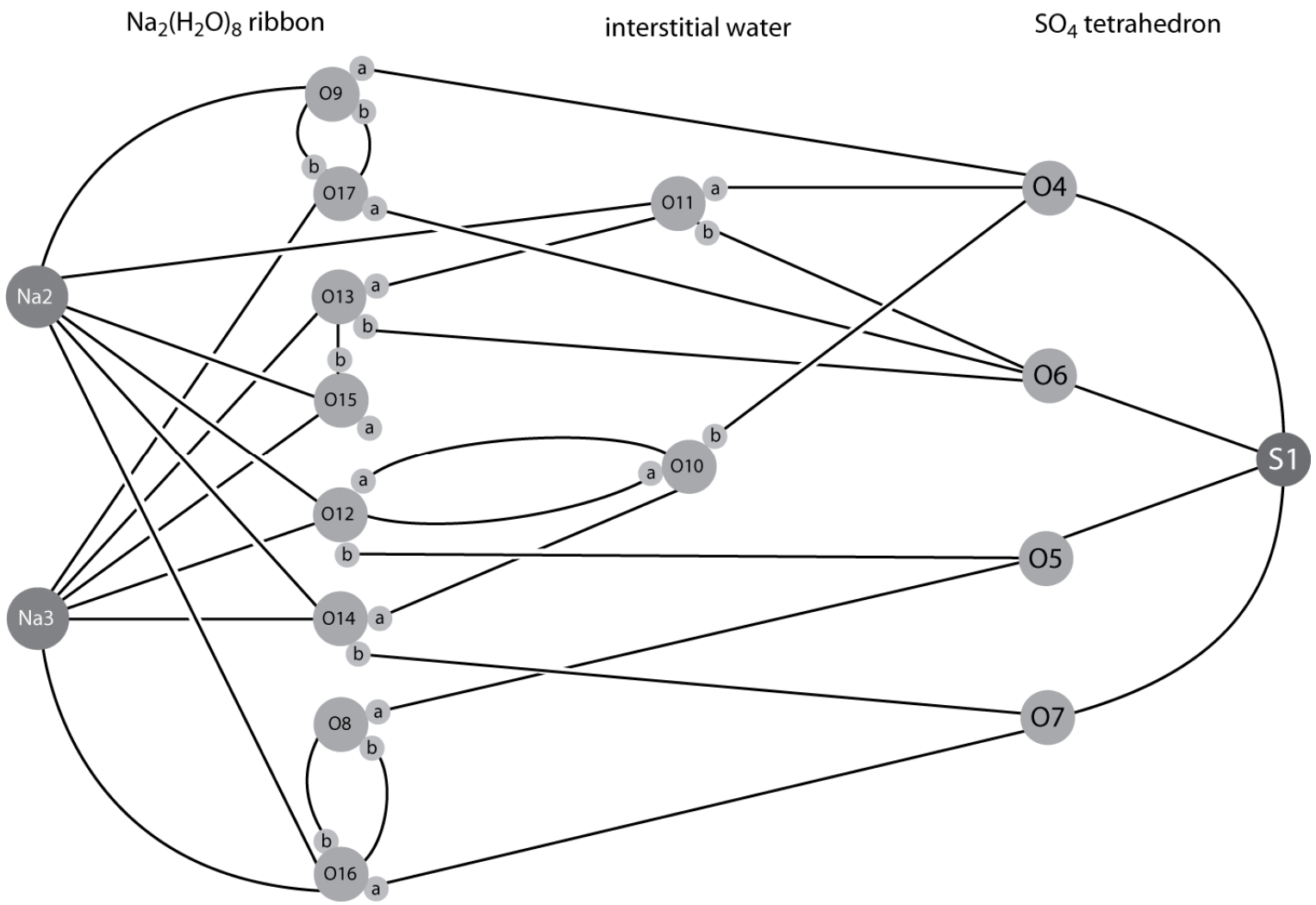

Figure 6.8 Connectivity map illustrating the relationship between structural elements in mirabilite in the second intermediate phase (the "odd point") at a pressure of 10.8 GPa.

The most notable structural changes at high pressure involve the ribbons of Na ions and their coordination polyhedra of water molecules. In the high-pressure phases these ribbons become more buckled; this buckling changes firstly the molecules that lie at the vertices of the coordination polyhedron of Na2 and then, at higher pressure, the number of vertices in both of the polyhedra. The changes that occur across the 7.5 GPa discontinuity are as follows. Although in both the low-pressure and intermediate pressure states the sodium atoms are coordinated to 6 oxygens in an octahedral arrangement, in the intermediate-pressure phase: the water molecule containing O16 now forms one of the vertices of the polyhedron around Na2 as well as that around Na3; the interstitial water molecule containing O11 moves closer to Na2 and forms another of the octahedral vertices; the water molecules containing O8 and O13 move further away (in the second intermediate phase - that represented by a single point on Figures 6.1- 6.3 - the same changes in the coordination of Na2 occur). In the high-pressure phase, above ~20 GPa, both of the sodium atoms are coordinated to 7 oxygen atoms in a decahedral arrangement; Na2 loses the molecules containing O11 and O16, replacing them with those containing O8 and O13 (as in the low-pressure phase), and, in addition, gains the water molecule containing O17; Na3 gains the water molecule containing O8. In the low- and intermediate-pressure phases the octahedra are edge-sharing, but at high pressures these polyhedra have a pair of shared faces, defined by planes joining O12-O15-O17 and O8-O13-O14.

To accommodate the coordination change around the sodium atoms, there must be a major reorganisation of the hydrogen-bond framework which forms the 'scaffolding' within which sits the $Na(H_2O)_8$ ribbons and the SO_4 tetrahedra. In the intermediate-pressure phases, the square rings involving O8 and O16, and O9 and O17 are preserved, but the transition to the high-pressure phase results in the destruction of the square ring involving O8 and O16, although the ring comprised of O9 and O17 is preserved. Despite the loss of the O8/16 ring, these molecules do form a new square ring (without the 2-fold rotation axis, clearly) involving O14 and the interstitial water molecule O10 (Figure 6.11). Another new square ring is also formed from a Na-coordinated water (O12) and an interstitial water (O10), with an axis of 2-fold rotational symmetry passing through its centre. Both O8/16 and O9/17 each swap one of their hydrogen atoms (as marked on Figure 6.11), which is in agreement with the observation that these are the only O-H bonds that increase in length as a function of pressure.

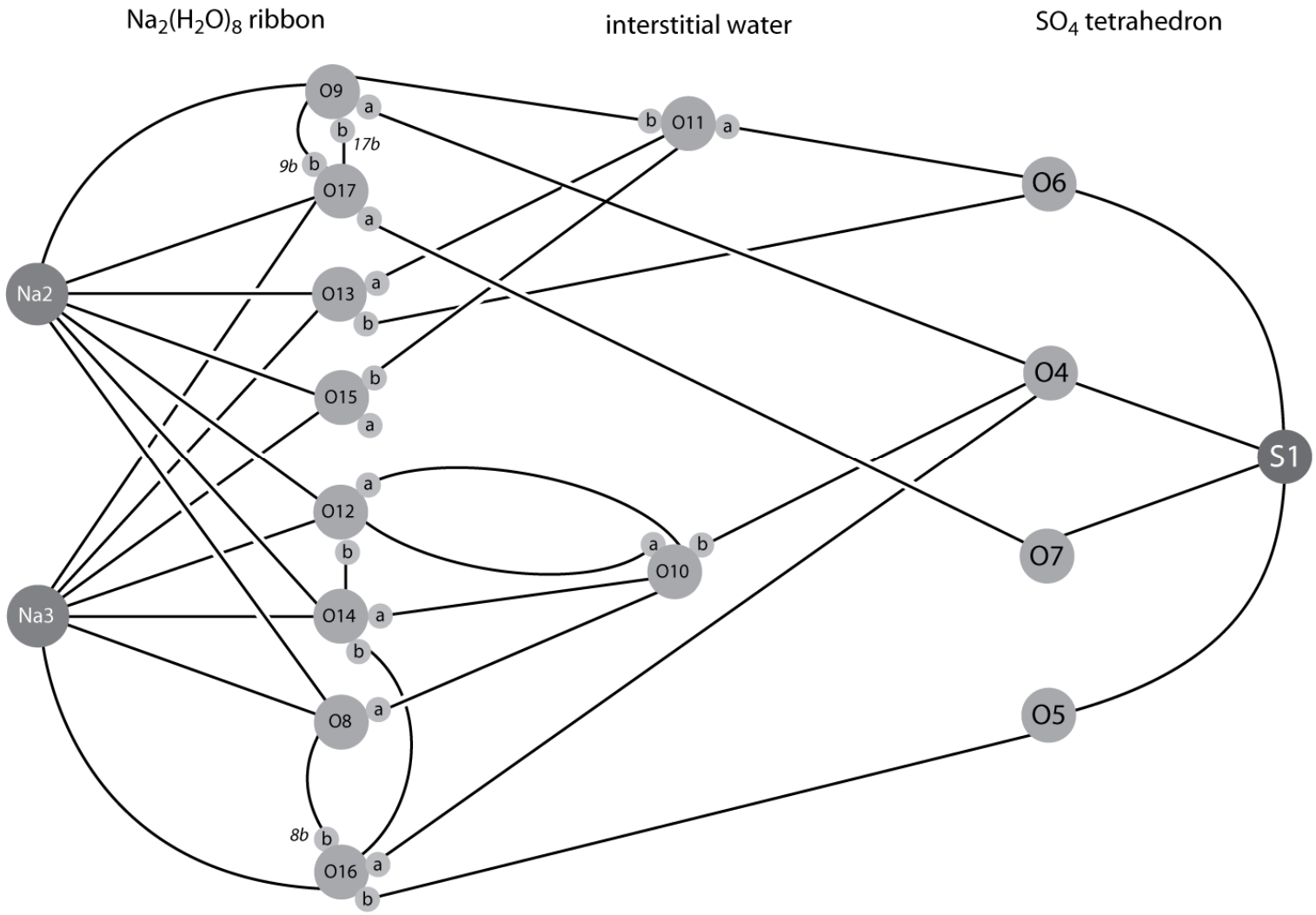

Figure 6.9 Connectivity map illustrating the relationship between structural elements in mirabilite at a pressure of 32.9 GPa. Note changes in the order of the sulphate oxygens with respect to Figure 6.7, and also the exchange of hydrogen atoms between O9/17 and O8/16.

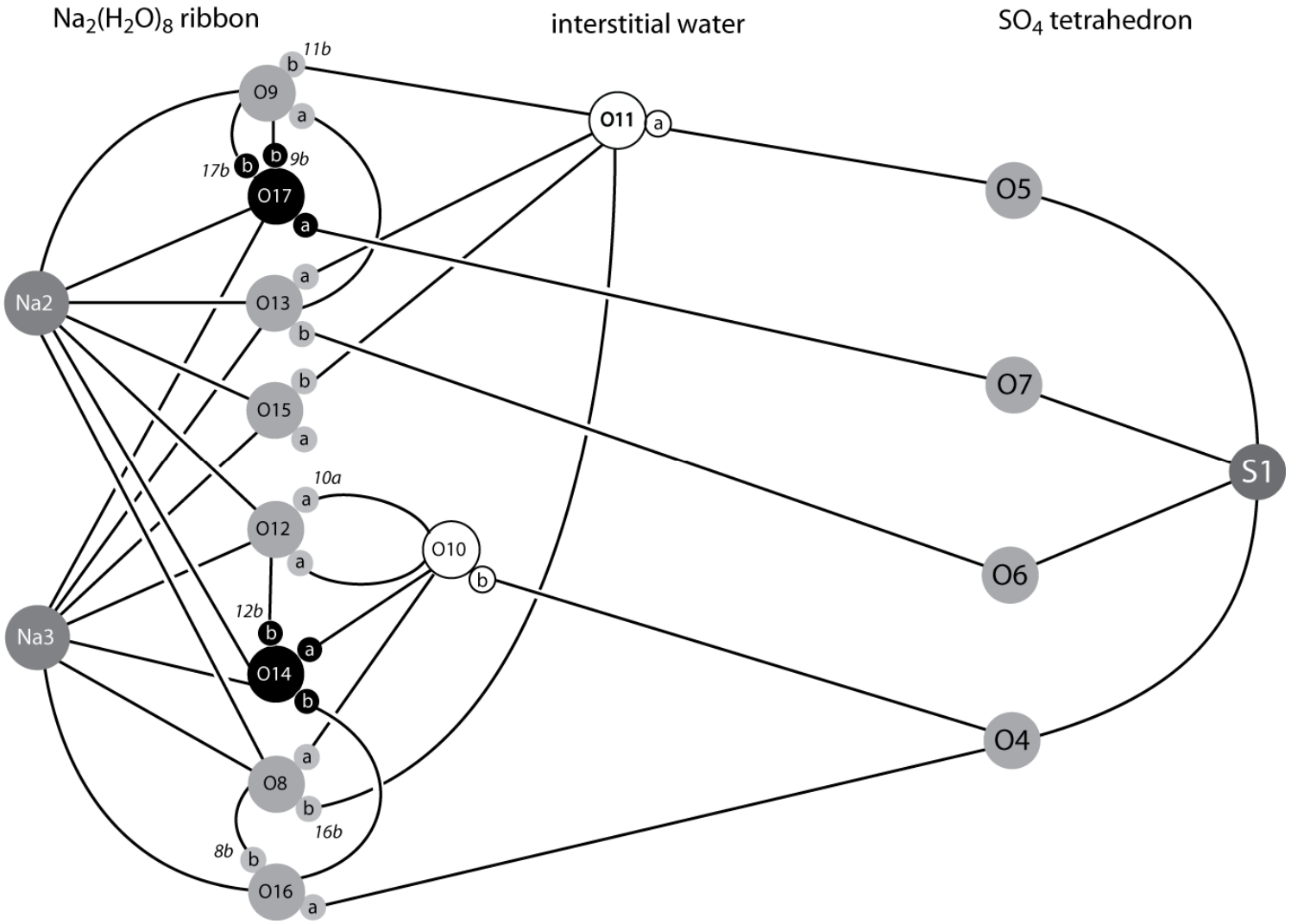

Figure 6.10 Connectivity map illustrating the relationship between structural elements in mirabilite at a pressure of 61 GPa. Note that the order of the sulphate oxygens differs again from Figures 6.7 – 6.99. The hydronium ions are marked with black circles, and the hydroxide ions with white circles.

The practical effect of this re-organisation is to concentrate hydrogen bonds around the $Na(H_2O)_8$ ribbon and to reduce the number of H-bonds donated to the sulphate tetrahedron, from 12 in the low-P phase to 9 in the intermediate-pressure phase (or 10 in the case of the second intermediate phase represented by a single point on Figures 6.1 – 6.3). In the high-P phase, this number is further reduced, initially to 7 (Figure 6.9) and then, with increasing pressure, to 5 (Figure 6.10).

Even after the hydrogen-bond network has been re-organised, further changes occur within the new network up to the highest pressures simulated (61 GPa), shown in the differences between Figures 6.9 and 6.10. There are continued changes in the relative strength of the hydrogen bonds resulting finally in a step-wise series of proton transfers from each of the two interstitial water molecules (O10 and O11) to neighbouring Na-coordinated water molecules (O14 and O17). The interstitial waters therefore become hydroxide (OH^-) ions, and the recipients of these protons become hydronium (H_3O^+) ions (Figure 6.10). Interestingly, for both O14 and O17, the donation process occurs via an intermediary; in the former, O10 donates H10a to O12, and then O12 loses H12b to O14; in the latter, O11 donates H11a to O9, and then O9 loses H9b to O17. This process also results in a further decrease in the number of H-bonds donated to the SO_4 unit to only five bonds at the highest pressures simulated. Notice that, of all the water molecules in the structure, only O13 and O15 retain their original hydrogen atoms at very high-pressure.

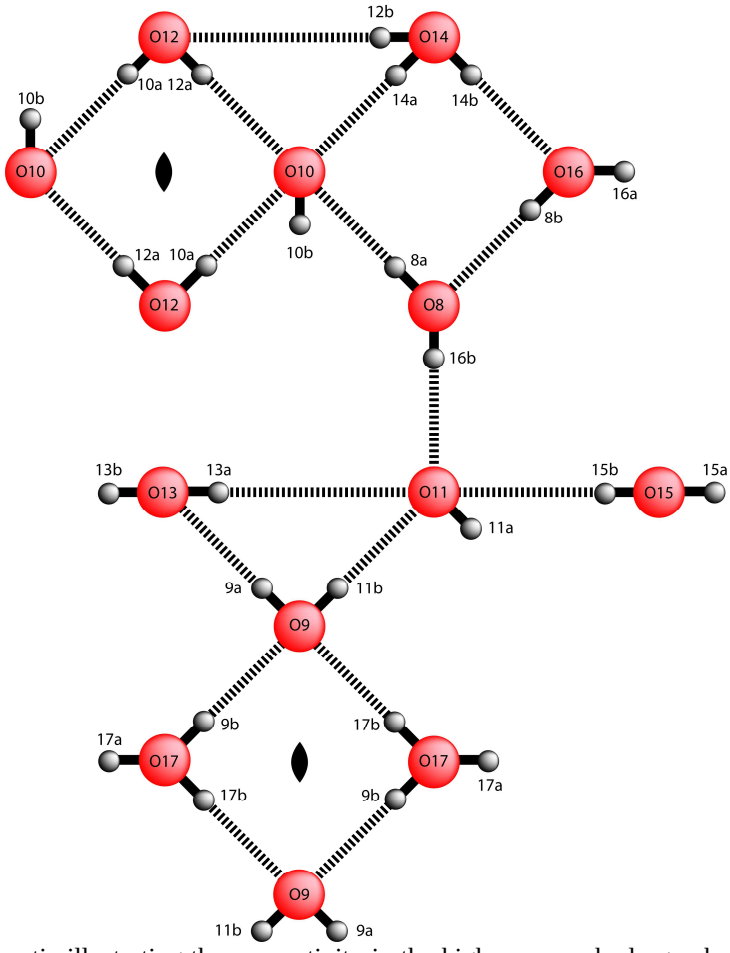

Figure 6.11 Schematic illustrating the connectivity in the high-pressure hydrogen-bond network into a series of three- and four-sided rings. This format elucidates some of the spatial relationships which are difficult to detect in structure maps such as Figure 6.9. Notice that hydronium O14 is directly H-bonded to the hydroxide ion O10 whereas hydronium O17 is not directly bonded to hydroxide O11.

Similar (albeit more direct) proton transfers have been seen in *ab initio* calculations of ammonia monohydrate (Fortes *et al.*, 2001), ammonia dihydrate and ammonia hemihydrate (Fortes, 2004). These findings have been confirmed computationally, and the occurrence of ionisation in solid ammonia demonstrated recently by Pickard and Needs (2008). It is not clear why the structure undergoes proton transfer rather than settling into a hydrogen-bond symmetric state, such as is observed in ice X. Possibly the longer range interactions perturb the otherwise symmetric potential well between neighbouring oxygens, such that a symmetric H-bond is not possible.

Previous computational studies have shown that in the gas phase the hydronium ion (H_3O^+) has a flattened trigonal structure with O-H bond lengths of 0.961 Å, and H-O-H angles of 114.7° (Hermida-Ramon & Karlström, 2004); in the high-pressure ionised form of mirabilite it can be seen that these ions experience considerable geometrical distortion (Table 6.6), this being greater for O14 than O17. The H···O hydrogen bonds donated by both H_3O^+ ions are significantly shorter (i.e., significantly stronger) than other H-bonds in the structure, and this results in the ion's O-H bonds being lengthened significantly above the average O-H bond length found in normal water molecules at the same pressure (1.0132 Å). This is in agreement with the general observation that H_3O^+ typically donates very strong H-bonds (Markovitch & Agmon, 2007). Hydronium ions are relatively common in low-pressure mineral structures, often substituting for Na^+ and K^+ ions, and well-known examples include the hydronium-bearing alunite- and jarosite-group minerals (e.g., Ripmeester *et al.*, 1986).

O14 hydronium geometry					
O14-H14a	1.0567 Å	H14a···O10	1.2775 Å	∠ H14a-O14-H14b	96.30°
O14-H14b	1.0815 Å	H14b···O16	1.2849 Å	∠ H14a-O14-H12a	109.49°
O14-H12a	1.0543 Å	H12a···O12	1.3136 Å	∠ H14b-O14-H12a	93.47°
O17 hydronium geometry					
O17-H17a	1.0256 Å	H17a···O7	1.3164 Å	∠ H17a-O17-H17b	103.44°
O17-H17b	1.0571 Å	H17b···O9	1.3934 Å	∠ H17a-O17-H9b	101.20°
O17-H9b	1.0432 Å	H9b···O9	1.3712 Å	∠ H17b-O17-H9b	105.01°
O10 hydroxide geometry					
O10-H10b	0.9733 Å	H10b···O4	1.4744 Å	∠ O10-H10b-O4	141.19°
O11 hydroxide geometry					
O11-H11a	0.9763 Å	H11a···O5	1.6397 Å	∠ O11-H11a-O5	138.63°

Table 6.6 Geometry of the ionic species in the high-pressure phase of mirabilite, and their donated hydrogen bonds.

Conversely, the OH^- ions have much shorter O-H bond lengths than the average (Table 6.6), and their donated H···O bonds are both longer and much more bent (O-H-O angles ≈ 140°, compared to 160-180° for 'normal' straight H-bonds). The hydroxide ion is known to be a very strong hydrogen bond acceptor (e.g., Giguerre *et al.*, 1983) but a very weak H-bond donor (e.g., Botti *et al.*, 2004); both of the OH^- ions in the high-pressure phase of mirabilite accept four H-bonds.

At the very highest pressures, a gradual reduction in the distance between Na2 and the sulphate oxygen O6 is observed, and between Na3 and O11. Although the coordination polyhedra surrounding the sodium cations are characterised by Na-O bond lengths of ~ 2.1 - 2.2 Å, the O6 and O11 oxygens are approaching to within 2.3 - 2.4 Å of their respective Na

cations. Arguably, these atoms may be considered to be coordinated to the Na cation at this (and higher) pressures, forming face-sharing NaO_8 triskaidecahedra. Interestingly, direct coordination of the Na cation by sulphate oxygens is observed in the newly discovered octahydrate of sodium sulphate, which is only stable under high-pressure (Oswald *et al*., 2009).

6.8. Discussion

As well as making comparison with the high-pressure neutron diffraction experiments it is also of interest to compare the elastic response of the mirabilite structure to pressure with the elastic response of the structure to temperature, which has been measured in detail for the perdeuterated isotopologue (see Chapter 3). In this experimental study, an estimate of the bulk modulus was obtained by applying a Grüneisen approximation to the thermal expansion, with the necessary internal energy contribution calculated from the measured specific heat capacity (Wallace, 1998). This procedure gave a value for the ratio of the bulk modulus to the Grüneisen parameter, $K_0/\gamma = 29(1)$ GPa; since γ is typically of order 1, it is reasonable to predict that $K_0 \approx 29$ GPa, in tolerable agreement with the results from the *ab initio* calculations and the results from the compression experiments in Chapter 4.

The analysis of the anisotropic thermal expansion given in Chapter 3 showed that the *b*-axis corresponds to the direction of smallest thermal expansion, whereas the principal axis of the thermal expansion tensor closest to the *c*-axis has the largest thermal expansivity and that closest to the *a*-axis an intermediate value. This agrees with the DFT results in as much as the least compressible direction in the crystal has the smallest thermal expansion, and the most compressible direction has the largest thermal expansion. Furthermore, the intermolecular bonds with the largest temperature-dependent changes, those H-bonds donated by interstitial waters to sulphate oxygens, are also the most compressible bonds in the structure.

Generally speaking, the effect of pressure on highly hydrated crystalline salts is to stabilise lower hydrates (e.g., Sood & Stager, 1966; Hall & Hamilton, 2008; Hamilton & Hall, 2008; Oswald *et al*., 2009). For example, epsomite has been shown experimentally to undergo a series of polymorphic phase transitions below 5 GPa (Fortes *et al.*, 2006a) and a similar series of transformations might be expected in mirabilite, possibly culminating in a transformation to a lower hydrate (either by incongruent melting, or solid-state exsolution of ice) instead of the transformations reported in this chapter. However, the general structural

trends are expected to apply to any high-pressure phases of sodium sulphate hydrates, namely the trend towards proton transfer rather than H-bond symmetrisation, the reduction in the number of H-bonds donated to the SO_4 tetrahedron and a trend towards increasing coordination of the Na cation, including coordination by sulphate oxygens as seen in sodium sulphate octahydrate.

Summary

This chapter reports the results of the first *ab initio* density functional theory calculations on the ambient-pressure phase of sodium sulphate decahydrate. There is excellent agreement between the *ab initio* calculations and experimental structure; the calculated zero-pressure unit-cell volume is over-inflated by approximately 2.2 % compared to that measured at 4.2 K by neutron powder diffraction, which is similar to other DFT computational results obtained recently at UCL for hydrogen bonded molecular crystals (e.g., Fortes *et al*., 2001, 2003abc, 2006b). The agreement with experimentally observed bond lengths and angles, particularly the hydrogen-bond network, is extremely good. The only particular area of difference involves the square H-bonded rings, within which the calculated structure is deliberately missing the partially occupied hydrogen sites.

These calculations have been used to determine the coefficients of the elastic stiffness tensor in the range $-2.7 < P < 61$ GPa. Mirabilite undergoes phase changes at around 7.5 GPa (characterised by a change in the water molecules forming the primary coordination polyhedron around one of the sodium cations) and at around 20 GPa (characterised by a change from 6-fold to 7-fold coordination of both of the sodium cations by water molecules). Both transitions involve re-organisation of the hydrogen-bond network. In the pressure range 7.5 – 20 GPa there are at least two competing metastable structures which have very similar energies and similarly-coordinated Na cations, but distinct sulphate tetrahedron coordination numbers. Structural changes continue in the high-pressure phase, resulting in a series of proton transfers and the formation of H_3O^+ and OH^- ions.

Chapter 7

Ab intio simulations III:

The compressibility of meridianiite.

The $MgSO_4$ – H_2O salt-hydrates form another system of importance in terrestrial environments and are also a possible component of the mantles of icy moons. In contrast to the Na_2SO_4 – H_2O system where there are relatively few hydrate phases, the $MgSO_4$– H_2O system has a wealth of hydrate phases. Meridianiite, $MgSO_4.11H_2O$, MS11, the most water-rich of these hydrates has also been suggested to be an important mineral phase on Mars (see Chapter 1, Section 1.1.2 for more information on the phase relations, crystal structure and geological associations of meridianiite). The present chapter reports the results of *ab initio* simulations (using VASP) of the effects of pressure on meridianiite.

7.1 Simulation of the structure of meridianiite.

Structurally, MS11 is simpler than mirabilite, in that it has fewer (78) atoms in the unit-cell and does not show any of the fractional occupancy or disorder of the mirabilite structure. However, MS11 is triclinic, a lower symmetry than monoclinic mirabilite. The initial atomic coordinates for the simulations of MS11 were taken from the 4.2 K structure obtained in the time-of-flight neutron diffraction study of Fortes *et al*. (2008a). Using these atomic coordinates and cell parameters, the athermal simulations were begun by relaxing the crystal structure and cell parameters until a minimum energy was found with zero pressure on the unit cell; this point corresponded to a unit-cell volume of ~701 $Å^3$. Starting from this structure, a series of relaxations were then performed with the unit-cell volumes fixed both at successively smaller and successively larger volumes; in each case the unit-cell (subject to the constraint of fixed volume) and atomic coordinates were relaxed. The simulations were performed stepwise, with the structure from the previous simulation used as the starting structure for the next. Details of the VASP setup for these calculations are given in Chapter 5, section 5.3.2.

It should be noted that for the analysis of these calculations the atom naming scheme of Fortes *et al*. (2008a) has been modified to make it similar to the naming scheme used for mirabilite. Oxygen atoms *O1* – *O4* are the sulfate oxygens, *O5* – *O10* are Mg-coordinated oxygens and the remaining 5 oxygens, *O11* – *O15* are the free water molecules. The hydrogen atoms are named for their associated oxygen atoms, for example the water molecule containing *O11* will then also contain *H11a* and *H11b*. In this scheme, the water molecule with the bifurcated H – bond (see Fortes et al., 2008) is denoted *O14*.

Structural relaxations were carried out at a series of fixed unit-cell volumes in the range 547 < V < 799 $Å^3$ ($1.14 < (V/V_0)^{1/3} < 0.78$); the corresponding pressure range is 9.69 < P < -2.05 GPa. The volume dependence of the total energy, E(V), and pressure, P(V), from VASP are shown in Figure 7.1. There is a break in slope at V ≈ 640 $Å^3$ which is indicative of a phase transition. Unlike the simulated phase changes in the mirabilite structure described in the preceding chapter, there is no evidence of a large range of volumes where the structure is in a transition state from a low-pressure phase to a high-pressure phase; the phase change seems to be instantaneous. As for mirabilite, the relaxed atomic coordinates were analysed using the program "Endeavour" and again, the higher-pressure phase retains the symmetry of the ambient-pressure phase.

The remaining sections of this chapter are laid out as follows: section 7.2 describes the bulk compressibility of meridianiite, section 7.3 then reports the axial compressibilities, sections 7.4, 7.5 and 7.6 describe the various elements of the crystal structure and their variation with pressure.

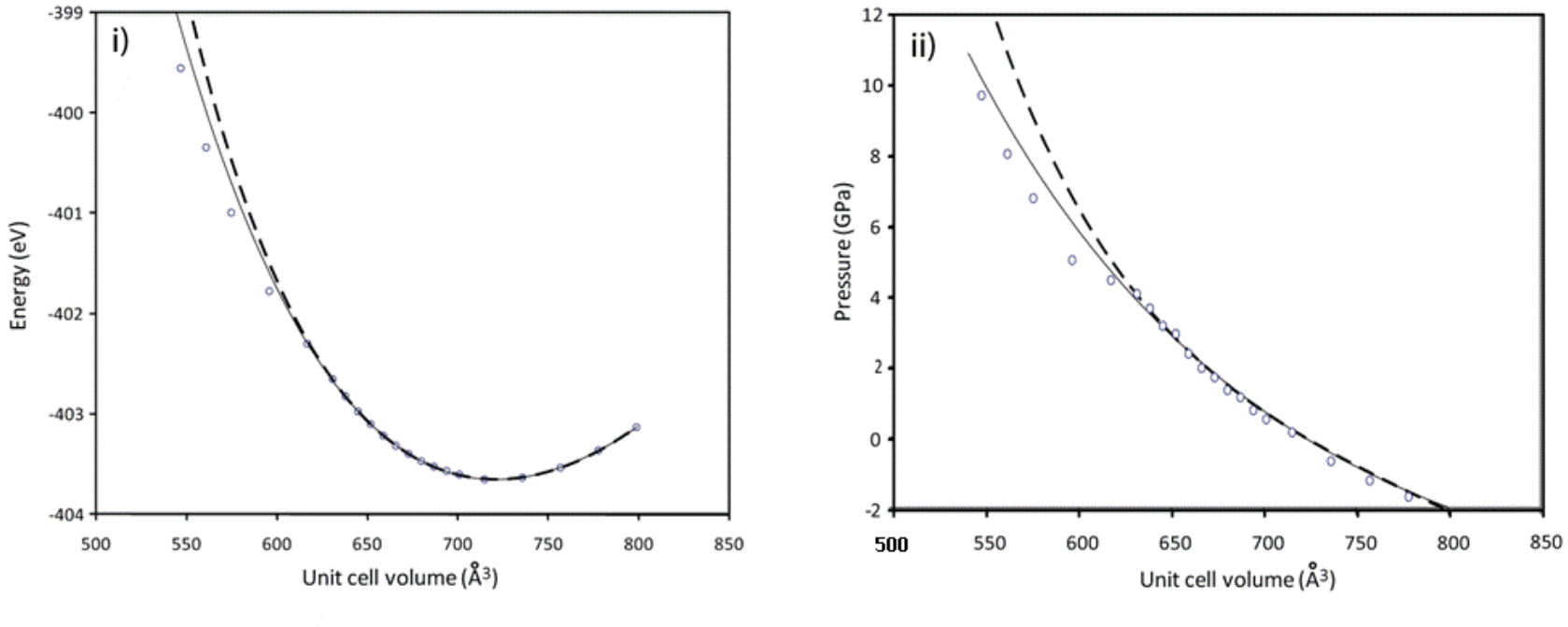

Figure 7.1 Energy - Volume and Pressure - Volume curves for calculations of meridianiite. In both cases, the plots are over the entire range of simulated volumes, $547 < V < 799$ Å^3 ($1.14 < (V/V_0)^{1/3} < 0.78$); the open circles are the calculated values and the full and dashed lines are respectively fits of 3BMEOS and 4LNEOS (the pressure values of the points in the plot are directly from VASP) to the simulations. See Section 5.4, Chapter 5 for definitions of 3BMEOS and 4LNEOS.

7.2 The equation of state of meridianiite.

The low pressure section of the E(V) curves shown in Figure 7.1 ($1.14 < (V/V_0)^{1/3}) < 0.91$), was fitted with an integrated form of the third-order Birch-Murnaghan equation of state and an integrated form of the 4th-order logarithmic equation of state (as for mirabilite). The fitted parameters are given in Table 7.1; note that the agreement in all of the parameters for the low-pressure phase between 3BMEOS and 4LNEOS is not as good as for mirabilite but is still acceptable. Both fitted curves are also shown in Figure 7.1, the full line is the 3BMEOS and the dashed line the 4LNEOS; the two equations of state are indistinguishable to the eye in this figure over the range in which they have been fitted: $1.14 < (V/V_0)^{1/3}) < 0.91$. The behaviour of the fitted lines outside this volume range highlights that such equation-of-state fits should not be extrapolated beyond their boundaries.

	3BMEOS	4LNEOS
V_0	721.6 (3)	722.0 (3)
K_0	23.1 (2)	22.3 (4)
K_0'	3.4 (3)	3.0 (3)
K_0''	-25.253397	1.4 (8)
E_0	-403.668 (2)	-403.665 (2)

Table 7.1 Fitted equation of state parameters for the calculations of meridianiite. For the 3BMEOS the implicit non-zero value of K" was calculated from the expression:

$$K_0'' = \left(K_0'/K_0\right)\left(7 - K_0'\right) - (143/24)(8/3K_0)$$

As for mirabilite, the agreement between the DFT unit-cell parameters and the experimental values is excellent. Fortes *et al.* (2008) found that the unit-cell volume of meridianiite was 701.140(6) $Å^3$ at 4.2 K; the difference in volume ($\Delta V/V \approx 3.0$ %) corresponds to a difference in pressure of only 0.7 GPa, which is small, both in absolute terms and relative to the incompressibility of the material. Surprisingly, the incompressibility, K_0, and the first derivative of the incompressibility, K_0', of meridianiite are very similar to the values for mirabilite (see Chapter 6), despite significant differences in interatomic bonding within the two structures.

As for the high pressure phases of mirabilite, the instability at low pressures of the high-pressure phase of meridianiite has meant that it has not been possible to calculate the total energy of this phase around its value of V_0 and so the high pressure EOS remains unconstrained. Fitting an unconstrained 3BMEOS to the pressure – volume outputs of VASP, yields values of V_0 = 728 (89) $Å^3$, K_0 = 12 (20) GPa and K_0' = 8 (8). A 3BMEOS fitted with K_0' fixed at 4, but otherwise unconstrained, yields the values V_0 = 684 (4) $Å^3$, K_0 = 27 (1) GPa.

The low- and high-pressure structures will be discussed in more detail in Sections 7.4 and 7.5 but first the axial behaviour will be discussed.

7.3 The axial compressibilities of meridianiite.

The unit-cell parameters of meridianiite (Figure 7.2) were also fitted with 3BMEOS expressions in order to obtain information about the axial incompressibilities. In Figure 7.2 Panels i) – iii) show the *a*, *b* and *c* axes; the points are the simulations and the lines are 3BMEOS fits to the simulations. The pressure values in all cases are taken directly from the VASP output. The fits are in two sections, a lower pressure section $0.91 < (V/V_0)^{1/3} < 1.14$ and a high pressure section $0.78 < (V/V_0)^{1/3} < 0.85$. In panel iv) the open squares and dashed lines are the α - angle and the filled circles and full line are the β - angle. Panel v) shows the variation of the γ - angle. In the angle plots (panels iv) and v)), the lines are fitted to the same sections of pressure range as were used for the axes; the low-pressure regions were fitted with 2nd order polynomials and the high-pressure regions with straight lines. Table 7.2 gives the parameters of the low pressure axial EOS fits.

	a - axis	**b - axis**	**c - axis**
a^3_0 (Å³)	299(1)	326(1)	5304(14)
K_0(GPa)	37 (3)	17 (1)	40 (2)
K_0'	11 (3)	1.8 (3)	11 (2)

Table 7.2 Axial incompressibilities of the low pressure phase of meridianiite determined from 3BMEOS fits to the cube of the lattice parameters.

At low pressures all three unit-cell axes behave normally, decreasing in length with increasing pressure. The negative thermal expansion of the *c*-axis of meridianiite (Fortes et al., 2008) is not echoed in the behaviour of this axis under compression. At the phase change, the *b* and *c* axes both decrease in length while the *a* - axis increases in length. All three axes then continue to stiffen at a decreased and more linear rate with increasing pressure. The greatest changes associated with the phase transition are seen in the behaviour of the three angles in the unit cell; α and β behave similarly, with γ compensating by acting conversely. In the low-pressure phase, as pressure increases the α - and β angles increase in value to ~ 90^o (while γ decreases from ~63^o to ~61^o). There is then an apparent jump in the value of all the angles at the phase transition giving a ~1^o increase in α and β and a 2^o decrease in γ, but these apparent discontinuities are likely an artefact of the coarseness of the chosen volumes at which the calculations were performed. After the transition, the β – angle appears to saturate and the α and γ - angles resume their previous behaviours but at a much reduced rate.

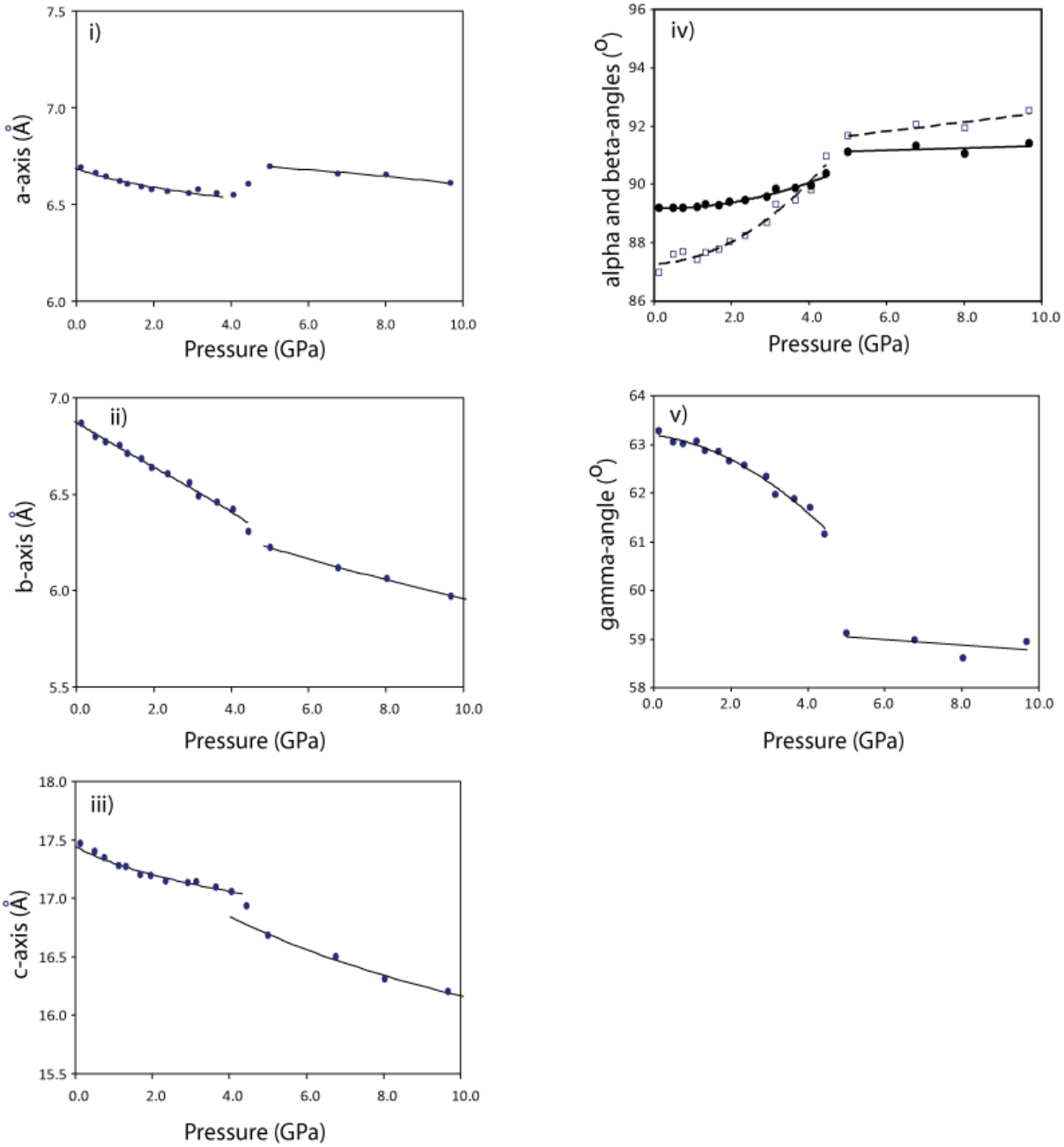

Figure 7.2 Simulated lattice parameters with pressure for meridianiite. Panels i) – iii) are the *a*, *b* and *c* axes; the points are the simulations and the lines are 3BMEOS fits to the simulations. The fits are in two sections, a lower pressure section: $0.91 < (V/V_0)^{1/3} < 1.05$ and a high pressure section: $0.78 < (V/V_0)^{1/3} < 0.85$. In panel iv) the open squares and dashed lines are the α angle and the filled circles and full line are the β angle. Panel v) shows the variation of the γ angle. In the angle plots (panels iv) and v)) the lines are fitted to the same sections of pressure range - the low pressure section with a 2nd order polynomial and the high pressure section with a straight line.

7.4 The zero-pressure structure of MS11.

Figure 7.3 shows a connectivity map of the structure of MS11 (after Fortes *et al.*, 2008a). MS11 is made up of SO_4 tetrahedra and $Mg(H_2O)_6$ octahedra which are connected through a network of hydrogen bonds also involving the five remaining free water molecules. In contrast to mirabilite, where the two $Na_2(H_2O)_8$ octahedra have similar bonding patterns, in MS11 the two octahedra exhibit different bonding schemes. The other major feature of the MS11 structure which is not seen in mirabilite, but is common in the $MgSO_4$–H_2O system, is a bifurcated H-bond. MS11 is, however, the only material in the $MgSO_4$–H_2O system where the bifurcated hydrogen bond is donated to an Mg–coordinated water molecule rather than to a sulfate oxygen.

Tables 7.3 and 7.4 show calculated bond lengths at zero-pressure in the athermal limit for meridianiite. Table 7.3 shows both the calculated *S–O* and *Mg–O* bond lengths in comparison to the 4.2 K neutron diffraction values of Fortes *et al.* (2008a), while table 7.4 shows the distances associated with the hydrogen bonding in MS11. The simulated sulfate tetrahedra are inflated by 2% in volume compared to the experimental structure and have an average bond length of 1.4994 Å, 3% longer. The S-O bond angles in the SO_4 tetrahedra agree with the published experimental values to within 0.1%. For the $Mg(H_2O)_6$ octahedra, the average *Mg – O* distance is 2.0798 Å, 2% longer than the 4.2 K experimental average and yet the calculated volumes for the two octahedra are 2 and 4% *smaller*, clearly the simulated angles are smaller than the experimental values.

S -O lengths (Å)		
	This work	Experimental values at 4.2 K
S – O1	1.4922	1.453(14)
S – O2	1.5075	1.390(15)
S – O3	1.5079	1.503(15)
S – O4	1.4901	1.459(16)

Mg1 – O lengths (Å)			Mg2 – O lengths (Å)		
	This work	Experimental values at 4.2 K		This work	Experimental values at 4.2 K
Mg1 – O5	2.0974	1.998(10)	Mg2 – O8	2.0601	2.065(9)
Mg1 – O6	2.0684	2.080(9)	Mg2 – O9	2.1127	2.083(10)
Mg1 – O7	2.0724	2.057(9)	Mg2 – O10	2.0680	2.051(9)

Table 7.3 S - O and Mg - O distances in meridianiite at zero pressure from the simulation compared to the 4.2 K experimental values of Fortes *et al.* (2008a).

As for mirabilite, the hydrogen-bond network in MS11 is extensive. Table 7.4 shows the H-bonds from these simulations and Table 7.5 reports the values from Fortes *et al*. (2008a) for comparison. The average simulated *O – H* distance is 0.9917 Å. The only significant difference between the experiment and the simulation is in the bifurcated hydrogen-bond. The *O14–H14a* bond length is identical (within experimental error), to the experimental value but one of the arms *(the H14a-O9 bond)*, of the bifurcated bond (the dashed sections of Figure 7.3), is 0.1 Å shorter in the simulations, while both the *O–O* distances are significantly shorter, 0.2 Å and 0.5 Å respectively for *O14–O9* and *O14–O10*, compared to the experiments.

Table 7.4 Hydrogen bonding in MS11 at zero pressure from this simulation. *Italics* are used to indicate the bifurcated H-bond; all bond lengths are in Angstroms and angles in degrees.

	O – H	**H---O**	**O---O**	**∠ O---H–O**	**∠ H–O–H**
O5-H5a-O1	0.9832	1.8818	2.8640	176.936	108.406
O5-H5b-O12	0.9887	1.8233	2.8049	171.501	
O6-H6a-O11	0.9955	1.7074	2.6987	173.345	106.844
O6-H6b-O1	0.9798	1.8881	2.8584	170.136	
O7-H7a-O11	0.9928	1.7169	2.7066	174.341	106.857
O7-H7b-O1	0.9819	1.8553	2.8241	168.412	
O8-H8a-O14	0.9921	1.7393	2.7265	172.865	106.594
O8-H8b-O13	0.9931	1.7318	2.7190	172.194	
O9-H9a-O12	0.9961	1.786	2.7671	167.537	105.430
O9-H9b-O13	1.0059	1.6628	2.6673	176.200	
O10-H10a-O14	0.9943	1.7505	2.7376	171.356	105.108
O10-H10b-O15	0.992	1.7266	2.7090	169.973	
O11-H11a-O4	0.9951	1.7263	2.7199	176.204	106.831
O11-H11b-O2	0.9872	1.8332	2.8093	169.349	
O12-H12a-O2	0.9906	1.8057	2.7959	178.037	106.804
O12-H12b-O3	0.9892	1.8583	2.8291	166.308	
O13-H13a-O15	1.0032	1.6749	2.6775	177.602	104.502
O13-H13b-O2	0.9924	1.7377	2.7101	165.564	
O14-H14a-O9	*0.9896*	*1.9137*	*2.8372*	*154.124*	*103.692*
O14-H14a-O10		*2.5731*	*2.7376*	*121.933*	
O14-H14b-O3	0.9899	1.8134	2.7969	171.893	
O15-H15a-O3	0.9891	1.7637	2.7347	166.293	107.456
O15-H15b-O4	0.9962	1.6748	2.6614	169.940	

Table 7.5 Experimental hydrogen bonding in MS11 at 4.2 K from Fortes *et al*. (2008a). *Italics* are used to indicate the bifurcated H-bond; all bond lengths are in Angstroms and angles in degrees.

	O-D	D···O	O···O	∠ O-D···O	∠ D-O-D
O5-D5a-O1	0.950(9)	1.946(12)	2.894(16)	174.6(11)	109.4(12)°
O5-D5b-O12	0.949(8)	1.929(11)	2.872(13)	172.0(9)	
O6-D6a-O1	0.949(8)	1.851(10)	2.786(10)	167.5(9)	109.0(11)°
O6-D6b-O11	0.993(10)	1.760(12)	2.749(16)	174.0(11)	
O7-D7a-O8	0.959(9)	1.784(11)	2.769(17)	175.6(9)	101.3(12)°
O7-D7b-O1	0.961(9)	1.993(11)	2.934(11)	165.8(9)	
O8-D8a-O14	0.967(9)	1.794(11)	2.753(15)	169.7(9)	109.2(14)°
O8-D8b-O13	0.949(8)	1.716(11)	2.663(13)	176.2(9)	
O9-D9a-O12	0.949(8)	1.833(11)	2.767(12)	168.5(9)	104.7(11)°
O9-D9b-Ow9	0.976(10)	1.791(11)	2.763(15)	173.8(11)	
O10-D10a-O14	0.982(10)	1.824(11)	2.838(14)	168.4(10)	102.7(11)°
O10-D10b-O15	0.944(9)	1.769(12)	2.695(13)	176.9(9)	
O11-D11a-O3	0.946(8)	1.907(10)	2.838(13)	167.4(8)	105.3(11)°
O11-D11b-O4	0.953(9)	1.867(11)	2.818(15)	175.2(10)	
O12-D12a-O2	0.940(9)	1.909(11)	2.829(13)	165.9(10)	107.9(13)°
O12-D12b-O3	0.949(10)	1.884(12)	2.833(14)	177.2(12)	
O13-D13a-O15	0.978(7)	1.821(10)	2.798(11)	178.5(8)	103.2(9)°
O13-D13b-O3	0.977(7)	1.735(9)	2.703(11)	170.5(5)	
O14-H14b-O3	0.939(7)	1.837(10)	2.775(11)	176.2(9)	*102.4(10)°*
O14-H14a-O9	*0.980(8)*	*2.176(13)*	*3.018(12)*	*143.1(9)*	
O14-H14a-O10		*2.530(12)*	*3.245(13)*	*129.6(8)*	
O15-D15a-O4	0.945(9)	1.742(10)	2.681(14)	171.2(10)	107.1(11)°
O15-D15b-O2	0.973(9)	1.851(12)	2.807(16)	166.9(11)	

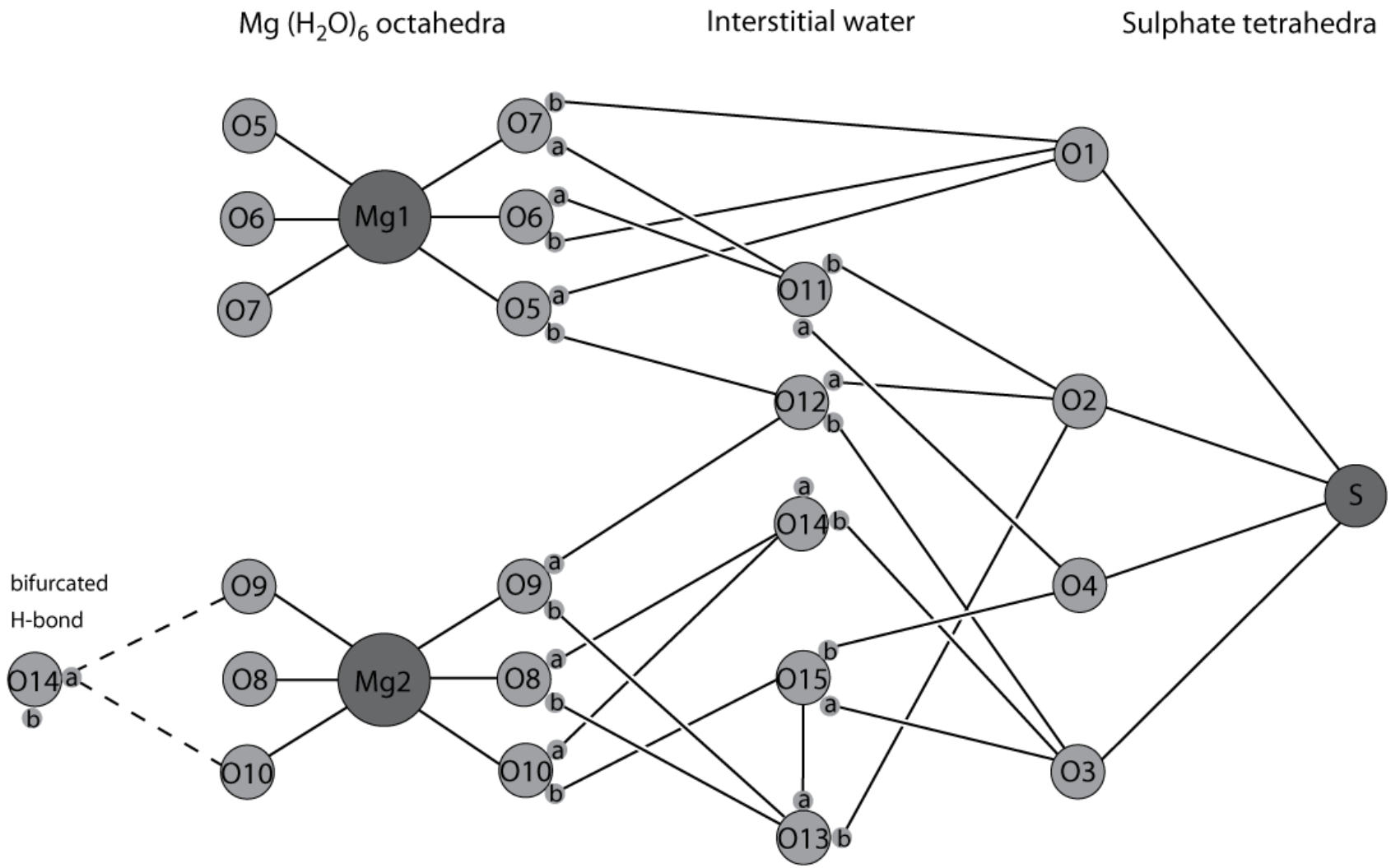

Figure 7.3 Connectivity map for MS11 at zero pressure, after Fortes *et al*. (2008a).

7.5 The Pressure dependence of the structural parameters of the SO_4 and $Mg(H_2O)_6$ Coordination Polyhedra.

In the simulations of mirabilite, the variation in the volume of the coordination polyhedra proved an important quantity in the investigation of structural changes with pressure. Figure 7.4 shows the volumes of the coordination polyhedra for MS11. The SO_4 tetrahedral volume is shown in panel i) in comparison to the tetrahedra from epsomite (MS7) over the same pressure range. As for mirabilite, the MS11 SO_4 tetrahedral volumes have been fitted with a 3BMEOS over the pressure range $3.647 < P < -2.05$ GPa. The SO_4 tetrahedra in MS11 show very similar values of V_0 and K_0' to mirabilite and a K_0 value intermediate between mirabilite (170 GPa) and epsomite, (244 GPa). The MS11 values are: $V_0 = 1.7347(4)$ Å^3, $K_0 = 187(4)$ GPa, and $K_0' = 19(4)$ in the low-pressure phase (see Table 7.6 below). This disparity in stiffness between hydrates has previously been suggested to be due to a difference in electron density around the apical oxygens caused by the difference in the number of accepted hydrogen bonds (see Chapter 6, Section 6.7.1). These MS11 simulations seem to further confirm this as there are twelve such H – bonds in mirabilite, eleven in MS11 and eight in epsomite. There is a discontinuous change in the MS11 SO_4 volumes with pressure which coincides with the phase transition at around 5 GPa. At this point the tetrahedra increase in volume and follow a similar trend to the tetrahedra in epsomite. This points to a change in the coordination of the sulfate tetrahedra in MS11 at the transition. This is echoed in panel ii) of Figure 7.4 which shows a similar, but smaller, discontinuity in the volume of the $Mg(H_2O)_6$ octahedra.

Table 7.6 EOS fit parameters for the SO_4 tetrahedra in MS11 in comparison to mirabilite and epsomite (Fortes *et al*. 2006).

	MS11 - this study	Epsomite from Fortes *et al.* (2006b)	Mirabilite from the *ab initio* simulations of Chapter 6.
V_0 (Å^3)	1.7347(4)	1.7374(7)	1.7358(5)
K_0 (GPa)	187(4)	244(11)	170(5)
K_0'	19(4)	25(8)	17(3)

Investigation of the bond lengths within the MS11 structure confirms that there is indeed a change in coordination. Firstly, the number of hydrogen bonds donated to the SO_4 tetrahedron in MS11 decreases from eleven to ten following the high-pressure phase transition at ~5 GPa. At low pressures, the sulfate oxygen, *O4,* accepts two H–bonds but at high pressure it no longer accepts the H–bond from *H11a*. With increasing pressure, there is a rotation of the *Mg1* octahedron which facilitates the breaking of the *H11b–O4* H – bond. The H–bond from *H11a* then reforms to *O5* which is coordinated to the *Mg1* octahedron.

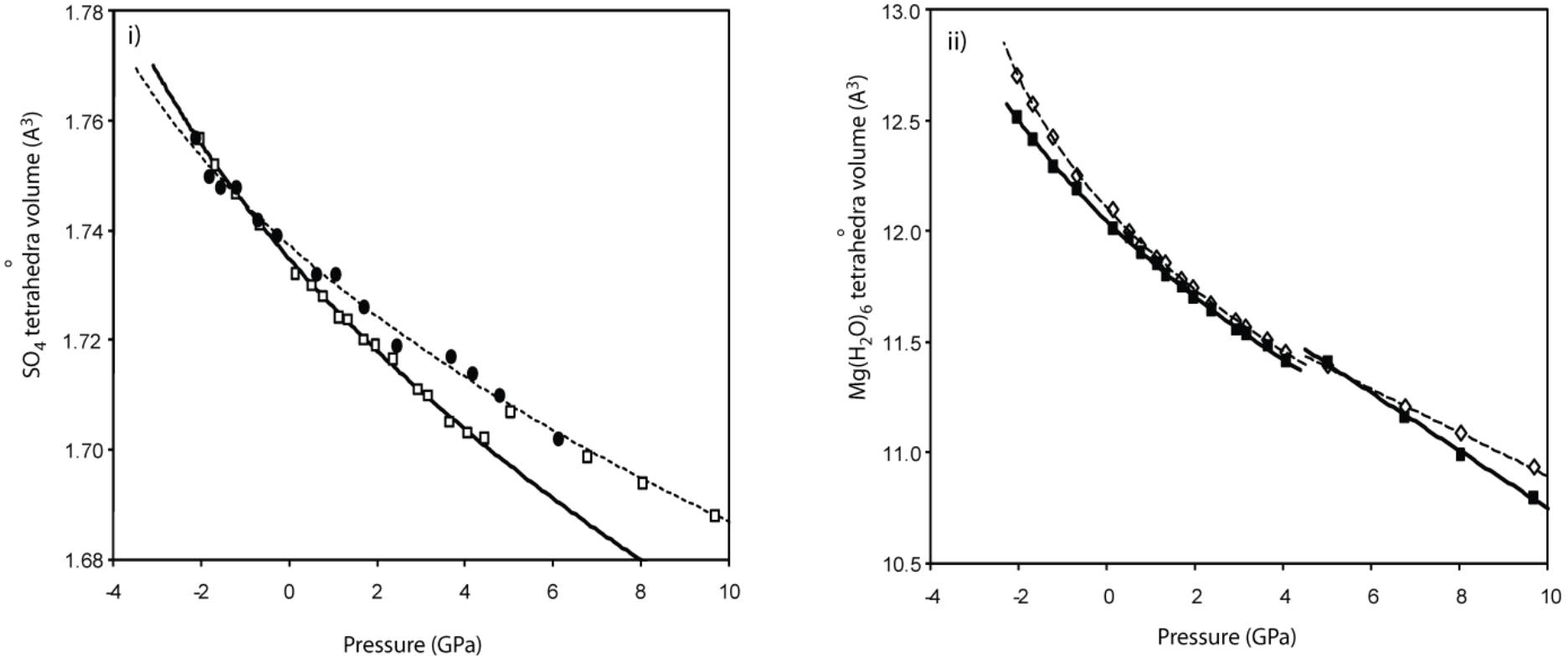

Figure 7.4 Calculated polyhedral volumes for MS11. Panel i) is the SO_4 tetrahedral volume for MS11 (open squares and full line), compared to the tetrahedral volume in epsomite (MS7 – filled circles and dashed line). Panel ii) shows the volumes of the $Mg(H_20)_6$ octahedra, the open diamonds and dashed lines are the volumes of the octahedra designated *Mg1* while the filled squares and full line are for *Mg2*.

7.6 The Pressure dependence of the bifurcated hydrogen bond

Figure 7.5 shows that the bifurcated H-bond *(O14 – H14a)* lengthens with pressure. It is common for H–bonds in hydrated materials to lengthen with pressure as a result of increased electron density in the bond (Fortes *et al*. 2008). Unlike the polyhedral volumes discussed above, there is no obvious break in slope in the bifurcated bond length to signify a phase change.

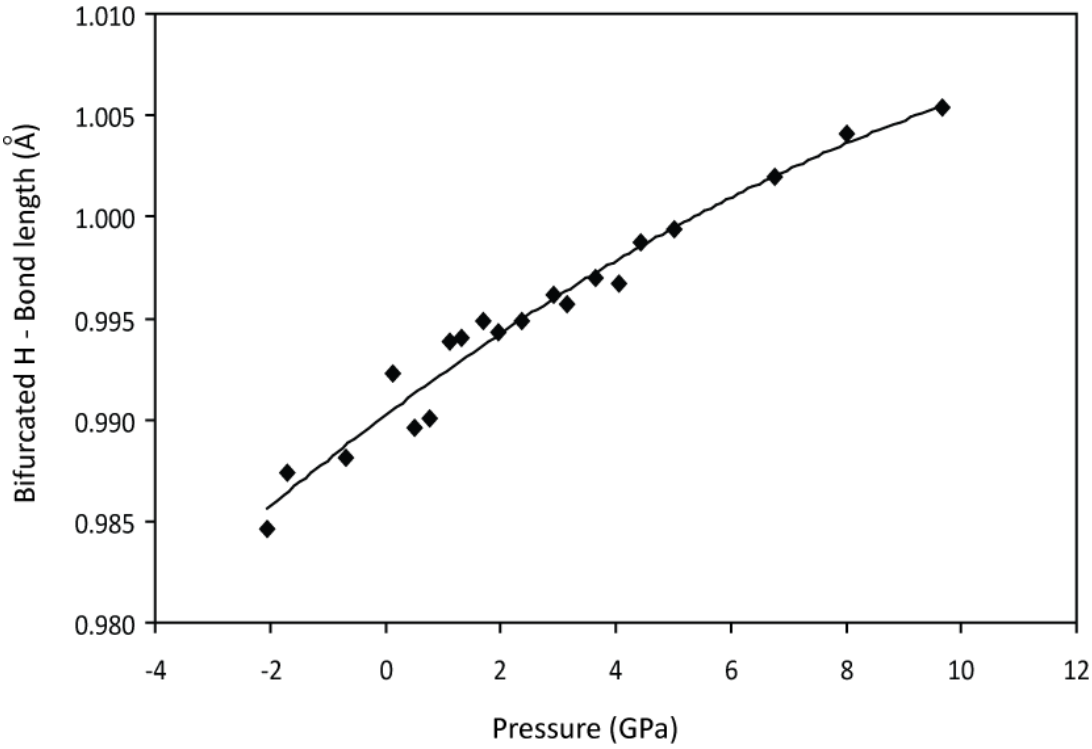

Figure 7.5 Length of the bifurcated H – Bond *(O14 – H14a),* in MS11 with pressure.

7.7 The high-pressure phase of meridianiite.

At pressures above 5 GPa, the *ab initio* simulations predict that MS11 will be in the form shown in the connectivity map given in Figure 7.6. The major change to the structure from that at ambient pressure is the change in the hydrogen bonding network described previously in Section 7.5. Meridianiite seemingly undergoes a much simpler structural change with pressure than mirabilite, although the pressure range investigated here is not as extensive as was used for mirabilite. However, it is likely, as was suggested in the mirabilite simulation chapter, that salt hydrates such as meridianiite will dehydrate with pressure rather than undergo structural phase transitions and so it is probable that these high pressure phases will not exist in nature.

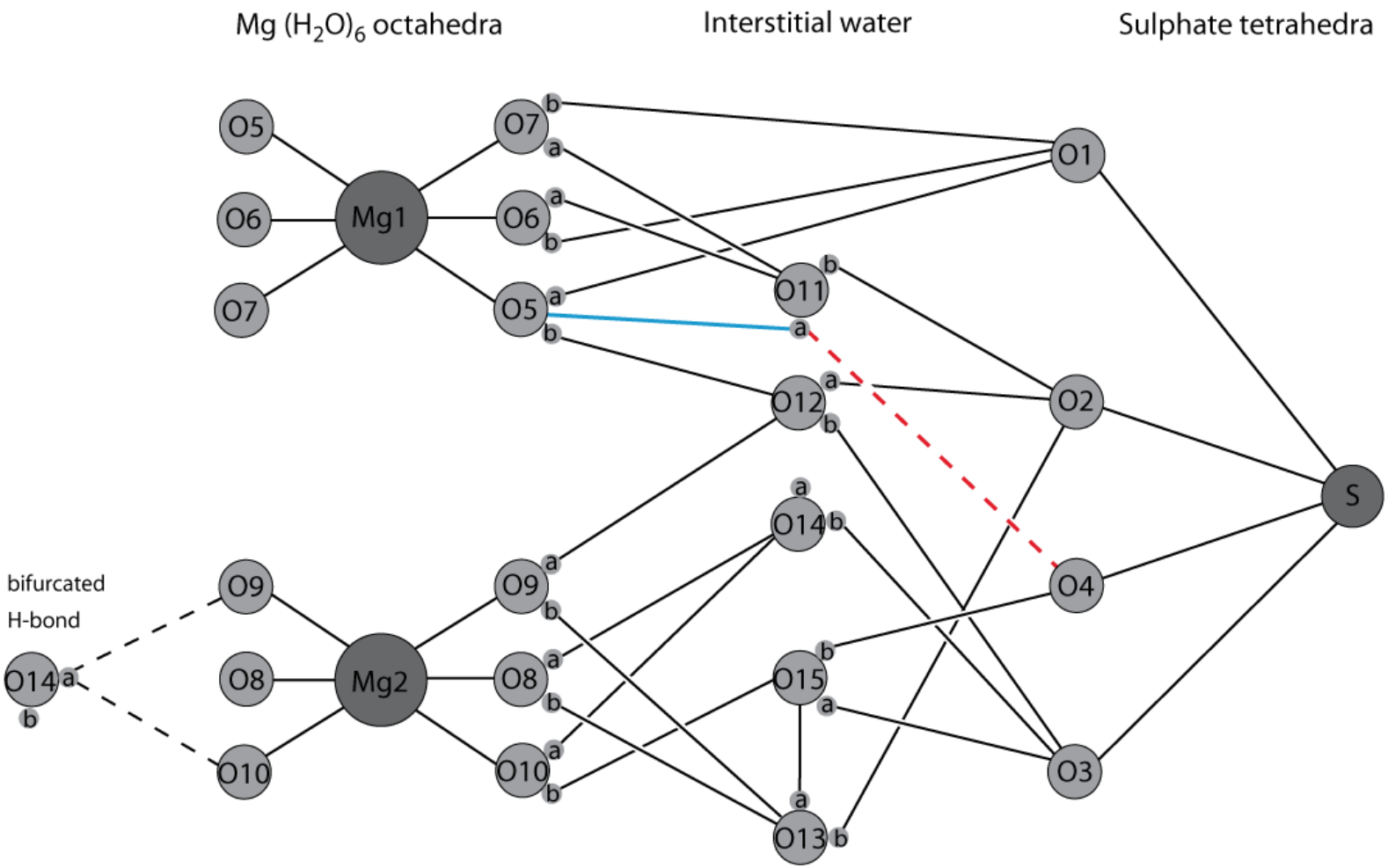

Figure 7.6 Connectivity map for MS11 at 8.0 GPa. The bond highlighted in blue indicates the hydrogen bond which forms at pressures > ~5 GPa and the red dashed line is the *O4 – H11a* bond which it replaces.

Summary

This chapter reports the results of *ab initio* simulations of $MgSO_4.11H_2O$, meridianiite. The unit-cell volume from these simulations is in good agreement with the published experimental 4.2 K structure (Fortes *et al*. 2008a). Fitting of a 3BMEOS to the calculations yields values of V_0 = 723.3 (8), K_0 = 20 (1), K_0' = 6 (1) and E_0 = -403.665 (2). The energy–volume curve reveals a second-order phase transition at ~5 GPa. Analysis of the structural elements with pressure shows this phase transition occurs when lengthening of the bifurcated H–bond with pressure, combined with a rotation of the $Mg(H_2O)_6$ octahedra, prompts a reorganisation of the H–bond network so that an H–bond previously donated to a sulfate oxygen is now donated to an oxygen atom coordinated to one of the $Mg(H_2O)_6$ octahedra.

Chapter 8

Summary, Application of results and Future work.

This chapter is a summary of the work reported in this thesis, together with future applications and uses of the results. It is laid out as follows: Section 8.1 précis the results in Chapters 3, 4, 6 and 7, before Section 8.2 suggests further work which is needed to complete the understanding of the salt hydrates studied here as well as future work arising from the findings of this work. Finally, Section 8.3 briefly describes an example of how this work can be applied to geological structures.

8.1 Summary of results

8.1.1 Neutron diffraction experiments to determine the thermal expansion of mirabilite. (Chapter 3)

Chapter 3 describes thermal expansion determined via neutron diffraction at the ISIS facility at the Rutherford Appleton Laboratory. High resolution neutron powder diffraction patterns were collected from $Na_2SO_4 \cdot 10D_2O$ over the temperature range 4.2 K to 300 K following rapid quenching in liquid nitrogen, and over a series of slow warming and cooling cycles. In addition, crystal structures were refined to R_P values better than 2.5 % at 4.2 K (quenched and slow cooled), 150 K and 300 K. The sulfate disorder reported previously by Levy and Lisensky (1978) was not observed in this specimen, although changes with temperature in deuteron occupancies of the orientationally disordered water molecules coordinated to Na were observed. The coefficient of volume thermal expansion, α_V, is positive above 40 K, and displays a similar magnitude and temperature dependence to α_V in deuterated epsomite and meridianiite. The relationship between the magnitude and orientation of the principal axes of the thermal expansion tensor and the main structural elements shows that freezing in of deuteron disorder in the quenched specimen affects the thermal expansion, manifested most obviously as a change in the behaviour of the unit-cell parameter β.

8.1.2. Neutron diffraction experiments to determine the compressibility of mirabilite. (Chapter 4)

Chapter 4 reports the results of neutron diffraction experiments to determine the compressibility of mirabilite from 0 – 0.55 GPa at 80 K and 260 K. The bulk moduli at 80 K and 260 K are found to be 22.7 (6) GPa and 18.0 (5) GPa respectively when K_0' is constrained to the *ab initio* value of 5.6 obtained in Chapter 6. The variation in the bulk modulus with temperature has also been investigated. The change in K_0 with temperature is similar to that of epsomite over the same temperature range but mirabilite shows a less linear relation and its incompressibility is somewhat more temperature sensitive than that of epsomite. However, the data-points are limited to two temperatures and further measurements at intermediate temperatures and pressures are required before these data can be properly put into context.

8.1.3. Ab initio simulations to determine the equation of state of mirabilite from 0-62 GPa (Chapter 6)

Chapter 6 reports the results of *ab initio* calculations using density functional theory to determine the elastic properties of mirabilite, and to obtain information on structural trends caused by the application of high pressure, up to a pressure of ~60 GPa. There are substantial isosymmetric discontinuous structural re-organisations at ~ 7.7 GPa and ~ 20 GPa caused by changes in the manner in which the sodium cations are coordinated by water molecules. The low-pressure and intermediate-pressure phases both have sodium in six–fold coordination but in the high-pressure phase the coordination changes from six-fold to seven-fold. These coordination changes force a re-arrangement of the hydrogen-bond network in the crystal. The trend is towards a reduction in the number of hydrogen bonds donated to the sulfate group (from twelve down to five over the range 0 – 60 GPa, see Figure 8.1) and an increase in hydrogen bonding amongst the Na-coordinated water molecules and the two interstitial water molecules. Proton transfers from the interstitial waters (forming OH^- ions) to two of the Na-coordinated waters (forming a pair of H_3O^+ ions) are observed at the upper end of the pressure range examined. The equation of state in the athermal limit of the low-pressure phase of mirabilite, parameterised by fitting an integrated form of the 3rd-order Birch Murnaghan expression to the calculated energy as a function of unit-cell volume yields the zero-pressure unit-cell volume, V_0 = 1468.6(9) $Å^3$, the incompressibility K_0 = 22.21(9) GPa and the first pressure derivative $(\partial K/\partial P)_0$ = 5.6(1).

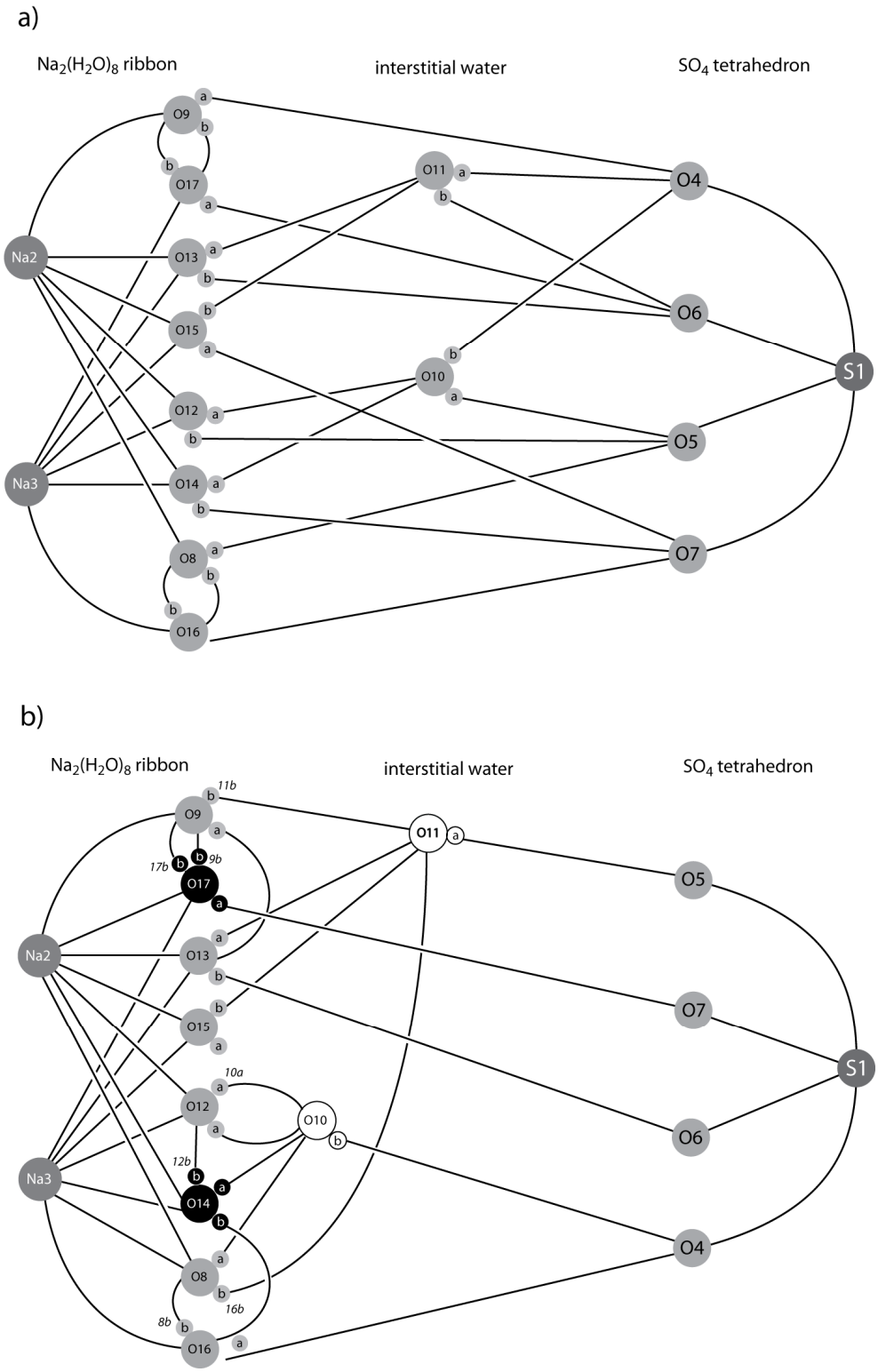

Figure 8.1 a) Connectivity map illustrating the relationship between structural elements in mirabilite at zero pressure; the hydrogen bond structure depicted corresponds to the full ordering of the 'b' sites attached to O9/17 and O8/16. b) Connectivity map illustrating the relationship between structural elements in mirabilite at a pressure of 61 GPa. Note that the order of the sulfate oxygens differs from a). The hydronium ions are marked with black circles, and the hydroxide ions with white circles.

8.1.4 Ab initio simulations to determine the equation of state of MS11. (Chapter 7)

Chapter 7 reports the results of *ab initio* simulations of $MgSO_4.11H_2O$, meridianiite. The unit-cell volume from these simulations is in good agreement with the published experimental 4.2 K structure (Fortes *et al*., 2008a). Fitting of a 3BMEOS yields values of: V_0 = 723.3 (8), K_0 = 20 (1), K' = 6 (1) and E_0 = -403.665 (2). The energy–volume curve reveals a second-order phase transition at ~5 GPa. Analysis of the structural elements with pressure shows this phase transition occurs when lengthening of the bifurcated H–bond, *O14–H14a*, with pressure, combined with a rotation of the $Mg(H_2O)_6$ octahedra prompts a reorganisation of the H–bond network so that an H–bond, *O4 – H11a*, which was previously donated to a sulfate oxygen is now donated to one of the oxygen atoms which is coordinated to the *Mg1* octahedron; the new bond is *O5 – H11a*. This process is shown in Figure 8.2.

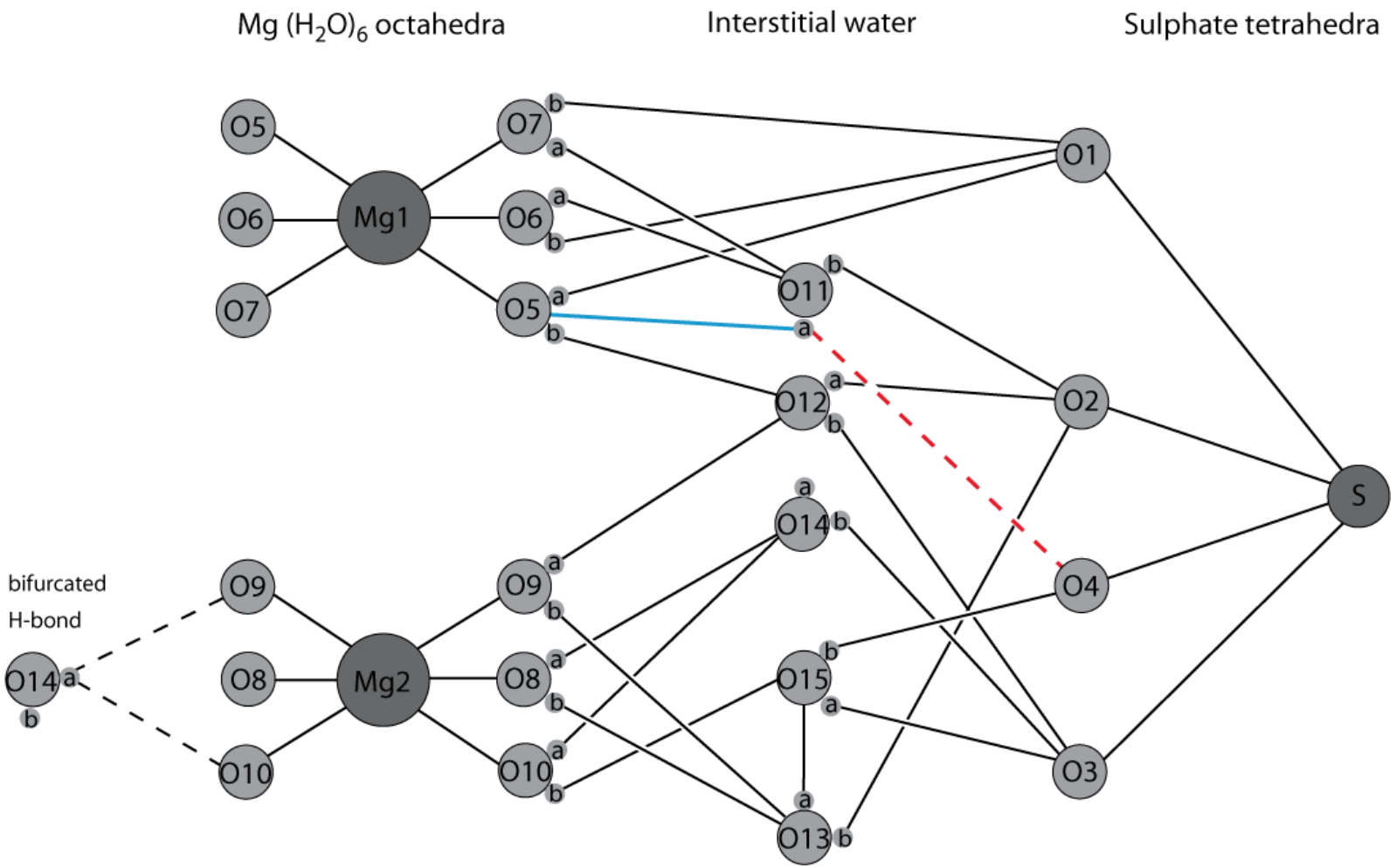

Figure 8.2 Connectivity map for MS11 at 8.0 GPa. The bond highlighted in blue indicates the hydrogen bond which forms at pressures > ~5 GPa and the red dashed line is the *O4 – H11a* bond which it replaces.

8.2 Future work

The experiments and calculations carried out here provide a significant amount of new thermoelastic data for mirabilite. However, there is still a lack of data available for the other phases in the Na_2SO_4 – H_2O system, neither are the phase relations of the system fully understood at non-ambient pressures. It is imperative for the understanding of deposits containing such material that further phase relations and properties over a range of temperatures and pressures are determined. It would be interesting, for example, to investigate the general structural trends of the high-pressure phases of sodium sulfate hydrates, namely the trend towards proton transfer rather than H-bond symmetrisation, the reduction in H-bonds donated to the SO_4 tetrahedron, and towards increasing coordination of the Na cation, including coordination by sulfate oxygens as seen in sodium sulfate octahydrate (Oswald *et al.* 2008).

The structure of mirabilite is now well established in all regards except that of the possible disorder in the sulfate tetrahedra. The neutron diffraction experiments of Chapter 3, performed on mirabilite do not find any evidence of the sulfate disorder described by Levy and Lisensky (1978) - See section 3.1.1.2 in Chapter 3. It is unclear whether this is a result of the deuteration of the sample in this experiment, or that it is due to the thermal history of the sample during the diffraction data collection or some other aspect of the crystal growth or sample preparation prior to the start of the experiment. In addition, morphologically, the deuterated crystals seem different from the protonated crystals: the deuterated crystals grow as lumps with few well defined crystal faces while the protonated crystals have well defined crystal faces.

A proposal to investigate the disorder in mirabilite further by single-crystal neutron diffraction was successfully submitted to the ISIS beamtime panel and was scheduled time on SXD, the single crystal diffractometer, in March 2009 (see Appendix.5 for beamtime application). The proposed experiment was a single crystal study of both a deuterated and a protonated crystal of mirabilite at 4 temperatures between 4.2 and 300 K. This would allow the temperature evolution of any sulfate disorder to be investigated to determine any differences between the two isotopomers. Unfortunately, 1 day into the allocated 5 days, there was a problem with one of the ISIS methane moderators which was followed by a site wide power cut which put an end to the experiment in this user cycle and so the experiment is still outstanding, and scheduled for later this year.

The *ab initio* calculations of MS11 and mirabilite in this study predict new high-pressure structures for both materials. Generally speaking, the effect of pressure on highly hydrated crystalline salts is to stabilise lower hydrates (e.g. Sood & Stager, 1966; Hall & Hamilton, 2008; Hamilton & Hall, 2008; Oswald *et al*., 2009), so it would be of interest to study MS11 and mirabilite experimentally at these pressures to see if these predicted structures actually occur, or whether decomposition into lower hydrates occurs first. This could be achieved with a qualitative high pressure diamond anvil study.

The *ab initio* calculations performed here have also highlighted what may well be another common trait in the high pressure behaviour of sulfate hydrates, namely that the rate of increase in stiffness of the sulfate tetrahedra is related to the coordination number of the sulfate tetrahedra, with the V_0 value of the sulfate tetrahedra independent of the crystal structure. This is seen in Figure 8.3 which shows the SO_4 tetrahedral volume for mirabilite and MS11 (from this work) and for epsomite (Fortes *et al.*, 2006b). A wider study of the variation in tetrahedral volume for other hydrated sulfates would be of interest in order to see how universal this effect is.

The $Na_2SO_4 – H_2O$ and $MgSO_4 – H_2O$ systems are both extremely important in the study of planetary materials; however, neither of these systems will exist in isolation as other cations are likely to be present. While there is little or no solid solution between Mg and Na_2SO_4, there are several ternary systems where solid solutions between all end-members do exist, (e.g. $K_2SO_4 – H_2O – Na_2SO_4$), the dynamics and phase relations of which must be investigated.

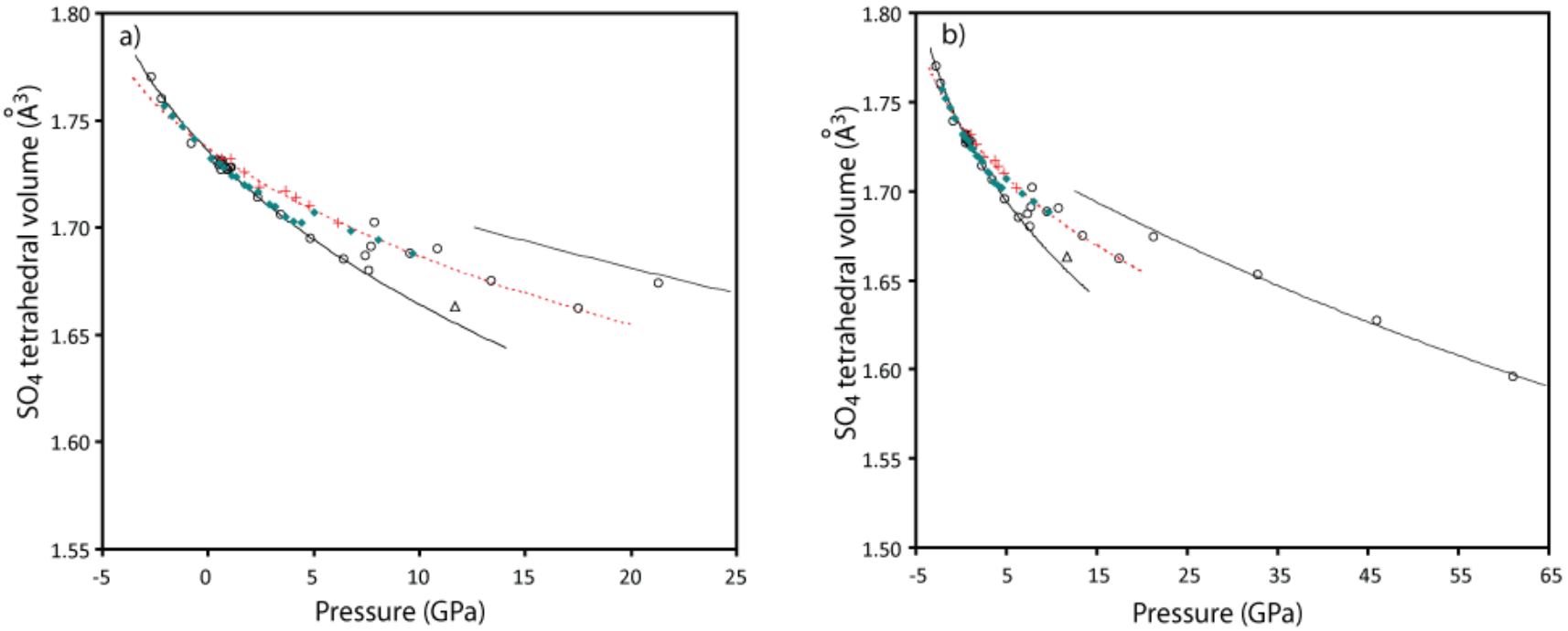

Figure 8.3(a) Sulfate tetrahedral volumes with increasing pressure for epsomite (red crosses, Fortes *et al*., 2006b), MS11 (green filled diamonds, this work) and for mirabilite (open circles, this work). The lone point denoted by the open triangle is the "odd" point where the calculation was not carried out step-wise (see Chapter 6). The solid lines are 3BMEOS fits to the SO_4 volumes in mirabilite for the low-pressure and high-pressure phases, and the dashed line is a 3BMEOS fit to the SO_4 volumes in epsomite.
(b) Variation of the SO_4 volume in mirabilite, epsomite and MS11 over the entire pressure range simulated for mirabilite. The solid black line and the dashed line are the same as in panel (a). The line at higher pressure is a 3BMEOS fit to the four values above 20 GPa with V_0 fixed equal to 1.736 Å^3 (for details see Chapter 6).

8.3 Application of thermoelastic properties of salt hydrates to geological structures: Diapiric modelling.

Once the thermoelastic properties of a material have been constrained, they can be used to understand and predict the behaviour of geological structures and processes. Such properties can be used in both large, planet-scale, thermal evolution models (e.g. Grindrod *et al*., 2008) and in the modelling of small scale geological features such as diapir evolution (Beyer *et al*., 2007). In this final section, a very simple model of the evolution of a diapir of salt hydrate material is constructed. It should be noted, however, that such models depend crucially upon the values adopted for the viscosities of the materials used; viscosity is a thermoelastic property that has proved extremely challenging to measure experimentally. This section is laid out as follows: 8.3.1 describes the methodology behind the diapir model, before Sections 8.3.2 – 8.3.4 describe the setup and results of application of this model to conditions found on Earth, on Mars and on the icy satellites of Jupiter.

8.3.1 Diapiric model methodology

One of the most important properties of evaporitic materials is their ability to flow relatively quickly on a geological timescale. The presence of an evaporitic salt hydrate layer may set up a density inversion leading to a diapiric uprising. The mechanism for forming diapir structures is well known on the Earth; small Rayleigh-Taylor instabilities in the evaporite layer at the interface between it and the overlying sediment promote flow and may grow to form structures similar to terrestrial salt diapiric features.

The model used and described here is taken from Schubert, Turcotte and Olson (2006). This model describes the speed of ascent and likely scale of any surface features produced as a result. The first, key assumption of the model is that Rayleigh-Taylor instabilities have already given rise to a diapir; there is no consideration of the conditions necessary for initial diapir formation. Figure 8.4 shows the initial setup of the model for all environmental conditions. Initially, there are two layers of material: a buoyant lower layer overlain by a denser overburden layer. The top surface of the overburden is a free surface and is assumed to be unconstrained. In contrast, the lower surface of the buoyant layer is assumed to be a non-slip contact. Both layers are assumed to be viscous. The properties of the layers, e.g. density (ρ), viscosity (η), etc. are denoted with subscript "*o*" and "*b*" for the overburden and buoyant layers respectively. Thus, the thickness of the layers becomes h_o and h_b.

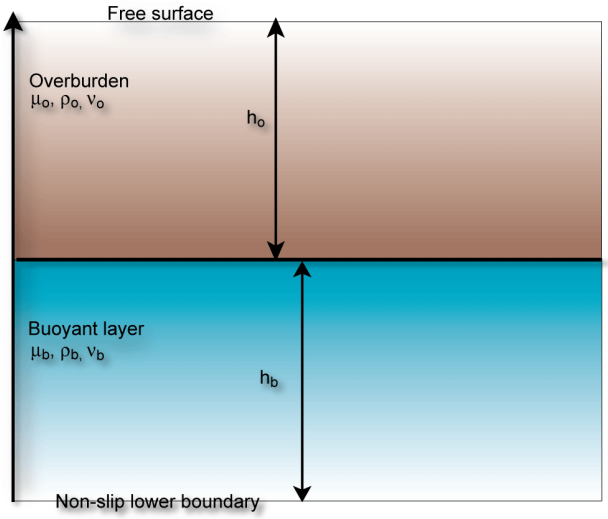

Figure 8.4 Initial layer model. The brown layer is the dense overburden layer denoted by the subscript *o* and the blue layer is the buoyant layer denoted by a subscript *b*. The thickness of these layers is h_o and h_b. The top boundary of the overburden is a free surface and the bottom of the buoyant layer is a non-slip contact.

The diapir formed is taken to be spherical and rising at a uniform rate through a more viscous medium (the overburden layer), as seen in Figure 8.5. It is also assumed that the diapiric feature has a constant volume and that the system is isothermal. The properties of the system are not considered to vary with depth. The model then relates a scale factor R, involving the ratio of the viscosities of the buoyant and denser layers and the thickness of the buoyant layer, to the speed of ascent.

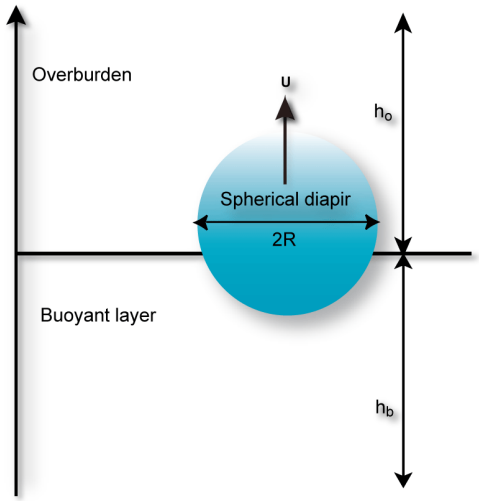

Figure 8.5 Schematic illustration of the model diapir against the layers from Figure 8.4. The spatial scale of the diapir is R and the ascent speed of the diapir is U_∞.

The first quantity calculated in the model is the spatial scale of the diapir, *R*, akin to the radius of the diapir.

$$R = \left(\frac{\eta_o}{\eta_b} \right)^{\frac{1}{3}} \cdot h_b \qquad \textbf{Equation 8.1}$$

Where η is the effective viscosity of the appropriately subscripted layer and h_b is the thickness of the buoyant layer. This means that the size of the diapir is related to the amount of material available in the buoyant layer and the ability of the buoyant layer to move relative to the overburden layer. It also tells us that $h_{b,}$ the buoyant layer thickness, is an important parameter in the determination of the size of the diapir. Figure 8.6 is a logarithmic plot of *R* against layer thickness at a series of viscosity contrasts; it illustrates just how quickly the size of the diapir increases with order of magnitude changes in viscosity contrast. Thus, the values adopted for the viscosity of the layers must be chosen with care.

N.B. It is common in planetary dynamics to speak of the viscosity of a material even though the term is not fully descriptive of a non-Newtonian rheology. The "effective viscosity", η_{eff}, of a material can be used in this way provided that σ, the stress, or $\dot{\varepsilon}$, the strain rate have been specified, which they will be in this case. η_{eff} can be defined as:

$$\eta_{eff} = \frac{\sigma}{3\dot{\varepsilon}} \qquad \textbf{Equation 8.2}$$

The factor of 3 in the denominator is due to the flow being axisymmetric and divergent rather than along straight, parallel lines (Durham and Stern, 2001).

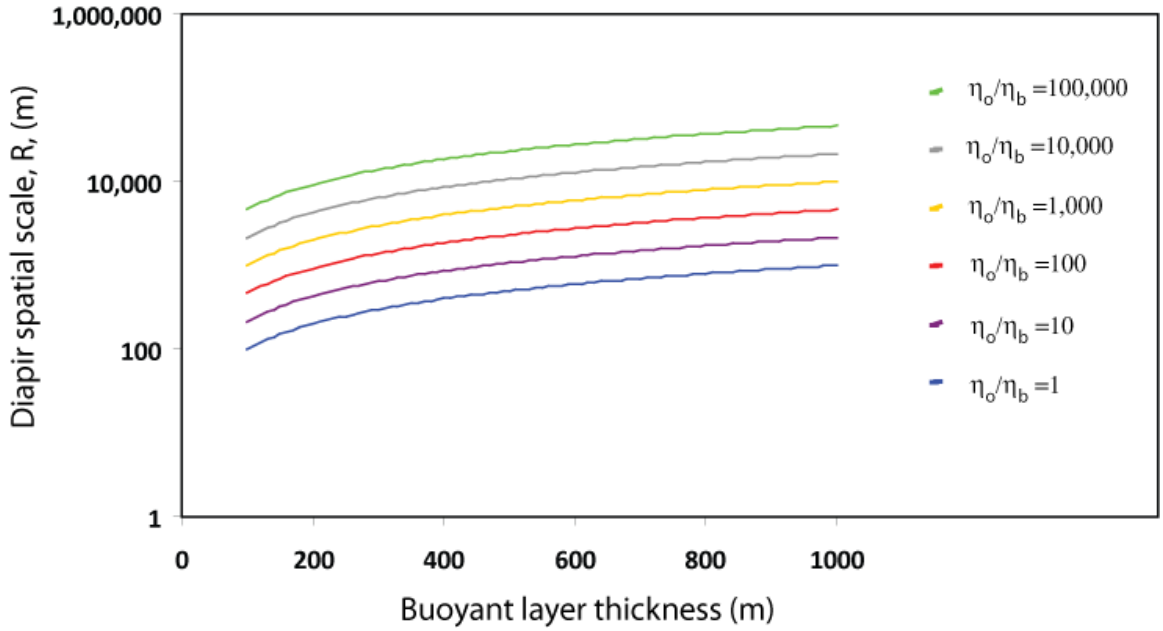

Figure 8.6 Logarithmic plot of diapir size against buoyant layer thickness for different ratios of viscosity between the overburden and buoyant layers.

The rate at which a sphere of material, with a length-scale R, will rise through a medium with viscosity of η_o is equal to the Stokes velocity and can be calculated from:

$$U_\infty = \frac{g'R^2}{3\eta_o} \qquad \textbf{Equation 8.3}$$

Where R = initial length scale of diapir, U_∞ = Stokes velocity, η_o = effective viscosity of the overburden layer, and g′ can be defined as:

$$g' = g\left(\frac{d\rho}{\rho_b}\right) \qquad \textbf{Equation 8.4}$$

With,

$$d\rho = \rho_o - \rho_b \qquad \textbf{Equation 8.5}$$

(and "g" being the acceleration due to gravity on that particular planetary body)

For each planetary scenario as described in the following sections, the material properties have been adjusted for the particular environmental conditions of that planetary body. In each case, layer thicknesses are varied over the range 100 – 1000 m for both the buoyant and overburden layers to explore a parameter space comparable to that found on Earth. The range of densities and viscosities used in each of the scenarios can be seen in Table 8.1. The viscosities are taken from various sources as described in the caption to Table 8.1 and their values have been adjusted for varying temperature on each planetary body as much as is possible from available experimental data. The temperature for each layer is taken as the temperature at the central depth of the relevant layer for a given geotherm. For example, for the Earth a modest crustal geotherm of 25 K km^{-1} has been used (Best, 2003), together with an average surface temperature of 293 K (20^{o}C).

Table 8.1 Density and viscosity values for the materials used in each of the planetary settings. ^ from Shukurina *et al*. (1978), # from Durham *et al*. (2005), + from Goldsby and Kohlstedt (2001), * from Beyer *et al*. (2000) [&] from this work, [$] from Shofield *et al*. (1996) and [£] from Fortes (2004).

	Density (kgm^{-3})	Viscosity (Pa Sec)		
		Earth	Mars	Ganymede
Gypsum	2317[$]	1×10^{16}^	-	-
Mirabilite	1490 [&]	1×10^{12} #	1×10^{14} #	1×10^{16} #
Ice (1h)	917 [£]	1×10^{13} +	1×10^{15} +	1×10^{16} +
Basalt	2800 *	1×10^{19} *	1×10^{19} *	-

8.3.2 Diapirs on Earth

The first scenario for which this model will be tested is a basalt overburden layer overlaying a salt hydrate buoyant layer composed of gypsum ($Ca_2SO_4 \cdot 2H_2O$). Halite and gypsum are the most common evaporitic minerals on Earth. Terrestrial salt domes have length scales of a few hundred meters to a few km and typically reach the surface in times of order 10^4-10^6 years. Table 8.2 shows the range of values of scale factor determined for all the different scenarios. Using this model to create a gypsum diapir from a layer overlain by basalt on Earth would give diapirs with a range of length scales from 0.5 – 10 km, in excellent agreement with the size of features seen. For example Figure 8.7 shows an image of salt diapirs in Iran along with circles of radii 10 and 20 km for comparison.

	gypsum - basalt	mirabilite - basalt
R (km)	0.5 - 10	1 - 20
Range of ascent times for given buoyant layer : overburden layer thickness ratio (million years)		
$h_b : h_o$	gypsum - basalt	mirabilite - basalt
1 : 1	3 – 70	0.7 - 15
2 : 1	1.3 - 16	0.3 - 4
5 : 1	0.7 - 3	0.15 – 0.6
10 : 1	0.3 – 0.7	0.08 – 0.15

Table 8.2 Range of spatial scales and ascent times calculated for diapirs on Earth using layer thicknesses of 100 – 1000m for both the overburden and the buoyant layer..

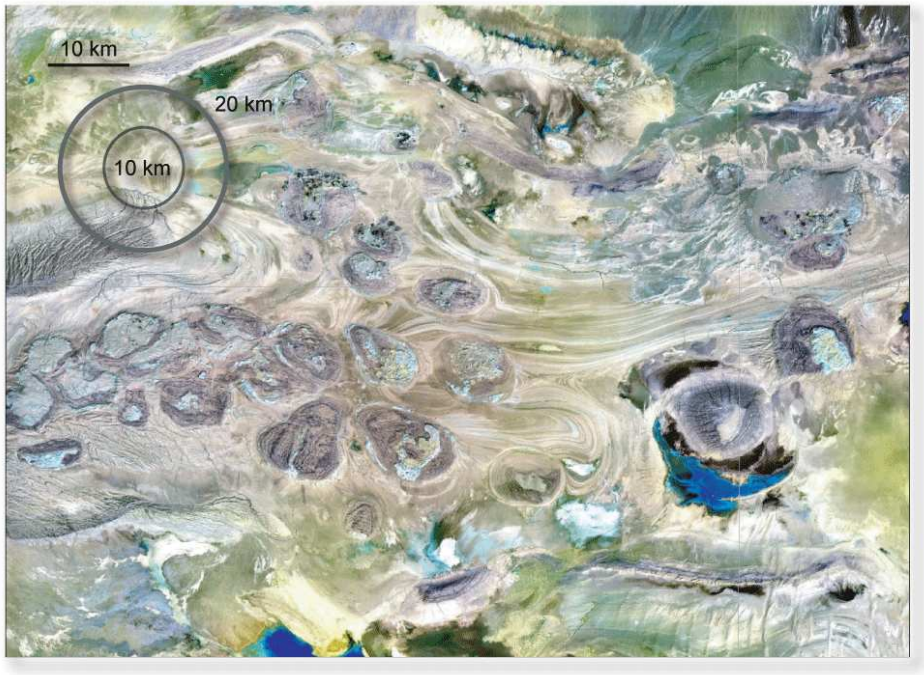

Figure 8.7 Landsat image of salt diapirs in Iran together with scale bar for comparison with simulated diapir sizes. Image: USGS/NASA.

It is also interesting to consider the time taken for a diapir to rise up through the overburden above it. Diapir ascent time is also reported in Table 8.2. For buoyant layer to overburden thickness ratios of 1, there are a range of ascent times from 3 – 70 Ma corresponding to thicknesses of the buoyant layer of 100 – 1000m. For a buoyant layer to overburden thickness ratio = 5 the time-of-ascent range is reduced to 0.7 – 3 Ma.

However, as we know, gypsum is not the only evaporitic material which can form in thick deposits on the Earth. It is not unreasonable to imagine that given the right environmental conditions a thick deposit of mirabilite or other salt hydrates could be laid down, buried and

form a diapiric structure, so the second scenario is a mirabilite buoyant layer overlain by basalt. The results of this are also seen in Table 8.2. The range of sizes of feature produced by a mirabilite diapir on the Earth is slightly larger than the range for a gypsum feature. A larger density difference between the mirabilite and the basalt overburden layer has produced a faster ascent speed for the mirabilite diapir by approximately an order of magnitude. This may lead to a mirabilite feature being exposed to erosion at the surface earlier in its history, compared to a gypsum body, and so it may not persist as long in the geological record.

8.3.3 Diapirs on Mars.

For Mars, the model has been used to simulate firstly, as for Earth, a basalt overburden overlying a mirabilite buoyant layer, and secondly, a buoyant ice layer overlain by a basalt overburden. Mars is unique amongst the terrestrial planets as a place where the climate allows ice layers to persist over geological timescales within the subsurface; currently, ice is stable in the Martian subsurface to depths of around 4 km given a crustal geotherm of 12 K km^{-1} (Montesi and Zuber, 2003) and assuming an average surface temperature of 220 K.

The viscosities of the layers used have been adjusted accordingly from terrestrial temperature to appropriate Martian values and g, the gravitational constant recalculated. Values of $1x10^{15}$, $1x10^{19}$ and $1x10^{14}$ Pa s were used respectively for the viscosities of the ice (Goldsby and Kohlstedt, 2001), basalt (Beyer *et al*., 2000) and mirabilite (Durham *et al.,* 2005). The densities employed for each layer are, respectively: 917 kg m^{-3} for ice (Fortes, 2004), 2800 kg m^{-3} for basalt (Beyer *et al*., 2000) and 1490 kg m^{-3} for mirabilite (this work).

The simulated Martian diapirs have larger length scales than the terrestrial diapirs (see Table 8.3) with the mirabilite diapir approximately doubling in size at Mars compared to Earth. The model calculates that ice diapirs ascend quickly and so may have a shorter lifetime in the geological record than their salt-hydrate equivalents. For 1:1 layer thicknesses the ice diapir ascends in 0.3 – 5 Ma, while the mirabilite diapir ascends in 0.6 – 13 Ma. A layer thickness ratio of 2:1 yields ascent times of 10,000 years – 1.3 Ma, and a 5:1 ratio yields ascent times from 50,000 years – 0.2 Ma. This is significantly faster than the halite diapirs modelled by Beyer *et al* (2000), where timescales of 40 – 70 Ma were reported for similar conditions.

It is unclear how long the evidence of an ice diapir feature will persist in the Martian geological record, but it is possible that there are areas of Mars where suitable amounts of

subsurface ice have existed recently enough for features to survive to present day. One such area which has been suggested to contain features which might be diapiric in origin is Candor chasma, where Beyer *et al*. (2000) describe features of a similar size to the diapirs predicted here.

	mirabilite - basalt	Ice - basalt
R (km)	2 - 46	1 - 22
Range of ascent times for given buoyant layer : overburden layer thickness ratio (million years)		
$h_b : h_o$	mirabilite - basalt	Ice - basalt
1 : 1	0.6 - 13	0.3 - 5
2 : 1	0.3 - 3	0.1 – 1.3
5 : 1	0.13 – 0.5	0.05 – 0.2
10 : 1	0.07 – 0.1	0.02 – 0.05

Table 8.3 Range of spatial scales and ascent times calculated for diapirs on Mars using layer thicknesses of 100 – 1000m for both the overburden and the buoyant layer.

8.3.4 Diapirs on the icy satellites

This modelling can also be extended to the icy satellites where evaporite minerals are also likely to be present. For the diapirs described in the previous sections, the salt hydrate layer has always formed the buoyant layer; however, at the icy satellites of Jupiter, it is possible that ice may form this buoyant layer, with salt hydrates as an overburden layer. For this exercise the properties have been adjusted to values for Ganymede. It is interesting that on Ganymede the two layers have the same viscosity, so the size of the diapir is entirely reliant on the thickness of the buoyant layer. There is also not as large a density contrast between the overburden and buoyant layer in the outer solar system case (see Table 8.1) so the diapir will grow more slowly. Table 8.4 shows that this is indeed the case, and that diapirs on Ganymede are of the same scale as the buoyant layer thickness and rise at a slower rate than those on Mars.

	Ice - mirabilite
R (km)	0.05 - 1
Range of ascent times for given buoyant layer : overburden layer thickness ratio (million years)	
$h_b : h_o$	Ice - mirabilite
1 : 1	1 - 20
2 : 1	0.4 - 5
5 : 1	0.2 – 0.9
10 : 1	0.1 – 0.2

Table 8.4 Range of spatial scales and ascent times calculated for diapirs on Ganymede using layer thicknesses of 100 – 1000m for both the overburden and the buoyant layer.

8.3.5 Discussion

Although the model discussed above illustrates the processes involved in diapir formation and gives estimates of the size of the resulting features and the timescales required for ascent of the diaper to the planetary surface, it is very simplistic and capable of much improvement. Using this simple model the size of the feature produced is very dependent on the viscosity contrast between the buoyant layer and the overburden. In the absence of tighter constraints on actual values for material viscosities, to fully investigate the relation between the composition of the buoyant layer and the size of the surface feature, a range of viscosities for each material will have to be chosen; this would add another dimension to the parameter space investigated. In contrast to the size of the feature, which is controlled by the buoyant layer thickness, the driving forces which control the speed of ascent of the diapir are: 1) the differing density contrasts between the scenarios, and 2) the ratio of layer thicknesses within each scenario..

In this simple model it has been assumed that the diapir is initiated solely by compositional rather then thermal buoyancy. Future work should address thermal buoyancy, as well as accommodating possible phase changes (including change of hydration state) in candidate materials under the appropriate conditions. Polymineralic diapirs, incorporating, for example, Mg- and Na-sulfate hydrates, might also be considered. Furthermore, a more sophisticated linear analysis methodology, which would allow a more complete treatment of the dynamics governing the interactions of the buoyant and overburden layers could be used.

In the case of most icy satellites, the evaporite layers are likely to form the denser overburden overlying less dense ice layers, although on Titan's surface it is possible that low-density organic evaporites will exist where methane-ethane lakes have dried up; in this case the overburden might be dominated by solid acetylene and ethylene. Thus, due to the temperature ranges encountered on these satellites, in the outer solar system it is important to consider also the phase relations of other systems thought to occur on the surfaces of these icy bodies, such as methane clathrates and the ammonia-water system.

References

Alfè D., M.J. Gillan and G.D. Price (1999). The melting curve of iron at the pressures of the Earth's core from ab initio calculations. *Nature* **401** 462-464.

Allan, N.L., A. L., Rohl, D. H. Gay, C. R. A. Catlow, R. J. Davy and W. C. Mackrodt, (1993) Calculated Bulk and Surface Properties of Sulfates *Faraday Discussions*. **95**, 273 – 280.

Alietti, A. (1959): Osservazioni sulla mirabilite di figno e sul solfato di sodio decidrato. *Rend. Acc. Naz. Lincei*, ser. 8ª, **26**, 689-694.

Ahmad M. M. (2006) Ionic conduction and dielectric relaxation in polycrystalline Na_2SO_4 *Solid State Ionics* **177**, 21-23.

Anderson, J.D., G. Schubert, R. A. Jacobson, E. L. Lau, W. B. Moore, and W. L. Sjogren (1998) Europa's Differentiated Internal Structure: Inferences from Four Galileo Encounters. *Science* **281** (5385), 2019 – 2022.
DOI:10.1126/science.281.5385.2019

Anderson, O.L. and D. G. Isaak, (1993), The dependence of the Anderson-Gruneisen parameter [delta]T upon compression at extreme conditions, *J. Phys. Chem. Solids*, **54**(2), 221-227
DOI: 10.1016/0022-3697(93)90313-G.

Balarew, Chr. (2002): Calculation of the free gibbs energy of phase transitions using solubility data. 1. The system Na_2SO_4 - Na_2SeO_4 - H_2O at 15°C: stable and metastable equilibria. *Pure Appl. Chem.* **74**(10), 1793-1800
DOI:10.1351/pac200274101793

Belonoshko A. B., R. Ahuja, and B. Johansson (2000) Quasi–Ab Initio Molecular Dynamic Study of Fe Melting *Phys. Rev. Lett*. **84**, 3638 – 3641.
DOI: 10.1103/PhysRevLett.84.3638

Best M.G. (2003) Igneous and metamorphic petrology. Blackwell Science ISBN: 1-40510-588-7

Beyer, R. A., H. J. Melosh, A. S. McEwen, and R. D. Lorenz (2000) Salt Diapirs in Candor Chasma, Mars? *Lunar and Planetary Science Conference* **30** Houston, Texas, abstract # 2022.

Birch, F. (1952) Elasticity and constitution of the Earth's interior. *J. Geophys. Res*., **57**(2), 227-286
DOI:10.1029/JZ057i002p00227

Blöchl, P. E. (1994) Projector augmented-wave method. *Phys. Rev. B*., **50**(24), 17953 – 17979
DOI:10.1103/PhysRevB.50.17953

Block, E. A. (1913): Über die schmelzkurven einiger stoffe. *Z. Phys. Chem. Stoich. Verwandt.* **82**, 403-438.

Botti, A., F. Bruni, S. Imberti, M. A. Ricci, and A. K. Soper, (2004) Ions in water: the microscopic structure of concentrated NaOH solutions. *J. Chem. Phys*., **120**(21), 10154-10162
DOI:10.1063/1.1705572

Braitsch, O. (1971): Salt deposits, their origin and composition. Springer, New York.

Brand, H. E. A., A. D. Fortes, I. G. Wood, M. Alfredsson, & L. Vočadlo (2006): High-pressure properties of planetary sulphate hydrates determined from interatomic potential calculations. *Lunar Planet. Sci. Conf*. **37**, abstract #1310

Brand, H. E. A., A. D. Fortes , I. G. Wood and L. Vočadlo (2009) The thermal expansion and crystal structure of mirabilite ($Na_2SO_4 \cdot 10D_2O$) from 4.2 to 300 K, determined by time-of-flight neutron powder diffraction. *Phys. Chem. Min.* **36** (1) 29 – 46.
DOI: 10.1007/s00269-008-0256-0

Bray V. (2008) Impact cratering on the Icy Satellites. PhD thesis, Imperial College.

Bridges, J.C. and M. M. Grady (2000) Evaporite mineral assemblages in the nakhlite (martian) meteorites. *Earth and Planetary Science Letters* **176**, (3-4), 267-279
DOI: 10.1016/S0012-821X(00)00019-4.

Bridgman, P. W. (1935) The pressure-volume-temperature relations of the liquid, and the phase diagram of heavy water. *J. Chem. Phys* **3**, (10), 579 – 605.
DOI: 10.1063/1.1749561

Brodale, G. E. & W. F. Giauque (1972): The heat of hydration of sodium sulphate. Low temperature heat capacity and entropy of sodium sulphate decahydrate. *J. Phys. Chem.* **76**(5), 737-743
DOI: 10.1021/j100649a024

Brooke, H. J. (1824): On the crystalline forms of artificial salts. *Annals of Philosophy* **7**, 20-22.

Carlson, R. W., W. Calvin, J. B. Dalton, G. B. Hansen, R. Hudson, R. E. Johnson, T. B. McCord, and M. H. Moore (2007): Europa's surface compositions: what we know, what we would like to know, and how we can find out. *EOS, Trans. Am. Geophys. Union.* **88**(54), Fall Meeting Suppl., abstract P51E-02.

Cochran, W. 1973 The dynamics of atoms in crystals, Edward Arnold Publishers, London

Colman, S. M., Kelts, K. R. and Dinter, D. A., (2002) Depositional history and neotectonics in Great Salt Lake, Utah, from high-resolution seismic stratigraphy. *Sed. Geol.*, **148**(1-2), 61-78 DOI:10.1016/S0037-0738(01)00210-X

Cocco, G. (1962): La struttura della mirabilite. *Rend. Acc. Naz. Lincei*, ser. 8^{a}, **32**, 690-698. ICDD entry 01-072-0495.

Cocco, G., & V. Rossetti (1959): La cella elementare della mirabilite. *Periodico di Mineralogia - Roma* **28**, 231-232.

Dalton, J. B., O. Prieto-Ballesteros, J. S. Kargel, C. S. Jamieson, J. Jolivet, and R. Quinn (2005) Spectral comparison of heavily hydrated salts with disrupted terrains on Europa. *Icarus,* **177**(2), 472-490
DOI:10.1016/j.icarus.2005.02.023

Daimon, K. and E. Kato, (1984). High temperature modification of anhydrous magnesium sulfate *Yōgyō Kyōkai-shi* **92**(3), 153-155

Day S, E. Asphaug, and L. Bruesch (2002) Cumulates, dykes and pressure solution in the ice-salt mantle of Europa. *EOS, Transactions of the American Geophysical Union*, **84**, (46), Fall Meeting Supplement, Abstract P72B–0507

de Coppet, L.C., (1907). Recherches sur la surfusion et la sursaturation. *Ann. Chim. Phys*. **8** (10), 457–527.

Dougherty, A.J., D. L. Hogenboom, J.S. Kargel, and Y. F. Zheng (2006) Volumetric and optical studies of high pressure phases of $Na_2SO_4 \cdot 10H_2O$ with applications to Europa. *Lunar and Planetary Science conference*, **37**, #1732.

Durham, W. B. and L. A. Stern, (2001) Rheological properties of water ice; Applications to satellites of the outer planets (review), *Annu. Rev. Earth Planet. Sci*., **29**, 295-330,

Durham, W. B., L. A. Stern, T. Kubo, and S. H. Kirby (2005), Flow strength of highly hydrated Mg- and Na-sulfate hydrate salts, pure and in mixtures with water ice, with application to Europa, *J. Geophys. Res*., **110**, E12010
DOI:10.1029/2005JE002475.

Eysel, W., H. H. Hofer, K. L. Keestert and T. H. Hahn, (1985) Crystal chemistry and structure of Na_2SO_4(I) and its solid solutions *Acta Cryst*. **B41**, 5 - 11
DOI: S0108768185001501

Finger, L. W., M. Kroecker, & B. H. Toby (2007): DRAWxtl, an open-source computer program to produce crystal structure drawings. *J. Appl. Cryst*. **40**, 188-192
DOI:10.1107/S0021889806051557

Finney, J. L. (1995): The complimentary use of X-ray and neutron diffraction in the study of crystals. *Acta Cryst* B**51**, 447-467
DOI:10.1107/S0108768195002734

Fortes, A. D., I. G. Wood, J. P. Brodholt, and L. Vočadlo, (2001) *Ab initio* simulation of ammonia monohydrate ($NH_3 \cdot H_2O$) and ammonium hydroxide (NH_4OH). *J. Chem. Phys*., **115**(15), 7006-7014
DOI:10.1063/1.1398104

Fortes, A. D., I. G. Wood, J. P. Brodholt, and L. Vočadlo, (2003a) *Ab initio* simulation of the ice II structure. *J. Chem. Phys*., **119**(8), 4567-4572. DOI:10.1063/1.1593630

Fortes, A. D., I. G. Wood, J. P. Brodholt, and L. Vočadlo (2003b) Hydrogen bonding in solid ammonia from Density-Functional Theory calculations. *J. Chem. Phys*., **118**(13), 5987-5994. DOI:10.1063/1.1555630

Fortes, A. D., I. G. Wood, J. P. Brodholt, and L. Vočadlo, (2003c) The structure, ordering, and equation of state of ammonia dihydrate ($NH_3 \cdot 2H_2O$). *Icarus*, **162**(1), 59-73 DOI:10.1016/S0019-1035(02)00073-8

Fortes, A. D., I. G. Wood, D. Grigoriev, M. Alfredsson, S. Kipfstuhl, K. S. Knight, & R. I. Smith (2004): No evidence of large-scale proton ordering in Antarctic ice from powder neutron diffraction. *J. Chem. Phys*. **120**(24), 11376-11379 DOI:10.1063/1.1765099

Fortes, A. (2004a) Computational and experimental studies of solids in the ammonia-water system Ph.D Thesis UCL, University of London. 230pp.

Fortes, A. D., I. G. Wood, K. S. Knight, M. Alfredsson and L. Vočadlo (2006a):The thermoelastic properties of epsomite ($MgSO_4 \cdot 7D_2O$) from powder neutron diffraction and ab initio simulation *European Journal of Mineralogy*, **18**, (4), 449-462. DOI:10.1127/0935-1221/2006/0018-0449

Fortes, A. D., I. G. Wood, L. Vočadlo, H. E. A. Brand, P. M. Grindrod, K. H. Joy & M. Tucker (2006b) The phase behaviour of epsomite ($MgSO_4 \cdot 7H_2O$) to 50 kbar: planetary implications. *Lunar Planet. Sci. Conf*. **37**, abstract #1029

Fortes, A. D., I. G. Wood, M. Alfredsson, L. Vočadlo, K. S. Knight, W. G. Marshall, M. G. Tucker, & F. Fernandez-Alonso, (2007b) The high-pressure phase diagram of ammonia dihydrate. *High Press. Res*., **27**(2), 201-212. DOI:10.1080/08957950701265029

Fortes, A. D., I. G. Wood, & K. S. Knight (2008): The crystal structure and thermal expansion tensor of $MgSO_4 \cdot 11D_2O$ (meridianiite) determined by neutron powder diffraction. *Phys. Chem. Min.*, in press. DOI:10.1007/s00269-008-0214-x

Gans, W. (1978): Thermodynamic stability of sodium sulfate heptahydrate. *Z. Phys. Chem.* **111**(1), 39-46.

Garrett, D. E. (2001): *Sodium sulfate: handbook of deposits, processing, properties, and use.* Academic Press.

Geller A (1924) Über das verhalten verschiedener minerale der salzlager bei hohen drucken und wechselnden temperaturen. *Z Krist* **60**:415–472

Genkinger, S., & A. Putnis (2007): Crystallisation of sodium sulfate: supersaturation and metastable phases. *Environ. Geol*. **52**, 329-337 (doi:10.1007/s00254-006-0565x).

Giguère, P. A. (1983) Hydrogen-bonds in aqueous solutions of alkalis. *Rev. Chim. Min*. **20**(4-5), 588-594.

Gillan M.J. (1997). The virtual matter laboratory. *Contemporary Physics*, **38**(2),115-130 DOI: 10.1080/001075197182450

Glauber (1658) Tractatus de natura salium (as Sal mirabile).

Goldsby, D. L. Kohlstedt, (1997) Grain boundary sliding in fine-grained Ice I, *Scripta Materialia*, **37**, (9), 1399-1406
DOI: 10.1016/S1359-6462(97)00246-7.

Goudie, A.S. and Viles, H. (1997) Salt weathering hazards. Wiley, Chichester.

Grindrod, P. M., A. D. Fortes, F. Nimmo, D. L. Feltham, J. P. Brodholt, and L. Vočadlo (2008): The long-term stability of an aqueous ammonium sulfate ocean inside Titan *Icarus*, **197**, (1), 137-151 DOI:10.1016/j.icarus.2008.04.006

Grasset O, L. Mevel, O. Mousis and C. Sotin (2001) The pressure dependence of the eutectic composition in the system $MgSO_4$–H_2O: implications for the deep liquid layer of icy satellites. *Lunar Planet Sci Conf* **31**, abstract #1524.

Groth, P. von (1908) Die anorgischen oxo- und sulfosalze. *Chemische Kristallographie* **2** 371-372

Hall, C. and A. Hamilton (2008) The heptahydrate of sodium sulphate: does it have a role in terrestrial and planetary geochemistry? *Icarus*, online DOI:10.1016/j.icarus.2008.07.001

Hamann, D.R. (1997) H_2O hydrogen bonding in density-functional-theory *Phys. Rev. B.***55**(16) 157 – 160.

Hamilton, A., and C. Hall (2008): Sodium sulphate heptahydrate: a synchrotron energy-dispersive diffraction study of an elusive metastable hydrated salt. *J. Anal. Atom. Spectrom.*, **23**, 840-844 DOI:10.1039/b716734b

Hanawalt, J. D., H. W. Rinn & L. K. Frevel (1938): Chemical analysis by X-ray diffraction. *Ind. Eng. Chem: Analytical Edition*. **10**(9), 457-512. DOI:10.1021/ac50125a001: ICDD entry 00-001-0207.

Hardie, L. A. (1991) On the significance of evaporites. *Ann. Rev. Earth Planet. Sci*., **19**(1), 131-168. DOI:10.1146/annurev.ea.19.050191.001023

Hartley, H., Jones, B.M., Hutchinson, G.A., 1908. The spontaneous crystallisation of sodium sulphate solutions. *J. Chem. Soc. Trans*. **93**, 825–833.

Hazen, R. M., & L. W. Finer (1979) Bulk modulus-volume relationship for cation-anion polyhedra. *J. Geophys. Res*., **84**(B12), 6723-6728. DOI:10.1029/JB084iB12p06723

Hazen, R. M., R. T. Downs, and C. T. Prewitt (2000) Principles of comparative crystal chemistry. *Reviews in Mineralogy and Geochemistry,* **41**. Mineralogical Society of America, Washington DC.

Hermida-Ramon, J. M., and G. Karlström, (2004) Study of the hydronium ion in water. A combined quantum chemical and statistical mechanical treatment. *J. Mol. Struct. Theochem.,* **712**(1-3), 167-173. DOI:10.1016/j.theochem.2004.10.017

Hill, A. E. & J. H. Wills (1938): Ternary systems. XXIV, calcium sulphate, sodium sulphate and water. *J. Am. Chem. Soc*. **60**(7), 1647-1655. DOI: 10.1021/ja01274a037

Hohenberg, P., and W. Kohn. (1964) Inhomogenous electron gas. *Phvs Rev*., **136**(B3), B864-B87.1DOI:10.1103/PhysRev.136.B864

Hogenboom DL, J. S. Kargel, J. P. Ganasan and L. Lee (1995) Magnesium sulfate-water to 400 MPa using a novel piezometer: densities, phase equilibria, and planetological implications. *Icarus* **115**(2):258–277. DOI:10.1016/icar.1995.1096

Hogenboom, D. L., J. S. Kargel, and P.V. Pahalawatta. (1999) Densities and Phase relationships at high pressures of the sodium sulphate-water system. *Lunar and Planetary Science conference*, **30**, # 1793

Hudec M. R. and M. P. A. Jackson (2007) Terra infirma: Understanding salt tectonics. *Earth-Science Reviews* **82** 1- 28.

Ireta J. Neugebauer, J. and Scheffler M. (2004) On the accuracy of DFT for describing hydrogen bonds: Dependence on the bond directionality. *J. Phys. Chem.* **108** 5692 – 5698

Jackson, R.A., Computer modelling of molecular ionic materials. (2001) *Current Opinion in Solid State and Materials Science,* **5** (5) 463-467. DOI: 10.1016/S1359-0286(01)00029-8.

Kargel, J. S. (1991) Brine volcanism and the interior structure of asteroids and icy satellites. *Icarus*, **94**(2), 369-390. DOI:10.1016/0019-1035(91)90235-L

Kargel J. S. (2004) Mars, a warmer, wetter planet. Springer Praxis publications. 557p
ISBN: 978-1-85233-568-7.

Keys, J. R. & K. Williams (1981) Origin of crystalline, cold desert salts in the McMurdo region, Antarctica. *Geochim. Cosmochim. Acta*, **45**(12), 2299 – 2309. DOI:10.1016/0016-7037(81)90084-3

Kohn, W., & L. J. Sham (1965)Self-consistent equations including exchange and correlation effects. *Phys. Rev.*, **140**(4a), A1133-A1138. DOI:10.1103/PhysRev.140.A1133

Kresse, G. & J. Furthmüller (1996) Efficient iterative schemes for ab initio total-energy calculations using a plane-wave basis set. *Phys. Rev B.* **54**(16), 11169-l1186
DOI:10.1103/PhysRevB.54.11169

Kryukov, P. A., & V. I. Manikhin (1960) Characteristics of the melting of Glauber salt at high pressures. *Russian Chemical Bulletin* **9**(12), 2077-2078. DOI:10.1007/BF00912067

Laasonen, K., Csajka, F., and Parrinello, M. (1992) Water dimer properties in the gradient-corrected density functional theory, *Chemical Physics Letters*, **194**, (3) 172-174,
DOI: 10.1016/0009-2614(92)85529-J.

Laio, A., S. Bernard, G. L. Chiarotti, S. Scandolo, and E. Tosatti (2000) Physics of Iron at Earth's Core Conditions *Science* **11** 287: 1027-1030. DOI: 10.1126/science.287.5455.1027

Langlet, J., J. Bergès & P. Reinhardt (2004) An interesting property of the Perdew-Wang 91 density functional. *Chem. Phys. Lett*. **396**(1-3), 10-15 . DOI:10.1016/j.cplett.2004.07.093

Larsen, A. C., & R. B. Von Dreele (2000): General Structure Analysis System (GSAS). Los Alamos National Laboratory Report LAUR 86-748, Los Alamos, New Mexico.

Levy, H. A. & G. C. Lisensky (1978): Crystal structures of sodium sulfate decahydrate (Glauber's salt) and sodium tetraborate decahydrate (borax).Redetermination by neutron diffraction. *Acta Cryst*. **B34**, 3502-3510 DOI:10.1107/S0567740878011504

Livshits, L. D., YU. S. Genshaft, and YU. N. Ryabin (1963): Equilibrium diagram of the crystal hydrates of $MgSO_4$ at high pressures. *Russian Journal of Inorganic Chemistry* **8**, 676-678. [Translated from, Фазовая диаграмма кристаллогидратов $MgSO_4$ при высоких давлениях. Zhurnal Neorganicheskoi Khimii 8, 1302-1306 (1963)].

Louisnathan, S. J., R. J. Hill, and G. V. Gibbs (1977): Tetrahedral bond length variations in sulphates. *Phys. Chem. Min*. **1**, 53-69 DOI:10.1007/BF00307979

Löwel, H. (1850): Observations sur la sursaturation des dissolution salines. Premier mémoire. *Annales de Chimie et de Physique, 3^{me} série*, **29**, 62-127.

Löwel, H. (1851): Observations sur la sursaturation des dissolution salines. Second mémoire. *Annales de Chimie et de Physique, 3^{me} série*, **33**, 334-390.

Löwel, H. (1853): Observations sur la sursaturation des dissolution salines. Troisième mémoire. *Annales de Chimie et de Physique, 3^{me} série*, **37**, 155-179.

Löwel, H. (1857): Observations sur la sursaturation des dissolution salines. Sixième mémoire. *Annales de Chimie et de Physique, 3^{me} série*, **49**, 32-57.

Markovitch, O., and N. Agmon (2007) Structure and energetics of the hydronium hydration shells. *J. Phys. Chem. A.*, **111**(12), 2253-2256 DOI:10.1021/jp068960g

Marliacy, P., R. Solimando, M. Bouroukba and L. Schuffenecker (2000) Thermodynamics of crystallization of sodium sulphate decahydrate in H_2O-NaCl-Na_2SO_4: application to $Na_2SO_4.10H_2O$-based latent heat storage materials. *Thermochim. Acta*, **344**(1-2), 85-94 DOI:10.1016/S0040-6031(99)00331-7

Marzal, R., M., E. and G. W. Scherer (2008) Crystallisation of sodium sulphate salts in limestone. *Environ. Geol*., **56**, 605-621 DOI: 10.1007/s00254-008-1441-7

McCarthy C., R. F. Coope, S. H. Kirby, K. D. Rieck and L. A. Stern (2007) Solidification and microstructures of binary ice-I/hydrate eutectic aggregates. *Am Min* **92**(10):1550–1560. DOI:10.2138/am.2007.2435

McCord T. B., G. B. Hansen, F. P. Fanale, R. W. Carlson, D. L. Matson, T. V. Johnson, W. D. Smythe, J. K. Crowley, P. D. Martin, A. Ocampo, C. A. Hibbitts, J. C. Granahan and the NIMS Team (1998) Salts on Europa's Surface Detected by Galileo's Near Infrared Mapping *Spectrometer* Science **280** (5367), 1242-1245. DOI: 10.1126/science.280.5367.1242

Meenan, P. Ph.D. thesis, University of Strathclyde (1992).

Mueller, S. and W. B. McKinnon (1988) Three-layered models of Ganymede and Callisto: Compositions, structures, and aspects of evolution, *Icarus*, **76**(3)437-464
DOI: 10.1016/0019-1035(88)90014-0.

Monkhorst, H. J., & J. D. Pack (1976) Special points for Brillouin-zone integrations. *Phys. Rev. B.*, **13**(12), 5188-5192 DOI:10.1103/PhysRevB.13.5188.

Montési L. G. J., and M. T. Zuber, (2003). Spacing of faults at the scale of the lithosphere and localization instability: 1. Theory, *J. Geophys. Res*., **108** (B2), 2110 DOI:10.1029/2002JB001923

Moore J.M., M. A. Bullock, H. E. Newsom and M. J. Nelson (2008) Laboratory simulations of Mars evaporite geochemistry. *Lunar and Planetary Science conference* **39** #1955

Moriarty J. A. (1986) First-principles phonon spectrum in bcc Ba: Three-ion forces and transition-metal behavior *Phys. Rev*. ***B*** **34**, 6738 – 6745 DOI: 10.1103/PhysRevB.34.6738

Muller-Dethlefs K. and Hobza (2000) Noncovalent Interactions: A Challenge for Experiment and Theory. *Chemical Reviews* **100** (1), 143-168 DOI: 10.1021/cr9900331

Negi, A. S., & S. C. Anand (1985): *A textbook of physical chemistry*. New Age Publishers.

Orlando, T. M., T. B. McCord, & G. A. Grieves (2005): The chemical nature of Europa's surface material and the relation to a subsurface ocean. *Icarus* **177**(2), 528-533 DOI:10.1016/j.icarus.2005.05.009

Nimmo F. and E. Gaidos (2002) Strike-slip motion and double ridge formation on Europa. *J. Geophys. Res.* **107**(E4) DOI: 10.1029/200JE001476

Ohno, H., M. Igarashi, and T. Hondoh, T. (2006) Characterisation of salt inclusions in polar ice from Dome Fuji, East Antarctica. *Geophys. Res. Lett*. **33**, article L075050 DOI:10.1029/2006GL025774.

Orlando, T. M., T. B. McCord and G. A. Grieves (2005) The chemical nature of Europa's surface material and the relation to a subsurface ocean. *Icarus*, **177**(2), 528-533 DOI:10.1016/j.icarus.2005.05.009

Oswald I. D, A. Hamilton, C. Hall, W. G. Marshall, T. J. Prior and C. R. Pulham. (2008) In situ characterization of elusive salt hydrates - the crystal structure of the heptahydrate and octahydrate of sodium sulphate. *J. Am. Chem. Soc*., **130** (52), 17795–17800 DOI: 10.1021/ja805429m
.

Palache, C., H. Berman, & C. Frondel (1951): Dana's System of Mineralogy. 7th Edition, Volume **II**, 439-442.

Payne, M. C., M.P. Teter, D.C. Allan, T. A. Arias and J.D. Joannopoulos. (1992) Iterative minimization techniques for *ab initio* total-energy calculations: molecular dynamics and conjugate gradients. *Rev. Modern Phys*. **64**(4)1045 – 1097.

Perdew, J. P. (1991) In, Electronic Structure of Solids (P. Zeische and H. Eschrig, Eds), Akademie, Berlin.

Perdew, J. P., & Wang, Y. (1992) Accurate and simple analytic representation of the electron-gas correlation energy. *Phys. Rev. B* **45**(23), 13244-13249 DOI:10.1103/PhysRevB.45.13244

Perrin C. L. & Neilson J. B, (1997) “Strong” hydrogen bonds in chemistry and biology. *Annu. Rev. Phys. Chem.***48** 511 – 544. DOI:10.1146/annurev.physchem.48.1.511

Petersen V. K. (2005) Lattice parameter measurement using Le Bail versus structural (Rietveld) refinement: A caution for complex, low symmetry systems. *Powder Diffr*. **20**, 14-17, DOI:10.1154/1.1810156

Peterson RC, R. Wang (2006) Crystal molds on Mars: melting of a possible new mineral species to create Martian chaotic terrain. *Geology* **34**(11):957–960.DOI:10.1130/G22768A.1

Peterson RC, W. Nelson, B. Madu and H. F. Shurvell (2007) Meridianiite ($MgSO_4 \cdot 11H_2O$): a new mineral species observed on Earth and predicted to exist on Mars. *American Min* **92**(10):1756–1759 DOI:10.2138/am.2007.2668

Pickard, C. J., & Needs, R. J. (2008) Highly compressed ammonia forms and ionic crystal. *Nature Geosci.* **7**, 775-779
DOI:10.1038/nmat2261

Pinto V., A. Casas, L. Rivero and R. Lázaro (2002) Modelización Gravimétrica 3D del diapiro de Cardona, Cuenca del Ebro (NE de España). *Acta Geologica Hispanica* **37** (4) 273 – 284.

Pistorius, C. W. F. T. (1965). Phase Diagrams of Sodium Sulfate and Sodium Chromate to 45 kbar. *J. Chem Phys*. 43(8) 2895

Pitzer, K. S., & L. V. Coulter (1938): The heat capacities, entropies, and heats of solution of anhydrous sodium sulfate and of sodium sulfate decahydrate. The application of the third law of thermodynamics to hydrated crystals. *J. Am. Chem. Soc.* **60**(6), 1310-1313
DOI:10.1021/ja01273a010

Poirier, J. P., and A. Tarantola (1998) A logarithmic equation of state. *Phys. Earth Planet. Inter*., **109**(1-2), 1-8 DOI:10.1016/S0031-9201(98)00112-5

Putz, H., J. C. Schoen and M. Jansen (1999) Combined Method for "Ab Initio" Structure Solution from Powder Diffraction Data, *J. Appl. Cryst*. **32**, 864-870.

Rasmussen, S. E., J. E. Jorgensen, & B. Lundtoft (1996): Structures and phase transitions of Na_2SO_4. *J. Appl. Cryst*. **29**(1), 42-47 DOI:10.1107/S0021889895008818

Rijniers, L. A., H. P. Huinink, L. Pel., and K. Kopinga (2005) Experimental evidence of crystallisation pressure inside porous media. *Phys. Rev. Lett*. **94**, article 075503 DOI:10.1103/PhysRevLett.94.075503

Ripmeester, J. A., C. I. Ratcliffe, J. E. Dutrizac and J. L. Jambor (1986) Hydronium ion in the alunite-jarosite group. *Canadian Min*. **24**(3), 435-447.

Robinson, K., G. V. Gibbs, & P. H. Ribbe (1971): Quadratic elongation: a quantitative measure of distortion in coordination polyhedra. *Science* **172**, 567-570. DOI:10.1126/science.172.3983.567

Röttger, K., A. Endriss, & J. Ihringer (1994): Lattice constants and thermal expansion of H_2O and D_2O ice Ih between 10 and 265 K. *Acta Cryst.* B**50** 644-646 DOI:10.1107/S0108768194004933

Rowe J. J., G. W. Morey, C. C. Silber, (1967) The ternary system K_2SO_4-$MgSO_4$-$CaSO_4$ *J. Inorg. and Nuc. Chem.* **29**, (4), 925-942, DOI:10.1016/0022-1902(67)80075-7.

Ruben, H. W., D. H. Templeton, R. D. Rosenstein, & I. Olovsson (1961): Crystal structure and entropy of sodium sulfate decahydrate, *J. Am. Chem. Soc*. **83**(4), 820-824 DOI:10.1021/ja01465a019: ICDD entry 01-074-0937.

Sabine T.M. Extinction in polycrystalline materials. (1985) *Aust. J. Phys*. **38** 507 -518.

Sabine T. M., R.B. Von Dreele, J.E. Jorgensen Extinction in time-of-flight neutron powder diffractometry. (1988) *Acta Cryst* A **44** 374 – 379.

Schlenker, J. L., G. V. Gibbs, and M. B. Boison (1975): Thermal expansion coefficients for monoclinic crystals: a phenomenological approach. *Am. Min*. **60**, 823-833.

Schofield P.F., K .S. Knight and I. C. Stretton (1996) Thermal expansion of gypsum investigated by neutron powder diffraction. *Am. Min*. **81** 847-851.

Schofield P. F., & K. S. Knight (2000): Neutron powder diffraction studies of the thermal behaviour of deuterated chalcanthite. *Physica B* **276-278**, 897-898 DOI:10.1016/S0921-4526(99)01282-X

Silvestrelli, P. L. (2009) Improvement in hydrogen bond description using van der Waals-corrected DFT: The case of small water clusters. *Chem. Phys. Lett.* **475** 285 – 288.

Schubert, G., D L Turcotte and P Olson (2006) Mantle convection in the earth and planets Cambridge University Press 940p ISBN 0521798361

K. P. Shkurina, D. N. Osokina, A. V. Mikhailenko and N. Yu. Tsvetkova (1978) *Journal of Mining Science* **14** (3) 310 – 313 DOI:10.1007/BF02499332

Sood, R. R., & Stager, R. A. (1966): Pressure-induced dehydration reactions and transitions in inorganic hydrates. *Science* **154**, 388-390 DOI:10.1126/science.154.3747.388

Spain, I.L. and Seagal, S. (1971) The equation of state of solid helium: A pressure scale to 20 kbar for high pressure measurements at low temperature *Cryogenics* **11**(1) 26 – 38. DOI:10.1016/0011-2275(71)90006-3

Tammann, G. (1929) Über die Schmelzkurven einiger Salzhydrate. *Z. Anorg. Allgem. Chem*., **178**(1), 309-316 DOI:10.1002/zaac.19291790114

Tanaka, Y., Hada, S., Makita, T. & Moritoki, M. (1992) Effect of pressure on the solid-liquid phase equilibria in (water + sodium sulphate) system. *Fluid Phase Equil*., **76**(1), 163-173 DOI:10.1016/0378-3812(92)85085-M

Toby, B. H. (2001): EXPGUI, a graphical user interface for GSAS. *J. Appl. Cryst*. **34**, 210-213 DOI:10.1107/S0021889801002242

Tomlinson, C. (1868): On supersaturated saline solutions. *Phil. Trans. Royal Soc. London* **158**, 659-673.

Tomlinson, C. (1871) On the behaviour of supersaturated saline solutions when exposed to the open air. *Proceedings of the Royal Society of London*. **20**, 41-45.

Tsui, N, R. J. Flatt & G.W. Scherer (2003): Crystallization damage by sodium sulphate. *J. Cultural Heritage* **4**, 109-115 DOI: 10.1016/S1296-2074(03)00022-0

Tsuzuki, S., & Lüthi, H. P. (2001) Interaction energies of van der Waals and hydrogen bonded systems calculated using density functional theory: Assessing the PW91 model. *J. Chem. Phys.* **114**(9), 3949-3957 DOI:10.1063/1.1344891

Tuma, C., Boese, A.D. and Handy, N. C. (1999) Predicting the binding energies of H-bonded complexes: A comparative DFT study. *Phys. Chem. Chem. Phys.* **1** 3939 – 3947

Vanderbilt D. (1990) Soft self-consistent pseudopotentials in a generalized eigenvalue formalism *Phys. Rev. B* **43** 7892 – 7895 DOI:10.1103/PhysRevB.41.7892

Viollette, C. (1866): Mémoire sur la sursaturation. *Annales Scientifique de l'École Normale Supérieur* **30**, 202-252

Vočadlo, L., K. S. Knight, G. D. Price, & I. G. Wood (2002): Thermal expansion and crystal structure of FeSi between 4K and 1173K determined by time of flight neutron powder diffraction. *Phys. Chem. Minerals* **29**(2), 132-139 DOI:10.1007/s002690100202

Vočadlo, L., D.Alfe, GD Price and MJ Gillan 2004 *Ab initio* melting curve of copper by the phase coexistence approach. *J. Chem. Phys.*, **120**, 2872-2878.

Von Bayh, W. (1966). Elastische und mechanische Eigenschaften von Na_2SO_4(thenardit). *Acta. Cryst.* **20**, 931-932 DOI:10.1107/S0365110X66002184

Van't Hoff J. H., Meyerhoffer W, Smith (1901) Untersuchungen über die bildungsverhältnisse der oceanischen salzablagerungen, insbesondere des Stassfurter salzlagen. XXIII. Das auftreten von Kieserit bei 25°. Sitzungsberichte der Preussichen Akademie der Wissenshaften, 1034–1044

Wallace, D. G. (1998): Thermodynamics of crystals. Dover, New York.

Waltham D. (1997) Why does salt start to move? *Tectonophysics* **282** 117 – 128.

Warren J. K. (2006) Evaporites: Sediments, Resources and Hydrocarbons Springer 1036p ISBN-10: 3540260110

Wang, Y., & Perdew, J. P. (1991) Correlation hole of the spin-polarized electron gas, with exact small-wave-vector and high-density scaling. *Phys. Rev. B.*, **44**(24), 13298 – 13307 DOI:10.1103/PhysRevB.44.13298

Wang, Y., M. Akaishi and S. Yamaoka (1999) Diamond formation from graphite in the presence of anhydrous and hydrous magnesium sulfate at high pressures and high temperatures. *Diamond and Related Materials*, **8**(1) 73-77 DOI:10.1016/S0925-9635(98)00396-3.

Washburn, E.R. and W. J. Clem, (1938). The transition temperature of sodium sulfate heptahydrate.*J. Am. Chem. Soc*. **60**, 754–757.

Wood I. G., K. S. Knight, G. D. Price, & J. A. Stuart (2002): Thermal expansion and atomic displacement parameters of cubic $KMgF_3$ perovskite determined by high resolution neutron powder diffraction. *J. Appl. Cryst*. **35**, 291-295 DOI:10.1107/S0021889802002273

Wuite, J. P. (1914): The sodium sulphate - water system. *Z. Phys. Chem. Stoich. Verwandt.* **86**, 349-382.

Appendix 1:

Na_2SO_4 Interatomic potential paper

Title: Studies of anhydrous sodium sulfate polymorphs: fitting of interatomic potentials and calculation of elastic properties.

Authors: H. E. A. Brand,[1] M. Alfredsson,[1] A. D. Fortes,[1] I. G. Wood,[1] L. Vočadlo.[1]

Author affiliations: (1) Department of Earth Sciences, University College London, Gower Street, London, WC1E 6BT, U. K.

Lead author email: h.brand@ucl.ac.uk

1. Introduction

Sodium sulfates are important geological and engineering materials; on Earth Na_2SO_4 occurs in evaporitic sequences as the mineral thenardite or the hydrated mineral mirabilite ($Na_2SO_4.10H_2O$), and often forms in association with dislocations in thrust terrains and as the metasomatic products of the weathering of alkaline igneous rocks.[1] Moreover, sodium sulfates are a major component of the millions of tons of salts found in the dry valleys of Antarctica.[2] Recently the importance of sulfates throughout the solar system has been recognised; Na_2SO_4 is the second most important leachate after $MgSO_4$ from chondritic materials which probably form the rocky cores of the solar system's large icy moons.[3] Mirabilite will therefore be a major rock-forming mineral in the mantles of these icy moons. The use of sodium sulphate as an economic resource has been mainly confined to its inclusion in building concretes and for this reason information concerning the long-term behaviour and weathering of this compound has become sought after.

The dearth of hydrates in the Na_2SO_4 - H_2O system, compared with the $MgSO_4$ - H_2O system (one versus eight), the comparative ease of growing single crystals, and the low decomposition temperature of mirabilite (30°C), has meant that anhydrous sodium sulfate has received more attention than anhydrous magnesium sulfate in the literature. Nonetheless, the structures and phase transitions of anhydrous sodium sulphate have not been studied fully, mainly due to the complexity and metastability of the phase relations. The physical properties of this substance have also been neglected. Several studies have concentrated on the ionic conduction and electrical properties of sodium sulphate[4], but ignored the thermo-elastic properties. The only investigations of the phase diagram of sodium sulphate[5] were to 45kbar using a piston-cylinder and an investigation of the elastic properties of thenardite using interferometry.[6]Anhydrous sodium sulphate is thought to have as many as eight polymorphs up to 4.5 kbar[6] (Fig. 1), but to date, only four of these have been structurally characterised; I, II, III and V[7] (the latter being the naturally occurring phase called thenardite). Phase I, which occurs above 510K, is hexagonal, space group $P6_3/mmc$ and is characterized by complete orientational disorder of the SO_4 tetrahedra[8]. Phase II [is orthorhombic, space group Pbnm], but is only stable over a very small temperature range (503 – 510K) and has been considered by some to be metastable.[5] Phase III (orthorhombic, space group Cmcm) is stable between 473 and 503K at atmospheric pressure, whilst the room P,T form of Na_2SO_4 is phase V (orthorhombic, space group Fddd[9,10]). There is still some debate in the literature as to the existence of a phase IV but recent studies have failed to report any evidence of this phase. The higher pressure polymorphs, VI, VII, and VIII, have yet to be investigated.

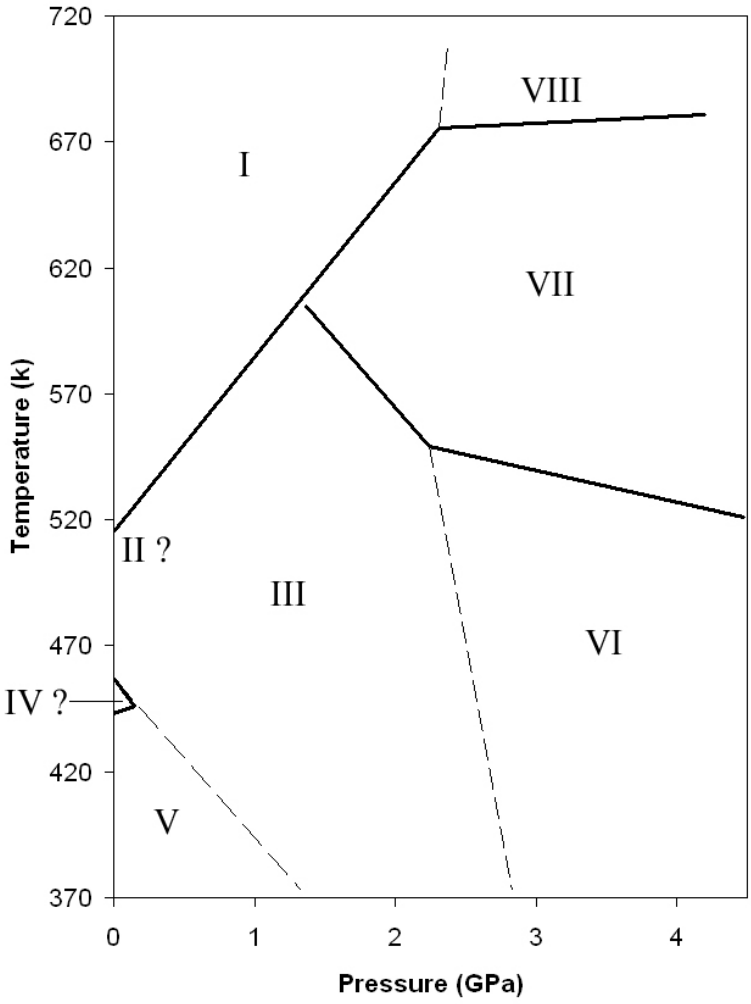

Figure 1. The P,T phase diagram of sodium sulfate from 370 – 720 K, 0 – 4.5 GPa. After Pistorius.[8]

There have been comparatively few computational investigations of molecular ionic materials, such as sulfates. Such complex systems present a challenge to potential calculations as both bonded and non-bonded interactions must be accounted for by any potential model. The models that have been developed are adapted versions of models applied to ionic materials. The earliest investigation of the sulfates[11] developed potentials for potassium sulfate which were then transferred to sodium sulfate. However, these potentials did not discriminate between the bonded and non-bonded interactions present in the structures. A subsequent study by Allan *et al*[12]. did distinguish between these interactions through the inclusion of a Morse potential and was successful in simulating a range of sulfates, including $MgSO_4$ and Na_2SO_4. Most recently, Jackson, (2001)[13] modified the results of Allan *et al*.(1993)[12] by including a harmonic potential (in place of the Morse potential) to represent the S-O interaction.

However, neither Allan *et al*.(1993)[12] nor Jackson (2001),[16] refitted the sulfate potentials to reflect a change in cation; only the cation – oxygen interaction has been modified with each new sulfate system modelled. This means that the interactions, although generally adequate for simulating the bulk lattice parameters of the sulfates as a group, lack the individual complexities needed to represent accurately the multiple phases for each different cation sulfate system which may only differ marginally in their parameters. Another drawback to their method is that it does not take into account the coulombic interactions associated with the sulfate ion itself.

Our goal is to understand the structure and history of large icy moons from the physical properties of the constituent salts; we have recently carried out detailed neutron diffraction studies of mirabilite[14] and of hydrated magnesium sulfate salts.[15] This experimental work is complemented by a mixture of computationally expensive high-level quantum mechanical (QM) calculations and cheaper interatomic potential (IP) calculations. The objective of this paper is to derive Na – O and S – O potentials (without the added complication of bound water) from empirical data on the structure of Na_2SO_4 polymorphs. In a companion paper[16] we present results from the fitting of potentials to structural data for anhydrous magnesium sulfate polymorphs. Such potentials will extend greatly our ability to understand the more structurally complex Na_2SO_4 decahydrate that is so important on Earth and in the outer solar system. We then present a comparison of elastic properties from the IP calculations with experimentally determined elastic stiffness coefficients.

2. Method

2.1 Fitting of interatomic potentials

The basis for the potentials developed here were parameters calculated by Allan *et al*. (1993)[12] Sulfates present a challenge to empirical potential fitting as they consist of a cation ionically bonded to a molecularly bonded sulfate. The model employed by Allan *et al*. (1993)[12] is a rigid ion model which differentiates between inter- and intra–molecular forces. This differentiation allows the sulfate ion to be modelled as a molecular system through the use of Morse and three-body (intramolecular) potentials while the intermolecular forces are modelled by Buckingham potentials (Table 1).

Intermolecular interactions	
Buckingham potential	$U_{ij}^{\text{Buckingham}} = \frac{q_i q_j}{r_{ij}} + A\exp\left(\frac{-r}{\rho}\right) - \left(\frac{C}{r^6}\right)$

Intramolecular interactions	
Morse potential	$U_{ij}^{\text{Morse}} = D_e[1-\exp(-a(r-r_0))]^2 - 1]$
Three-body potential	$U_{ijk}^{\text{three body}} = \frac{1}{2}k_2(\theta-\theta_0)^2$

Table 1 The forms of the interatomic potentials used, r is the interatomic distance over which the potential is operating, q is the atomic charge,θ is the angle between the vectors $\mathbf{r}_{12}$ and $\mathbf{r}_{13}$ while A, ρC, D_e, a, r_0, K_2 and θare the coefficients which have been obtained through empirical fitting.

The potentials derived here have been fitted to existing structural data for Na_2SO_4 phases II, III, and V, ensuring full transferability between polymorphs. To achieve this, the input coefficients required by a particular potential were systematically varied until the output lattice parameters and unit cell volume agreed with the experimental values to within a suitable range (5% for the lattice parameters, 6% for the volume).

During the fitting processes it was found that moderate variation in the Buckingham and Morse potentials and no variation in the three-body potential, from the values established by Allan *et al*.(1993)[12] were needed to produce an extremely satisfactory agreement to published experimental lattice. The fitting and energy minimization calculations reported here were carried out using GULP, General Utilities Lattice Program[17] which calculates bulk and elastic properties for a given potential.

3. Results

The potential coefficients derived by fitting to the available structural data are given in table 2. The agreement between the calculated lattice parameters in the athermal limit and the measured values (at or above room temperature) are presented in table 3. Structural relaxations and calculations of the total energy of the crystal were carried out at a series of fixed unit cell volumes. An integrated form of the 3rd order Birch-Murnaghan equation of state (BMEOS3)[18] was fitted to the E(V) points to determine the zero-pressure volume, V_0, the zero-pressure bulk modulus, K_0, and its first pressure derivative, $(\partial K/\partial P)_0$ or K'_0. The lattice parameters as a function of the calculated pressure were also fitted with a 3rd order Birch-Murnaghan expression to obtain the axial incompressibilities and their pressure derivatives; i.e., $K_a = (1/a^3)(\partial a^3/\partial P)$, and $K'_a = (\partial K_a/\partial P)_T$. The parameters resulting

from these various fits are given in tables 4, and a discussion of how they compare with experimental values follows in Section 4.

Buckingham potentials					
Species	Potential coefficients				Cutoffs (Å)
	A (eV)	ρ (Å)	C (eV Å^6)		
Na – O	550.0	0.296	0.0		18.0
O - O	103585.02	0.2	30.0		18.0
Morse potential					
Species	Potential coefficients				Cutoffs (Å)
	D (eV)	a (Å^{-2})	r_0 (Å)		
S - O	5.0	1.2	1.505		1.8
Three-body potential					
Species	Potential coefficients		Cutoffs (Å)		
	θ (°)	k_2 (eVrad^{-2})			
O – S - O	109.47	15.0	1.6	1.6	3.2

Table 2. Empirically derived potential coefficients for Na_2SO_4.

Na_2SO_4-V (thenardite)		
Lattice parameter	IP	Experimental (Ref. 10) (293 K)
a (Å)	5.9981	5.85820
b (Å)	11.9194	12.29900
c (Å)	9.6297	9.81380
V ($Å^3$)	688.463	707.084
b/a	1.9872	2.0995
c/a	1.6055	1.6752
Na_2SO_4-II		
Lattice parameter	IP	Experimental (Ref. 10) (493 K)
a (Å)	5.2404	5.30991
b (Å)	9.5005	9.46928
c (Å)	6.8246	7.14360
V ($Å^3$)	339.772	359.188
b/a	1.8129	1.7833
c/a	1.3023	1.3453
Na_2SO_4-III		
Lattice parameter	IP	Experimental (Ref. 10) (463 K)
a (Å)	5.6800	5.63041
b (Å)	8.8361	9.04343
c (Å)	6.7681	7.03771
V ($Å^3$)	339.684	358.348
b/a	1.5557	1.6062
c/a	1.1916	1.2499

Table 3. Comparison of calculated (interatomic potential, IP, and Density Functional theory, DFT) athermal lattice parameters to previously published experimental data for three Na_2SO_4 phases.

	Na_2SO_4-V (IP)	Na_2SO_4-II (IP)	Na_2SO_4-III (IP)
V_0 (Å^3)	688.2	339.5	339.5
K_0 (GPa)	45.7	46.7	47.8
K'	6.2	5.8	5.6
K_a (GPa)	49.15(16)	42.8(2)	43.1(3)
K'_a	11.278(10)	4.27(4)	6.81(15)
K_b (GPa)	67.12	42.3	42.33(8)
K'_b	4.7	3.51	3.51(3)
K_c (GPa)	32.45	50.13(15)	61.57(12)
K'_c	4.4	7.70(8)	7.97(5)

Table 4. The calculated (IP) values for the bulk elastic properties of Na_2SO_4. No experimental values exist at present.

	Na_2SO_4-V (thenardite) IP	**Na_2SO_4-V (thenardite)** experimental	**Na_2SO_4-II** IP	**Na_2SO_4-III** IP
c_{ij} (GPa)				
c_{11}	85.17 (+6.0)	80.35	78.35	139.97
c_{22}	117.82 (+11.8)	105.40	77.51	119.81
c_{33}	74.43 (+10.5)	67.36	87.62	136.61
c_{44}	15.18 (+2.8)	14.77	24.04	31.92
c_{55}	18.84 (+4.6)	18.02	15.92	38.64
c_{66}	31.97 (+35.5)	23.59	31.85	16.83
c_{12}	38.83 (+30.3)	29.81	34.57	24.90
c_{13}	23.88 (-6.6)	25.58	29.02	50.42
c_{23}	45.89 (+174.0)	16.75	35.85	43.64
K_0 (GPa)	50.6	42.6	49.0	69.3
K_H (GPa)	52.8	43.4	49.1	69.9
G_H (GPa)	23.3	22.3	23.3	33.5
E (GPa)	61.0	57.0	60.4	86.7
ν	0.308	0.281	0.295	0.293
K_a (GPa)	41.1	48.7	44.3	70.0

K_b (GPa)	158.8	57.1	49.9	55.3
K_c (GPa)	34.9	30.9	53.9	91.7
θ_D (K)	331	322	331	396

Table 5. Calculated (IP) elastic stiffnesses, c_{ij}, for three Na_2SO_4 polymorphs, and some derived quantities: K_0 is the 'relaxed single crystal isotropic bulk modulus', K_H and G_H are the Hill average bulk and shear moduli, E is the Young's modulus, ν is Poisson's ratio, K_a, K_b, and K_c are the axial incompressibilities, and θ_D is the Debye temperature. See Ravindran *et al*. (ref. 19) for the derivation of these quantites from the elastic stiffnesses and compliances. The experimental values are from Von Bayh (ref. 9), and the numbers in brackets in column one give the percentage difference between the calculated and empirical stiffnesses.

Additionally, the elastic stiffness matrix is routinely calculated in GULP through the second derivatives of the energy density with respect to strain:

$$c_{ij} = \frac{1}{V}\left(\frac{\partial^2 U}{\partial \varepsilon_i \partial \varepsilon_j}\right) \qquad \text{Equation 1}$$

where V is the unit cell volume, U the internal energy, ε the strain and c_{ij} are the elastic stiffness coefficients. The calculated elastic constants appear in table 5. Using the method described by Ravindran *et al*.(1998),[19] we have also used the elastic stiffnesses (and compliances, s_{ij}, calculated by matrix inversion) to obtain a number of bulk elastic quantities for comparison with experimental data, where available (table 5).

4. Discussion

Table 3 reveals that the IP calculations yield over-inflated unit cells (by ~ 3 - 5 %) at zero pressure in the athermal limit. However, the experimental values are at much higher temperature (300 - 500 K), so future measurement of the limiting low temperature unit cell dimensions will yield much better agreement. As we found with $MgSO_4$,[16] the unit cell shapes (*b/a* and *c/a*) are not so well replicated (and this is unlikely to be improved by making measurements at low-T), which suggests that some directional aspect of the intermolecular interaction is not being correctly modelled by the potentials, and indicates that anisotropic properties, such as elastic constants and thermal expansion, will not be well reproduced, as discussed below.

Tables 4 presents the bulk elastic properties for the three polymorphs studies. At present, there is no high-pressure experimental data with which to compare our calculated bulk and axial incompressibilities. However, we can gain some insight into how well the

elasticity is being modelled by comparison of the calculated elastic stiffness matrix (table 6) with values determined interferometrically.[9] The table indicates the percentage difference between calculated and measured values (the experimental uncertainties are 0.5 % on c_{11}, c_{22}, and c_{33}, 3 % on c_{12}, c_{13}, and c_{23}, and 2% on c_{44}, c_{55}, and c_{66}), and it is clear that there are some extremely large discrepancies - most notably c_{23}, which is nearly three times larger than the measured value. Figure 2 depicts the calculated (a,b) and experimental (c,d) elasticity tensor (c_{ij}), and a slice in the *y*-*z* plane which highlights the difference in shape due to c_{23}. When we calculate bulk properties from these elastic constants we find that the greatest effect is upon the stiffness of the *b*-axis; K_b becomes almost three times greater than expected, whereas K_a and K_c agree tolerably well. Indeed a very similar phenomenon is seen in our calculation of the elastic constants of α-$MgSO_4$, which yields an *a*-axis stiffness much larger than observed experimentally. For β-$MgSO_4$, by contrast, the elastic constants yield K_a, K_b, and K_c, which are in reasonable agreement with the *ab initio* calculation, so it is also possible that the elastic constants for Na_2SO_4-II and III are well determined.

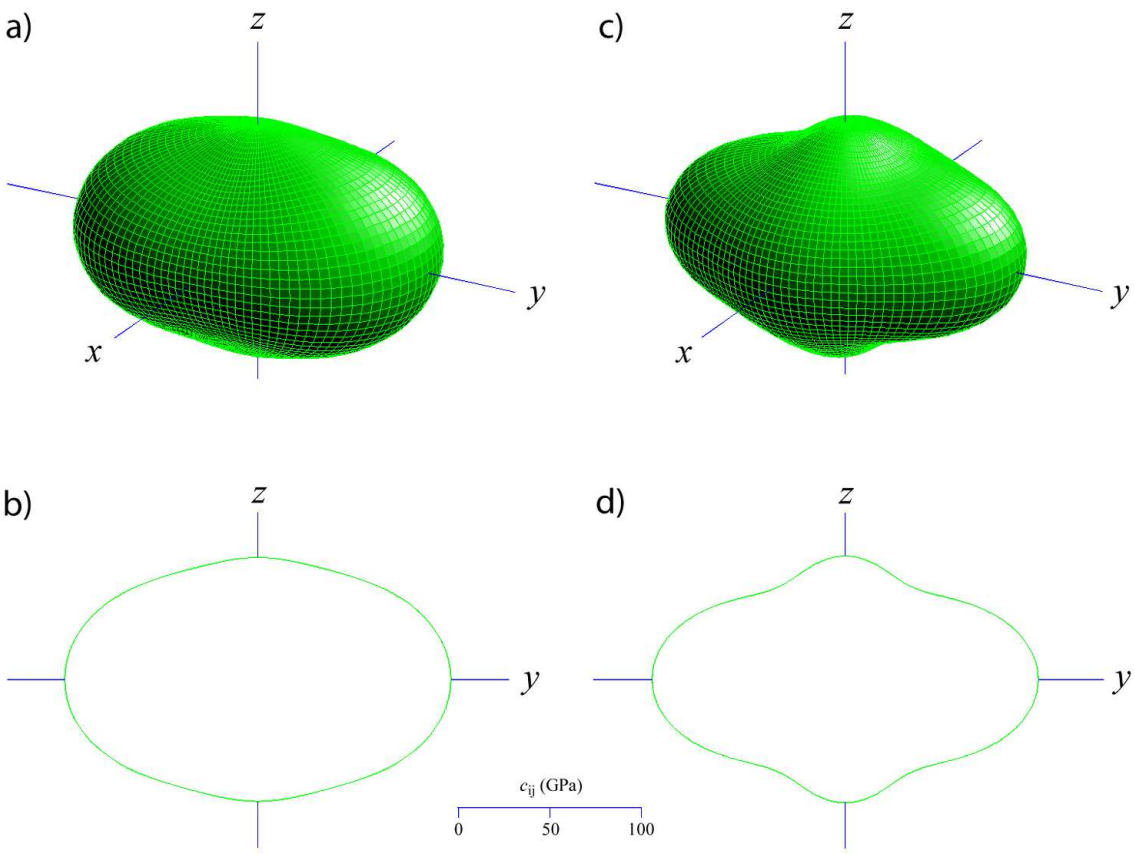

Figure 2. The calculated (a and b) and experimental (c and d) elastic stiffness tensor (c_{ij} surface, units of GPa with a common scale for each panel), with slices in the *y*-*z* plane to illustrate the shape change brought about by the large difference in c_{23} between the two.

It remains to be seen whether the predicted bulk and axial incompressibilities of Na_2SO_4-II, III, and V agree with future experimental data. Moreover, high P,T studies of phases VI, VII, and VIII will help us to elucidate the subtleties of the intermolecular interactions due to minor differences in packing arrangements, which present challenges for the simplistic potential model employed here in terms of longer-range directional forces.

5. Summary

In this paper we have fitted new interatomic potential models to structural data for anhydrous sodium sulfate polymorphs. These models have been used to calculate elastic properties, which we have compared with experimentally determined elastic constants. The derived potentials are shown to be transferable between polymorphs of the same sulfate and the lattice parameters obtained by these potentials agree very well with empirical data.

The fitting of interatomic potentials provides a more cost effective means of calculating structural and elastic properties than quantum mechanical simulation (more so at finite temperatures), allows us to investigate P,T space untrammelled by the constraints of pressure vessels, cryostats or furnaces, and yields 'single-crystal' data for substances where single crystals of the right size are difficult to grow.

Sulfates present a particular challenge to empirical potential fitting as they consist of a cation ionically bonded to a covalent sulfate group. Thus, any model developed must be able to accurately represent a mixture of both bonded and non-bonded interactions over a range of polymorphic phases. The anhydrous sodium sulfate interatomic potential refinements have shown that GULP is an effective tool to mimic the behaviour of salts; the lattice parameters obtained are accurate to within a few percent of the published values. Further application of these potentials in the study of hydrated sulfates will be valuable in supporting existing experimental and *ab initio* data.

Acknowledgments

HEAB acknowledges a postgraduate studentship from the Natural Environment Research Council (NERC): ADF is funded by the Particle Physics and Astronomy Research Council (PPARC), grant number PPA/P/S/2003/00247.

5. References

[1] L. A. Hardie, Annu. Rev. Earth Planet. Sci. 19, 131 (1991).

[2] J. R. Keys, and K. Williams, Geochim. Cosmochim. Acta 45, 2299 (1981).

[3] J. S. Kargel, Icarus 94(2), 368 (1991).

[4] M. M. Ahmad, Solid State Ionics 177, 21 (2006).

[5] C. W. F. T. Pistorius, J. Chem Phys. 43(8) 2895 (1965).

[6] W. Von Bayh, Acta. Cryst. 20, 931 (1966).

[7] S. E. Rasmussen, J-E. Jorgensen and B. Lundtoft, J Appl. Cryst. 29, 42 (1996).

[8] W. Eysel, H. H. Hofer, K. L. Keestert and T. H. Hahn, Acta Cryst. B41, 5 (1985).

[9] F. C. Hawthorne, and R.B. Ferguson, Canadian Mineralogist, 13, 181 (1975).

[10] A. G. Nord, Acta. Chem. Scandia., 27, 814 (1973).

[11] P. Meenan, Ph.D. thesis, University of Strathclyde (1992).

[12] N. L. Allan, A. L. Rohl, D. H. Gay, C. R. A. Catlow, R. J. Davy and W. C. Mackrodt, Faraday Discussions. 95**,** 273 (1993).

[13] R. A. Jackson, Current opinion in solid state and materials science. 5, 463 (2001).

[14] H. E. A. Brand *et al*., ISIS Experimental Report RB610128, submitted for publication in the 2006 Annual Report.

[15] A. D. Fortes, I. G. Wood, K. S. Knight, M. Alfredsson and L. Vočadlo, Eur. J. Min. 18(4), 449 (2006): A. D. Fortes, I. G. Wood, L. Vočadlo, and K. S. Knight, to be submitted to J. Appl. Cryst.

[16] H. E. A. Brand, M. Alfredsson, A. D. Fortes, I. G. Wood, and L. Vočadlo (this volume).

[17] J. D. Gale, J. Chem. Soc., Faraday Trans. 93(4) 629 (1997).

[18] F. Birch, J. Geophys. Res. 57(2), 227 (1952).

[19] P. Ravindran, L. Fast, P. A. Korzhavyi, and B. Johansson, J. Appl. Phys. 84, 4891 (1998).

Appendix 2

Experimental unit-cell parameters for mirabilite on warming and slow-cooling from 4.2 – 300 K from the ambient pressure thermal expansion experiment of Chapter 3.

Warming					
Temperature (K)	**a-axis (Å)**	**b-axis (Å)**	**c-axis (Å)**	**β-angle (°)**	**Unit-cell volume (Å^3)**
4.2	11.4419(1)	10.3428(1)	12.7532(1)	107.838(1)	1436.68(1)
10	11.44180(2)	10.3426(1)	12.7533(2)	107.836(1)	1436.67(2)
20	11.4419(2)	10.3428(1)	12.7531(2)	107.838(1)	1436.67(2)
30	11.4423(2)	10.3426(1)	12.7530(2)	107.838(2)	1436.69(2)
40	11.4425(2)	10.3420(1)	12.7525(2)	107.836(2)	1436.58(2)
50	11.4434(2)	10.3418(1)	12.7524(2)	107.835(2)	1436.66(2)
60	11.4444(2)	10.3418(1)	12.7525(2)	107.836(2)	1436.79(3)
70	11.4460(2)	10.3415(1)	12.7533(2)	107.837(2)	1437.03(2)
80	11.4476(2)	10.3421(1)	12.7540(2)	107.836(2)	1437.41(2)
90	11.4495(2)	10.3425(1)	12.7558(2)	107.834(2)	1437.91(3)
100	11.4521(2)	10.3429(1)	12.7575(2)	107.834(2)	1438.49(2)
110	11.4545(2)	10.3437(1)	12.7592(2)	107.831(2)	1439.11(2)
120	11.4569(2)	10.3443(1)	12.7621(2)	107.833(2)	1439.80(3)
130	11.4592(2)	10.3454(1)	12.7646(2)	107.829(2)	1440.57(3)
140	11.4619(2)	10.3461(1)	12.7686(2)	107.832(2)	1441.43(3)
150	11.4645(2)	10.3467(1)	12.7717(2)	107.829(2)	1442.22(3)
160	11.4668(2)	10.3482(1)	12.7749(2)	107.821(2)	1443.15(3)
170	11.4695(2)	10.3493(1)	12.7781(2)	107.811(2)	1444.09(3)
180	11.4717(2)	10.3511(2)	12.7814(2)	107.804(2)	1445.03(3)
190	11.4744(2)	10.3521(2)	12.7856(2)	107.794(2)	1446.07(3)
200	11.4772(2)	10.3536(2)	12.7898(2)	107.791(2)	1447.14(3)
210	11.4803(2)	10.3544(2)	12.7944(2)	107.783(2)	1448.23(3)
220	11.4832(2)	10.3562(2)	12.7991(2)	107.777(2)	1449.42(3)
230	11.4862(2)	10.3572(2)	12.8038(2)	107.770(2)	1450.54(3)
240	11.4895(2)	10.3585(2)	12.8092(2)	107.763(2)	1451.80(3)
250	11.4928(3)	10.3597(2)	12.8148(2)	107.754(2)	1453.10(4)
260	11.4965(3)	10.3606(2)	12.8205(3)	107.750(2)	1454.36(4)
270	11.5014(3)	10.3612(2)	12.8268(3)	107.753(3)	1454.75(4)
280	11.5049(3)	10.3624(2)	12.8333(2)	107.750(2)	1457.15(4)
290	11.5097(3)	10.3637(2)	12.8396(2)	107.754(2)	1458.61(4)
300	11.5144(3)	10.3650(2)	12.8461(3)	107.751(3)	1460.14(4)
Slow Cooling					
Temperature (K)	**a-axis (Å)**	**b-axis (Å)**	**c-axis (Å)**	**b-angle (°)**	**Unit-cell volume (Å^3)**
300	11.5149(2)	10.365(1)	12.8466(2)	107.757(1)	1460.22(2)
295	11.5123(3)	10.3643(2)	12.8439(3)	107.756(3)	1459.49(4)
285	11.5077(3)	10.3632(2)	12.8363(3)	107.754(2)	1457.91(4)
275	11.5032(3)	10.3618(2)	12.8304(3)	107.756(2)	1456.45(4)
265	11.4991(3)	10.3609(2)	12.8241(2)	107.754(2)	1455.12(4)
255	11.4950(2)	10.3599(2)	12.8183(2)	107.757(2)	1453.77(3)
245	11.4916(2)	10.3585(2)	12.8127(2)	107.758(2)	1452.51(3)
235	11.4879(2)	10.3573(2)	12.8073(2)	107.762(2)	1451.21(3)
225	11.4845(2)	10.3558(2)	12.8024(2)	107.770(2)	1449.95(3)
215	11.4815(2)	10.3540(2)	12.7973(2)	107.773(2)	1448.73(3)
205	11.4786(2)	10.3526(2)	12.7931(2)	107.779(2)	1447.63(3)
195	11.4757(2)	10.351(2)	12.7888(2)	107.785(2)	1446.53(3)
185	11.4732(2)	10.3503(2)	12.7847(2)	107.793(2)	1445.57(3)
175	11.4705(2)	10.3487(2)	12.7809(2)	107.799(2)	1444.55(3)
165	11.4682(2)	10.3480(2)	12.7769(2)	107.814(2)	1443.58(3)

155	11.4656(2)	10.3466(2)	12.7737(2)	107.818(2)	1442.65(3)
145	11.4630(2)	10.3454(2)	12.7711(2)	107.829(2)	1441.78(3)
135	11.4603(2)	10.3447(2)	12.7677(2)	107.835(2)	1440.92(3)
125	11.4581(2)	10.3438(2)	12.7649(2)	107.837(2)	1440.18(3)
115	11.4555(2)	10.3432(1)	12.7624(2)	107.838(2)	1439.46(3)
105	11.4532(2)	10.3425(1)	12.7590(2)	107.842(2)	1438.73(3)
95	11.4509(2)	10.3417(1)	12.7579(2)	107.843(2)	1438.15(3)
85	11.4488(2)	10.3418(1)	12.7565(2)	107.846(1)	1437.70(3)
75	11.4471(2)	10.3413(1)	12.7553(2)	107.848(1)	1437.28(3)
65	11.4454(2)	10.3413(1)	12.7541(2)	107.848(1)	1436.93(3)
55	11.4443(2)	10.3413(1)	12.7541(2)	107.849(1)	1436.78(2)
45	11.4433(2)	10.3416(1)	12.7538(2)	107.849(1)	1436.67(2)
35	11.4426(2)	10.3420(1)	12.7541(2)	107.849(1)	1436.65(2)
25	11.4426(2)	10.3424(1)	12.7542(2)	107.848(1)	1436.71(2)
15	11.4422(2)	10.3424(1)	12.7547(2)	107.847(1)	1436.75(2)
4.2	11.4423(2)	10.3425(1)	12.7547(1)	107.849(1)	1436.77(1)

Appendix 3.

H-bond lengths from each of the long soaks in Chapter 3

1. Hydrogen bond lengths and angles in mirabilite at 4.2 K slow cooled.

4.2K Slow cooled	O - D	D---O	O---O	O - D --- O
O8 - D8B---O16	0.9897(21)	1.842(6)	2.748(6)	157.7(5)
O16 - D16C---O8	0.9880(22)	1.886(6)	2.748(6)	149.6(8)
O9 - D9C---O17	0.9905(22)	1.757(6)	2.730(6)	166.5(9)
O17 - D17B---O9	0.9924(21)	1.753(6)	2.730(6)	167.5(5)
O8 - D8C---O16	0.9902(22)	1.766(7)	2.748(6)	170.7(7)
O16 - D16B---O8	0.9886(21)	1.766(6)	2.748(6)	171.6(5)
O9 - D9B---O17	0.9899(21)	1.786(6)	2.730(6)	168.8(6)
O17 - D17C---O9	0.9894(22)	1.816(9)	2.730(6)	159.3(15)
O12 - D12A---O10	0.9845(21)	1.863(6)	2.847(6)	177.7(5)
O13 - D13A---O11	0.9842(21)	1.866(6)	2.850(6)	177.0(5)
O14 - D14A---O10	0.9876(21)	1.802(6)	2.775(6)	168.1(4)
O15 - D15B---O11	0.9865(21)	1.829(6)	2.797(6)	166.5(4)
O8 - D8A---O5	0.9845(21)	1.811(6)	2.775(6)	165.7(4)
O10 - D10A---O5	0.9864(21)	1.839(5)	2.817(5)	170.4(4)
O12 - D12B---O5	0.9813(20)	1.946(5)	2.919(5)	170.7(5)
O10 - D10B---O4"	0.9836(21)	1.849(5)	2.823(5)	170.2(5)
O11 - D11A---O4"	0.9856(21)	1.848(5)	2.831(5)	174.8(5)
O9 - D9A"---O4"	0.9851(21)	1.764(6)	2.747(6)	174.8(4)
O11 - D11B---O6"	0.9860(21)	1.855(5)	2.821(5)	165.9(4)
O13 - D13B---O6"	0.9869(20)	1.938(5)	2.918(5)	171.6(4)
O17 - D17A"---O6"	0.9847(21)	1.941(6)	2.916(5)	170.5(5)
O14 - D14B---O7"	0.9901(21)	1.828(5)	2.805(5)	168.3(5)
O15 - D15A---O7"	0.9892(21)	1.825(5)	2.798(5)	167.4(4)
O16 - D16A"---O7"	0.9850(21)	1.821(5)	2.785(5)	165.4(5)

2. Hydrogen bond lengths and angles in mirabilite at 4.2 K rapidly cooled.

4.2K Quenched	O - D	D---O	O---O	O - D --- O
O8 - D8B---O16	0.9898(22)	1.846(7)	2.755(6)	157.6(6)
O16 - D16C---O8	0.9877(23)	1.881(6)	2.755(6)	151.1(8)
O9 - D9C---O17	0.9900(23)	1.781(6)	2.755(6)	167.2(9)
O17 - D17B---O9	0.9932(22)	1.774(6)	2.755(6)	168.7(6)
O8 - D8C---O16	0.9902(23)	1.773(7)	2.755(6)	170.5(7)
O16 - D16B---O8	0.9881(22)	1.772(6)	2.755(6)	172.6(6)
O9 - D9B---O17	0.9886(22)	1.783(7)	2.755(6)	171.1(7)
O17 - D17C---O9	0.9890(23)	1.804(8)	2.755(6)	162.8(14)
O12 - D12A---O10	0.9869(21)	1.859(6)	2.844(6)	176.6(5)
O13 - D13A---O11	0.9840(21)	1.862(6)	2.845(6)	176.5(5)
O14 - D14A---O10	0.9865(21)	1.797(6)	2.769(6)	168.1(4)
O15 - D15B---O11	0.9843(21)	1.822(6)	2.789(6)	166.5(4)
O8 - D8A---O5	0.9816(22)	1.805(6)	2.767(6)	165.8(5)
O10 - D10A---O5	0.9874(21)	1.847(5)	2.826(5)	170.7(4)
O12 - D12B---O5	0.9855(21)	1.935(5)	2.913(5)	171.0(5)
O10 - D10B---O4"	0.9856(21)	1.841(5)	2.816(5)	169.6(5)
O11 - D11A---O4"	0.9871(21)	1.863(5)	2.848(5)	175.0(5)
O9 - D9A"---O4"	0.9826(21)	1.763(6)	2.743(6)	174.4(4)
O11 - D11B---O6"	0.9878(22)	1.846(5)	2.816(5)	166.3(4)
O13 - D13B---O6"	0.9887(21)	1.944(5)	2.928(5)	172.7(5)
O17 - D17A"---O6"	0.9855(21)	1.932(6)	2.909(6)	170.7(5)
O14 - D14B---O7"	0.9888(22)	1.822(6)	2.799(6)	169.3(5)
O15 - D15A---O7"	0.9868(21)	1.830(5)	2.802(5)	167.4(4)
O16 - D16A"---O7"	0.9842(21)	1.819(5)	2.779(6)	164.0(5)

3. Hydrogen bond lengths and angles in mirabilite at 150 K.

150K	O - D	D---O	O---O	O - D --- O
O8 - D8B---O16	0.9890(19)	1.868(7)	2.715(7)	155.2(7)
O16 - D16C---O8	0.9893(20)	1.888(7)	2.715(7)	151.4(8)
O9 - D9C---O17	0.9898(20)	1.748(7)	2.721(7)	166.8(10)
O17 - D17B---O9	0.9910(19)	1.752(7)	2.721(7)	164.9(6)
O8 - D8C---O16	0.9893(20)	1.732(8)	2.715(7)	171.8(9)
O16 - D16B---O8	0.9871(19)	1.737(7)	2.715(7)	169.8(6)
O9 - D9B---O17	0.9913(19)	1.798(8)	2.721(7)	171.4(8)
O17 - D17C---O9	0.9890(20)	1.830(9)	2.721(7)	160.7(14)
O12 - D12A---O10	0.9881(19)	1.869(7)	2.856(7)	176.8(6)
O13 - D13A---O11	0.9870(19)	1.870(7)	2.856(7)	176.2(6)
O14 - D14A---O10	0.9883(19)	1.813(7)	2.787(7)	168.0(4)
O15 - D15B---O11	0.9860(19)	1.827(7)	2.790(7)	164.8(4)
O8 - D8A---O5	0.9850(19)	1.814(7)	2.774(7)	163.9(6)
O10 - D10A---O5	0.9889(19)	1.847(6)	2.829(6)	171.4(4)
O12 - D12B---O5	0.9876(19)	1.943(6)	2.920(6)	169.6(5)
O10 - D10B---O4"	0.9878(19)	1.825(6)	2.802(6)	169.2(5)
O11 - D11A---O4"	0.9895(19)	1.861(6)	2.848(6)	175.9(5)
O9 - D9A"---O4"	0.9859(19)	1.777(7)	2.757(7)	172.2(5)
O11 - D11B---O6"	0.9882(19)	1.842(6)	2.812(6)	166.3(5)
O13 - D13B---O6"	0.9900(19)	1.946(6)	2.932(6)	173.4(5)
O17 - D17A"---O6"	0.9872(19)	1.974(6)	2.948(6)	168.6(5)
O14 - D14B---O7"	0.9897(19)	1.827(6)	2.804(6)	168.7(6)
O15 - D15A---O7"	0.9883(19)	1.819(6)	2.790(6)	166.7(4)
O16 - D16A"---O7"	0.9870(19)	1.836(6)	2.798(6)	164.0(5)

4 Hydrogen bond lengths and angles in mirabilite at 300 K rapidly cooled

300K	O - D	D---O	O---O	O - D --- O
O8 - D8B---O16	0.9897(15)	1.851(10)	2.716(10)	157.4(8)
O16 - D16C---O8	0.9903(15)	1.872(9)	2.716(10)	153.0(9)
O9 - D9C---O17	0.9902(15)	1.813(10)	2.749(12)	163.6(11)
O17 - D17B---O9	0.9907(15)	1.831(10)	2.749(12)	158.6(10)
O8 - D8C---O16	0.9895(15)	1.741(11)	2.716(10)	167.5(11)
O16 - D16B---O8	0.9898(15)	1.750(9)	2.716(10)	164.1(12)
O9 - D9B---O17	0.9899(15)	1.774(11)	2.749(12)	167.5(12)
O17 - D17C---O9	0.9905(15)	1.764(12)	2.749(12)	172.1(11)
O12 - D12A---O10	0.9897(15)	1.919(10)	2.908(10)	176.3(7)
O13 - D13A---O11	0.9892(15)	1.843(10)	2.827(10)	173.1(7)
O14 - D14A---O10	0.9896(15)	1.767(11)	2.746(10)	169.5(6)
O15 - D15B---O11	0.9897(15)	1.874(12)	2.840(11)	164.5(6)
O8 - D8A---O5	0.9892(15)	1.818(10)	2.782(10)	164.1(7)
O10 - D10A---O5	0.9888(15)	1.904(10)	2.875(10)	166.7(7)
O12 - D12B---O5	0.9880(15)	1.961(9)	2.938(9)	169.3(8)
O10 - D10B---O4"	0.9883(15)	1.815(8)	2.799(9)	173.4(8)
O11 - D11A---O4"	0.9883(15)	1.843(9)	2.831(9)	177.9(6)
O9 - D9A"---O4"	0.9894(15)	1.831(9)	2.816(9)	172.7(6)
O11 - D11B---O6"	0.9885(15)	1.838(9)	2.809(10)	166.7(7)
O13 - D13B---O6"	0.9886(15)	1.965(10)	2.943(9)	169.8(8)
O17 - D17A"---O6"	0.9891(15)	2.123(10)	3.058(9)	157.1(8)
O14 - D14B---O7"	0.9898(15)	1.823(9)	2.794(10)	166.2(9)
O15 - D15A---O7"	0.9899(15)	1.767(9)	2.740(10)	166.6(7)
O16 - D16A"---O7"	0.9886(15)	1.988(10)	2.929(10)	158.1(8)

Appendix 4.

Unit-cell parameters for mirabilite determined in the high pressure experiment of Chapter 4.

Temperature (K)	Pressure (GPa)	*a* – axis(Å)	*b* – axis(Å)	*c* – axis(Å)	β-angle (°)	Unit –cell volume (Å^3)
260	0.048	11.487(3)	10.359(2)	12.816(4)	107.77(3)	1452.1(5)
260	0.048	11.489(3)	10.356(2)	12.818(4)	107.78(3)	1452.1(5)
260	0.103	11.476(3)	10.351(2)	12.799(4)	107.75(2)	1448.1(5)
260	0.152	11.464(4)	10.346(2)	12.786(4)	107.72(3)	1444.7(5)
260	0.2	11.460(3)	10.340(2)	12.773(4)	107.70(3)	1441.9(5)
260	0.248	11.450(3)	10.336(2)	12.759(4)	107.67(3)	1438.7(5)
260	0.3	11.439(3)	10.331(2)	12.742(4)	107.61(3)	1435.3(5)
260	0.35	11.425(3)	10.322(2)	12.720(5)	107.60(3)	1429.8(6)
260	0.393	11.416(3)	10.315(2)	12.697(4)	107.58(3)	1425.3(5)
260	0.453	11.408(3)	10.312(2)	12.681(4)	107.57(3)	1422.2(5)
260	0.501	11.399(3)	10.305(2)	12.672(4)	107.57(3)	1419.3(5)
260	0.541	11.393(3)	10.305(3)	12.662(4)	107.56(3)	1417.3(5)
240	0.54	11.389(3)	10.300(2)	12.664(4)	107.53(3)	1416.4(5)
220	0.539	11.386(3)	10.299(2)	12.661(4)	107.57(3)	1415.5(5)
200	0.538	11.385(2)	10.296(2)	12.659(4)	107.53(3)	1415.0(4)
180	0.537	11.382(2)	10.292(2)	12.667(4)	107.53(2)	1415.0(4)
160	0.536	11.380(3)	10.289(3)	12.664(4)	107.53(2)	1414.0(4)
140	0.535	11.379(3)	10.290(3)	12.659(4)	107.57(2)	1413.2(4)
120	0.534	11.379(3)	10.287(2)	12.653(4)	107.64(2)	1411.5(4)
100	0.532	11.373(2)	10.290(3)	12.646(4)	107.61(2)	1410.6(4)
80	0.473	11.378(2)	10.294(2)	12.649(4)	107.65(2)	1411.7(4)
80	0.413	11.384(2)	10.297(2)	12.667(4)	107.60(2)	1415.4(4)
80	0.352	11.394(2)	10.308(2)	12.673(3)	107.64(2)	1418.4(4)
80	0.293	11.405(2)	10.316(2)	12.694(3)	107.64(2)	1423.3(4)
80	0.231	11.416(2)	10.322(1)	12.708(3)	107.65(2)	1426.9(4)
80	0.167	11.423(3)	10.329(3)	12.714(1)	107.67(2)	1429.3(4)
80	0.105	11.437(3)	10.337(2)	12.732(3)	107.71(2)	1433.8(3)
80	0.041	11.445(2)	10.344(2)	12.747(5)	107.72(2)	1437.5(3)
80	0.002	11.452(2)	10.347(1)	12.754(3)	107.73(2)	1439.4(3)

Appendix 5.

Beamtime application to study protenated and deuterated mirabilite.

Measuring the Grüneisen and Anderson-Grüneisen parameters of mirabilite ($Na_2SO_4.10D_2O$)

Introduction – scientific rationale

Multiply hydrated salts, such as hydrated sodium sulfate ($Na_2SO_4.10H_2O$) - the mineral mirabilite – Epsom salt ($MgSO_4.7H_2O$) and Fritzsche's salt, $MgSO_4.11H_2O$ are likely to be major 'rock-forming' minerals in the interiors of the solar system's large icy moons (Kargel, 1991). This supposition is supported by observational evidence from the Near Infrared Mapping Spectrometer (NIMS) instrument on the Galileo space-craft, which orbited Jupiter from 1995 to 2003; NIMS collected multispectral images of the surfaces of Jupiter's icy moons, Europa, Ganymede, and Callisto and these spectra have been interpreted as showing deposits of hydrated alkali salts associated with liquids erupted onto the surface (Dalton *et al*., 2005; Orlando *et al*., 2005). On Earth, mirabilite occurs in evaporites, often forming extremely thick deposits which are able to flow and form diapiric structures within sedimentary basins (e.g., Colman *et al*., 2002).

Whether we wish to model the behaviour of deeply lain evaporites on Earth, or to construct geophysical models of icy moons, it is necessary to know the phase behaviour and thermoelastic properties of the constituent materials under the appropriate pressure and temperature conditions; for the large icy moons we are concerned with pressures up to ~ 5 GPa, and temperatures from 100 – 300 K.

In our previous application (RB610128), we applied for four days to measure the ambient-pressure thermal expansion, and to study the high-pressure behaviour of mirabilite; we were awarded two days and, therefore, were able only to measure the thermal expansivity from 4.2 – 300 K (see experimental report RB610128). The purpose of this continuation is to request the additional two days necessary to carry out the high-pressure study. Since the specific heat of mirabilite is known (e.g. Brodale and Giauque 1957), measurements of its incompressibility at different temperatures will allow us to determine both its Grüneisen and Anderson-Grüneisen parameters (see below). The latter quantity has now been determined for some of the simple inorganic solids, such as magnesio-wüstite ($Mg_xFe_{1-x}O$), that form major components of the Earth's mantle; as planetary scientists it is of similar importance for us to determine it for the "rock-forming minerals" of the outer solar system.

Previous work on mirabilite in the literature.

Sodium sulfate decahydrate is the stable phase in equilibrium with a saturated solution at room temperature and is the only confirmed hydrate of sodium sulfate at ambient pressure, although there is some evidence for a heptahydrate (see below). Mirabilite is monoclinic, space group $P2_1/c$ ($Z = 4$, $a = 11.512(3)$ Å, $b = 10.370(3)$ Å, $c = 12.847(2)$ Å and $\beta = 107.789(10)$ ° at 25.3°C); the structure consists of edge sharing $Na(H_2O)_6$ octahedra with orientationally disordered interstitial water molecules (Ruben *et al*., 1960: Levy and Lisensky, 1978). Measurements of the heat capacity as a function of temperature suggested that the hydrogen bond disorder is frozen-in to limiting low temperatures (<150˚K) (Pitter and Coulter, 1938; Brodale and Giauque 1957; Ruben *et al*. 1960). The only high pressure studies have been concerned with the pressure dependence of the ice-mirabilite eutectic (Tanaka *et al*., 1992; Hogenboom *et al*. 1997) and the pressure dependence of the incongruent melting point (Tamman, 1929). Tanaka *et al.* (1992) investigated the system to 5 kbar, between 263 K and 343 K, and did not observe any high pressure phases; Hogenboom *et al*. (1997), who worked up to 3.5 kbar, saw evidence of other solid phases which they tentatively identified with the purported heptahydrate reported by Hills and Wills (1938).

Our earlier work on mirabilite.

Our previous experiment (RB 610128), carried out in July 2006, yielded excellent data (e.g., Fig. 1) over the range from 4.2 – 300 K. Samples that were cooled quickly or slowly were observed to behave differently (especially in their β angle) and so it was necessary to collect data both on warming and on cooling. These data were refined to yield unit-cell parameters (Fig. 2) and hence determine the full thermal expansion tensor, α_{ij}, as a function of temperature. We were also able to measure changes in the occupancy of partially filled sulfate oxygen sites (observing different behaviour upon quenching from that obtained during slow warming), and to investigate the hydrogen-bond disorder at limiting low temperatures. We have also recently carried out *ab initio* simulations of mirabilite from ambient pressures to 100GPa and these experiments would serve to validate the low pressure values of K (22(1)GPa) and K'(5(1)) obtained from these simulations and thus allow determination of thermoelastic cross-terms such as the Grüneisen parameter (= $\alpha KV/C_V$).

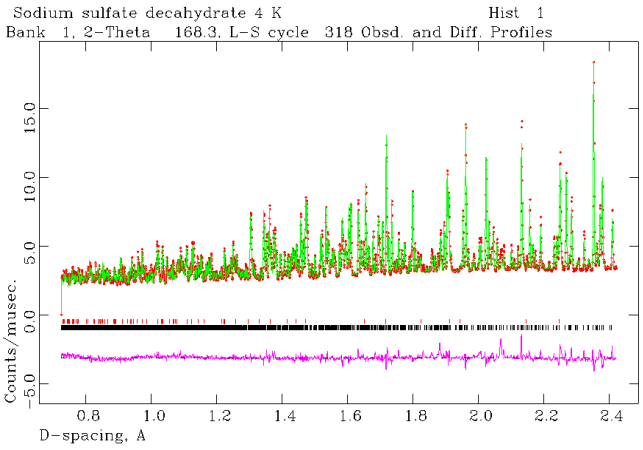

Fig. 1. Diffraction pattern of mirabilite at 4.2 K in the backscattering bank of HRPD. GSAS structure refinement (green); observed data (red); difference plot (purple).

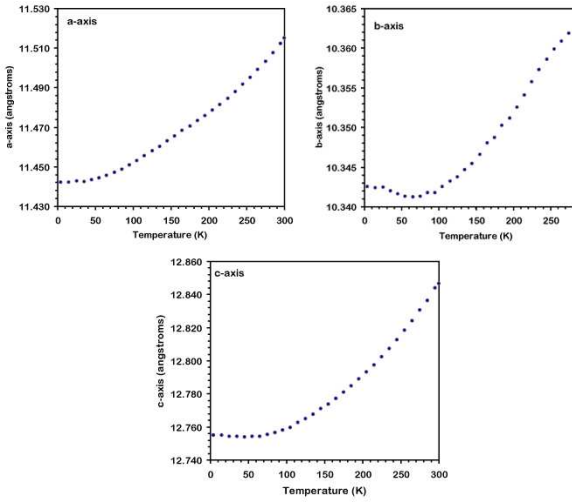

Fig 2. The temperature dependence of the *a*-, *b*- and *c*-axes. The symbols are comparable in size to the standard errors.

The proposed experiment

The objective of this continuation is to carry out the high-pressure study of mirabilite, which will form the final part of the neutron diffraction experiments required for Miss Helen Brand's Ph.D. thesis.

Our goals are to, 1) measure the unit cell parameters along two isotherms from 0 – 5.5 kbar, using a TiZr gas pressure vessel, and 2) measure the unit cell parameters along one or more isobars from 150 – 300 K. This same strategy was employed by us to characterize the thermoelastic properties of epsomite (Fortes *et al.*, 2006). As well as allowing determination of the Grüneisen parameter (see above), these measurements will enable us to obtain the pressure dependence of the thermal expansivity and the temperature dependence of the incompressibility, which are linked by the dimensionless quantity, δ_T, called the Anderson-Grüneisen parameter, defined such that $\delta_T = -(\partial \ln K_T/\partial \ln V) = (\partial \ln \alpha_P/\partial \ln V)$.

Moreover, it is quite possible that there will be either a polymorphic phase transformation or a dehydration reaction at high-pressure, either of which would have implications for planetary modelling.

Our earlier experience with deuterated mirabilite suggests that diffraction patterns suitable for unit-cell refinement may be collected in the gas cell on HRPD in around 120 minutes. The new HRPD beam guide should lead to a considerable improvement in counting statistics compared with our study of epsomite (Fortes *et al.*, 2006) and improved precision on the unit cell parameters. This experiment would be suitable for the commissioning program of the HRPD upgrade. Including temperature equilibration and cell

loading, we anticipate that a minimal twenty-two high pressure data points will require 72 hours to collect. Thus we request a total of 3 days on HRPD to complete this experiment.

References

Coleman *et al.* (2002) Sed. Geol. **148**, 61 – 78.
Dalton *et al.* (2005) Icarus **177**, 472 – 490.
Fortes *et al*. (2006) Eur. J. Min. **18**(4), 449 – 462.
Hill and Wills (1938) J. Am. Chem. Soc. **60**, 1647 – 1655.
Hogenboom *et al*. (1997) Lunar Planet. Sci. Conf. **28**, p 579.
Kargel (1991) Icarus **94**, 368-390.
Orlando *et al.* (2005) Icarus **177**, 528 – 533.
Tammann (1929) Z. für Anorg. Allgem. Chem. **179**(1), 186-192.
Tanaka *et al*. (1992) Fluid Phase Equil. **76**, 163 – 173.